UNIVERSITY OF KENT

DOCTORAL THESIS

Towards high-speed Swept Source Optical Coherence Tomography

Author:

Alejandro

MARTÍNEZ JIMÉNEZ

Supervisor:

Prof Adrian

Gh. PODOLEANU

A thesis submitted in fulfilment of the requirements

for the degree of Doctor of Philosophy

in the

Applied Optics Group

School of Physical Sciences

July 2024

Declaration of Authorship

I, Alejandro MARTINEZ JIMENEZ, declare that this thesis titled, "Towards high-speed Swept Source Optical Coherence Tomography" and the work presented in it are my own. I confirm that:

Signed:

_____

Date:

_____

Last compiled: Monday 7th April, 2025 at 5:40pm.

"La ciencia nos enseña, en efecto, a someter nuestra razón a la verdad y a conocer y juzgar las cosas tal como son, es decir, como ellas mismas eligen ser y no como quisiéramos que fueran."

Miguel de Unamuno, Spanish writer and philosopher

Abstract

OPTICAL coherence tomography (OCT) has evolved into an impactful biomedical imaging modality, with swept-source OCT (SS-OCT) emerging as a key technology for pushing axial scan rates from hundreds of Hz to tens of MHz. However, achieving these high speeds introduces critical challenges: (i) developing light sources capable of emitting stable multi-MHz sweeps, (ii) scaling lateral scanners to match axial speeds, and (iii) enabling real-time processing with digitizers exceeding tens of GSa/s. Resolving these limitations is imperative, as high-speed OCT unlocks transformative applications—from capturing dynamic processes to reducing motion artifacts in clinical imaging and enabling large-volume diagnostics. Advancements in this area promise to expand OCT's role in functional imaging, intraoperative guidance, and high-throughput screening, bridging the gap between laboratory innovation and real-world clinical impact.

At first, it remains hard to produce swept sources that are able to sweep at multi-MHz; for that, a sweep modality that is able to cope with high rates such as time stretch has been investigated in this thesis to overcome the issues above. A commercially available Erbium-doped amplifier is transformed into a mode-locked laser by nonlinear polarization rotation, which seeds a dispersion compensation fibre, stretching the pulse duration to nearly 200 ns. The OCT capabilities of the source are tested, and the main imaging parameters, such as axial resolution, range and drop-off, are characterized. Secondly, a 40 MHz swept source laser based on time-stretch after a supercontinuum is used along with an electro-optic deflector, a potassium tantalum niobate (KTN) crystal, producing a system that was able to capture volumes at 400 Hz. However, the processing to obtain the OCT images is not done in real-time. As such, in the final part of this thesis, alternative processing algorithms are explored to generate real-time in-vivo images of the retina and cornea; i) through numerical procedures, a novel FDML laser at 850 nm is used at 828 kHz with bidirectional sweeping. For the first time, an FMDL laser has been integrated with complex master-slave (CMS) systems; the laser has been fully characterized and enables real-time B-Scans and *en-face* imaging of the human retina. ii) A MEMS-VCSEL swept source centred at 1060 nm working at 1.6 MHz is used in a downconversion scheme where two interferometers are used, and the high frequencies generated in the measuring interferometer are mixed with a reference signal to downconvert the signal to lower frequencies and alleviate the requirements needed for a high sampling rate digitiser. The main similarities and differences between the numerical processing methods and analogue methods are given. Finally, *en-face* OCT images of the retina with the downconversion scheme are presented.

Acknowledgements

The completion of this thesis would not have been possible without the support and guidance of so many remarkable individuals. I am deeply grateful to have had the privilege of working alongside such an inspiring team throughout this journey.

First and foremost, I would like to express my profound gratitude to my supervisor, Prof. Adrian Podoleanu, whose unwavering belief in me from the very beginning has been instrumental. His relentless dedication, encouragement, and ability to motivate everyone around him have left an indelible mark on my academic and personal growth.

I am also immensely thankful to Dr. Adrian Bradu, whose expertise and patience helped me understand the intricacies of OCT in practice. His invaluable insights and practical advice were pivotal in shaping this work.

I would also like to thank the international connections I have made through this research path, particularly Sacha Grelet, from whom I learned about discipline, how things should be done, and numerous useful tips, and who shared many enjoyable moments during his secondments at Kent. Then Marie Klufts taught me not to destroy half of the electronic components in our lab. However, she also changed my perspective on the importance of enjoying our journey and discovering ourselves... Also, I would like to acknowledge all the people from the AOG, Lucy, for all her time correcting the language on this thesis and subsequent manuscripts; Julien Camard for being the friend that I needed during my time here in the UK; Adrian Fernandez Uceda, the weird Spaniard whose I've spent many, many hours, has taught me an incredible amount of interesting and also unnecessary facts; Gopika Venugopal for the love for Indian food; Dr Manuel Marques, to make me believe that Portugal should not be invaded; Dr Michael Hughes, for his calm and always smiley treat; Hal Dorrington who I needed 2 years to understand his British accent; Rene Riha for his professionalism; Dr Ramona Cernat for being the realistic person; Dr Gianni Nteroli for his tips and kindness; Dr Radu Stancu, the economical tips guy; Dr Rasmus Elliake, who hopefully will be Spanish citizenship sooner than later; Josh Fenell, the fruit guy; Taylor Sanderson, the handyguy; Apart from the people already mentioned, I need to mention the amazing help from everyone in the AOG and NETLAS consortium, without you this would not be possible. I have to expand the acknowledgements to former AOG member Dr Sophie Caujolle, who helped with thesis structure and many questions through the last year of the PhD. Dr Andy Thrapp is the most American person I have ever met. As well as Dr Sally Makin, who considerably helped me during the writing of my first manuscript.

Regarding funding, I want to acknowledge the Marie Curie Training International Training Network (ITN), through the European Commission (EC) under Grant Agreement NETLAS-860807 for funding my PhD.

Outside of academia, I must mention my Spanish crew, especially those with whom I've been in contact through Discord plenty of times: Ginés, Joel, Juanfran, Kako, Cristian, Mari, Irene Nepomuceno, Irene Sánchez, Salva, Victor, Jose Miguel, Myriam, Noelia, Guame, Bobby and many more. As well for those who made my life in the UK a better stay, from those who I shared house with Carla, Tamer, Catarina... to the Gaelic Football members, although I was not always there: Debora, Gabriel, Salvatore, Angus, Barry... As with every PhD, the last years have not been the easiest ones, and as such, I was lucky to find an amazing therapist which I would like to thank here. Last but not least, my deepest thank you to all my family for making this happen through all the difficulties. In particular, my parents, Jose Angel Martínez Rosique and Julia Jiménez Sanmartín, and my brother, Jose David Martínez Jiménez.

Thank you all!

Contents

List of Figures

List of Abbreviations

FWHM	**F**ull **W**idth at **H**alf **M**aximum
OCT	**O**ptical **C**oherence **T**omography
OPD	**O**ptical **P**ath **D**ifference
SMF	**S**ingle-**M**ode Fibre
MMF	**M**ulti-**M**ode Fibre
FD-OCT	**F**requency-**D**omain **O**ptical **C**oherence **T**omography *(also **F**ourier-**D**omain **O**ptical **C**oherence **T**omography, equivalent)*
TD-OCT	**T**ime-**D**omain **O**ptical **C**oherence **T**omography
SD-OCT	**S**pectral-**D**omain **O**ptical **C**oherence **T**omography
SS-OCT	**S**wept **S**ource **O**ptical **C**oherence **T**omography
FT	**F**ourier **T**ransform
MSI	**M**aster **S**lave **I**nterferometry
EM	**E**lectromagnetic **W**ave
DC	**D**irect **C**urrent
AC	**A**lternating **C**urrent
BPD	**B**alanced **P**hoto**D**etector
SNR	**S**ignal **N**oise **R**atio
DMS	**D**ownconversion **M**aster **S**slave
MS	**M**aster **S**lave
CMS	**C**omplex **M**aster **S**slave
RIN	**R**elative **I**ntensity **N**oise
MPE	**M**aximum **P**ermissible **E**xposure
DCF	**D**ispersion **C**ompensating **F**ibre
DL	**D**elay **L**ine
PM	**P**olarisation **M**aintaining
FDML	**F**ourier **D**omain **M**ode-**L**ocked
MEMS-VCSEL	**M**icro **E**lectro **M**echanical **S**ystem- **V**ertical **C**avity **S**urface **E**mitting **L**aser
RF	**R**adio **F**requency
PMD	**P**olarisation **M**ode **D**ispersion
CD	**C**hromatic **D**ispersion
COD	**C**atastrophic **O**ptical **D**amage
SOA	**S**emiconductor **O**ptical **A**mplifier
BOA	**B**ooster **O**ptical **A**mplifier
OSA	**O**ptical **S**pectrum **A**nalyzer
OSC	**O**scilloscope
PRR	**P**ulse **R**epetition **R**ate
SPM	**S**elph **P**hase **M**odulation
GDD	**G**roup **D**elay **D**ispersion
NPR	**N**onlinear **P**olarization **R**otation *(also **NPE** **N**onlinear **P**olarization **E**volution, equivalent)*

Chapter 1

Introduction to the thesis

My PhD was one of the 15 PhD positions of the ITN "Next generation of tunable lasers for optical coherence tomography". As the title of my thesis says, I have contributed to several aspects of fast OCT imaging, including a fast swept source, signal processing adapted to high-frequency photodetected signals up to 20 GHz, with new hardware for on-the-fly production of images and offline calculations, and introduced a fast electro-optic deflector paired with multi MHz tuning lasers. Mainly, the thesis aims to face, explore and overcome the boundaries of high-speed swept-source optical coherence tomography (SS-OCT). Since the first *in-vivo* cross-sectional image of a human eye reported by D. Huang in 1991 [1], the applications have not stopped growing. In fact, as the technology evolved, thanks to the availability of new optoelectronic components, new modalities have emerged: polarisation-sensitive OCT, phase-sensitive OCT, optical coherence elastography, and optical coherence microscopy. Among the main modalities of OCT operation, SS-OCT has demonstrated high value across various medical fields. Overall, SS-OCT stands out as a powerful diagnostic tool that combines high-speed acquisition with detailed high-resolution imaging and extended axial range, enhancing both the accuracy and efficiency of medical diagnostic and treatment.

1.1 Project motivation

SS-OCT has provided immense speed benefits compared with previous modalities such as SD-OCT and TD-OCT. Those benefits might be reflected in many applications, such as large-area scanning, 4D OCT for surgical applications, OCT-Angiography, and many more. However, several factors have hindered the commercial implementation of high-speed OCT systems, which exhibit fundamental issues that must be resolved before widespread adoption.

Initially, the swept-source availability for few/multi-MHz sweep rates was mainly restricted to the telecommunication band. The main reason for development at this wavelength is based on the availability and relatively low cost of electro-optic used for telecommunications. However, OCT has become popular on other wavelength bands, such as 850 nm and 1060 nm. In addition, as the tuning rate increases, the demand for the rest of the components, scanners, and acquisition panels increases. Therefore, an immediate consequence of high-speed sources is the demand for faster deflectors for lateral scanning. Galvanometer scanners became popular for their versatility and resonant scanners for coping with strokes at kHz rates. However, they might not be the optimal choice for multi-MHz sources. Slow scanners paired with multi-MHz sweep sources lead to massive unnecessary oversampling. Finally, the second immediate consequence of high-speed sources is the acquisition procedure. The larger the sweep rate, the higher the modulation, and with it, there is a need for larger bandwidth photodetection and sampling rates. Therefore, for conventional SS-OCT, high-speed balanced photodetectors are required along with digitizers able to cope with large bandwidths. However, these cards are costly and unavailable for the multi-GHz frequencies generated by the interferometers fed by fast-swept sources. Furthermore, even if such cards become available, the time for processing the data acquired during each sweep should be less than the sweep period,

i.e. $t_{processing} < \tau_{SweepRate}$, where τ is in the order of nanoseconds. For that reason, new processing alternatives should be investigated if live imaging is needed. One solution for this challenge is presented in my thesis.

1.2 Organization of the thesis

The thesis is divided into 5 main chapters, from which chapters 2 and 3 are the theory required for the experimental chapters, 4, 5 and 6. The theory chapters consist of:

- Chapter 2: The basics of OCT are introduced. Derivation of the optical principles used for time domain OCT and Fourier domain OCT are presented. Special attention is given to signal processing methods for SS-OCT.
- Chapter 3: Divided into two main parts: half of the chapter briefly introduces the main concepts needed for fibre pulsed lasers. The other half of the chapter is a brief review of swept sources available for SS-OCT. Principles of sweeping are reviewed and compared.

Next is the experimental work of the thesis, which is divided into three chapters. The construction of an ultrafast swept source and two dispersion techniques, the utilisation of an ultrafast swept source with a scanning element capable of handling the sweep rates, and finally, research on the signal processing and the use of lasers for ultra high-speed swept source OCT.

- Chapter 4: The construction of a mode-locked laser, followed by time-stretch, a swept source was designed and assembled that reached up to 9.65 MHz repetition rate. This demonstrated the challenges of using multi-MHz swept sources. Two techniques are presented for dispersion measurement. A characterisation of the source for use in OCT has been performed.

- Chapter 5: A multi-MHz swept source, provided by collaborators at NKT Photonics, was integrated into the build of two novel OCT systems. Initially, a system with the sample rotating in a chopper was used to demonstrate the OCT capabilities. Furthermore, a system capable of coping with the required sweep rate was assembled using electro-optic fast scanning, and images were acquired. The latest system reached OCT volume rates of 400 Hz. Then, a proof-of-concept system was evaluated to demonstrate the ultra-fast capability of an interferometer equipped with a fast-swept source for real-time visualisation in the time domain.

- Chapter 6: Two state-of-the-art swept sources with tuning speeds in the few-MHz range and bidirectional sweeping are demonstrated for real-time *in-vivo* imaging. Here, for the first time, signal processing from the interferometric signal of an FDML laser is computed by the complex master-slave. Moreover, the asymmetry due to the bidirectional sweeping is analysed for both sources. Finally, a downconversion system is employed with a bidirectional laser, and the intrinsic benefits of this processing method are explored. Instead of using conventional Fourier transform-based methods to process the interferograms computationally, the system is modified for processing the signal using analogue devices, achieving real-time processing. Aside from reducing the requirements for a high-speed digitiser, the downconversion system also allows using sources with asymmetric and unstable sweeps.

1.3 Outcome

The publications resulting from this research are listed in Appendix A. The Chapter 4 was published in a conference proceeding [1]. Results of chapter 5 are published in two peer reviewed articles [1, 2] and in a conference proceeding [2]. Finally, the results of chapter 6 are in two journal articles [3, 4], and two conference

proceedings [3,4]. The rest of the publications are part of NETLAS collaborations. For the work in the journal article [5], I contributed to the scripts to generate the roll-off. In [6], I contributed to the development of the system, design, experimental tests, and participated in the writing of the manuscript. In [7], the chinrest used for papers [3, 4] was used, and I participated in the optimization of the system, design of the OCT system and collaborated in the manuscript writing. Conference proceeding [5] was the result of an optical characterization for a MEMS-VCSEL swept source from our NETLAS partners, which I contributed to the assembly of the OCT system.

Chapter 2

Introduction to OCT

This chapter briefly introduces the theory and main characteristics of Optical Coherence Tomography (OCT). It also presents the two modalities used in the experimental chapters: Fourier Domain (FD) and Time Domain (TD) OCT. The chapter describes computational methods for signal processing and specialises in the swept source (SS) OCT method, which is relevant to this thesis.

Contents

2.1 History and chronology of source development

OCT is an optical, non-invasive 3D imaging technique that allows depth information to be obtained using interferometry. During the last three decades, OCT has evolved to become an important imaging modality in biomedical optics [2]. Images with sub-micron resolution and tens of centimetres axial range can be acquired in less than a second. OCT is now a mature technique within clinics. Since the first development, the evolution has not always been linear, and not all parameters have been improved simultaneously over the 32 years of OCT's existence. However, there are still new advances that enable OCT to reveal new information to users [3]. In the search for depth-resolved methodologies, research groups have tried to measure reflectivity through techniques that imply measuring the time difference between the emitted pulse and a received pulse. However, the configurations used in the early stages have proven expensive and complex, resulting in limited axial resolution [4]. The first demonstrations of heterodyne detection obtained an axial scan, but without an image, in the report [5]. The first paper considered to demonstrate OCT was published by Huang et al. [1], in which a cross-sectional image of retina tissue in vitro was shown and the term OCT was coined. To understand the value of this imaging technique, it is important to compare it with similar imaging modalities in terms of penetration depth, resolution, and acquisition time; see Figure 2.1. Considering only axial resolution and penetration depth, confocal microscopy can achieve higher resolution without the penetration depth. On the other hand, ultrasound is able to obtain a larger penetration depth but with much poorer resolution than OCT. Furthermore, in confocal microscopy, the axial resolution depends on the numerical aperture of

the interface optics, which, for certain samples, such as the eye, has a limited numerical aperture (focal length is large, the beam diameter is small). On the other hand, the axial resolution of OCT depends to a lesser extent on the numerical aperture but mainly on the spectral bandwidth of the light source employed. In fact, the bandwidth might be the most fundamental parameter of OCT technology. This makes OCT competitive in axial resolution, especially in the case of samples that cannot be examined in the desired conditions (i.e., samples limited by a given numerical aperture). Although one might think the penetration depth of confocal and OCT should be similar since they use the same wavelengths, the key reason for their differences is in how the depth is selected: OCT collects light from a larger numerical aperture (NA) but still maintains depth sensitivity due to interferometry. On the other hand, confocal microscopy requires high NA for resolution, but this reduces the working distance and increases sensitivity to scattering. Despite using similar wavelengths, OCT penetrates deeper because its interferometric detection scheme is more efficient at capturing weakly backscattered light.

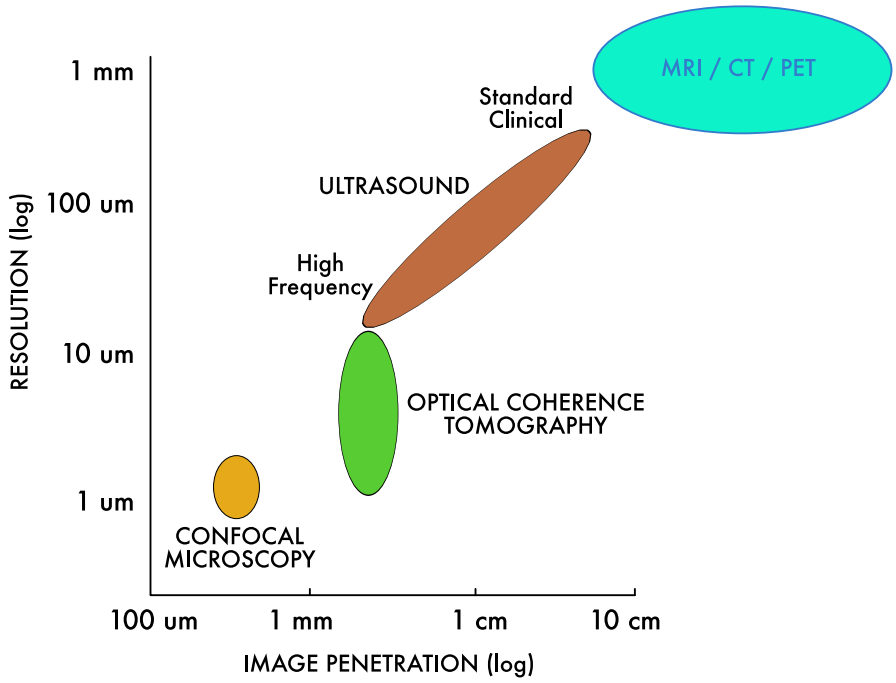

FIGURE 2.1: Comparison of optical imaging techniques.

OCT can be performed at any central wavelength but is limited by the availability of light sources in practice. The selection of the central wavelength is determined by considering the axial resolution and desired penetration depth into the sample. For this purpose, it is helpful to consider the therapeutic window to decide the wavelength of use for biomedical targets. Three main components absorb the light and therefore attenuate the signal Hb, HbO2 and water. These components, especially water, exhibit a low absorption coefficient around the 800 nm central wavelength. This is one of the reasons why this wavelength would be chosen compared to others. However, the amount of scattered light is proportional to $1/\lambda^4$, meaning that scattering is higher for shorter wavelengths. In other words, the light cannot penetrate as deeply as longer wavelengths.

In summary, depending on the sample requirements, three main wavelength bands are typically used: 800 nm, 1060 nm and 1300 nm. The resolution required might also define the wavelength to use since shorter wavelengths have better resolution for the same bandwidth. The water absorption at 1060 nm is still within an acceptable range for eye imaging, where the liquid inside the eye is mainly composed of water. In this way, 1060 nm will obtain a deeper penetration depth when used on the retina. On the other hand, 1300 nm exhibits larger absorption in water, so this wavelength is mainly used for skin.

Throughout this work, the following nomenclature shall be used. An A-scan represents a depth profile of reflectivity from the sample for a given lateral beam position, Figure 2.2 (a). A real example is given for an IR Card from Thorlabs, at the bottom row of Fig. 2.2. When multiple A-scans are recorded from the same lateral (x,y) position, it is known as an M-scan. A B-scan (or cross-section image) is the combination of more than one lateral adjacent A-Scans, for example, all the A-scans obtained during the movement of one galvanometer mirror, Figure 2.2 (b). A C-Scan or *en-face* image is a 2D map of reflectivity obtained for all lateral pixels in the image for a fixed depth. A C-Scan is achieved by scanning along horizontal and vertical directions to generate a raster. Lastly, a volume is a 3D

representation, which can also be equivalently obtained by a combination of *en-face* OCT images from all depths, as shown in Figure 2.2 (c). From a volume, all different sections can be extracted.

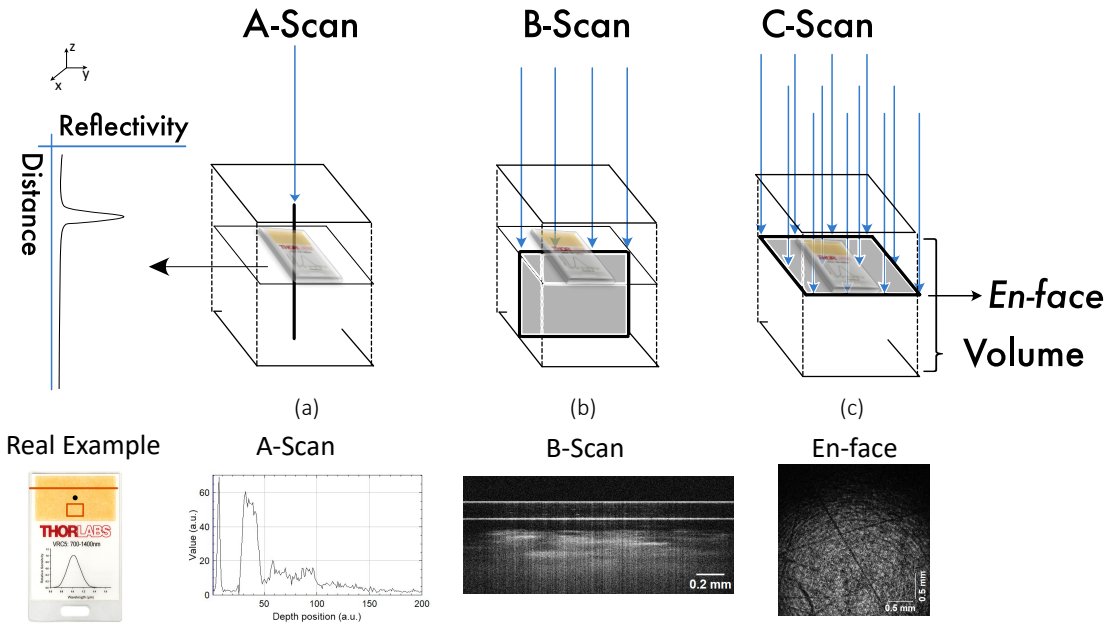

FIGURE 2.2: Representation of the beam path (arrows) towards the sample in (a) an axial scan, also known as A-Scan; (b) a cross-sectional 2D image, which one dimension the lateral scan (either x or y) while the other dimension must be axial, this image is also known as B-Scan; and finally (c) *En-face* also known as C-Scan, 2D image along the scanning directions fixed at one single depth. A real example of an IR Card is shown in the bottom row for each corresponding scan.

2.2 Physical principles

Optical coherence tomography is based on first-order interferences, i.e. interference of electromagnetic (EM) waves. The most common device to produce first-order interference is a Michelson or Mach-Zehnder interferometer. In the system shown in Figure 2.3, the light source emits an EM wave in the form of:

$$E_{int} = s\left(k\right) e^{j(kz-\omega t)} \tag{2.1}$$

where the subindex int refers to the initial wave from the light source, j denotes the imaginary number, and $s(k)$ is the electric field amplitude at the desired k, the wavenumber. The EM field is divided by a beamsplitter into a reference and a sample wave, where, considering the reflection coefficients from the respective arms, the following description for the two waves can be written as:

$$E_R = \frac{E_{int}e^{j\pi}}{\sqrt{2}} \left(r_R e^{j2kz_R}\right) \tag{2.2}$$

$$E_S = \frac{E_{int}e^{j\pi}}{\sqrt{2}} \left(\sum_{r=1}^{N} r_{S_r} e^{j2kz_{S_r}}\right) \tag{2.3}$$

where the $1/\sqrt{2}$ arising by normalization from the 50/50 beamsplitter is assumed. The electrical field reflected undergoes a π phase difference with respect to the reference. The fields in Fig. 2.3 and in Eqs. 2.3, 2.2 are shown after both have passed through the beam splitter twice. Therefore, an additional π phase is added to both waves. This is true for this bulk Michelson setup; however, systems with balance detection as the ones shown in Chapter 4, 5 and 6 use the phase introduced by the bulk beam splitters or directional couplers in its advantage to reduce noise and double the amplitude. Balanced detection will be explained further in Section 2.5. The summation of the electric field of the sample arm refers to the multiple reflectors from the different layers a sample could have, as shown in Fig. 2.3, an irregular sample with 3 depths. The Fresnel reflection coefficients r_{S_r} are connected to reflectivity by $R_{S_i} = |r_{S_i}|^2$, where coefficients connect amplitudes and reflectivity powers. Note that for most biological tissue samples, the reflectivity is typically very small, less than 10^{-5}; however, as it combines with the reference arm, those reflectivities are still reflected.

Once the EM fields from both arms are recombined in the photodetector, the detector responds to the power, which is proportional to the square of the electric field and produces an average over the response time of the photodetector. However, for interference to occur, the wave should fulfil 4 main requirements [6, 7]. Initially, both waves should coincide in polarisation (i.e. $\vec{A} \cdot \vec{B} \neq 0$, for $\vec{A}, \vec{B}$ EM

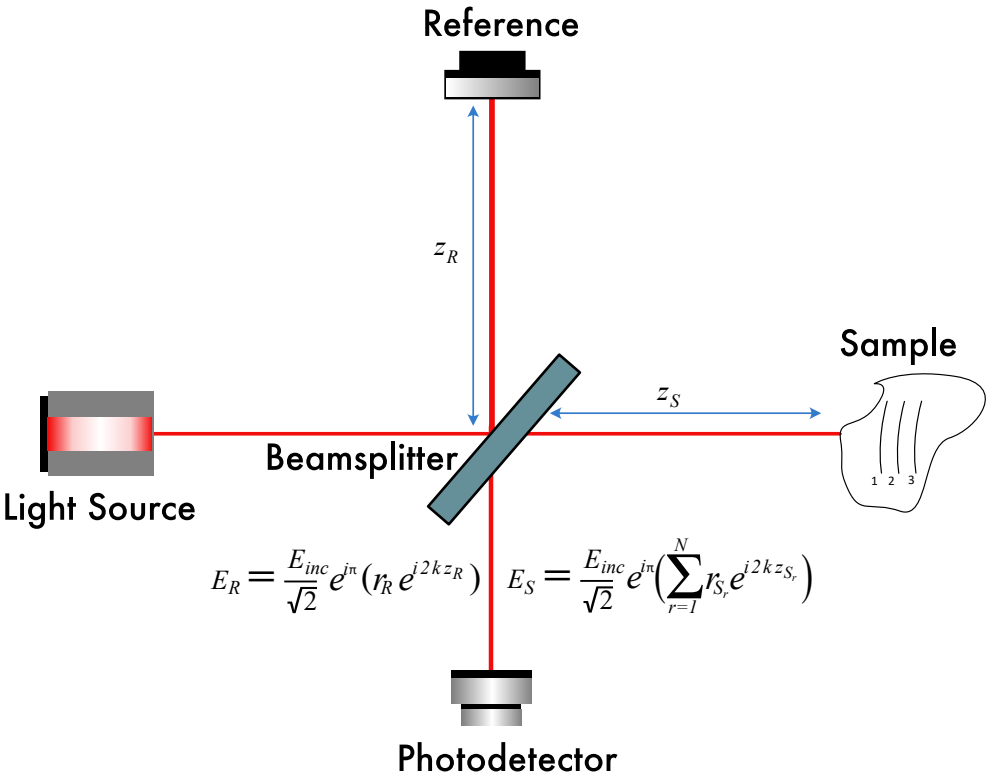

FIGURE 2.3: Schematic of a bulk Michelson interferometer used in OCT.

waves vectors from sample and reference arm). Secondly, the monochromaticity condition (the same frequency): as the speed is the same for both waves, an immediate consequence is that $k_1 = k_2$. Thirdly, the phase difference should be constant or varying slower than the photodetector response, and finally, the coherence condition. The detected intensity, which is the time average (over the response time of the photodetector) of modulus-squared of the fields, takes the form of:

$$\begin{aligned} I_D(k) &= \rho\langle|E_R + E_S|^2\rangle \\ &= \frac{\rho}{2}\langle|\frac{s(k)}{\sqrt{2}} r_R e^{j(2kz_R - \omega t)} + \frac{s(k)}{\sqrt{2}} \sum_{i=1}^{N} r_S e^{j(2kz_{S_i} - \omega t)}|^2\rangle \end{aligned} \tag{2.4}$$

where ρ is the responsivity of the photodetector expressed in A/W. Expanding the magnitude squared functions in Eq. 2.4 and eliminating the terms pulsating with the temporal angular frequency $\omega = 2\pi\nu$, which is reasonable since ν, the frequency of the wave is much faster than the frequency response of the detector

(red coloured in the equation). It leaves the equation 2.4 to the developed version as follows:

$$\begin{aligned} I_D(k) = & \frac{\rho}{4}\left[S(k)\cdot\left(R_R + R_{S_1} + R_{S_2} + \cdots\right)\right] \\ & + \frac{\rho}{4}\left[S(k)\cdot\sum_{i=1}^{N}\sqrt{R_R R_{S_i}}\left(e^{j2k(z_R - z_{S_i})} + e^{-j2k(z_R - z_{S_i})}\right)\right] \\ & + \frac{\rho}{4}\left[S(k)\cdot\sum_{i\neq m=1}^{N}\sqrt{R_{S_m} R_{S_i}}\left(e^{j2k(z_{S_m} - z_{S_i})} + e^{-j2k(z_{S_m} - z_{S_i})}\right)\right] \end{aligned} \tag{2.5}$$

Here, $S(k) = \langle s(k)^2 \rangle$ is the power spectral density of the light source. This has important implications for the axial resolution. The shape of the spectrum, $S(k)$, gives the coherence function by its inverse Fourier transform $\gamma(z)$. As an example, for a Gaussian shape, the coherence function is given by:

$$S(k) = \frac{1}{\Delta k\sqrt{\pi}} e^{-\left[\frac{(k-k_0)}{\Delta k}\right]^2} \leftrightarrow \gamma(z) = e^{-z^2\Delta k^2} \tag{2.6}$$

where k_0 is the central wavenumber, and Δk is the bandwidth expressed in wavenumber. The axial resolution is defined by the full-width half maximum (FWHM) of the coherence function, as will be shown in the next steps. Therefore, the spectral dependence should be adjusted to minimize the width of the coherence function, i.e. maximize the spectral bandwidth. The coherence length is the propagation distance over which a wave (e.g. an electromagnetic wave) maintains a specified degree of coherence. In this case, it is possible to quantify the axial resolution as the FWHM of the light source coherence function, l_c:

$$l_c = \frac{4\ln 2}{\pi}\frac{\lambda_0^2}{\Delta\lambda} \tag{2.7}$$

where λ_0 is the central wavelength and $\Delta\lambda$ is the source bandwidth. Note here that the factor $\frac{4\ln 2}{\pi}$ is only related to the shape of the spectrum. In others, such as flat top or triangular, this factor differs. Carrying on with Eq. 2.5 and applying

the Euler rule, the intensity can be rewritten into:

$$\begin{aligned} I_D(k) = \frac{\rho}{4}\left[S(k)\cdot\left(R_R + R_{S_1} + R_{S_2} + \cdots\right)\right] \\ + \frac{\rho}{4}\left[S(k)\sum_{i=1}^{N}\sqrt{R_R R_{S_i}}\cos[2k(z_R - z_{S_i})]\right] \\ + \frac{\rho}{4}\left[S(k)\sum_{m\neq i=1}^{N}\sqrt{R_{S_i} R_{S_m}}\cos[2k(z_{S_m} - z_{S_i})]\right] \end{aligned} \tag{2.8}$$

where all the values are real, Eq. 2.8 is composed of three main terms: DC, cross-correlation, and auto-correlation. The DC terms are dominant when the EM field from the reference dominates the sample, i.e. $E_R \gg E_S$. The cross-correlation terms depend on the light source and the path length difference between the reference and sample arm. In absolute values, the cross-correlation terms are several orders of magnitude lower than DC terms. In fact, the cross-correlation holds the most valuable information from the sample. Finally, the auto-correlation terms represent the interference between the reflections from different depths. These terms will typically be 4-5 orders of magnitude below that of the sample signal in the absence of extremely strong sample reflections. Moreover, because the amplitude of the auto-correlation term depends directly on the reflectivity of the different surfaces, they can be avoided using an appropriate power in the reference. In practice, DC terms are usually removed using high-pass filters or balanced detection, which suppresses or subtracts the majority of DC terms. The auto-correlation terms are weak for the biological samples typically used, such as the retina.

2.2.1 Time-Domain OCT

Time domain is one of the two methods (TD and FD) to perform OCT, and the first one used [1]. The ideal source for TD-OCT is a continuous wave with a broadband spectrum. Superluminescent diodes (SLDs) and supercontinuum lasers are commonly used. TD-OCT is based on the interference of the wavetrains from the

reference and sample arm within a coherence length, i.e., overlapping the two wavetrains in time. Therefore, to obtain an axial scan, the OPD of the reference arm has to be varied until the desired depth. The interference given in TD also depends on the shape of the spectrum. Assuming a Gaussian shape for the spectrum and removing the auto-correlation terms, since z_{S_i} is always different from z_{S_j} for the time-domain case, then Eq. 2.8 results in:

$$I_D\left(z_R\right) = \frac{\rho}{4}[S_0[R_R + R_{S_1} + R_{S_2} + \cdots]] + \frac{\rho}{2}\left[S_0 \sum_{i=1}^{N} \sqrt{R_R R_{S_i}} e^{-(z_R - z_{S_i})^2 \Delta k^2} \cos[2k_0(z_R - z_{S_i})]\right] \tag{2.9}$$

where $S_0 = \int_0^\infty S\left(k\right) dk$ is the spectrally integrated power emitted by the light source over the whole spectrum, continuing with the physical interpretation, in TD, the interferogram is resolved by moving the reference mirror with respect to the sample. One of the most important points to realise in this OCT method is that interference always occurs when the length of both arms is matched and spans through the coherence length of the source. As such, for each lateral position of the scanning beam, a single depth is generated, which makes volume construction time-consuming. Therefore, *en-face* images are obtained by scanning the beam laterally without changing the OPD of the reference arm. In practice, TD uses a mirror in the reference arm that is attached to a translation stage or an optical scanning delay line using a grating; this creates a modulation at the Doppler shift that plays the role of a carrier. Subsequently, phase modulation through lateral scanning has been demonstrated to be effective in generating the carrier. [8, 9]. Another important parameter that is worth mentioning is the noise; TD-OCT has been investigated using Michelson and Mach-Zehnder interferometers, i.e. unbalanced and balanced photodetection. The implementation of a balanced scheme allows for a higher SNR overall by reducing the receiver noise [10]; this will be further discussed in Section 2.5.

2.2.2 Fourier-Domain OCT

Fourier Domain (FD) is the second method which allows us to perform OCT. As such, the spectrum is photodetected using either a continuous wave and a spectrometer or a swept source and a single-pixel photodetector. FD-OCT is based on the same principles explained in Section 2.2. However, producing the axial scan through interferences in the temporal space, the axial scan is obtained by performing a Fourier transform of the photodetector signal $I_D(k)$. Mathematically, performing a Fourier transform can be seen as the Eq. 2.8 becomes:

$$\begin{aligned} i_D(z) = & \frac{\rho}{8}[\gamma(z)[R_R + R_{S_1} + R_{S_2} + \cdots] \\ & + \frac{\rho}{8}\left[\gamma(z) \otimes \sum_{i=1}^{N} \sqrt{R_R R_{S_i}}\delta[(z \pm 2(z_R - z_{S_i}))]\right] \\ & + \frac{\rho}{8}\left[\gamma(z) \otimes \sum_{m \neq i=1}^{N} \sqrt{R_{S_m} R_{S_i}}\delta[(z \pm 2(z_{S_m} - z_{S_i}))]\right] \end{aligned} \tag{2.10}$$

where $\gamma(z)$ has been defined previously as the coherence function, $\delta(z)$ is the delta function, and $\otimes$ is the convolution operation. Making use of the Fourier transform (FT) properties, FT of the cosine leads to two delta functions. Also, the FT of a convolution of two functions is the product of their FTs [11]. If one of the factors in the convolution is a delta function, then the FT of a delta function is a constant, and Eq. 2.10 is reduced to:

$$\begin{aligned} i_D(z) = & \frac{\rho}{8}[\gamma(z)[R_R + R_{S_1} + R_{S_2} + \cdots] \\ & + \frac{\rho}{4}\sum_{i=1}^{N} \sqrt{R_R R_{S_i}}[\gamma[2(z_R - z_{S_i})] + \gamma[-2(z_R - z_{S_i})]] \\ & + \frac{\rho}{4}\sum_{m \neq i=1}^{N} \sqrt{R_{S_i} R_{S_m}}[\gamma[2(z_{S_m} - z_{S_i})] + \gamma[-2(z_{S_m} - z_{S_i})]] \end{aligned} \tag{2.11}$$

Some conclusions can be drawn from the equation above. First, the intensity is now a function of depth with the reference coordinate z. Secondly, for each of the cross-correlation terms and the auto-correlation terms, there are two "mirror"

coherence functions. These show that the same result is obtained for the same OPD but for a different sign, i.e. the other side of zero OPD. These are known as mirror terms. Thirdly, as mentioned before, the axial resolution is defined by the shape of the coherence function. As an illustration, the calculated convolution operation of the delta function with the coherence function in Eq. 2.11 is shown in Figure 2.4

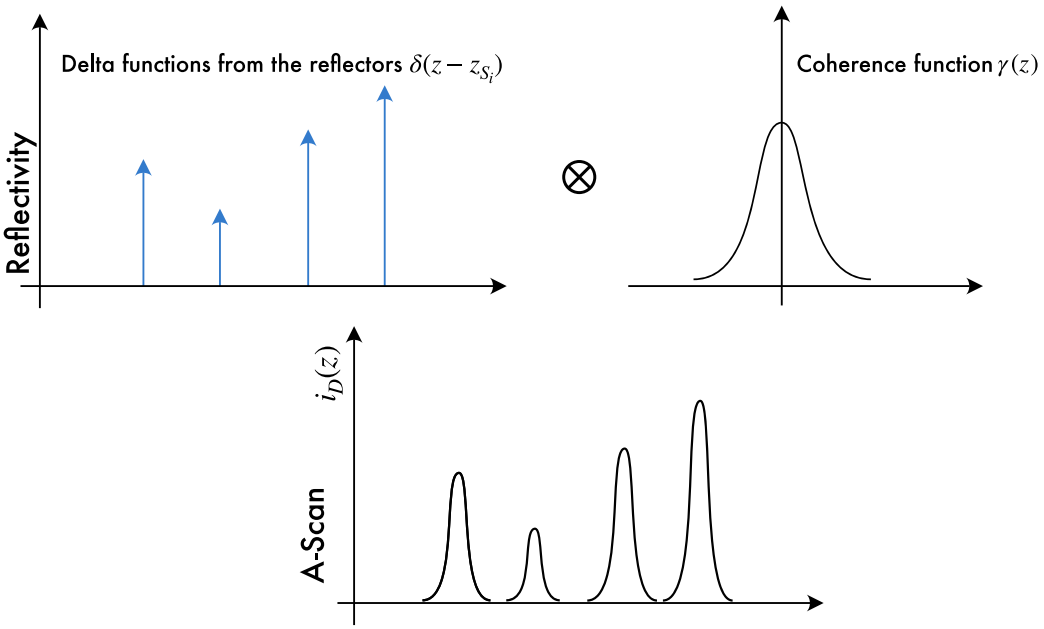

FIGURE 2.4: Illustration of the convolution operation in Eq.2.10 presented above.

Auto-correlation terms are commonly described as artifacts in images. They are undesirable and are often removed. Although a high-pass filter can remove the DC and auto-correlation terms, in practice, the DC can saturate the photodetector and reduce the dynamic range. One of the immediate advantages of using FD-OCT is that there is no need to mechanically scan the OPD to obtain the modulation needed in TD-OCT. This advantage means that FD-OCT can overtake TD-OCT in terms of speed. On the other hand, one of the main drawbacks of FD-OCT is its sensitivity dependence on depth, explained in Section 2.4.0.1.

2.2.2.1 Spectral domain OCT

This method can be considered an extension of the work from Smith et al. [12] with white light interferometry. The most common version of spectral domain OCT (SD-OCT) uses a grating to decode the modulated spectrum. A Michelson interferometer (see Figure 2.5) is typically used for SD-OCT. Here, the selection of the coupler ratio varies depending on the application and the power requirements in the sample. For example, for skin or eye, the power is limited by the safety regulations [13]. In those cases, a coupler that allows maximum transmission of optical power to the reference while preserving the maximum allowed power in the sample arm is used. Instead of using a single photodetector over time, as in TD-OCT, a diffraction grating together with a line scan camera is employed to acquire the spectrum.

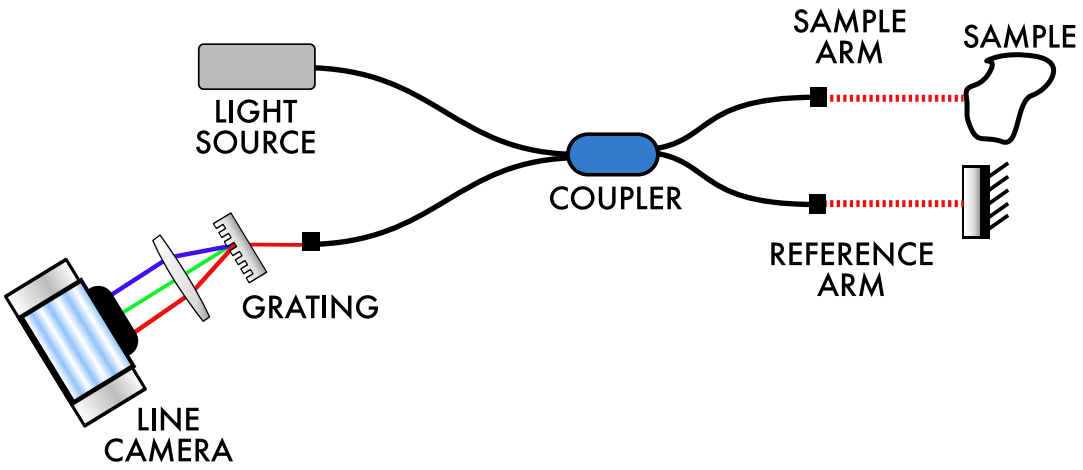

FIGURE 2.5: **Typical SD-OCT design.** Michelson interferometer in fibre.

Once the wavetrains from both arms are recombined in the photodetector, the spectrum becomes channelled. Since the light source used in SD-OCT does not need to sweep, continuous waves can be used; the complexity of the source lies in generating broad spectra. As in TD-OCT, identical light sources can be used; therefore, the resolution is the same as in time domain systems if the spectrum is preserved along the interferometer. Large bandwidths and consequently high resolution (1-10 μm) systems are expected from this modality [14–17].

Previously, a link was made between the coherence length of the wave and the spectral linewidth. The linewidth to consider will determine the axial range, which should be that of the wave after the diffraction, i.e., the diffracted wave. The larger the number N of grooves engaged on the grating, the better the spectral resolution, i.e. the smaller the associated linewidth of the diffracted wave. In fact, the first extension of the wavepacket in the n-th order of diffraction is $nN\lambda$ [18, 19]. The linewidth is associated with the process $l_c \sim\simeq \lambda/N$ (as per the theory of diffraction used for spectrometry). However, the pixel size on the line camera also determines a finite linewidth, $\delta\lambda_{cam}$ (the distance along the camera between two consecutive pixels). The decay of sensitivity with $\delta\lambda_{cam}$ is described by a sinc factor [20]. As a design rule, λ/N, and $\delta\lambda_{cam} = \Delta\lambda/M$, where M is the number of camera pixels, should be made as small as possible. For instance, for a beam diameter of 1 mm on a grating with 1,000 groves/mm, and a wavelength of $1\mu m, \lambda/N = 1\ nm$ while for a bandwidth of $\Delta\lambda$ of 100 nm, with $M = 1,000$ pixels, $\Delta\lambda/M\ = 0.1\ nm$. One or the other linewidth can be made dominant depending on N, M and $\Delta\lambda$ values.

Nonetheless, common spectrometer-based OCT systems are able to achieve an axial range of the order of $3 - 4$ mm, which is enough for posterior segment eye imaging applications, although not enough for full-eye imaging. One of the most important constraints of SD-OCT, in comparison with other TD-OCT and SS-OCT, is the difficulty of implementing balanced detection. Although some reports have proven the benefits of balance detection in SD-OCT systems [21–23], the complexity of the systems is indeed high. For balance detection in SD-OCT, two identical cameras are needed. Moreover, each pixel in each line-camera must see the same wavelength. Hence, not only must the alignment with the grating be perfect in both cameras, but also, this is even more tedious for high-speed SD-OCT as the frequencies generated are higher, and therefore, the time precision in reading each spectral element should match pixel by pixel [24]. For these reasons, balanced detection in the spectral domain is only used in research prototypes. At

the same time, it is noted that the speed of the system does not depend on the light source, as the source is usually a continuous wave. In fact, the speed is derived from the reading of the camera. The maximum speed the camera can read gives the fastest A-Scan production. However, the transition from TD-OCT to SD-OCT represented an enormous step towards higher OCT speed. Modern line cameras can run up to 300 kHz, which is a considerably high rate (e2V, Teledyne). Alternatives using multiple cameras have demonstrated higher A-Scan rates. However, the complexity and cost increase is considerable [25].

2.2.2.2 Swept Source OCT

Swept-source optical coherence tomography (SS-OCT) is another approach within Fourier domain techniques. In this case, the principle is the same: decoding the spectral modulation. However, the method for reading the spectrum is different. A tunable laser (swept source) is used, which emits a single wavelength at a time and changes its wavelength over a tuning bandwidth. In practice, the width of the single wavelength emitted is known as the instantaneous linewidth. The instantaneous linewidth defines the length of the wavetrain by the coherence length $l_c \propto \lambda_0/\delta\lambda$. The instantaneous linewidth is swept over the tuning bandwidth. Thus, the tuning bandwidth must be considered when calculating the axial resolution. A commonly used type of interferometer for SS-OCT is a Mach-Zehnder interferometer (see Figure 2.6), which enables balanced detection implementation, explained in 2.5.2. As the detector is now a single pixel, the optics alignment is largely simplified because the detection configuration can be implemented in fibre. Moreover, single photodetectors can reach a high speed of operation in comparison with spectrometers of several GHz bandwidth (Silicon, for lower wavelengths than $1\mu m$) and over 100 GHz (GaAs, for larger wavelengths than $1\ \mu m$). In addition, the coherence length of modern swept sources can exceed meters, making SS-OCT capable of imaging large objects extended in depth. All these advantages combined make the SS-OCT method superior to

SD-OCT in terms of speed, axial range and assembly cost. However, one parameter where SS-OCT lags behind SD-OCT is bandwidth (i.e. axial resolution) due to the complexity of building tunable mechanisms able to sweep across a large bandwidth (>100 nm).

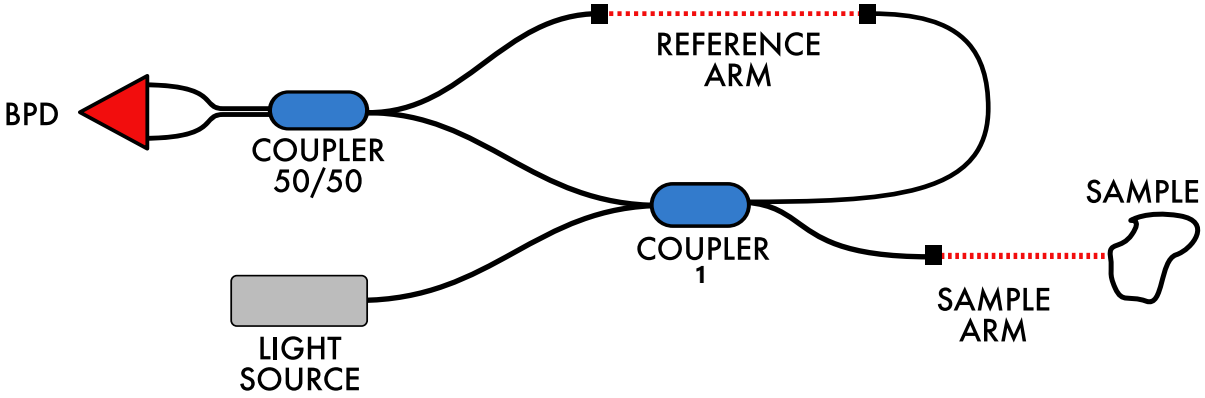

FIGURE 2.6: **Commonly used asymmetric balanced SS-OCT configuration.** Mach-Zehnder interferometer in fibre.

The coupler 1 shown in Fig. 2.6 shares the same property as in the SD-OCT 2.5; the coupling ratio can be varied depending on the application and sample requirements. The achievable tuning bandwidth highly depends on the tuning modality and will be described in the next chapter. The instantaneous linewidth, in this case, is not limited by the acquisition system. This is limited by the principle and device employed to perform tuning. Although this is the topic of the next chapter, it is important to say that in many cases, the sweep cannot be stopped. Therefore, for those sources, it is not possible to directly measure the FWHM of the linewidth using a spectrometer. However, one can estimate the linewidth by measuring the interference strength decay with OPD, i.e. the axial range.

2.3 Resolution

2.3.1 Axial resolution

The axial resolution in OCT depends on three factors: the bandwidth of the optical spectrum, the central wavelength and the shape of the spectrum from the

source. The axial resolution can be calculated as:

$$\Delta z = \text{shape factor} \cdot \frac{\lambda_0^2}{\Delta\lambda} \tag{2.12}$$

where the shape factor is 0.44 for a Gaussian shape and 0.62 for a top hat shape; those factors are calculated as the FWHM of the spectral shape. For example, an optical spectrum with a top-hat shape does have more components with higher power spectral density than a Gaussian shape. However, the wavelengths outside the FWHM contribute less to the top hat than the Gaussian shape. In a mathematical approach, this can be seen as the relation of the FWHM from the Fourier Transform of a Gaussian and a top-hat shape [26]. Therefore, a higher resolution is expected from a Gaussian shape. According to Eq. 2.23, assuming two light sources with the same optical bandwidth but different central wavelengths, the axial resolution for lower central wavelengths is improved over that for longer central wavelengths, which is one of the reasons that makes visible OCT (500-650 nm) appealing. As described in Figure 2.7, the axial resolution is plotted versus bandwidths for four values of the central wavelengths. The graphs also show that for shorter central wavelengths, less bandwidth is needed to achieve the same axial resolution.

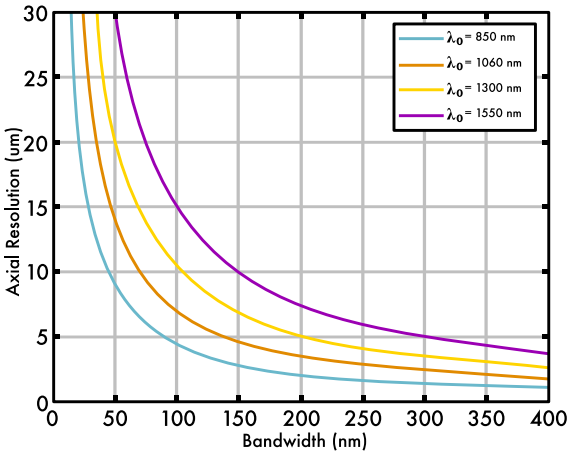

FIGURE 2.7: Bandwidth and resolution connection as a function of the central wavelength.

2.3.2 Lateral resolution

Any flying spot OCT system is based on a confocal microscope, on top of which a reference arm is added. The lateral resolution in a confocal microscope is determined by the size of the focused beam inside the sample at the depth of interest. An approximation of such dimension is obtained by considering the Airy disk size, calculated for diffraction of a beam through a circular aperture [27]. This is written as $\delta x = 0.61\lambda/\text{NA}$. Here, NA refers to the numerical aperture of the interface optics used after the lateral scanner. The numerical aperture (NA) is a dimensionless number that characterizes the range of ray angles that the system can accept from a scattering feature. The NA is defined as $\text{NA} = n\sin\theta \simeq n\frac{D}{2f}$ where θ is the half angle covered by the lens, D is the diameter of the lens, n is the index of refraction of the medium between the lens and the sample and f is the focal length of the lens. According to the theory of confocal microscopy, because the last lens is used twice, if a pinhole is used (assimilated to the tip of a single mode fibre), the lateral resolution in a confocal microscope is slightly better than that of a conventional microscope by a factor no larger than 1.4 [28]. Hence, an Airy disk calculation would be acceptable for the estimation of the lateral resolution achievable using single-mode fibre launching and a lens.

However, achieving a small spot size (and thus higher lateral resolution) comes at the cost of a reduced depth of focus, which is the range over which the beam remains tightly focused. This is not a problem for time domain OCT, where the focus in depth can be adjusted in synchronism with depth scanning, a procedure known as dynamic focus[29]. For spectrometer-based and swept source-based OCT methods, a Fourier transform leads to reflectivity along depth; hence, the signal from all scattering points along depth is calculated at once. Therefore, a compromise is always established between the lateral and axial resolution. Such

an interdependence is detailed in the 3rd equation below, [3]:

$$\Delta x \simeq \frac{0.61\lambda_0}{NA}, \qquad \Delta z = \frac{2\lambda_0}{NA^2} \quad \Rightarrow \Delta z \simeq 3.27\frac{\Delta x}{NA} \tag{2.13}$$

When imaging the retina, because the retina is away from the eye lens by more than 2 cm, the NA is small and, therefore, approximately all depths in the retina are within the Rayleigh range (i.e., the Rayleigh range is similar to the retina thickness). However when imaging the cornea (or embryos), short focal length objectives can be used for enhanced lateral resolution, in which case depth of focus becomes smaller than the cornea thickness (or embryo thickness). In such cases, repetition of acquisition for several successive positions of the focus is recommended [30].

Furthermore, the lateral resolution can be compromised if the beam is deflected between spectral interrogation events by more than the beam size on the target, leading to undersampling. To ensure high-quality imaging, the lateral step between successive spectral interrogations should be less than the optical resolution, allowing for oversampling. According to the Nyquist criterion, two interrogations per lateral optical pixel should be planned for an accurate representation of pixels along lateral dimensions.

In practice, optical aberrations such as spherical or chromatic aberrations can further degrade the lateral resolution, and these must be carefully managed in the design of the interface of the OCT system. Alternatively, a combination of OCT with adaptive optics can be adopted [31].

2.4 Sensitivity

The signal-to-noise ratio (SNR) for any system is defined as the signal power divided by the noise variance. For TD-OCT systems, the SNR follows assuming

only one sample reflector, Eq. 2.9 is reduced to the following:

$$I_D\left(z_R\right) = \frac{\rho S_{\mathrm{TD-OCT}}}{2}\left[R_R + R_S + 2\sqrt{R_R R_S}e^{-(z_R - z_S)^2\Delta k^2}\cos\left(2k_0(z_R - z_S)\right)\right] \tag{2.14}$$

where the mean square peak signal power would be when $z_R = z_S$ and is given by:

$$\langle I_D\rangle^2 = \frac{\rho^2 S^2_{TD-OCT}}{2}[R_R R_S] \tag{2.15}$$

Considering that the system is shot noise limited. Its main contribution comes from the reference arm, which has the dominating power hence the noise variance can be written as:

$$\sigma^2_{TD-OCT} = \rho e S_{\mathrm{TD-OCT}} R_R B_{\mathrm{TD-OCT}}. \tag{2.16}$$

where ρ is the responsivity of the detector (units amperes/watts), e is the electron charge, R_R is the reflectivity from the reference, and B_{TD-OCT} corresponds to the electronics detection bandwidth of the photodetector. Therefore, the signal-to-noise ratio becomes:

$$SNR_{\mathrm{TD-OCT}} = \frac{\langle I_D\rangle^2_{TD-OCT}}{\sigma^2_{TD-OCT}} = \frac{\rho S_{TD-OCT} R_S}{2eB_{TD-OCT}}, \tag{2.17}$$

This shows that the SNR can be improved using a higher responsivity detector, which is independent of the reference arm power level. Obviously, the larger the sample reflectivity, the larger the SNR. For larger reference power, excess photon noise that varies proportional to the square of power exceeds the shot noise and limits or lowers the SNR [9, 32, 33]. On the other hand, for Fourier Domain systems, a significant SNR advantage over TD-OCT was documented and theoretically demonstrated [33–36]. In the theory using Eq. 2.8 for a single reflection,

the spectral interferogram is reduced to:

$$I_D\left[k_m\right] = \frac{\rho}{2} S_{\mathrm{FD-OCT}}\left[k_m\right] \left[R_R + R_S + 2\sqrt{R_R R_S}\cos\left[2k_m(z_R - z_s)\right]\right] \tag{2.18}$$

Here, it is important to notice that $S_{\mathrm{FD-OCT}} = \frac{S(k)|_{k=k_m}}{2}$ is the portion of the instantaneous power incident on the sample that corresponds to a spectral channel m of the detection system. In the discrete case, the summation for all M the spectral channels contributes to the interference term as:

$$\begin{aligned} i_D\left(z_R - z_S = 0\right) &= \frac{\rho}{2}\sqrt{R_R R_{S_i}} \sum_{m=1}^{M} S_{FD-OCT}[k_m] \\ &= \frac{\rho}{2}\sqrt{R_R R_S} S_{\mathrm{FD-OCT}} M \end{aligned} \tag{2.19}$$

Here, it has been assumed that all the spectral channels have equal power. However, that is only true when a flat-top spectrum is in use. So a correction factor can be applied depending on the shape of the spectrum, for example, for a Gaussian shape, $\sum_{i=1}^{M} S_{FD-OCT}[k_i] = S_{FD-OCT}[k_{M/2}] \cdot M \cdot 0.598$. Therefore, the mean-square peak signal power in FD-OCT is given by:

$$\langle I_D^2 \rangle = \frac{\rho^2 S_{FD-OCT}^2}{4}[R_R R_S] M^2 \tag{2.20}$$

To complete the calculations of the SNR in the FD-OCT, the noise signal should also be transformed into the z-domain. Although the main noise source depends on the light source, let us assume that the system is shot-noise-limited. In this sense, the noise variance in the z-domain can be written as $\sigma^2_{\mathrm{FD-OCT}}[z] = \sum_{i=1}^{M} \sigma^2_{FD-OCT}[k_i] = e\rho S_{FD-OCT} R_R B_{FD-OCT} M$. Thus, the SNR of FD-OCT, in general, is given by:

$$SNR_{\mathrm{FD-OCT}} = \frac{\langle I_D \rangle^2_{FD-OCT}}{\sigma^2_{FD-OCT}} = \frac{\rho S_{FD-OCT} R_S}{4eB_{FD-OCT}} M, \tag{2.21}$$

An experimental and theoretical comparison between sensitivity in TD-OCT against

FD-OCT has been reported in several reports [34–36]. The sensitivity values can exceed 90 dB, which is not feasible to measure with a digitizer of 12 bits. In fact, to measure the value of the total sensitivity of the system, an attenuation has to be placed to avoid saturation of the digitiser. Therefore, the common way to measure the sensitivity is by using attenuation in the sample arm. Then the sensitivity, S, can be obtained as:

$$S\,[dB] = SNR\,[dB] + Attenuation\,[dB] \tag{2.22}$$

Several parameters can cause a decrease in sensitivity, and special attention must be taken when using high-speed sources. In fact, an upper limit exists on the overall power applied to the eye and skin under safe conditions [13], known as the maximum permissible exposure (MPE). This may limit the use of high-speed swept sources in eye imaging, where power would be increased proportionally to compensate for the reduction of the integration time. Still, OCT eye imaging has been demonstrated [37] using swept sources at 1060 nm sweeping at a rate of 3.3 MHz with 1.9 mW on the sample. In the case of other non-biological samples, the overall power incident into them is not restricted by [13], and therefore, it can be increased to take advantage of even faster-swept sources.

2.4.0.1 Sensitivity decay with depth

It is important to clarify where the sensitivity decay with depth arises in Fourier domain OCT. The wavetrains from the reference and sample arm are superposed on the photodetector with a delay, which is given by the optical path difference (OPD) between the reference and sample arm. Here, we assimilate the extension of the wavetrain with the instantaneous coherence length $l_c \propto \lambda_0/\delta\lambda$ of the waves being superposed, where $\delta\lambda$ is the instantaneous linewidth. In Fig. 2.8, the wavetrains are of length l_c, and they are delayed in time by OPD/c. The

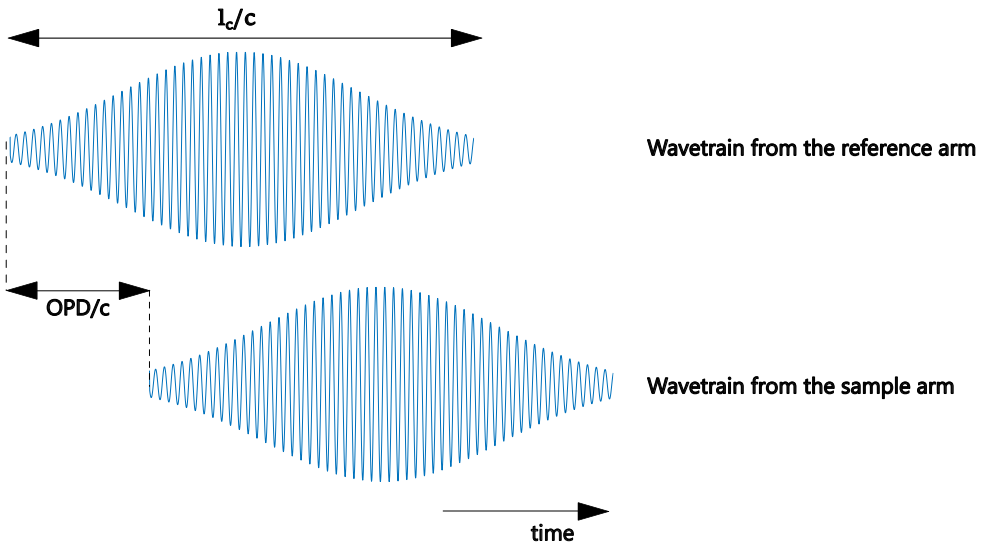

FIGURE 2.8: Wavetrains from the reference and sample arm, separated by OPD/c.

oscillations shown are at the frequency of hundreds of THz. This simple superposition shows that the larger the delay, the less overlap there is between the two wavetrain lengths [38]. This behaviour is described in the practice of OCT by the roll-off curve. This curve represents the reduction in the interference amplitude versus OPD and represents an important parameter of the OCT system, as it determines the practical achievable axial range. The longer the coherence length, the larger the axial range. For a wave of instantaneous linewidth $\delta\lambda$ of Gaussian shape, the axial range is approximated by half of the coherence length, which can be calculated as:

$$z_{-6dB} = 2\frac{\ln 2}{\pi}\frac{\lambda_0^2}{\delta\lambda} \tag{2.23}$$

where λ_0 is the central wavelength of the spectrum. The explanation in Fig. 2.8 above is the same for both SD-OCT and SS-OCT, with the difference that in SS-OCT, the spectral width $\delta\lambda$ is the instantaneous linewidth of the tuning laser (i.e. that in dynamic regime, usually larger than in static regime), whilst in SD-OCT this is assimilated to the spectral resolution of the spectrometer used. Also, the coherence length associated with the wavetrains in Fig. 2.8 in the SD-OCT case is that of the waves after dispersion (diffraction). In both cases, SD-OCT and SS-OCT, the superposition of waves takes place on a photodetector device, a single

photodetector in the SS-OCT and an array of photodetectors in SD-OCT.

In short, the roll-off decay can be considered as a consequence of spectral sampling, which, in the case of SS-OCT, is performed by sampling the photodetected signal corresponding to the channelled spectrum with a narrow window determined by the linewidth. In SD-OCT, the same spectrum at the interferometer output is sampled spectrally, but in this case, with the resolution of the spectrometer. In SD-OCT, a simple equivalent to $\delta\lambda$ is the spectral window sampled by each photocell in the spectrometer camera, i.e. $\Delta\lambda/N$, where N is the number of camera pixels, where $\Delta\lambda$ is the bandwidth of the optical source, that for similar axial resolutions in SD-OCT and SS-OCT is commensurate to the bandwidth of the swept source.

To obtain the mentioned roll-off, a mirror is used in the sample arm of the OCT interferometer, and A-scans are obtained by processing the photodetected signal corresponding to the channelled spectrum at the interferometer output. Such graphs showing A-scan peaks measured for different values of OPD convey information on the axial range possible to be covered by the OCT system, as well as on the accuracy of signal processing. If the channelled spectrum is chirped, good processing has to take that into account, which leads to A-scan peaks of similar width irrespective of OPD. Such signal processing is performed either via resampling followed by an FT or by Master Slave protocols, as will be explained in the thesis. If the width of A-scan peaks increases with OPD, that means that the signal processing failed in correcting for the chirp; this is why the roll-off measurement is widely used in OCT practice to characterise the performance of the OCT system in producing accurate structural representations in depth in the sample. Its envelope is connected to the axial range while variations of the A-scan peak width are due to the uncorrected chirp.

It is important to note that there is no sensitivity decay with OPD in TD-OCT since both wavetrains are completely superimposed with no delay in between them, as TD-OCT operates at OPD$= 0$, as explained in Section 2.2.1.

2.5 Acquisition and signal processing in SS-OCT: *k*-clock, PCDC, CMS

2.5.1 Link between OPD and frequency

In order to acquire the interference signal delivered by the OCT interferometer, it is important to know the bandwidth of the photodetected signal. The sampling rate of the acquisition card should be chosen to be at least double the maximum frequency that can arise at the photodetector signal for the maximum value of the OPD targeted.

An approximate value of the maximum frequency can be obtained by evaluating the expected number of cycles in the channel spectrum, where the larger the OPD, the larger the number of cycles. Let us suppose a swept source system sweeping from k_{min} to k_{max}, where the bandwidth in wavenumber is $\Delta k = k_{max} - k_{min}$. Let us also consider that the modulus of the optical path difference is d. Then, as described previously, the intensity received by the photodetector can be simplified as $I(k) \sim \cos(kd)$. Taking into account that the fringes will cross 0 for every $n\pi$ value, that means that $kd = n\pi$, where n is an integer. Then, for any given OPD, d, the integer number n varies within an interval Δn that can be written as:

$$\Delta n = d\frac{\Delta k}{\pi} \tag{2.24}$$

This is, in fact, the number of half-cycles in the channelled spectrum M. This shows that the larger the bandwidth and the larger the OPD, the larger the number of half cycles. This relation can be expressed now in terms of the source bandwidth Δk. Since

$$\Delta k = -\frac{2\pi\Delta\lambda}{\lambda^2} \tag{2.25}$$

combining the two equations above, an expression for M is achieved:

$$M = \frac{d}{\lambda^2/\Delta\lambda} \tag{2.26}$$

As the denominator is proportional to a constant, the axial resolution, Δz,

$$M \propto \frac{OPD}{\Delta z} \tag{2.27}$$

having the number of half cycles, then this means that during a sweeping interval, the frequency of the signal is practically:

$$f_{modulation} = f_{SweepRate} M/2 \tag{2.28}$$

In the case of spectrometer-based OCT, the photodetected signal is read in a time that is proportional to the camera reading interval, i.e. in this case, the frequency to consider for the digitiser should be calculated by replacing $f_{SweepRate}$ with $f_{CameraReading}$

2.5.2 Balanced detection

Balanced detection is a technique where two photodetectors measure complementary interference signals from the output ports of a fibre interferometer, then subtract them to cancel common-mode noise, and double the amplitude. Two different configurations, balanced and unbalanced detection, are commonly used in the OCT practice. In spectral-domain OCT (SD-OCT), unbalanced detection is typically employed, as illustrated in Fig. 2.5. Here, the photodetected spectral interferogram $I_D(k)$ consists of an AC modulation component—encoding depth-resolved sample information—superimposed on DC terms arising from the reference and sample arm intensities. In the specific case of swept-source OCT, one of the many fibre interferometer configurations that can be used is presented in Fig. 2.9. There are two main differences compared with unbalanced detection:

the photodetector unit and the interferometric design. A balanced photodetec-

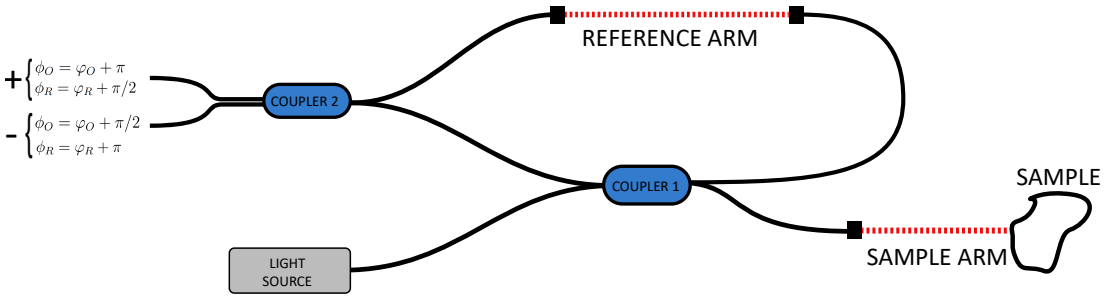

FIGURE 2.9: **Principle of balanced detection** An asymmetric fibre configuration with balanced detections, equations are given for the corresponding intensity measured in each photodiode.

tor is used; those units have two inputs (positive and negative), each of them corresponding to a photodiode. The photodiodes are commonly mounted in series so that their photocurrents cancel each other when they are equal. Then, the difference in photocurrent is sent to a transimpedance amplifier. The asymmetric configuration in Fig. 2.9 allows for generating a π phase difference between the two photodiodes. This is a consequence of directional couplers introducing a phase shift of $\pi/2$ between the transmitted wave and the reflected wave [39]. An analogy can be made with bulk beam splitters where a π phase is introduced between the transmitted and reflected waves. If we analyze the accumulated phase shift from the reference and from the sample at each photodiode, it is possible to observe that for the positive photodiode, the phase shift from the reference and the sample are the following:

$$\phi_O = \varphi_O + \pi \tag{2.29}$$

$$\phi_R = \varphi_R + \pi/2 \tag{2.30}$$

as well, it can be computed for the negative photodiode as:

$$\phi_O = \varphi_O + \pi/2 \tag{2.31}$$

$$\phi_R = \varphi_R + \pi \tag{2.32}$$

Therefore, the intensity sensed from each photodiode in this particular configuration is can be described as:

$$I_{D+} \propto |O|^2 + |R|^2 + 2|O||R| \cos(\phi_O - \phi_R) = |O|^2 + |R|^2 + 2|O||R| \cos(\varphi_O - \varphi_R + \pi/2) \tag{2.33}$$

$$I_{D-} \propto |O|^2 + |R|^2 + 2|O||R| \cos(\phi_O - \phi_R) = |O|^2 + |R|^2 + 2|O||R| \cos(\varphi_O - \varphi_R - \pi/2) \tag{2.34}$$

Finally, an overall π phase difference is observed between each photodiode, positive and negative. Thus, when subtracting the photocurrents from each photodiode, the DC terms are eliminated, and the signal doubles in amplitude. Further benefits are recognized and investigated in several reports [10, 40].

2.5.3 Signal processing

The interferometric signal, i.e. the channel spectra, has to be acquired and processed for A-Scan construction. For swept source OCT, the signal is commonly acquired with a balanced detection system due to natural implementation on a Mach-Zehnder interferometer. After photodetection and amplification, the signal is digitised to start the signal processing. Typically, a Fourier transform is used to reconstruct the spectral information encoded in the channel spectrum. However, there are different numerical procedures that also allow the reconstruction of the spectral information, such as complex master-slave and phase calibration by dispersion compensation [41, 42].

As shown in the previous section 2.2.2, the A-Scan $I_D(z)$ is given by the Fourier transform of the channel spectra $I_D(k)$. Using here the case of a discrete Fourier transform (DFT), the link between $I_D(z)$ and $I_D(k)$ can be expressed in terms of a summation of consecutive harmonics as:

$$I_D\left(z_m\right) = \sum_{i=1}^{N} I_D\left(k_i\right) e^{j\frac{2\pi}{\Delta k} k_i z_m} \tag{2.35}$$

where I_D is the intensity along k received in the photodetector, and $I_D(z_m)$ is the detected intensity of the A-Scan at the position z_m. Furthermore, the Eq.2.35 can be expressed with matrix notation with the exponential forms in what is known as the Vandermonde matrix [43], following the expression:

$$I_D(z) = |V \cdot I_D(k_i)| = \left| \begin{pmatrix} e^{jk_1 z_1} & \dots & e^{jk_1 z_N} \\ \vdots & \ddots & \vdots \\ e^{jk_N z_1} & \dots & e^{jk_N z_N} \end{pmatrix} \begin{pmatrix} I_{k_1} \\ \vdots \\ I_{k_N} \end{pmatrix} \right| \tag{2.36}$$

where V, is a matrix composed of the harmonics at different depths. In order to compute the A-scan and, i.e. decode the spatial information from the spectral information, the signal must fulfil certain conditions. Among these conditions, in the case of using DFT to process the signal, the most important is that $\Delta k = constant$ from the temporal pixel to the next over the whole bandwidth. In that case, the DFT will accurately represent the A-Scan. However, this condition is normally not achieved in real systems. In practice, a swept source does not tune the wavelength linearly over time; an example is shown in Figure 2.10, which is a typical tuning curve of a galvo-mirror deflector-based swept source (as well as the tuning curve of a MEMS-VCSEL and FDML). Most tuning principles will exhibit similar behaviour, where k varies nonlinearly. In addition to the nonlinear variation of k during sweeping, there could be differences caused by the dispersion in the system. Even if the reading of the spectra is linear in k, the dispersion will make wavelengths arrive at different times. Therefore, uncompensated dispersion will cause further chirp in the signal.

Those nonlinearities can be corrected by acting on the channelled spectra (CS) or modifying the Vandermond matrix. The most practical procedure to correct the differences in k due to nonlinear sweeping on SS-OCT is using what is known as a k-clock. A k-clock is a squared signal with an uneven distribution (chirp) at a high frequency, reproducing a clock with the original chirp of the source. The

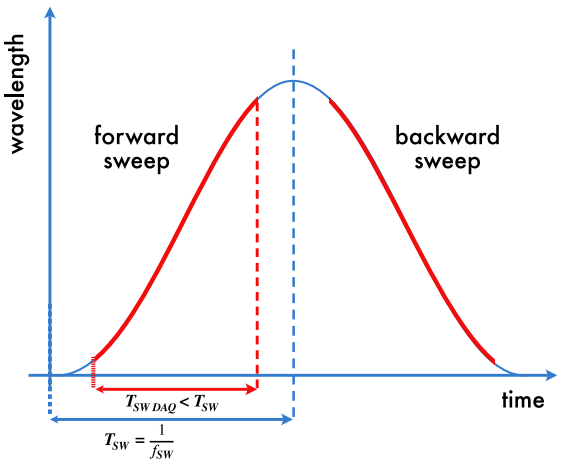

FIGURE 2.10: Example of the sweeping linearity of a tunable light source.

k-clock is used in the acquisition card to acquire the electrical signal with a constant k. In order to generate a k-clock, another interferometer with two mirrors separated at an OPD reaching the maximum axial range achievable is used. Such an OPD will generate a high frequency needed to sample the imaging interferometer properly. In this way, the chirped CS from the imaging interferometer is sampled by a clock of similar chirp and events in time are now separated by constant advances in k. Since the k-clock is used to sample the interference, it is important to place it at a high frequency since the frequency selected will limit the maximum OPD acquired. Therefore, a resampled CS is obtained due to a nonlinear digitalization.

This method, using the k-clock, is applied in real-time and exhibits several benefits. Due to real-time sampling, fewer operations are needed to generate the A-Scan; only a DFT on the acquired CS is needed. However, this is a pricey alternative in terms of computational power and hardware, as another interferometer and photodetector are needed. In addition, if the dispersion of both interferometers is not the same, a second processing step is required to correct the chirp due to dispersion.

There exist different numerical alternatives that can be done to generate the A-Scan [43, 44], apart from using the k-clock. However, those may be time-consuming, which can be a problem for real-time processing. For example, for

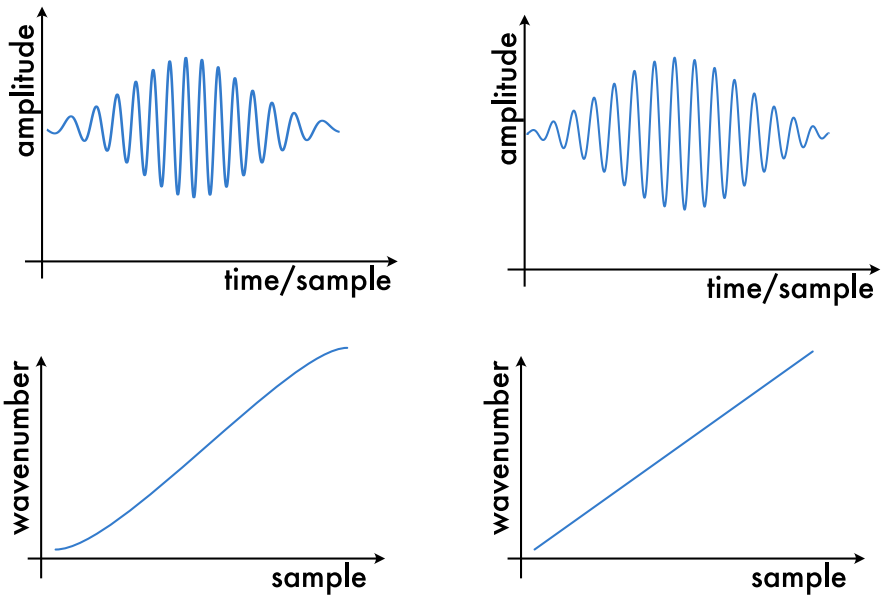

FIGURE 2.11: Raw channel spectrum with nonlinear phase, on the left. Channel spectrum with linearized phase.

phase calibration by dispersion compensation (PCDC) [45], same as in the original procedure, the Vandermonde matrix is used to convert $I_D(k)$ into $I_D(z)$. However, the acquired intensity along k, $I_D(k)$ is now resampled in postprocessing in such a way that the condition of $\Delta k = constant$ is satisfied. The A-Scan, $I_D(z)$ can be expressed in terms of the new resampled channelled spectra as:

$$I_D\left(z_m\right) = FFT\left(I_D\left(\hat{k}_i\right) e^{-jh(\hat{k}_i)}\right) \tag{2.37}$$

where $\hat{k}_i$ denotes that the wavenumber has been resampled in order for Δk remaining constant. The phase information is extracted from a set of previously acquired channel spectra to resample the new channel spectra. Then the phase is linearized, and consequently, the CS is as well, as is shown in Figure 2.11. Figure 2.11 presents a simulation of a chirped signal with a Gaussian envelope on the left side while a non-chirped signal is displayed on the right side.

Alternatively, complex master-slave is an alternative numerical procedure to produce A-scans [43, 46–49], which does not resample the channelled spectra. Instead, the obtained raw channel spectra are multiplied with theoretically inferred masks incorporating the same chirp. In the original idea of master slave [41],

those theoretically inferred masks were channel spectrums acquired equally displaced OPDs. However, in complex master slave, a few (at least two) experimental channel spectra are acquired and used to infer a pair of calibration functions $g\left(k\right)$ and $h(k)$, which are related to the phase of the interference signal as:

$$\varphi_{CS}\left(k,z\right)=g\left(k\right)z+h\left(k\right)+\varphi_{\text{rand}} \tag{2.38}$$

where φ_{rand} is assumed to be zero on average, $g\left(k\right)$ and $h(k)$ correspond respectively to the nonlinearities of the system and the unbalanced dispersion in the OCT interferometer. It is important to understand the behaviour of those two functions. At first, $g(k)$ corresponds to the nonlinearities in the system, which follows the movement of the "sweeping" object. As an example, a laser where a Fabry-Perot is used to sweep over the tuning bandwidth, the mirror will not move linearly, specifically when the mirror has to stop and move back in the opposite direction; this movement can be similar to the galvoscanner's movements at high speed [50]. Therefore, $g(k)$ is expected to exhibit a linear behaviour towards the central part of the spectrum and a non-linear behaviour towards the edge of the spectrum. Secondly, here, $h(k)$ corresponds to the unbalanced dispersion of the OCT; once assembled, the reference and sample arm of an interferometer, the overall OPD between them might be similar, i.e. OPD$\simeq 0$. However, the dispersion in each of the arms might be quite different, which depends on the fibres and optics that are used for each of them. In many systems, the sample arm has many lenses, i.e. a telescope to make larger beams and a lens system to focus the light into the sample. In contrast, the reference arm normally only has two lenses, one for collimating the light and another to launch the light back into the fibre. Therefore, those different optics between the reference and sample arm are expected to influence $h(k)$. The two calibrating functions $g(k)$ and $h(k)$ are calculated from the phase $\varphi\left(k,z\right)$ of the set of channel spectrum acquired at different OPD values, obtaining an equation system with $g\left(k,z\right)$ and $h(k)$. Those steps are

known as the calibration stage, where a set of at least two channel spectra from a single reflector is acquired. Furthermore, the calibration stage mentioned here is not unique to SS-OCT. Other systems like SD-OCT will have the same issues; the diffraction grating gives $g(k)$ in the case of SD-OCT; spectrometers are, in general, not fully linear, and this has to be calibrated for OCT. Moreover, $h(k)$ becomes more noticeable for systems at lower central wavelengths, 800 nm, 600 nm, etc. This is because the fibre dispersion is usually higher and with a more prone slope than 1060 nm. The acquired channel spectra must be from a single reflector since we need to extract the phase from a known OPD at a single frequency. The phase is extracted using a Hilbert transform. Later, a system of equations as follows is used to determine $g(k)$ and $h(k)$:

$$\varphi_{CS}\left(k, z_1\right) = g\left(k\right) z_1 + h\left(k\right) \tag{2.39}$$

$$\varphi_{CS}\left(k, z_2\right) = g\left(k\right) z_2 + h\left(k\right) \tag{2.40}$$

Once these functions are computed, the theoretically inferred channel spectra, also known as masks, can be computed. The masks take the form of:

$$Mask(z_1) = e^{j(g(k)z_1 + h(k))} \tag{2.41}$$

Finally, a matrix $T(k, z)$ is built using the theoretically inferred CS, placing the masks for different z positions in each column.

$$I_D\left(z_m\right) = \sum_{i=1}^{N} T\left(k, z\right)\ I\left(k_i\right), \quad \text{where } T\left(z\right) = dg_i e^{j(g_i z + h_i)}; \tag{2.42}$$

where dg is the difference between $g(k)$ values in k, i.e. $dg = dg(k)/dk$. It is worth commenting on a few differences between PCDC and CMS. At first, in terms of computational power, for PCDC, the number of operations to perform is $N \log N$, for CMS, the number of operations becomes $Q(2N - 1)$, where Q is the number of axial points on the A-Scan. Bradu et al. [43] reported no major differences

between PCDC and CMS. However, one of the main differences between CMS and PCDC is that there is more control over the number of axial points in an A-Scan. The Nyquist theorem determines the number of axial points for PCDC, *k*-clock or simple FFT. As a difference, in CMS, this is defined by the number of theoretically inferred masks used in the matrix $T(k, z)$. Consequently, the number p of axial points appears as a free-parameter. In its limits, the maximum number of axial points is dictated by the Nyquist limit as well. For a number p of cycles in the channel spectra, the number of spectral samples should be double the number of cycles, $2p$. After FT, p is also the number of axial points. The minimum number of axial points should be obtained by the theoretical resolution of the system, i.e. at least two axial points on each axial resolution interval. Moreover, the depth region of the A-Scan can be selected according to the intended application; for instance, if a single *en-face* OCT image is to be displayed, only a single mask is needed and not p.

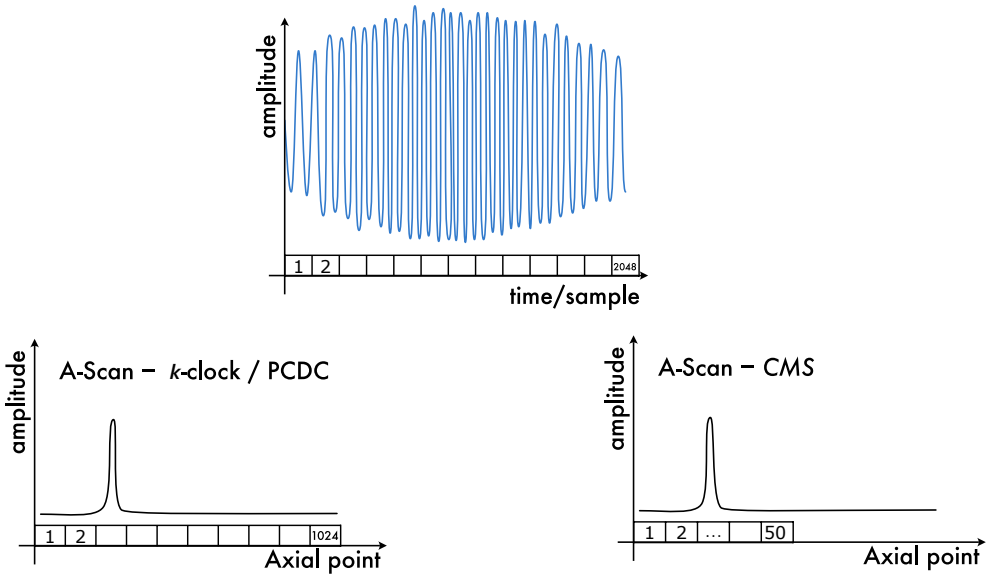

FIGURE 2.12: Comparison of the number of axial points in an A-Scan for (a) k-clock or PCDC processing vs (b) CMS processing.

Figure 2.12 depicts an example of these three procedures and shows the behaviour of CMS in terms of axial points. For a 2048 points channel spectrum, *k*-clocking and PCDC deliver half of the points in the A-Scan, having to process

1024 points. In contrast, CMS will provide a desired number of points in the A-Scans. This number of points can start at one particular depth previously given to the processing and have the desired number of points. Further, the selection of depths that the A-Scan will display can be seen as a form of band-pass filtering since frequencies lower than the starting depth and ending depth are not seen. In fact, for retinal eye imaging, a matrix $T(k, z)$ can be built to focus only on the retina and avoid many operations by using fewer points. However, it is worth noticing that this benefit is also possible using a simple DFT, but as a difference, CMS calibrates the non-linearities added due to the source and system.

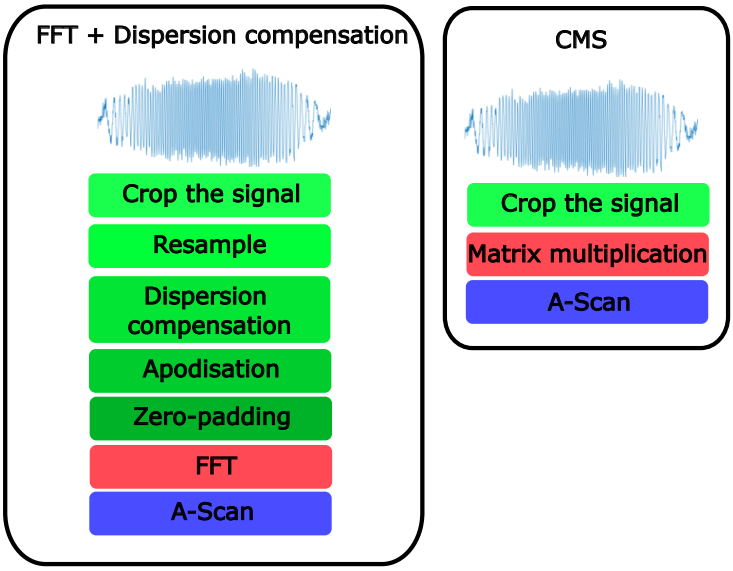

FIGURE 2.13: Comparison of OCT processing based on calibrated FFT on the left, and based on CMS on the right.

Overall, the OCT processing has been summarised for FFT-based and CMS as in Figure 2.13. In the Fig. 2.13, the green blocks correspond to the action on the raw channel spectra, red blocks correspond to the main operation done, and finally, the blue blocks correspond to the A-Scan. At first, the signal must be cropped according to the number of points desired to use. Later, the signal has to be resampled, typically with spline interpolation, the phase is then compensated for the dispersion, a window is applied to the channel spectra, typically Gaussian or Hanning, and zero-padding is often used to obtain the desired number of points in the z direction. Once all those mentioned steps are done, FFT should be

performed, and the A-Scan is finally produced. On the other hand, for CMS, once the calibration stage is done, only matrix multiplication is needed, obtaining, as a result, the A-Scan.

2.6 Lateral scanning and Imaging considerations

In the process of scanning the sample, different optical configurations can be used depending on the sample. The optical designs used in the thesis are the following [51–54]:

- Case 1: The light is collimated onto the sample, for example, for the posterior segment, i.e., the human retina. A 4f system can be used (see Figure 2.14 (a)). A $4f$ system consists of two positive lenses with the input at focal length f_1 in front of lens 1 and the output plane located one focal length f_2 after lens 2. The magnification is equal to f_2/f_1, making it beneficial to expand the beam into a large beam with a diameter equal to the pupil size. Because the eye has an effective lens focusing on the retina, the beam should be collimated before reaching the cornea.

- Case 2: The light is directly focused into the sample, for example, the anterior segment of the eye, i.e., the human cornea. A simpler system with a positive lens at f distance between the sample and the mirror will be enough; see Figure 2.14 (b).

Typically, achromat lenses are used in order to compensate for the wavelength focal shift. Achromat lenses are specially designed to limit the effect of chromatic aberrations. Moreover, telecentric lenses are also useful in compensating for the deviations created when the beam passes along the edges of the lens. Telecentric lenses (also known as scan lenses) generate a flat image plane and a spot size that experiences minimal distortion as the angle of the incident beam relative to the optical axis of the lens is adjusted. In general, doublets with air space

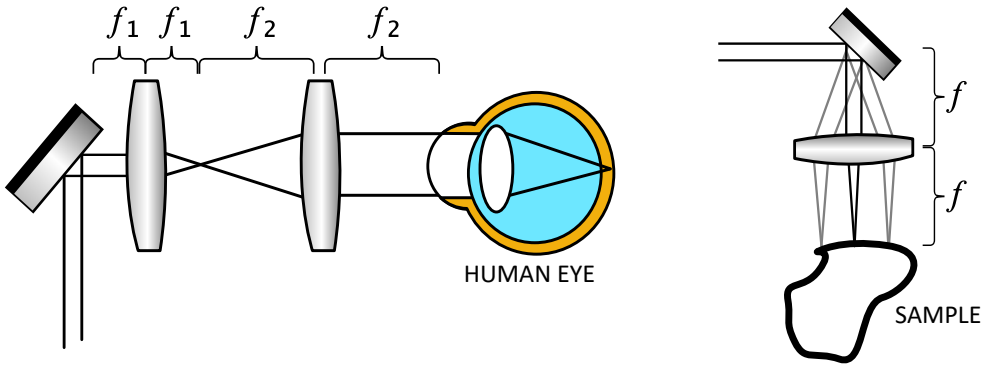

FIGURE 2.14: **Systems designs used for imaging samples in OCT.** (a) Case 1, in which the light is collimated onto the sample, for example, for the posterior segment, i.e. human retina. (b) Case 2, where the light is directly focused into the sample, for example, the anterior segment, i.e. human cornea.

between the lenses are avoided due to the ethalon effect that they can cause, i.e. multiple reflections. As mentioned before, the OCT systems, depending on the configuration, might be sensitive to reflections of orders of 10^{-5}, which can be the case of doublets.

2.6.1 Galvo, and resonant Scanners

In order to generate a B-Scan or even a volume, scanners are needed to deflect the beam through the lateral positions. For that purpose, movable mirrors are used. The main features and scanning procedures will be briefly discussed here [50, 55]. The speed of the stroke is the main parameter needed to decide what type of deflector should be used. Galvanometer scanners are practical in the sense that their speed and amplitude can be modified according to the needs. Commonly, the raster patterns used in OCT are square, and depending on the triggering between the two scanners, it is possible to observe two main raster patterns, see Figure 2.15.

When a scanning configuration to obtain volumes is used, two scanners are needed, and one of the two galvanometers will move at a faster rate than the other. In the following sections, they are named fast and slow. If the fast and slow scanners are synchronized, only triggering one time per volume at the start,

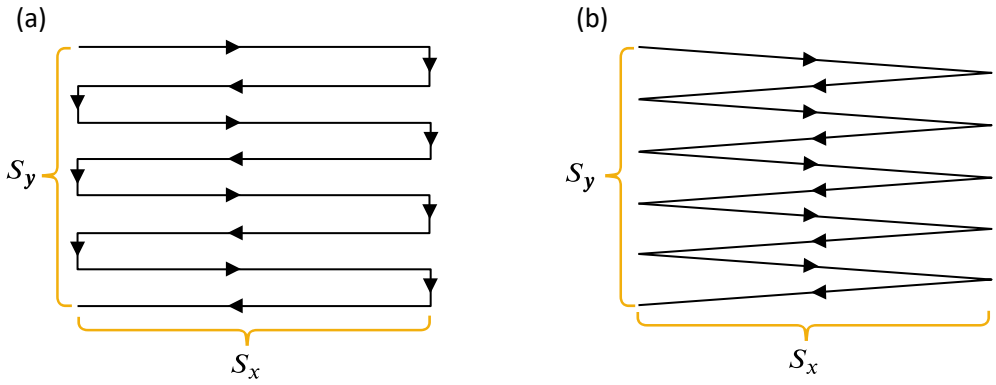

FIGURE 2.15: **Raster scanners.** (a) Stair step, and (b) free running.

then it is known as free-running (Figure 2.15 (a)). For a proper representation, the signal received at each point has to be slightly shifted upwards for each B-Scan line, due to both mirrors moving constantly. Furthermore, during the returning point, i.e. edges of the stroke, the scanner will move slower on the edges than in the central part; this is known as a fly-back and the image has to be processed afterwards for a clear representation.

On the other hand, if the slow scanner is synchronized to move only once the fast scanner has completed a stroke, then it is known as the stair pattern. In figure 2.15 (b), the slow scanner is waiting for the fast scanner to finish the process, which triggers the slow scanner to move a step further. On most occasions, this is the scanning pattern used. Furthermore, for OCT-Angiography, where lapse time between B-Scans needs to be adapted, the stair pattern is used so that the slow axis is moved back and forth to obtain the second B-Scan at the same position and allow longer time between consecutive B-Scans [53]. Table 2.1 presents the main specifications of galvanometers and resonant scanners. In general terms, inertia limits the maximum mass the magnets can move back and forth. Therefore, for slow speeds, a big mirror can be mounted over the magnet, and large scanning angles can be achieved, typically $30 - 40$ degrees. In contrast, inertia is to be counteracted for high-speed resonant scanners by utilising small angles, typically in the order of $\sim 10 - 20$ degrees. This means a lower tangential speed, and thin mirrors must be used. On the other hand, resonant scanners follow sinusoidal

movement, which requires further corrections to the image.

	Galvanometers	**Resonant scanners**
Speed	0-1.5 kHz	1-16kHz
Beam diameter size	Up to 40 mm for slow galvos	For the slowest, 4 mm
Scanning angle	Maximum at slow frequency of ± 40 degrees	At frequencies of 1 kHz, maximum of ± 20 degrees and decreasing with frequency
Programmable function	Yes, frequency adjustable	No, fixed frequency
Cost	$\approx 1.5k$£	>3k£

TABLE 2.1: Comparison between Galvanometer scanners and resonant scanners.

2.7 Conclusions and discussions

In this chapter, the theory of OCT has been briefly reviewed, from the motivation behind this imaging modality to the parameters that will be referenced in the following chapters. Fourier-domain OCT, encompassing spectral domain (SD-OCT) and swept-source (SS-OCT) techniques, has surpassed time-domain OCT in several critical parameters, including sensitivity, acquisition speed, and resolution. SD-OCT offers high sensitivity and resolution, making it ideal for applications requiring detailed cross-sectional images. In contrast, SS-OCT offers a long axial range and faster A-scan rates and excels in imaging deeper tissues and dynamic processes. A brief description of the procedures to generate A-Scans from the interferometric signal photodetected to the production of OCT images has been given, mainly for the case of SS-OCT but also applicable to SD-OCT. Two main procedures can be used, either by hardware means, i.e., using a k-clock or by using numerical methods. Those numerical methods involve reconstructing the phase for which a calibration stage is needed. The steps for the calibration stage are outlined for CMS and PCDC methods. Clearly, CMS serves as an equivalent to a non-uniform Fourier transform, where the non-uniformity in Δk is adjusted

in accordance with the system's dispersion and nonlinear properties. As with many imaging techniques, OCT parameters can be optimized based on the sample under test, though this often involves trade-offs, sensitivity and sweep rate, axial and lateral resolutions, etc. For instance, achieving high axial resolution (1-10 μm) requires broad bandwidths (100 nm or more, depending on the central wavelength of the light source). On the other hand, increasing the sweep rate in SS-OCT enables applications in large scanning areas, imaging of fast-moving objects, and its use in production lines. However, this may come at the cost of reduced sensitivity or increased system complexity. The numerical algorithms used to process A-scans in SS-OCT play a crucial role in image reconstruction, and they are essential for exploring the full potential of SS-OCT, particularly in real-time imaging applications.

Chapter 3

Review of optical sources used in SS-OCT

This chapter discusses two main types of optical sources: fibre-pulsed and swept sources. In the first part, the basic elements of fibre lasers are presented. Nonlinear polarisation rotation is briefly explained. Furthermore, the second section provides a review of swept sources for OCT, starting with a historical introduction to their development and ending with current requirements. Common tuning methods are presented for swept sources alongside their working principles.

Contents

3.1 Fibre pulsed lasers

3.1.1 History of pulsed lasers

Throughout the decades following the laser invention in 1960, pulsed operation has become a broad field of research and practical application [56, 57]. During the early years and for a long time, research was limited to bulk lasers only. The rise of fibre lasers came via three main experiments. The first one was in 1973; as a result of using an end-pumped fibre laser [58] it was possible to increase the pumping efficiency of doped fibre, which led to further developments. The second experiment, in 1985, demonstrated the amplification of a single transversal mode [59]. In 1988, the development of double-clad fibre marked a significant advancement, enabling highly efficient and high-energy pumping, thereby contributing to notable achievements in the field. Coupled with the rise of solid-state fibre pump diodes [60, 61], fibre lasers nowadays can achieve kilowatt-range powers, and pulsed lasers can produce megawatt peak powers with millijoule pulses [62]. A major advancement in pulsed fibre laser source technology consisted of the invention of the Er-doped, passively mode-locked laser that generated optical solitons [63]. Solitons are self-sustaining waves that can persist indefinitely in stationary settings, and their technical specifications are outlined in the subsequent section [64–66]. To produce a continuous train of pulses, a laser requires a mechanism that aligns the frequency modes of the cavity with a fixed phase relationship. This mechanism is known as "mode-locking". Over the last 50 years, researchers have been working to create a mechanism that can produce shorter and shorter pulse durations with higher energies whilst remaining simple and robust. Active mode-locking uses an electro-optic component to modulate the amplitude or frequency, while passive mode-locking utilizes the nonlinear responsiveness of materials and passive component configurations. Passive mode-locking can achieve narrower pulses than active mode-locking, through passive loss modulation. In the latest section of this chapter, it is discussed some of the passive

component arrangements that enable mode-locking [67]. There are two types of passive saturable absorbers: real and artificial. Real saturable absorbers are those in which the response is induced by a material. These include semiconductor saturable mirrors (SESAM) [68, 69], quantum dots [70], carbon nanotubes [71], etc. They are now widely used in mode-locking, as they are compact and simple to implement and use. However, real saturable absorbers suffer from realities of material constraints: they degrade over time and have low damage thresholds, usually limiting the output power of the laser. In contrast, artificial saturable absorbers utilise nonlinear optical effects like self-phase modulation or polarisation rotation to mimic the behaviour of saturable absorbers. Examples include nonlinear loop mirrors [72–74], nonlinear polarisation rotation [63, 75], additive-pulse mode-locking [76–79], and Kerr lens mode-locking [67]. The advantage of these methods is that they are generally capable of dealing with large amounts of power. Whether real or artificial, each mode-locking mechanism has applications where its pros outweigh its cons.

3.1.2 Optical Fibre

The principal characteristics of the main fibres in use are important for understanding several aspects of the thesis. Fibres are electromagnetic waveguides that guide light, used in a wide spectrum from ultraviolet (UV) to mid-infrared (MIR). They are normally cylindrically shaped with two main materials, whose difference in their indices of refraction produces wave confinement. The difference between the refractive index of the inner core and cladding is about 1-2%. When the two parts, core and cladding, each have a constant index of refraction throughout the material volume, the fibre is called step-index fibre. This type of fibre tolerates many modes of propagation. The rest of the thesis will focus more on single-mode operation. This means that the only mode which successfully traverses through the fibre is the fundamental mode which possesses a near Gaussian profile. In OCT, if multimode fibre is used, then mode-beating degrades the

signal. Hence, multimode fibre is not used for this application.. Due to a fibre's circular symmetry as a waveguide, the field is isotropic around its centre ($r = 0$). This simplifies the field equation, reducing it to a 1D formulation for field propagation. In passive fibres, the nonlinearities are minimal, while in active fibres, deliberate doping maximizes nonlinearity.

3.1.2.1 Passive fibre

Passive fibres are designed to transmit light without perturbing the spectral components. Passive fibres are normally characterised by losses measured in dB/km. Standard telecommunications fibres can be created with as low as 0.01 dB/km loss. The most common type of fibre is single mode, where the core has the size of the spatial mode for which the desired fundamental mode can propagate (Figure 3.1(b)).

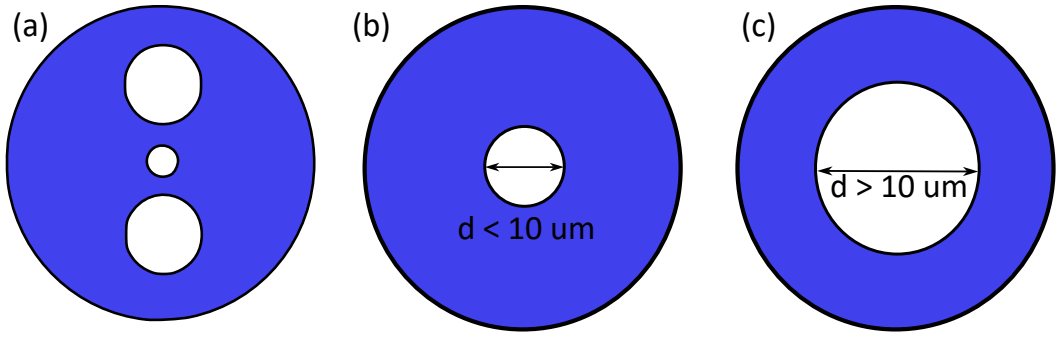

FIGURE 3.1: Sketch of (a) Polarisation Maintaining (PM) fibre PANDA version, (b) single mode fibre, (c) multimode fibre. Values of the core diameter d for 1060 nm.

Multimode fibre has a core of a larger size than the transverse spatial mode, and therefore, many modes can propagate at the same time. Polarisation-maintaining (PM) fibres, Figure 3.1(a), are fibres that have an asymmetry in their cross-section. The asymmetry is characterized by the refractive index in the fast axis and the slow axis. Some PM design possibilities are PANDA and bow-tie. The radial asymmetry in the refractive index produces a difference in the fast and slow index. When the linear polarisation is sent in the fast axis of the PM fibre, this is preserved across the whole fibre. In a PM fibre, there is a retardance between the

fast and slow axes by the difference in the refractive index on the fast and slow axes, as $\beta = \Delta n = n_{\text{fast}} - n_{\text{slow}}$. However, this creates a different speed for waves travelling in the fast axis than the slow axis, which is commonly known as polarisation mode dispersion (PMD). PMD is an undesired effect in OCT because when light propagates in a state different from linear, the light produces a beating. This beating is manifested as a modulation of the optical spectrum at the end of a PM fibre. Such modulation cannot be distinguished from similar modulation due to the delays inside the sample imaged. In other words, the interference signal contains pattern noise. Another type of fibre that employs polarisation is polarizing fibre. In such fibres, the slow axis is blocked, so only the projection of the polarisation into the fast axis will propagate. Apart from the actual design in the cross-section, the material itself can also be engineered [80]. This means that confinement can be modified. This is the purpose of dispersion compensating fibres; their index profile is modified by using slightly different materials over the cross-section. The dispersion of light through fibre has two main components: the material dispersion and the waveguide dispersion. Material dispersion arises from the change in the refractive index with wavelength. Waveguide dispersion arises from the geometry of the waveguide and can be either positive or negative.

$$D\left(\lambda\right) = D_{\text{material}}\left(\lambda\right) + D_{\text{waveguide}}(\lambda) \tag{3.1}$$

where $D(\lambda)$ uses units of ps/nm/km. Therefore, through material engineering, it is possible to fabricate a fibre with a desired dispersion slope versus wavelength. Another type of passive fibre is double-clad fibre, which normally has two different spectral bands of use. When used in a laser, this is normally employed in pumping, where a pumping wave is applied to the cladding, and another wave with a different wavelength propagates through the other region. In combined OCT fluorescence imaging systems, the core is used for illumination, while the cladding is used for fluorescence collection.

	Er+ [84]	Yb+ [85]	Ho+ [86]	Tm+ [87]
Central wavelength (μm)	1.55	1.03	1.7-2.1	2.1
Upper state lifetime (ms)	0.8	10	0.6	2

TABLE 3.1: Rare Earth doped materials characteristics.

3.1.2.2 Active fibre

Unlike passive fibre, active fibres are optical fibres with one or more doping agents; the doping agent is also known as a rare earth dopant. Rare earth-doped fibres have been key to the success of the telecommunication industry. The most popular earth dopants, Erbium and Ytterbium, are normally used for amplification by stimulated emission at 1550 nm and 1030 nm, respectively. There are three critical processes in laser operation: spontaneous emission, stimulated absorption, and stimulated emission, as identified by Albert Einstein in his 1916 publication on the quantum theory of radiation [81–83]. In his paper, Einstein postulated that an atom could absorb a quantum of light for a short time if the light had a specific wavelength corresponding to the band gap. This theory implies that excited atoms may emit their photon prematurely when influenced by a photon of the same wavelength. These two photons would then move together in the same direction, with matching phase and polarisation, also known as stimulated emission. These essential phenomena form the basis for the critical processes in a laser that enable the creation of coherent beams of light.

For a three/four-level system, a pump laser excites the energy from the ground state to an upper state through stimulated emission, and the material will emit photons to recover to the ground state through the more efficient transition, i.e. through phonon-photon, emitting a photon at 1030 nm in the process.

The gain bandwidth of these materials depends on the dopant amount and the sublevels of energy, see Table 3.1, but generally, the gain bandwidth do not exceed more than 50 nm. This has applications in booster stages for swept sources outside of the cavity [88] or in addition to other amplifiers in the cavity [89].

3.1.3 Pulses in a fibre medium

Within this thesis, some of the developments on swept sources are linked with mode-locked fibre lasers. For that reason, essential physics on pulse propagation in optical fibres is needed. A well-known equation that describes pulse propagation is the nonlinear Schrodinger equation (NLSE) which in its simplest version can be written as:

$$\frac{\partial A}{\partial z} = i\,\frac{\beta_2}{2}\frac{\partial^2 A}{\partial t^2} + i\gamma\,|A|^2\,A \tag{3.2}$$

where t is time in a reference frame moving at the group velocity of the pulse, z is the longitudinal coordinate, and $A = A(z,t)$ is a slowly varying envelope that describes the longitudinal amplitude, such that the power in Watts is given by $|A|^2$. To facilitate comprehension of the thesis, Equation 4.2 has been included to provide an intuitive understanding. The equation's right-hand side features two distinct terms, denoted in red and green, representing the fundamental physical dynamics examined in mode-locked fibre lasers: group velocity dispersion (GVD) and self-phase modulation (SPM). In the following sections, these phenomena will be presented along with other factors that are essential in characterizing high-power, femtosecond-duration fibre pulses. One of the most famous solutions to this equation leads to what is known as a soliton [90]. This occurs when GVD and SPM are compensated. Silica fibres have anomalous dispersion in the 1550 nm band. Therefore, combined with high power confined in an optical fibre, a soliton can be generated using a set-up as shown in Figure 3.2. How-

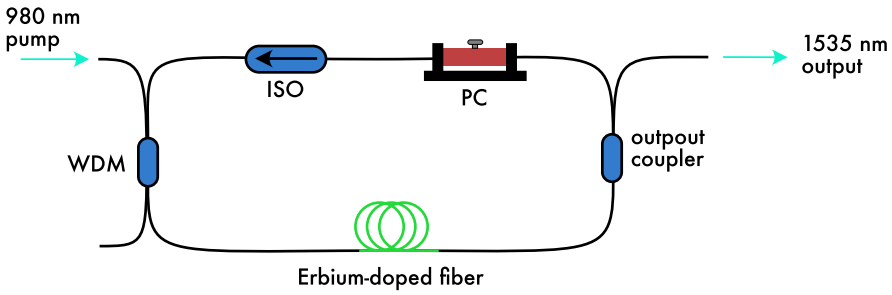

FIGURE 3.2: Setup design of a nonlinear polarisation rotation mode-locked laser. ISO: Isolator, WDM: Wavelength Division Multiplexing, PC: polarisation controller.

ever, this system has certain limitations. The duration is given by the area theorem [91]. The area theorem links the energy and pulse duration; hence, they are limited. The pulse formation becomes unstable for short pulses (shorter than a few picoseconds) due to high nonlinear phase shift per round-trip; such an effect becomes difficult to handle, even with a strong saturable absorber. Therefore, other alternatives must be considered for shorter pulses and higher pulse energies. A concept for significantly higher pulse energies and shorter pulses is that of the stretched-pulsed fibre laser [92], as shown in Figure 3.3. Here, the laser resonator contains pieces of fibres with different signs of group delay dispersion. The laser works as follows: The pulse originates from mode-beating between longitudinal modes in the cavity, forming a noisy seed that is amplified by the gain medium. As the pulse propagates through a segment of anomalous-dispersion fibre, it acquires a positive chirp and broadens temporally due to higher frequencies travelling faster. This stretched pulse enters a normal-dispersion fibre, where the reversed dispersion compresses it by slowing down higher frequencies. Finally, a polarization-sensitive isolator acts as a saturable absorber, preferentially transmitting the high-intensity pulse peak while attenuating the wings, further shortening the pulse duration and stabilizing mode-locking. Throughout each round-trip, the pulse undergoes dramatic changes in duration, chirp, and spectral width—stretching in anomalous fibre, compressing in normal fibre, and sharpening via the isolator. This dynamic balance between dispersion, nonlinearity, and loss ensures stable stretched-pulse operation, where the pulse cyclically breathes while maintaining a consistent profile after each full cavity transit. The interplay of these effects suppresses noise, enforces pulse shaping, and sustains the mode-locked state.

Thus, the achieved pulse duration depends on the location where the pulses are coupled out. External dispersive compression may be required to achieve transform-limited pulses. As the pulses are significantly chirped in most places within the laser resonator, nonlinear phase shifts do not have a strong limiting

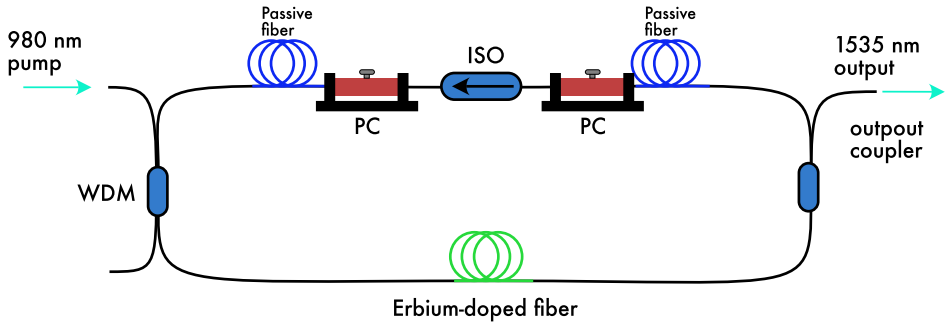

FIGURE 3.3: Stretched pulsed mode-locked laser, ISO: Isolator, PC: polarisation controller, WDM: Wavelength Division Multiplexing.

effect, as in a soliton fibre laser. Therefore, pulse durations well below 100 fs can be achieved, and the pulse energies are typically several nanojoules.

3.1.3.1 Chromatic dispersion

Ultrashort pulses have many spectral components. This can result in broadening due to the chromatic dispersion effects when the pulses propagate through the fibre (see Figure 3.4) or reflect from the laser mirrors.

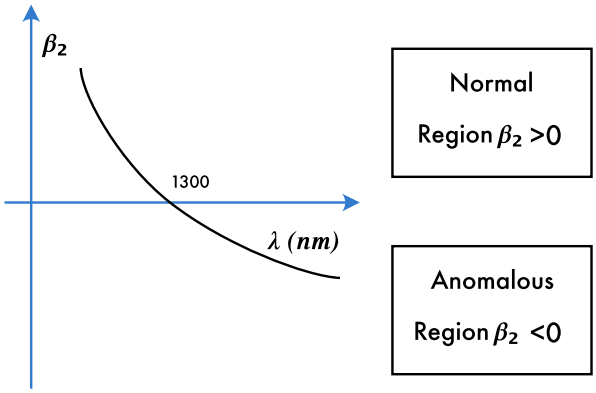

FIGURE 3.4: Chromatic dispersion of an optical fibre.

The effect of chromatic dispersion in an optical element (or for an entire resonator round-trip) can be described via the frequency-dependent wavenumber, $k(\omega)$, that a low-intensity wave experiences (nonlinear effects are excluded here). A Taylor expansion leads to the equation:

$$k(\omega) = k_0 + \frac{\partial k}{\partial \omega}(\omega - \omega_0) + \frac{1}{2}\frac{\partial^2 k}{\partial \omega^2}(\omega - \omega_0)^2 + \frac{1}{6}\frac{\partial^3 k}{\partial \omega^3}(\omega - \omega_0)^3 + \cdots, \tag{3.3}$$

where ω_0 is the frequency at the centre of the wave spectrum, and all derivatives are taken at this frequency. The meanings of these terms are as follows:

- The first derivative ($\frac{1}{v_g} = \frac{\partial k}{\partial \omega}$) is the group delay, that is, the temporal delay encountered by the wave for a narrowband spectrum.

- The second derivative ($\beta_2 = \frac{\partial^2 k}{\partial \omega^2}$) is the group delay dispersion (GDD), typically measured in units of fs^2 or ps^2. This determines, in the first order, the frequency dependence of the group delay. It is commonly accepted that when the refractive index decreases with increasing wavelength, it is known as the normal regime ($dn/d\lambda < 0$), and when the refractive index increases with increasing wavelength, it is known as the anomalous regime. The group velocity dispersion (GVD) is the group delay dispersion per unit length. Hence, the units in the SI are $[\frac{\mathrm{s}^2}{\mathrm{m}}]$. For optical fibres, a new parameter called the dispersion parameter is defined through the GVD:

$$D_\lambda = \frac{\partial}{\partial \lambda} \frac{1}{v_g} = -\frac{2\pi c}{\lambda^2} \beta_2, \tag{3.4}$$

  which usually has units of $\frac{\mathrm{ps}}{(\mathrm{nm \cdot km})}$, where λ is the wavelength and c is the speed of light in vacuum.

- The third derivative quantifies third-order dispersion (TOD) and is typically measured in units of fs^3.

3.1.3.2 Nonlinear effects

The Kerr nonlinearity phenomenon results in self-phase modulation (SPM) of a pulse as it travels through a medium. This modulation affects the phase delay and instantaneous frequency, causing a chirp to appear in the previously uniform pulse. The refractive index changes as,

$$n = n_0 + n_2 I \tag{3.5}$$

where n_0 is the initial refractive index, n_2 is the nonlinear refractive index, and I is the intensity of the wave. Equation 3.5 describes how light applied to a nonlinear medium can induce a change in the refractive index of that medium. One of the most important consequences of this effect is the cause of an intensity-dependent phase shift. First, the nonlinear coefficient, which relates to the effective area, A_{eff}, is defined as:

$$\gamma_{NL} = \frac{2\pi n_2}{\lambda_0 A_{\text{eff}}} \tag{3.6}$$

Using the nomenclature adopted for the NLSE, the nonlinear phase shift, after propagation through a fibre of length L, can be expressed as:

$$\Phi_{NL}(L,t) = \gamma_{NL} L \left|A(L,t)\right|^2 \tag{3.7}$$

When a pulse is subjected to nonlinear phenomena such as self-phase modulation (SPM), it generates frequency components at the edges of the spectrum. If a laser resonator experiences both chromatic dispersion and SPM, a multifaceted interplay of effects unfolds. The outcome differs qualitatively, contingent upon the extent and direction of these effects:

- The combination of normal dispersion (positive GDD) and self-phase modulation (with positive n_2) can exacerbate the problem since both lead to an upchirp near the pulse centre.
- The combination of a suitable amount of anomalous dispersion (negative GDD) with self-phase modulation (positive n_2) can lead to fundamental soliton pulses, where GDD and SPM essentially cancel each other, and no temporal or spectral pulse broadening occurs. This soliton mechanism works well for nonlinear phase changes larger than those tolerated without GDD. However, it becomes unstable again when the nonlinear phase change per resonator round-trip becomes too large.

- Strong nonlinear pulse shortening can occur with less anomalous dispersion, which usually leads to unstable pulse evolution due to insufficient dispersion for fundamental solitons.

In certain types of mode-locked lasers, such as fibre lasers, the relative placement of optical components in the cavity is a crucial factor. This is due to significant self-phase modulation and group velocity dispersion phenomena occurring within a resonator round-trip. It is important to note that these effects depend on the order of the optical components encountered by the propagating laser wave rather than solely on the total amount of self-phase modulation and group velocity dispersion.

3.1.4 Saturable absorber: Nonlinear polarisation rotation

For the scope of this thesis, only Nonlinear Polarisation Rotation (NPR), also called Nonlinear Polarisation Evolution (NPE) as a saturable absorber, will be described. In order to achieve a broadband pulse from a mode-locked cavity, one possibility is to employ NPR with a broadband gain medium. NPR has been widely studied during the '90s [63, 75], a technology that is revived nowadays to be used in tandem with time-stretching [93–95].

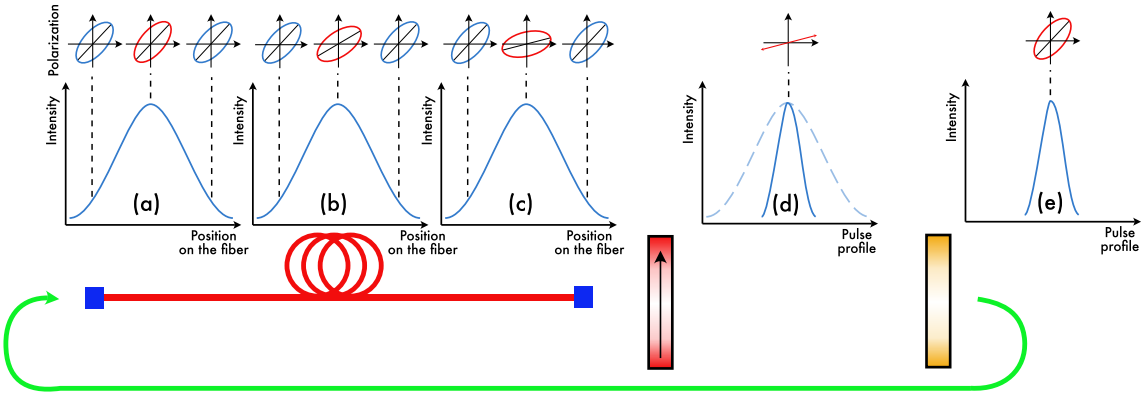

FIGURE 3.5: **Nonlinear polarisation rotation principle operation**: (a) A wide Gaussian pulse is set with an elliptical polarisation into a Kerr medium. (b,c) The angle of the ellipse for the high-intensity part of the pulse rotates. (d) A linear polariser is aligned.

NPE produces an artificial saturable absorber that induces passive mode-locking. Because of the fibre refractive index dependence, when an intense pulse of light of power P with elliptical polarisation is launched into a fibre, the polarisation state, which is originally settled on an ellipse, i.e. two orthogonal components with an original angle between the components ϕ_{ellip_0} evolves to ϕ_{ellip} according to:

$$\phi_{ellip} \approx P\, \gamma_{NL} A_c\, L \tag{3.8}$$

where A_c is the first Stokes parameter, a linear polariser in the cavity enables the fibre with varying azimuthal angles to act as a saturable absorber. For illustration, Figure 3.5 shows an elliptical polarisation state at the start of the fibre. Due to the temporal Gaussian intensity profile of the pulse in the fibre, the peak of the pulse acquires a larger rotation than the edges, with the edges being the temporal start and end of the pulse. At the end of the fibre, a linear polariser allows the high intensity to go through, whilst the low intensities are rejected, leading to the narrowing of the pulse. In the next step, a half-waveplate can be oriented in such a way as to generate an elliptical polarisation similar to the starting position. A saturable absorption effect takes place due to the changes along the optical fibre, power and nonlinearities, and it will only act to the benefit of the pulse growth when the working point is on the saturable gain, as seen in Fig.3.6. For this reason, a wrong working point selection will increase undesirable pulse power. These effects can overcome the power threshold of the optical elements and, therefore, cause optical damage and not find mode-locking, Figure 3.6.

3.2 Tuning lasers: Modalities & characteristics

In this section, a brief history of swept sources will be outlined, from the beginning, when they could only sweep at 1 Hz, to their current state, where reports exist on tuning rates of 400 MHz over 73 nm bandwidth at the central wavelength of 1550 nm [96], corresponding to a progress of eight orders in magnitude. Not

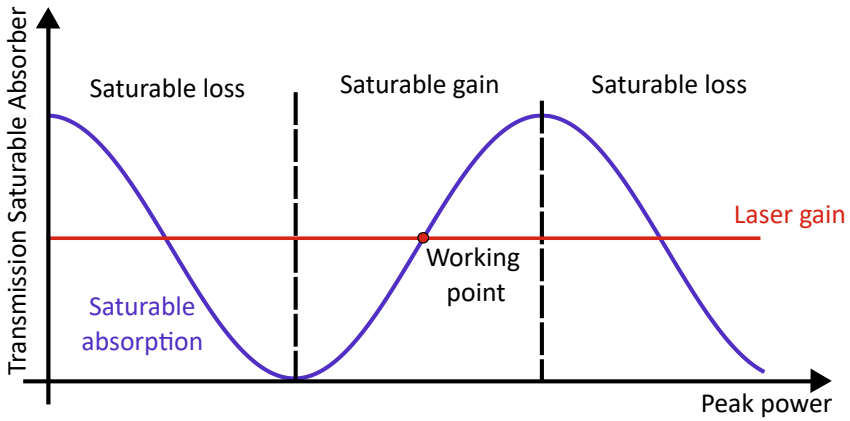

FIGURE 3.6: Sinusoidal saturable absorption in NPR scheme. The pulse power temporal variation determines whether the pulse lies within the saturable gain regime or the saturable loss regime.

only did their tuning speed evolve, but also their tuning bandwidth. We will delve into some of the most used, presenting potential key tuning mechanisms and providing clear explanations of their workings and outcomes. Of particular interest is the time-stretch modality, a primary focus of this thesis. As we near the end of the chapter, we will examine some of the most successful developments and their underlying reasons, culminating with a comprehensive comparison of the modalities considered.

3.2.1 History and chronology of source development

As it has been described in Chapter 2, swept-source OCT modality represents an important version of the OCT technology, which makes use of light sources that change their wavelength over a certain bandwidth. During the first years of this technology, the light source was also known as a tunable laser until 2003, when the first papers started to use the nomenclature of a swept source. Although these two terminologies, tunable and sweep, refer to two different categories of optical sources, both can be used for SS-OCT.

Tunable lasers are those whose output wavelength can be tuned in a desired way; for example, the emitted wavelength can be chosen at any given time. On the other hand, swept source wavelength emission is constantly sweeping its

wavelength over the tuning bandwidth, and the tuning cannot be stopped. For this reason, "sweeping" over a portion of the spectrum is a more appropriate description than tuning. The first demonstration of a functional swept source was given in 1997 by S. R. Chin et al. SS-OCT [97]. In a couple of years, by 1999, the speed increased by two orders of magnitude (see Figure 3.7) [98]; this was just the prelude of what was about to come. Then, for some time, a different terminology was employed in several reports, such as Chirp OCT [99]. Between 1999 and 2003, Wojtkowski and Leitgeb demonstrated the first decent-quality SD-OCT images in vivo by solving most of the main issues at the time, eliminating the effect of the chirp, linearization, removal of DC and reduction of auto-correlation components. An important understanding was the need for speed in spectral investigations in order to reduce the exposure time to avoid fringe wash-out [100–102]. Initially, OCT was commercialised as TD-OCT. Zeiss, a subsidiary formerly called AOD, started business in 1992 and was the first to produce a TD-OCT system. By 2003, the technology of SD-OCT started growing fast when many companies produced SD-OCT systems, such as Topcon and Optovue…[103]. It was at this time that research in SS-OCT exploded, and more groups started their research into different tuning modalities. It also coincided with studies on the sensitivity advantage of Fourier Domain methods over Time Domain, (Mitsui et al., Leitgeb et al., de Boer et al., Choma et al.) that provided theoretical derivation and an experimental confirmation of the sensitivity advantage of SD-OCT [33, 36] and SS-OCT [34].

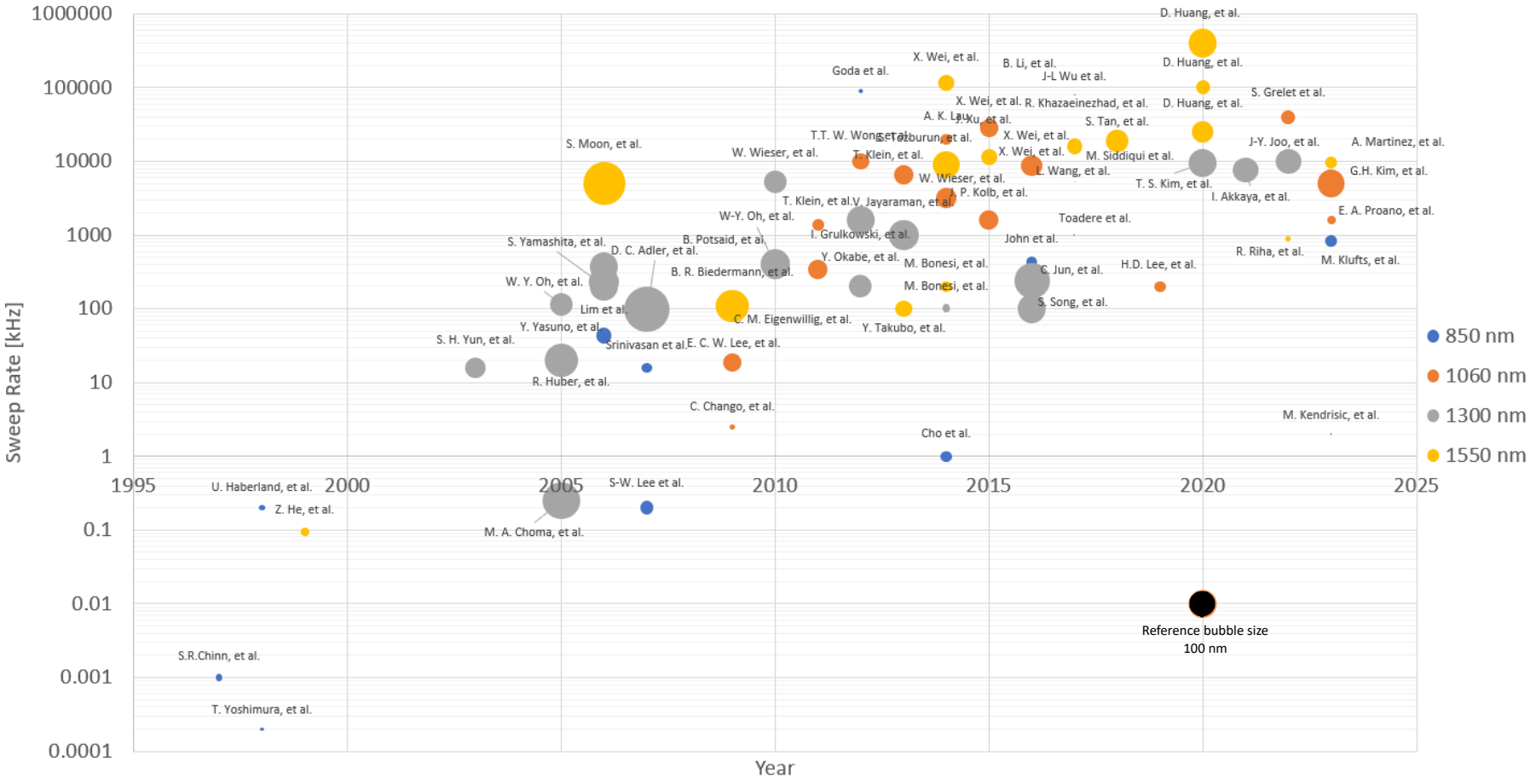

FIGURE 3.7: Most relevant swept sources from 1997 until 2023. Four main central wavelengths were selected: 850 nm in blue, 1060 nm in orange, 1300 nm in grey and 1550 nm in yellow. The bubble size in black represents a 100 nm bandwidth as a reference for the rest of the bubbles. All the references are given in Annex B

This type of technology has evolved rapidly thanks to its speed advantage. This has been one of the main successes of spectral processing applied to OCT. Both SS-OCT and SD-OCT are considered forms of Fourier Domain (FD)-OCT. Achieving high A-Scan rates has enabled comprehensive 3D images of tissue structures. It is also important to notice that the sensitivity of these SS-OCT systems remains high at more than 80 dB and can be achieved under safe eye power levels, i.e. under the MPE for the retina imposed by ANZI [13].

Sweep rate in SS

The increase in speed has come at the cost of expensive light sources, as well as complex data acquisition and synchronization. For these reasons, bringing high-speed SS into clinical use is still challenging. Compared with the Spectral Domain, the camera has been the limiting factor over the last few years in increasing the spectral reading rate and, therefore, the axial scan rate. Several ideas have come up, such as using multiple spectrometers in multiplex configurations [25]. However, these types of systems are complex and expensive. In terms of speed, the camera technology has been surpassed by using specialized and well-designed swept sources. For example, the axial range, which is mainly determined by the linewidth in SS, is a problem in SD. Since a higher axial range means more precision in reading the spectrum, i.e. longer time needed for the read-out of more spectral pixels. Overall, in SD-OCT there is a compromise between larger axial range and line rate. These are some of the multiple reasons that made SS-OCT more appealing than SD-OCT. A direction where SD-OCT is still preferred is that of phase-sensitive OCT, where camera-based OCT is better suited than the SS-OCT.

Spectral bands

Figure 3.7 shows a representation of the most relevant papers on the four main wavelength bands for OCT, 850 nm, 1060 nm, 1300 nm and 1550 nm. This figure

has been completed manually over the last 3 years, and the papers are linked in the Appendix B. It can be seen that there is a common trend in implementing SS-OCT at all wavelengths, and this is the speed of the swept source. The graph is plotted on a logarithmic scale for A-Scan rate. The same trend has been ongoing in the 850 nm band since 2022, and now M. Klufts et al. have reported the first competitive swept sources at this wavelength band [104].

New era: Ultrahigh-speed

Various methods have demonstrated the generation of multi-MHz swept sources. In certain cases, such as time-stretching, creating few-MHz swept source is easier than a kHz swept source. However, Figure 3.7 shows that the growth of sweep rate exhibits a plateau in the latest years, leading to different opinions on the technology evolution. The frequencies produced by these sources can exceed multi-GHz for data streaming, surpassing the current electronic technology capabilities. Consequently, the primary challenge faced by ultrafast SS-OCT is acquiring and processing the optical signal. High-speed, amplified, and balanced photodetectors are necessary for an optimal signal-to-noise ratio. At present, commercially available 20 GHz high-speed balanced photodetectors (BPDs) are only available in InGaAs.

Therefore, an implementation for a similar speed at 850 nm with Si photodetectors is not immediate. In fact, fast photodetectors at 100 GHz have been developed for the telecommunication band only, while fast photodetection at shorter wavelengths is still below 10 GHz. The speed of a photodetector is primarily restricted by three factors: carrier diffusion, drift transit time within the depletion region, and depletion region capacitance. Among these, the slowest process is the diffusion of carriers from outside into the high-electric field depletion region. InGaAs Photodetectors are generally faster due to higher carrier mobility and direct bandgap but are still limited by transit time and RC time constant. On the

other hand, Silicon Photodetectors are typically slower due to lower carrier mobility and indirect bandgap, with limitations from transit time, RC time constant, and longer carrier lifetimes [105].

Optimizing these factors through material engineering, device design, and advanced fabrication techniques might help achieve higher-speed photodetectors for InGaAs and Si in the future. Advancing ultra-high-speed technology to real-time poses a significant challenge in the realm of digitization. While high-speed digitizers (i.e. analogue to digital converters DAQ) can achieve a few GHz, they are limited in their capabilities. Real-time oscilloscopes can serve as an alternative, but they can only record several ms of data that must be transferred to a hard drive, lacking streaming capabilities. Even if DAQs were not a problem, processing the amount of data at the speed needed would become the next bottleneck. As discussed in Chapter 2.5, the interferometer-generated signal exhibits a chirp that must be corrected for A-Scan generation. Recalibration vectors can achieve this but require time. To apply these methods to the acquired signal, processing units must compute millions of calculations per second.

Computational power

The demand for real-time processing of high-frequency signals, such as the one encountered here in SS-OCT, often pushes conventional computing architectures to their limits. In the case of performing a Fast Fourier Transform (FFT) on a 2000-point vector at an 80 MHz sweep rate, the sheer volume of calculations required becomes a critical bottleneck. Each FFT operation on a vector of this size involves approximately 110,000 floating-point operations (FLOPs), and when repeated 80 million times per second, the aggregate computational load reaches 8.8 TFLOPS. This figure does not yet account for auxiliary processes like linearization, windowing, or filtering, which can easily inflate the total demand to 11 TFLOPS or higher. Such workloads are impractical for general-purpose CPUs, not because they lack the theoretical peak performance—modern multi-core processors as the

Intel Core i9-13900K can approach 1–2 TFLOPS under ideal conditions—but because they struggle with memory latency, thermal constraints, and sequential execution inefficiencies when handling massively parallelizable tasks like batched FFTs.

To bridge this performance gap, parallel computing architectures—particularly GPUs—have become the default solution. Graphics processing units, designed for inherently parallel workloads, excel at executing thousands of FFTs simultaneously. For instance, NVIDIA's CUDA-accelerated cuFFT library can process batched FFTs at a rate that saturates the GPU's memory bandwidth, allowing a high-end card like the RTX 4090 (capable of 82 TFLOPS FP32) to comfortably meet the 11 TFLOPS requirement. Even mid-range GPUs, such as the RTX 3060 (12 TFLOPS), can achieve real-time performance with careful optimization, such as overlap-add methods for continuous streaming or mixed-precision arithmetic to reduce computational overhead.

However, GPUs are not universally suitable—particularly in power-constrained, embedded, or low-latency applications where their high energy consumption and driver overheads become liabilities. In such cases, FPGAs (Field-Programmable Gate Arrays) offer compelling alternatives. These devices can implement hardware-accelerated linearization (as "k-clock" processing), which offloads the most compute-intensive preprocessing steps from the CPU/GPU into dedicated logic circuits. By doing so, the residual computational burden on the host system can be reduced by an order of magnitude—for example, from 11 TFLOPS to 0.5 TFLOPS—making it feasible to achieve real-time performance even with modest hardware. The trade-off, however, lies in design complexity: FPGAs require specialized programming (e.g., VHDL/Verilog), and their performance is highly sensitive to clock synchronization, especially at multi-MHz rates where even nanosecond jitter can degrade signal integrity.

Low cost

During the transition from SD-OCT to SS-OCT, the main cost changed from the spectrometer to the source due to the increased complexity of the swept source. Hence, there is currently a movement to create affordable sources for low-resource settings OCT systems. A cost-effective solution is to utilize MEMS-VCSEL, which is comparatively inexpensive. In a study by M. Kendrisic et al., a VCSEL capable of 2 kHz operation within a small bandwidth was developed [106]. With such technology, it is possible that OCT devices can reach daily care in the future. As an example, OCT at home could become a reality, resulting in affordable daily care systems that can be utilized by individuals to spot early symptoms of Age-Related Macular Degeneration [107].

Sensitivity at high-speed

As mentioned earlier, point scanning systems have encountered a hurdle when it comes to increasing their speed. Initially, the main obstacle was due to the optoelectronic components. However, another constraint in the 850 nm band that needs to be considered is the MPE limit [13] on power when imaging the eye. This restriction is especially strict in the near-visible range, where safety protocols dictate a maximum average power of 0.8 mW into the eye at 850 nm under scanning. For a fixed laser power, limited by the safety threshold, the higher the sweeping speed, the shorter the integration time (considered as the time the beam sits on a pixel) and hence the lower the energy, leading to a decrease in the number of photons backscattered, ultimately constraining the sensitivity of the system.

Figure 3.8 (a) shows the computed curve of sensitivity vs power on the sample arm for a given swept rate. As shown in Figure 3.8(a), for the safety powers at 850 nm and 1060 nm, the values of sensitivity achievable employing the photodetectors available are ≈ 84 dB and ≈ 94 dB. The sensitivity curves have been calculated using the formulation given by K. Tsia et al., in which the responsivity

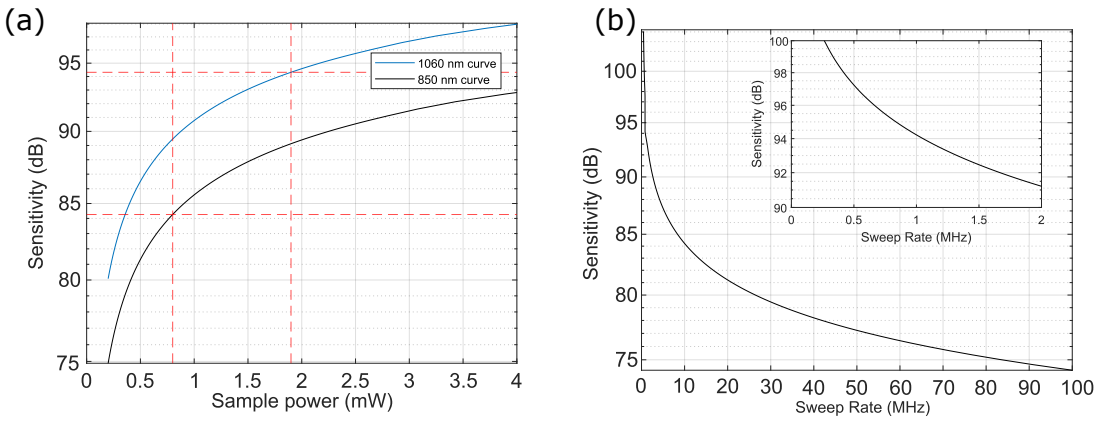

FIGURE 3.8: **Sensitivity simulation for 850 nm and 1060 nm detectors.** (a) The sensitivity curve depends on the responsivity of photodetectors at 850 nm in black and 1060 nm in blue, with 0.3 A/W and 0.7 A/W, respectively. The crossing point for the 850 nm laser at safety power arises at 84.4 dB. The crossing point for the 1060 nm curve at safety power arises at 94 dB. (b) Sensitivity curve for a span of sweep rates from 100 kHz to 100 MHz, the inset focused on values around 1 MHz. Both graphs are computed taking into account an asymmetric array configuration under a shot noise-limited condition.

and the sampling rate are taken into account [108]. In a research environment, 90 dB is considered enough for general imaging purposes. However, clinical products must have at least 95 dB [109]. For 850 nm, the only way to increase the sensitivity is by using new dopants in the photodetectors that enable a higher sensitivity. In Figure 3.8(b), the sensitivity curve is plotted with the sweep rate of the source. This graph is obtained assuming the balanced photodetector has 0.7 A/W responsivity, corresponding to the typical responsivity values of InGaAs at 1060 nm. Furthermore, the simulation corresponds to 1.9 mW in the sample arm with an asymmetric array configuration. The sensitivity rapidly decays in the range of multi-MHz, which indicates that these kinds of sources applied by flying spot scanning beams will have problems obtaining all clinical features required. A higher sweeping rate SS enables progress in other areas. For instance, a faster sweep will mean movement will have less of an impact on image quality. In case wider areas need to be scanned, then more time is required, and it would be advantageous to sweep faster to limit the acquisition time. Joint progress in fast-tuning swept sources and fast deflectors can open new avenues in imaging technology. In a research study, M. Gob et al. reported the use of few-MHz

swept sources together with robotic arms [110], as well as its use on large skin areas [111]. Another technique that takes advantage of the acquisition speed is OCT-Angiography, which requires multiple images to be acquired from the same spatial areas followed by evaluation of differences between them in terms of amplitude and phase [112, 113]. Repetition of two or more images requires time, where higher speed may help. Therefore, to reduce the movement artifacts, the time between consecutive images needs to be in the order of a few ms, which is only possible with hundreds of kHz or MHz swept sources. However, depending on the speed of events to be detected by such different procedures, different time intervals may be necessary where specialised lateral scanning protocols are devised, with different lapses of interlacing. For instance, if the events to be detected require an integration time of ms, microsecond sweeping could still be used since a ms delay is obtained after 1,000 sweeps, i.e., for at least a B-Scan. An alternative OCT method using swept sources is full-field OCT. It can be done either in 1D or in 2D, with line cameras [114, 115] or 2D cameras. Full-field swept source (FF-SS) OCT provides a sensitivity advantage over the flying spot. Using a 1D camera requires another lateral scanner to collect a volume. Using a 2D camera, the whole volume can be acquired with no mechanical scanning. FF-SS-OCT [116–119] method reduces the demand for fast sweeping light sources, where cameras need to acquire fast (in the order of kHz) to allow rapid collection of frames during one sweep. There are two main reasons to explain this advantage: 1) although the equivalent A-Scan rate when compared to flying spot is on the order of several MHz, the integrating time is higher, and therefore, the number of photons coming back is also higher, 2) the difference on the beam, where for instance flying spot uses a collimated beam entering to the pupil, line and full field use an extended source, a large beam. For the angular extensions that this covers, the power then applied with a line at 850 nm is a magnitude larger than the flying spot [120], resulting in higher beam powers that can be used on the eye under the safety considerations [13].

3.2.2 Tuning mechanism

Throughout the history of swept sources, multiple tuning mechanisms have been developed. Many of these mechanisms did not have any commercial impact. However, different approaches have inspired new modalities that are currently demonstrating impressive results. It is not easy to make a list of all tuning modalities. However, depending on whether mechanical movement is involved, we can separate them into two categories based on whether they are akinetic or kinetic. Initially, kinetic sources were developed first for their simplicity. In this sense, optomechanical means were quite developed as early as 1997. It is worth noticing that both modalities, kinetic and akinetic, can use two different approaches to build the frequency swept [121]. Approaches using "post-filtering" use a broadband light source, such as an SLD, to generate a broad spectrum and then a narrowband tunable filter with a transmission window narrow enough to the desired instantaneous coherence length. The benefit of this approach resides in the advantage that the tuning speed is limited only by the maximum tuning speed of the filter. However, the power of those light sources will usually be quite low. Considering a constant power spectral density in a bandwidth $\Delta\lambda$ with a filter of linewidth $\delta\lambda$, then the output power will be $\propto \delta\lambda/\Delta\lambda$, which may represent only a small fraction of the input power. Although an amplification stage could be adopted after the filtering process, the amplification will have severe limitations: i) the signal-to-noise ratio between the optical signal filtered and the ASE will affect the overall performance of the system, ii) furthermore, amplifying large bandwidths is not trivial and rare-earth doped fibres exhibit limited gain bandwidth. In such cases, SOAs may be better suited. A second approach is "cavity tuning," where the spectral filtering element is placed inside a laser cavity. This approach usually generates much higher energy since population depletion in the gain medium is concentrated on transitions within the filter spectral linewidth, hence less ASE and saturation, when achieved, which happens for wavelengths

in the centre of the transmission filter curve. Moreover, the mode competition in the laser will narrow the effective linewidth. In contrast to "post-filtering," the maximum frequency tuning speed is not limited by the maximum tuning rate of the filter but also by the time constant for building up laser operation. The second modality presented above is mostly used in the practice of swept source assembly. However, there is a modality related to the first modality which attracted a lot of attention recently, due to its capability for high-speed tuning. This consists of a large bandwidth sent in ultrashort pulses through a dispersive element, which is explained in Section 3.2.2.2.

3.2.2.1 Kinetic

Mechanical parts that are in motion are subjected to stress and strain, which can lead to fatigue and shorten their useful life. In contrast, tunable sources based on non-moving components exhibit longer lifetimes. In the following section, the most common implementations of non-moving mechanisms are described, including their working principles and applications.

Fabry Perot filter-based swept source

The wavelength selection in FDML and MEMS-VCSEL use a filter composed of two mirrors facing each other. One of the mirrors of the filter is actuated to provide a change in the cavity length change. In fact, it is important to mention what makes these cavity sources improved from just bulk filters is the narrowing effect on the instantaneous linewidth obtained by the light passing through the FP filter on several cavity round-trips [121]. To facilitate a large number of roundtrips, the reflectivity of mirrors must be close to 100%, ensuring a few nm flatness.

Long cavity: FDML

A Fourier-Domain Mode-Locked is a laser operating regime [51, 121, 122], which usually has three main elements in a cavity, a gain medium, a dispersion compensation module and a Fabry-Perot filter; this one is made of two mirrors in which a piezo is attached to one of the facets. The cavity has a gain medium, such as a semiconductor optical amplifier or a fibre amplifier. Semiconductors are preferred for their wide bandwidth, stability, modulation performance and high small signal gain. This kind of swept-source, the FDML laser, conceptually can be understood as a highly chirped broadband light field: Similar to a femtosecond mode-locked laser—defined by its pulse repetition rate and short pulses resulting from phase-stable mode superposition—the FDML laser functions in a distinct but related manner. Instead of pulses, it exhibits repetitive wavelength sweeps, with the sweep rate defining its periodic behavior. In contrast the modes each having a distinct, yet locked phase, the light field of the FDML laser is characterized by a swept phase: The phase is chirped to generate a swept wavelength light field where the colour is continuously changed over time. The name Fourier domain mode-locking comes from the fact that all the wavelengths bear a phase relation to each other [123]. The maximum achievable frequency tuning rate is limited by the characteristic time constant for building up laser activity inside the cavity [121]. This non-stationary operation mode has many drawbacks, such as increased amplitude noise, low power, and broad instantaneous linewidth. However, this can be overcome by extending the laser cavity and periodically driving the optical bandpass filter synchronously with the optical round-trip time of the propagating light wave in the cavity. This changes the operation mode to a quasi-stationary state where the light from one frequency sweeps propagates through the cavity and returns to the optical bandpass filter at the exact time when the transmission of the filter is at the same spectral position.

Bandwidth: The bandwidth of an FDML might be limited by the gain medium. Although rare-earth doped materials can be used, they present several disadvantages; firstly, the spectral shape is not Gaussian. Secondly, the typical response of this material is one to two orders of magnitude higher, which will make it impossible to buffer. In contrast, SOAs have a response time in the order of microseconds, although they still do not exhibit Gaussian shape characteristics in their emission. Furthermore, if all the emissions from the gain medium are to be preserved at the output, all wavelengths should travel around the cavity at the same rate, which means that chromatic dispersion in the system must be compensated. A dispersion compensating element, such as a chirped fibre Bragg grating (cFBG) or more, or dispersion-shifted fibres, is employed. An SOA, the dispersive element, and the FP filter are the three key elements to obtain broadband emission in an FDML laser, as shown in Figure 3.9.

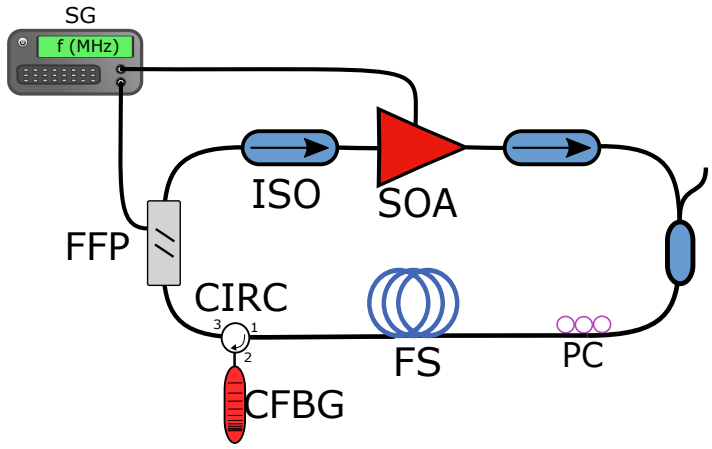

FIGURE 3.9: FDML set-up. SOA: Semiconductor Optical Amplifier, FS: Fibre spool, CFBG: Chirped Fibre Bragg Grating, FFP: Fabry Perot Filter, SG: Signal Generator, CIRC: Circulator, ISO: Isolator.

Noise: When talking about noise, the main noise source is the relative intensity noise (RIN) coming from the sources that appear as holes in the spectrum. The holes can be understood as spikes in the emission. Although the holes might happen at a high frequency, a few GHz, they still can deteriorate the coherence properties. These holes can disappear if the dispersion is fully compensated, what is called the sweet spot operation [124]. Some works have studied experimentally

the number of holes and their distribution, which seem to follow a non-linear function [122] T. Pfeiffer et al. demonstrated that when the filter is driven at a frequency matching the inverse of the roundtrip time, under no chromatic dispersion, the noise reduced considerably, reaching the so-called sweet spot.

Coherence length: The coherence length of the laser is intrinsically related to the phase noise properties and with the dispersion in the system [125–127]. The number of holes in the system is the main contributor to the degradation of coherence length. Although one could expect that mechanical means cannot be phase-stable, FDML has shown that the use of an FP filter for such a long cavity translates into an immediate advantage in sweep storage. The sweep storage means that for several roundtrips, the emitted wavelength is filtered down by many round trips.

Sweep rate: FDML lasers also benefit from their scalability on sweep rate by employing a buffer technology. The laser is modulated periodically but with a duty ratio of less than 100%, creating an empty time interval within which a copy of the original sweep is placed [128]. In this way, fast-sweeping lasers have been developed, reaching rates of 13.4 MHz [129]. Buffering is an elegant way to increase the sweeping rate of FDML, however this technique becomes harder to implement at multi-MHz sweep rates, see Figure 3.10. The energy on the piezo increases with the frequency, and the modulation that is applied to the SOA has upper limits [129].

The high rates of several MHz of buffered FDML lasers have enabled progress in different areas. For instance, wide-field scanning using a robotic arm [110] can accomplish whole-body scans in a short time. Well compensated for dispersion, FDML cavities exhibit low phase instabilities that allow phase elastography [130]. The good phase stability allows the detection of small variations as small as submicron.

Real-time applications: Another important application of few-MHz FDML is

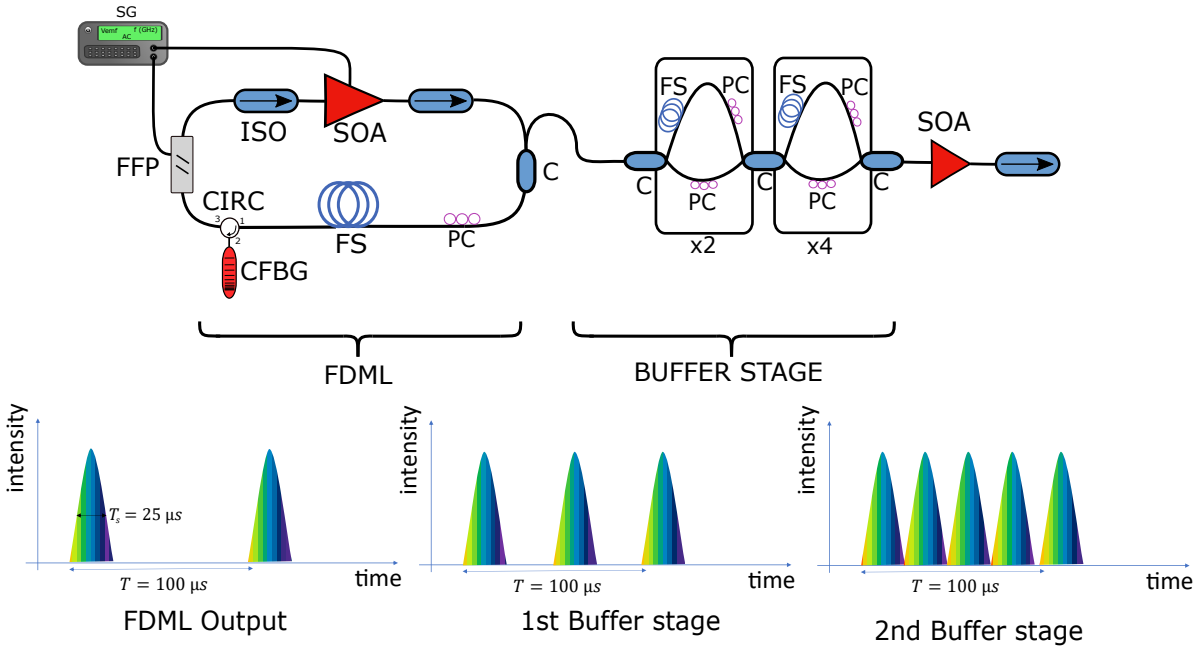

FIGURE 3.10: FDML on the left with a buffer stage on the right. Graphs on the bottom represent the output of the swept source at different stages, left; just output of the FDML, middle; after 1st buffer stage, right; after 2nd buffer stage.

real-time volumetric imaging. For this, works from W. Draxingler et al. reported combined use of clinical microscope with an FDML laser for OCT [131] Using GPUs around 30 volumes per second with only 1 volume lag were able to be displayed. Under test, and to optimize the output for the clinician, the 3D volumes were displayed via a virtual reality goggles [132, 133]. Optoretinography is also seeing the benefits of multi-MHz FDML, as demonstrated by L. Puyó et al. When the retina is stimulated with blue light focused in the RPE layers [134, 135], the RPE contracts, which creates a Fabry-Perot cavity which acts as a wavelength shifter when contracting. FDML lasers have shown that this contraction can be characterized using phase differences. Although this is not unique from FDML, the benefit of using FDML is the phase stability at that speed since, in optoretinography, variations in phase are small.

Short cavity: MEMS-VCSEL

Micro-electro-mechanical systems with vertical cavity surface emitting (MEMS-VCSEL) lasers are miniaturized swept sources. These cavities share the same design as that of an FDML, but all in one, a gain medium, which is usually a multiple quantum well (MQW), with a distributed Bragg reflector (DBR), designed for a certain wavelength range, with a movable mirror on top, Figure 3.11.

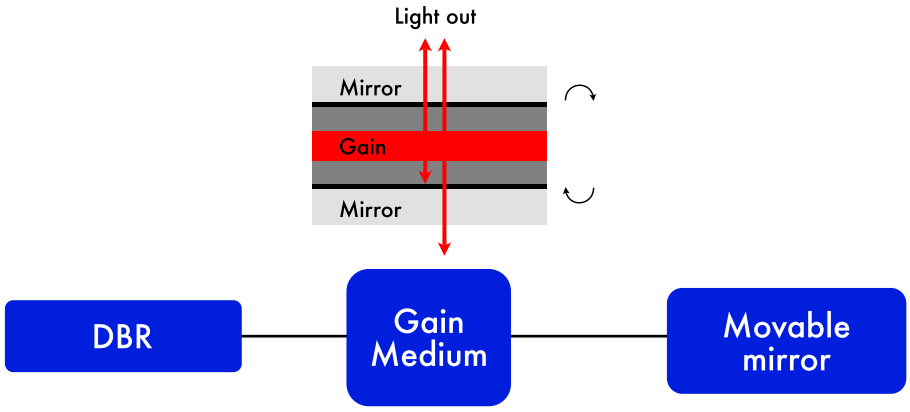

FIGURE 3.11: **Schematic arrangement of a MEMS-VCSEL**. MEMS-VCSEL are composed primarily of a fixed mirror, also known as a distributed Bragg reflector (DBR), a gain medium and a movable mirror.

The MEMS-VCSEL operates by generating a standing wave inside the cavity, the wavelength of which is dependent on the size. Then, the top mirror moves and the standing wavelength of the EM wave changes in response to the cavity size.

Bandwidth: The GaAs material is typically chosen as the gain medium due to its excellent amplification properties and broad emission spectrum, ranging from 850 nm to 1150 nm. Through material engineering, the bandgap can be adjusted for specific wavelengths. Additionally, materials like InP are applicable in the NIR range of 1300 nm to 1500 nm. Once gain is achieved in a structure, the next main question is: How can the mirror be tuned? There are different solutions to this question; one possibility consists of using electrostatic tuning [136] or electrothermal tuning [137]. A more detailed review of this swept source can be

found in [138]. Electrostatic tuning means that the movable mirror is floating in the air at a position controlled by applying a specific voltage to the hinges. In the case of MEMS-VCSEL, their bandwidth is limited not only by the gain medium but also by the cavity length. The bandwidth is limited due to the forces interacting in the system. The maximum voltage that can be applied to reach maximum displacement is called pull-in voltage and determines the maximum achievable bandwidth [139].

Sweep rate: In terms of sweep speed, it is not the build-up of the laser that is limiting; the limitation is how fast these mirrors can move. The mirror movement can be described as a harmonic oscillator in which the resonant frequency is given by:

$$f_r = \frac{1}{2\pi}\sqrt{\frac{k}{M}} \tag{3.9}$$

where k is the stiffness of the hinges, and M the mass of the mirror, The sweep speed cannot exceed the resonant frequency of the mirror. Therefore, for a higher speed, the stiffness should be increased. However, the pull-in voltage increases linearly with the stiffness. This requires a larger actuating voltage, but this is not a problem for the current electronics technology in terms of electronic gain and delivery of high voltage into a circuit of known impedance. A problem remains in terms of a bottleneck in the design. Although the stiffness of the hinge can, in principle, be increased, the curvature of the mirror will limit the spatial mode inside the cavity [140].

Performance: There are factors to consider when working with MEMS-VCSEL. In the case of power, these devices have a small aperture, usually only a few microns in width. Applying a high current can lead to the device emitting light in multiple modes, making it difficult to achieve single-mode operation and limiting power output to around one milliwatt. To increase power output, SOAs

are often used in conjunction with MEMS-VCSELs, leading to approximately 20 mW, which is sufficient for eye imaging applications. Alternatively, to obtain large power, optical pumping can be used since a high suppression mode can be achieved, which involves incorporating an optical pump into the device [141].

On the other hand, coherence length is one of the main advantages of MEMS-VCSEL. Because narrower linewidths are achievable in shorter cavities, coherence lengths of many meters have been reported [142].

Deflector based: EOM, polygon, resonant, galvo

Deflector-based swept sources are composed of three main elements inside a ring cavity: a gain medium (typically a SOA), a circulator and a dispersive element (prism or a diffraction grating). The deflector acts as a spectral filter, enabling a single wavelength to be recirculated in the cavity at any given time. The first attempts were almost rudimentary in the early years of tuning lasers for OCT. Because the optoelectronic components were not fully developed, initial reports refer to simple deflecting elements based on galvo scanners. For instance, a galvo scanner and a grating, were employed in [97] to obtain a tuning bandwidth of 25 nm at 10 Hz. Although they cannot achieve high-speeds, galvo-based swept sources represent a viable alternative for FFSSOCT systems. The time required to acquire a full volume is limited by the camera frame rate. For such configurations, sweep times range from sub-second to several seconds.

During the following years, the performance of swept sources steadily increased in sweep rate. In 2005, the polygon mirror-based swept source was developed [143, 144]. Polygon mirrors offer several advantages in comparison to galvo scanners. Firstly, galvo scanners move bidirectionally, while polygons move in a single direction. This means that using galvo scanners, the sweep is also bidirectional. However, the galvo scanner needs to first stop before it can begin to move in the opposite direction. The acceleration and deceleration make them inertia-limited [145], which leads to nonlinearities in sweeping. In order to reduce the

inertia, small mirrors are used, which applies other constraints to the optical design. In comparison, polygon mirrors having a constant angular speed present less nonlinearity in sweeping. The coherence length of such sources was investigated and slightly improved by using quasi-phase continuous tuning [146]. Different alternatives have been developed to extend the bandwidth of these sources; a common implementation is the use of two gain mediums. For the sources in Figure 3.12, SOAs are used as a gain medium. Two SOAs can work in parallel and then recombine to obtain a broadband sweep [144].

Nowadays, several types of deflectors are used in OCT, either for spectral filter tuning in swept sources or for scanning the optical beam over samples [50, 55, 141]. In addition to mechanical deflectors such as galvo scanners and resonant scanners, electro-optic modulators (EOM) have been devised, such as KTN elements. These can achieve operation at several hundreds of kHz and have found use in both swept sources [147, 148] and lateral scanning in time domain OCT. However, due to the high cost of EOM deflectors, galvo scanners and polygon-based scanners are still in use [149, 150].

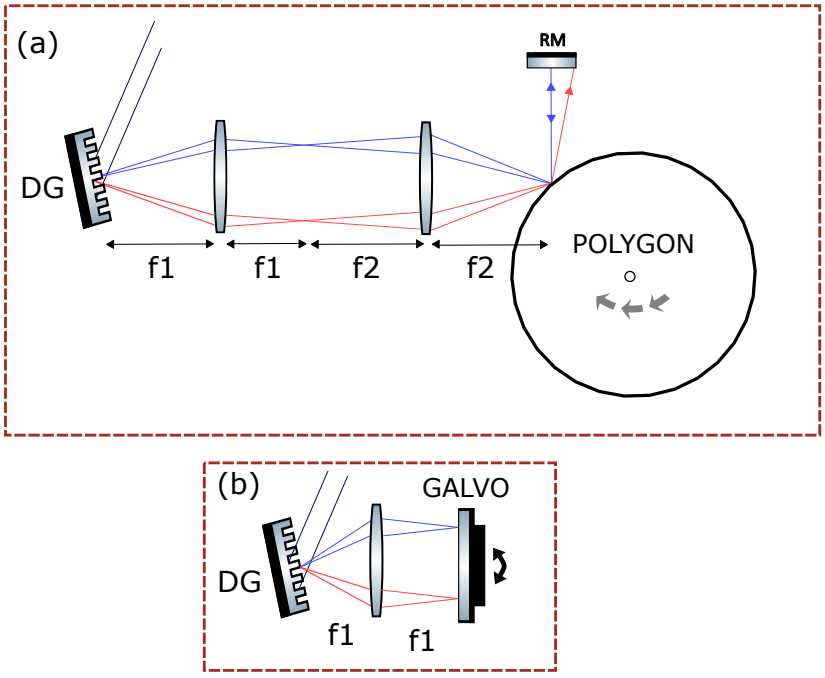

FIGURE 3.12: Deflector-based design for (a) polygon-based, and (b) galvo scanner-based.

There are two main parameters of swept sources: bandwidth and coherence length. The bandwidth, although mainly limited by the gain medium (i.e. the SOA or fibre amplifiers), can also be limited by the combination effect of the deflector and grating/prism, as described in previous works by M. Everson et al. [151].

Figure 3.12 shows a diagram of the spectral filtering conducted by (a) a polygon mirror and (b) a galvo grating configuration. For the polygon mirror, the laser light is sent collimated towards a dispersive element, which in this case is a diffraction grating working in reflection, DG. A two-lens confocal telescope, with lenses of focal lengths f1 and f2, collects the light and directs it onto the polygon mirror. From here, the light is either directly retro-reflected off the polygon or sent to an additional retroreflector mirror, RM, used when the polygon is positioned 'off-axis', depending on the incident angle. In a similar operational way, the galvo grating configuration is used; now, instead, the diffraction grating and galvos are placed at a distance f. Since the first order of the diffraction grating is sent to the galvo, only the light at the right incident angle back to the diffraction grating could couple back.

3.2.2.2 Akinetic

Akinetic swept sources came with the promise of achieving multi-MHz sweep rates without the need for any movable parts. In the following subsections, the most representative modalities of akinetic swept sources are presented.

Time-stretch based

Time-stretch method, also called stretched pulse, is a sweeping modality that uses chromatic dispersion to delay each wavelength by a different amount of time and creates an artificial swept source [152], as depicted in Figure 3.13.

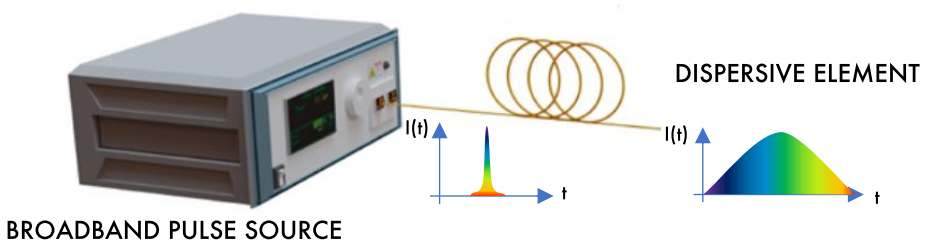

FIGURE 3.13: Time-stretch sketch composed of two main elements, a broadband pulse source on the left and a dispersive element, in this case, a long fibre.

This subsection presents the different mechanisms to generate chromatic dispersion and the best mechanisms for different wavelength bands. It will also describe the limitations on bandwidth and how the coherence length is defined.

Chromatic dispersion: There are a variety of ways to achieve chromatic dispersion, ranging from simple methods involving the use of single-mode fibre to more complex methods using tilted chirped mirrors. The most commonly used method for achieving chromatic dispersion is through the use of long SMF, as depicted in Figure 3.14 (a). This is a highly effective option in the telecommunication band where fibre such as SMF-28 exhibits low losses of approximately 0.16 dB/km and dispersion of $18\text{ps}/(\text{nm}\cdot\text{km})$.

Dispersion compensation fibres also exist at 1550 nm. They exhibit similar amounts of dispersion but of the opposite sign (i.e. normal dispersion) to SMF-28, making them a viable alternative for time stretching. Consequently, by simulating kilometres of fibre SMF-28, DCF fibres can achieve a long delay with acceptable losses. However, achieving chromatic dispersion at lower wavelengths becomes less practical. This is why there are few time-stretch sources available in the visible or lower wavelengths using fibres. Only one study by Hadadi et al. has reported the use of SMF-28 in the visible [153]. It is worth noting that losses increase as the wavelength decreases.

To overcome the problem of loss incurred in fibres used for their dispersion, chirped fibre Bragg gratings (cFBG) have been proposed, as illustrated in Figure 3.14 (c) [154]. cFBG devices represent a compact and stable solution for replacing

SMF. A few drawbacks of cFBG should be mentioned. Firstly, to produce a cFBG, a specialised phase mask that induces a chirp variation of the refractive index is needed and designed for a specific bandwidth and dispersion. The inscription, i.e. the change in the refractive index at a located position of a certain wavelength, has to be separated from the next inscription; for higher bandwidth, more reflectors at different distances have to be added. In order to achieve wide bandwidth and large dispersion, the length of cFBG may exceed reach even over a metre, making them expensive. For example, a 100 nm bandwidth cFBG will require over 10 m. Regardless of length, cFBGs are also hard to develop due to the photosensitive fibre used for the inscription having to move position and also ensure that the movement has been precise. These problems make cFBGs suffer in terms of cost and difficulty standardizing. Additionally, the light travelling through a broadband cFBG is redirected using broadband circulators, as described in Figure 3.14 (c). Circulators are hard to build with broadband characteristics and low losses. Previous reports indicate that circulators being used with broadband sources may also introduce undesired polarisation mode dispersion (PMD). Due to the birefringence of their crystals, the light divided into the fast and slow axis can interfere with each other if the path length of both waveguides is not the same. Therefore, if a cFBG is chosen as a dispersive solution for time stretch, then a sufficiently broadband circulator needs to be found. If the above issues were to be resolved, cFBGs would offer a promising solution to time-stretch technology.

Speciality fibres at $1\mu m$ (i.e. single mode fibres at $1\mu m$) are relatively expensive for long-haul. For that reason, lower-cost solutions have been investigated, such as few-mode fibres (FMF) or multimode fibre. In principle, multimode fibres generate mode-beating, which disturbs the wavelength-time mapping. For this reason, multimode fibre tends to be disregarded for time-stretch OCT. However, some solutions to avoid mode-beating are still being evaluated [153] and may become useful in the years to perform time-stretch with FMF. Although FMF seems an interesting alternative for expensive speciality fibres designed for $1\mu m$, one

has to pay special attention to the efficiency of FMF. The efficiency can be measured as the dispersion over loss per km [ps/(nm dB)]. FMF solutions present a high dispersion, but their losses are also high, and therefore, a trade-off should be evaluated between the two factors. Amplification to cover for the losses may not be a solution since amplification may add background noise. Yi Qiu et al. described a system using a supercontinuum (SC) laser centred at $1\mu m$, which is a favourable region for eye-imaging [155]. In their work, they present how mode-beating can be avoided when the light of both fibres is properly aligned and there is no offset in the cores.

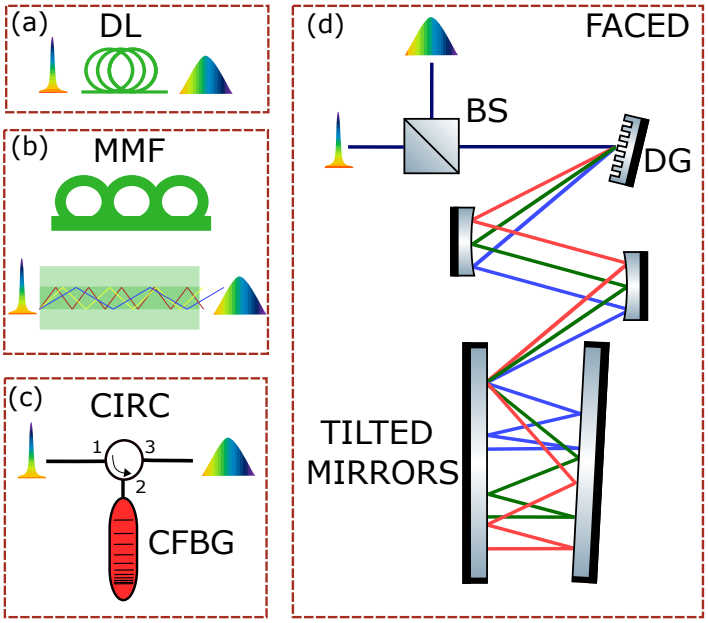

FIGURE 3.14: Mechanisms to generate chromatic dispersion. (a) Single-mode fibres are used, either standard fibres or dispersion compensating fibres. (b) Using multimode fibres. (c) Using chirped fibre Bragg gratings. (d) Free-space angular-chirp enhanced delay (FACED), BS: Beam splitter, DG: Diffraction grating.

An alternative for short wavelengths was extensively investigated by Wu et al. [156], shown in Fig. 3.14(d). In his work, a pair of chirped mirrors was used to create chromatic dispersion. The light is launched into a reflective diffraction grating, and the light deviated from the first order is sent to two mirrors that are placed facing each other; one of the mirrors has a slight angle with respect to the parallel position. This enables the beam to return along the same path. To achieve

chromatic dispersion, it is key that the light at the input is angularly dispersed, as depicted in Figure 3.14 (d).

Repetition rate: The frequency of the incoming pulses fundamentally limits the repetition rate of the source. Still, the duty cycle is given by the amount of chromatic dispersion created by the dispersive element. A broadband pulse is injected into a stretching element with high chromatic dispersion, as shown in Figure 3.15.

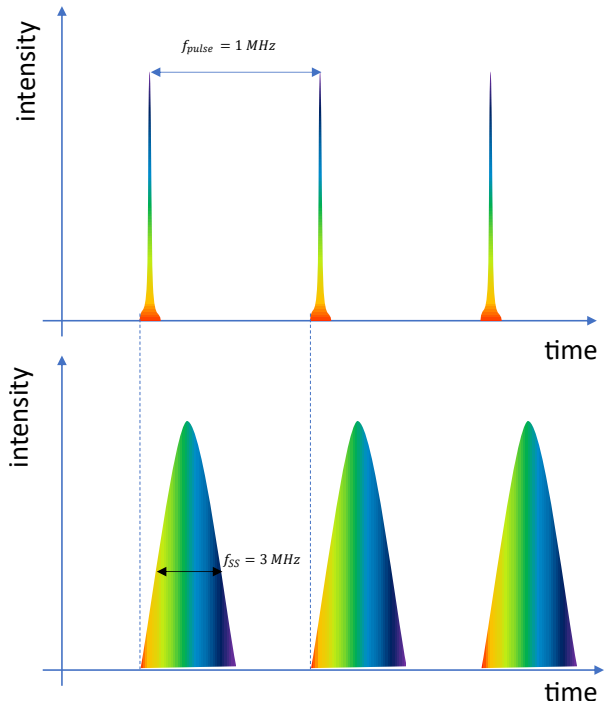

FIGURE 3.15: Seed pulse (top) and dispersed pulse (bottom) at the end of the dispersive element.

Since the first demonstrations of time-stretch by S. Moon et al. in 2006, the expectations for higher tuning speed went up [157]. SC sources used in spectrometer-based OCT led to ultra-high resolution (1-5 μm). However, the speed of such OCT solutions is limited by the speed of 1D cameras to a few hundred kHz. They have been successfully used in several applications [24, 158–165]. The SC has succeeded in reaching unexplored wavelengths, from visible wavelengths to few-microns, not covered by solid-state emitters such as SLEDs. Interestingly to note, the SC can also find use in SS-OCT via the time-stretch principle. The period of pumping pulses used to generate the SC represents the period of the stretched

spectra. S. Moon proved how to convert an SC source that was typically used for SD-OCT into SS-OCT systems. Significant progress in the field was enabled between 2010-2014 by the work of the groups led by K. Tsia and, in parallel, B. Jalali, which looked into both fundamentals of time-stretch as well as innovated both short broadband pulsed lasers as well as dispersive elements [109, 166–168]. In their work, they proposed distributed amplification to compensate for the losses in the dispersion element [169].

During the next years, this technique became popular in the 1550 nm band due to the low losses per kilometre of SMF-28; the method of FACED was also reported at this wavelength [156]. Some works tried innovative solutions at 1060 nm, such the mentioned FACED technique [165], and second harmonic generation [170]. However, FACED has been shifted from OCT to confocal microscopy [171] due to the complexity of stable output from the mirrors. During the last years, recent works from D. Huang et al. have demonstrated the capabilities of this sweeping modality when long dispersive elements are used, obtaining a 2.5 MHz sweep rate with 111 mm roll-off [172].

Coherence length: In sources using spectral filters, such as FP or MEMS, if the driving signal is stopped, then a static linewidth can be evaluated, and its inverse linewidth may be used to estimate the coherence length. This is not possible with time-stretch lasers. Evaluating the coherence length is important as this quantity is a good estimation of the axial range. The coherence length of time-stretch is described in detail by Goda et al. [166]. In summary, the maximum axial range (i.e. the coherence length) of time-stretch lasers depends on the dispersive element. Given that the GVD is large enough (i.e. in the far-field regime of optical time-stretch [166]), the instantaneous linewidth originates from the ambiguity in the wavelength-to-time mapping process. In the case where photodetection is the bottleneck, the temporal resolution of the photodetector (inversely proportional

to the electrical bandwidth), the instantaneous linewidth is given by [173]:

$$\delta\lambda_{det} = \frac{0.35}{D_{max} B_e}, \tag{3.10}$$

where D_{max} is the width of the temporal waveform at 80%. D_{max} units in (s/nm), i.e. the delay in time per nm of the dispersive element, and B_e the detection bandwidth in Hz. D_{max} has an inverse relationship to the A-Scan rate, which is expressed as $D_{max} = 0.8/(f_A\ \Delta\lambda)$, where f_A is the A-scan rate, and $\Delta\lambda$ is the bandwidth of the light source. According to the Nyquist sampling criterion, considering sweep rates in the order of MHz (equivalent to A-Scan rates), the required detection bandwidth B_e should exceed 1 GHz.

On the other hand, if the dispersion is not large enough, then not only one wavelength contributes to the temporal waveform at any time. The linewidth (in m) can be estimated as [173]:

$$\delta\lambda_{SPA} = \lambda \sqrt{\frac{2}{D[s/m]\ c[m/s]}} \tag{3.11}$$

where λ is the central wavelength of the light source, and $D = D_c L$ (measured in ns/nm) is the dispersion parameter, with D_c (in ps/(km $\cdot$ nm)) for a length L (in km), and c is the speed of light in vacuum. Equation 3.11 provides a sufficiently good approximation to estimate the achievable roll-off performance. For a Gaussian spectral shape, the coherence length l_c associated with the time-stretch source can be calculated from 2.23. In normal cases, the bandwidth of the photodetector is not the limiting factor, in which case the SPA approximation gives the roll-off. For example, let us assume a pulse of 100 nm bandwidth centred at 1060 nm. Using the above equation, the coherence length for each sweep rate can be calculated. As shown in Figure 3.16, the slower sweep rate, the smaller the roll-off, i.e. longer axial range.

Bandwidth: The output optical tuning bandwidth in time-stretch combines the

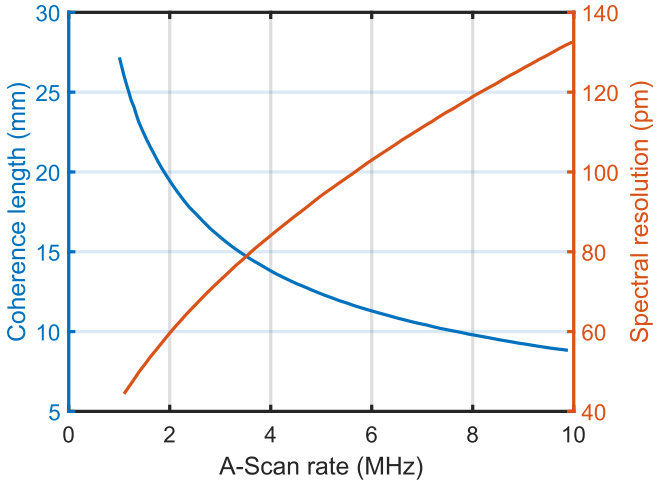

FIGURE 3.16: Coherence length as a function of the sweep rate. Blue coherence length, red spectral resolution. For this example, a 1060 nm central wavelength and 100 nm bandwidth were used.

input seed pulse with the attenuation of the stretching element. There are two common alternatives used for time-stretch: by SC generation [157, 174] or using a broadband mode-locked laser [71, 95, 173, 175]. In both cases, a broadband pulse is generated. In general, when using supercontinuum sources, they have a large pulse bandwidth (in the order of 100nm), which is higher than typically expected from mode-locked lasers. However, large bandwidth normally comes at the expense of high relative intensity noise. One way to work around this is to use coherence SC, as demonstrated recently [176]. On the other hand, mode-locked lasers could deliver, when optimised, 100 nm bandwidth [172]. However, the bandwidth of the original pulse is not the only limiting factor; the dispersive element also carries losses, and these losses can shape the spectrum, reducing the 3dB bandwidth. Using single-mode fibres, the loss profile (example of 980XP in Figure 3.17), will shape the bandwidth after only a few km in length.

The limited reflection bandwidth is a constraint which usually makes the cFBG narrower than using SMF as the dispersive element. Although research groups have tried to use more than one CFBG in different bands, [174] these alternatives lead to different dispersion amounts for the spectral band. Therefore,

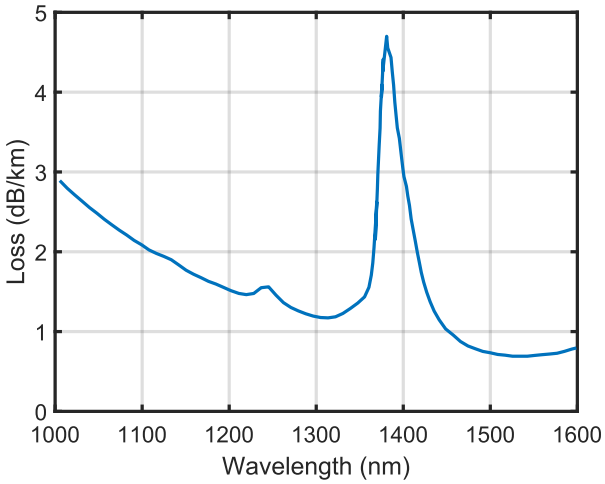

FIGURE 3.17: Typical optical attenuation in a 980XP fibre.

the bandwidth of time-stretched swept sources is the product of the pulse input spectrum with that of the transmission medium.

Dispersion Tuning Mode-Locked (DTML)

A Dispersion Tuning Mode-Locked (DTML) laser is comprised of three essential components: a gain medium (such as an SOA or a rare-doped fibre amplifier), a modulation element (employing either modulation of the SOA gain or a separate intensity modulation), and a dispersive element (either a long piece of fibre or a cFBG).

The initial iteration (Figure 3.18 (a)) of DTML lasers utilises long fibre pieces as a dispersive element, enabling coverage of varying wavelengths, including 850 nm [177], 1300 nm, and 1550 nm [178]. However, the long ring cavities limited the achievable sweep rates to only a few kHz. The second version, Figure 3.18 (b) of DTML, implemented cFBG as a substitute for long fibres, resulting in superior manufacturing and reduced cavity length. This modification led to larger sweep rates of tens of kHz at both 1300 nm [179] and 1550 nm [180]. Although both generations utilised SOA modulation, this approach resulted in a few drawbacks. In addition to gain modulation, spectral bandwidth was also impacted.

Furthermore, the SOA RF bandwidth was typically restricted to only 500 MHz, which limited the application of temporal windows shorter than 1 ns.

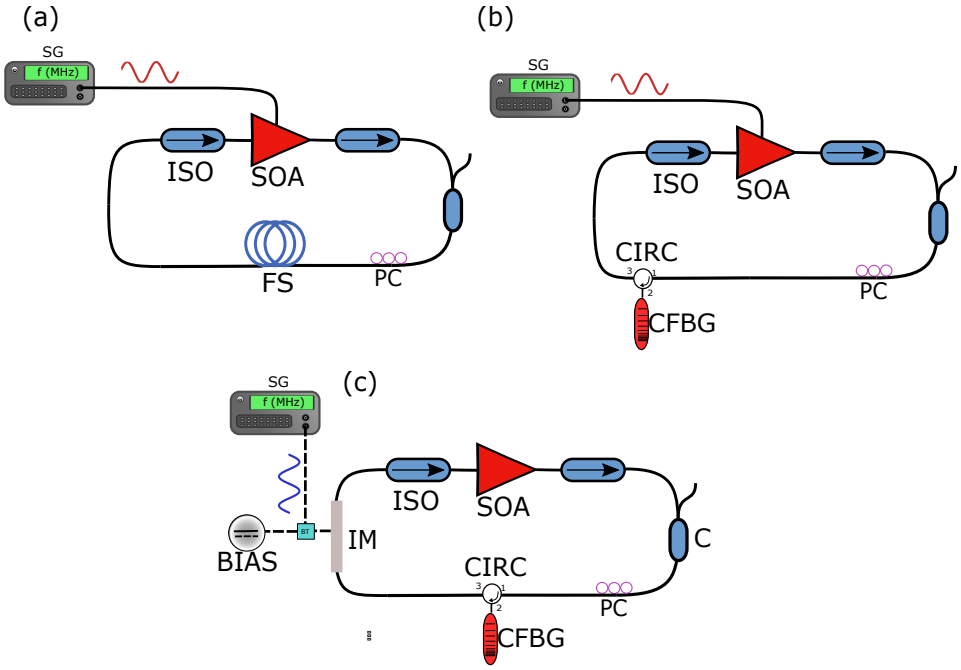

FIGURE 3.18: Sketch of the 3 different generations of DTML. (a) The first generation, a fibre spool, FS: Fibre spool, is used as a stretching element. (b) In the second generation of DTML, the FS is replaced by a cFBG and a circulator. (c) The third generation of DTML, the modulation element employs an intensity modulator, IM, instead of the SOA.

The third generation of DTML lasers, Figure 3.18 (c), employs an intensity modulator to induce mode-locking instead of the SOA. This change has been successfully reported for both 1060 nm [181] and 1550 nm [182]. Recently, a fourth generation was introduced by R. Riha et al [183], which utilised a dual resonance sweeping regime. This regime enabled laser tuning at rates of hundreds of kHz to even a few MHz in long-length cavities.

Stretched Pulsed Mode-Locked

Due to the limitations of DTML sources regarding increasing the speed, a stretched pulsed mode-locked laser (SPML) was proposed. The main idea of this configuration represents a mix between dispersion management mode-locking, presented

in Section 3.2.2.2, and DTML. The cavity described for the first time by S. Tozburun et al. [184] was presented as one of the fastest swept sources. Because chromatic dispersion is used instead of a mechanical wavelength scanning filter, there is almost no speed limitation.

As shown in Figure 3.19, the cavity contains four main components: a gain medium, either a SOA or a rare-earth doped material. Light is generated in the cavity by amplified spontaneous emission (ASE). Secondly, a dispersive element is used to compress the linewidth of the radiation before reaching the third element, an intensity modulator. The intensity modulator filters the broad optical emission, resulting in the transmission of a desired wavelength. Finally, a dispersion element with the exact same dispersion value as the compressor. This element stretches the pulse in time to obtain the sweeping and also avoid catastrophic optical damage (COD) in the SOA. It is important to note that positive and negative dispersion have to be matched perfectly for the laser to perform well.

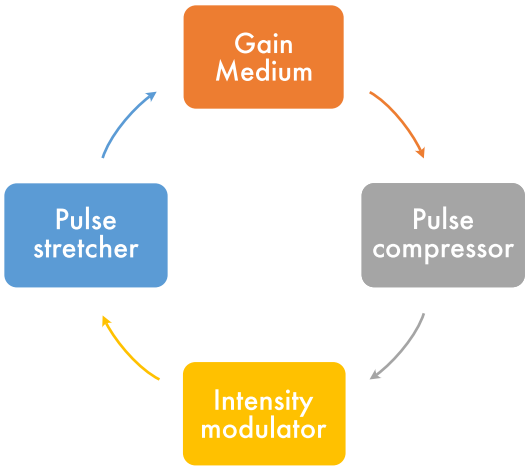

FIGURE 3.19: Sketch of the different stages of an SPML laser.

The first generation of SPML lasers, Figure 3.20 (a), used long fibres as dispersive elements [184, 185]. A proof of concept, 40 km of SMF-28 was added in conjunction with the analogous length of a dispersion-compensating fibre (DCF). DCF can only be used at 1550 nm. Figure 3.20 (b) shows in diagrammatic form

an SPML where instead of long fibres for dispersion, cFBG is used. The first implementations of this generation used two cFBGs with the exact same dispersion. However, one must notice that the direction from which the light passes through the fibre matters in terms of dispersion acquired by the pulse. Using a cFBG from two different inputs, two very similar cFBGs could be fabricated, in which the input is alternated. This idea was quickly replaced by a figure of eight. Even though, in principle, two very similar cFBGs could be fabricated, small fluctuations in the phase masks could create big differences.

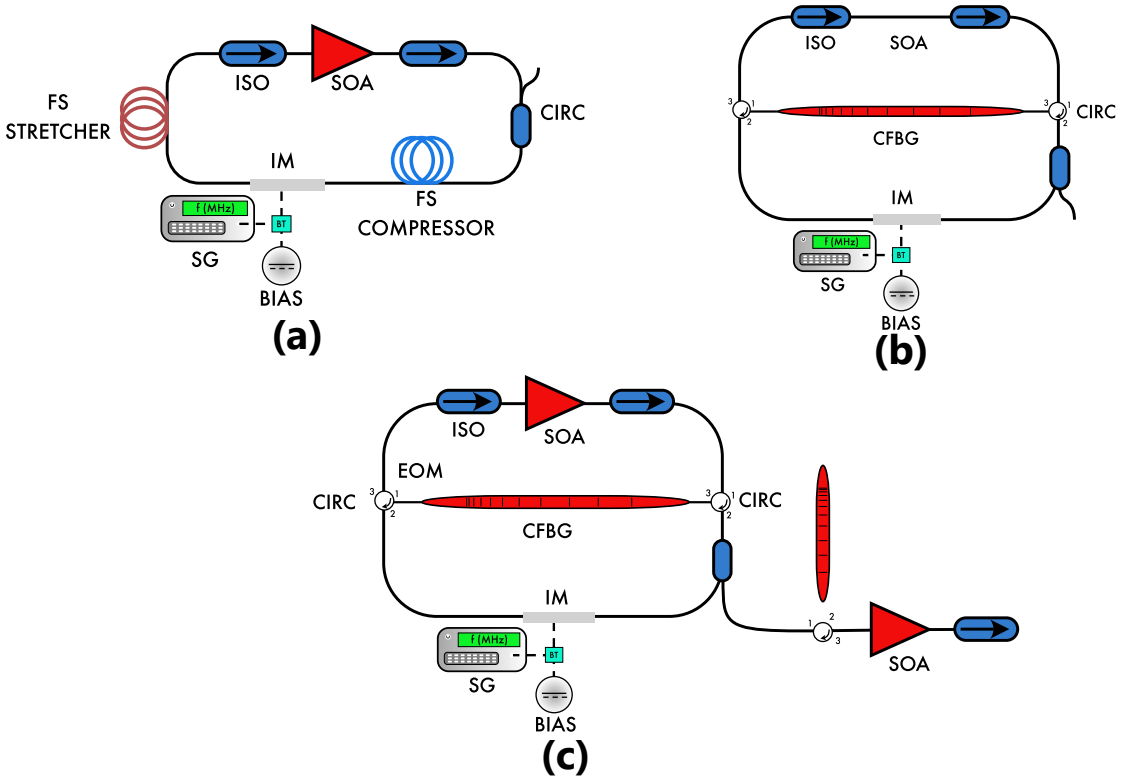

FIGURE 3.20: Set up of an SPML laser, (a) First and (b) second, and (c) third generation of SPML laser.

For this reason, an arrangement of one cFBG with two circulators was proposed in Figure 3.20 (c). R. Khazeinezhad et al. and T. S. Kim reported excellent results using such configuration at 1550 nm and 1060 nm, respectively [186, 187]. An SPML laser can also be assembled employing all polarisation maintaining (PM) components, which can improve the stability of the laser under environmental perturbations [152, 188]. The benefit of using all PM-fibres has

been demonstrated in numerous studies to be less sensitive to the environment [189–191]. Recently, a third generation has been realised, as shown in Figure 3.20. Because the intensity modulator blocks half of the light redirected from the cFBG, the maximum achievable duty cycle in cFBG-SPML is 50%. A larger duty cycle can be achieved by employing a buffer stage outside the laser cavity. However, it has been seen that long cFBG inside the laser can deteriorate its coherence. Therefore, minimising the intracavity length by adding another cFBG outside of the cavity [192] improves the coherence length. The coherence length of the SPML laser is closely related to the coherence length of the FDML. The chromatic dispersion is minimised in the design [193, 194]. Relative group delay (RDG), which means uncorrected chromatic dispersion, will degrade the coherence length. Some authors have pointed towards a mismatch between the two cFBGs as contributing to the largest degradation of performance, especially when using a long cFBG.

3.3 Conclusions

This chapter is divided into two main sections: an introduction to mode-locked lasers for the case of NPR and an introduction to swept-source modalities. At first, the general concepts of mode-locking are presented, as well as the type of fibres used. Furthermore, the working operation of NPR as a saturable absorber is described. As outlined, pulse power, dispersion and polarisation are key parameters that need to be chosen wisely for the correct operation of NPR as a saturable absorber. In fact, the fibre specifications will set those key parameters. The second half of the chapter presents a brief introduction to swept sources and the different modalities used to generate sweep rates from few-Hz to multi-MHz. In summary, as shown in Fig. 3.21, deflector-based swept sources are commonly used for slow sweep rates, 1 Hz - 30 kHz. In the range of repetition rates of 200 kHz – 3 MHz [195–199], MEMS-VCSELs are the right candidate. Moreover, MEMS-VCSELs

provide one benefit not yet exploited: miniaturisation and replication; they can be fabricated in a wafer with 1,000 light sources at a time [200]. From 400 kHz to 10 MHz, FDML lasers represent a better alternative. The FDML laser exhibits a long coherence length even when buffered multiple times, as reported at [51, 104, 128]. At further sweeping rates, the time stretch demonstrates the possibilities for a high repetition rate (>10 MHz), which, in fact, will be one of the modalities used in this thesis for obtaining multi-MHz repetition rates in Chapter 4 and 5. Furthermore, two of the most commercially successful swept sources are examined during the thesis: a MEMS-VCSEL at 1060 nm central wavelength operating at a sweep rate of 1.6 MHz and an FDML at 830 nm central wavelength operating at a sweep rate of 828 kHz, both exhibiting bidirectional sweeping.

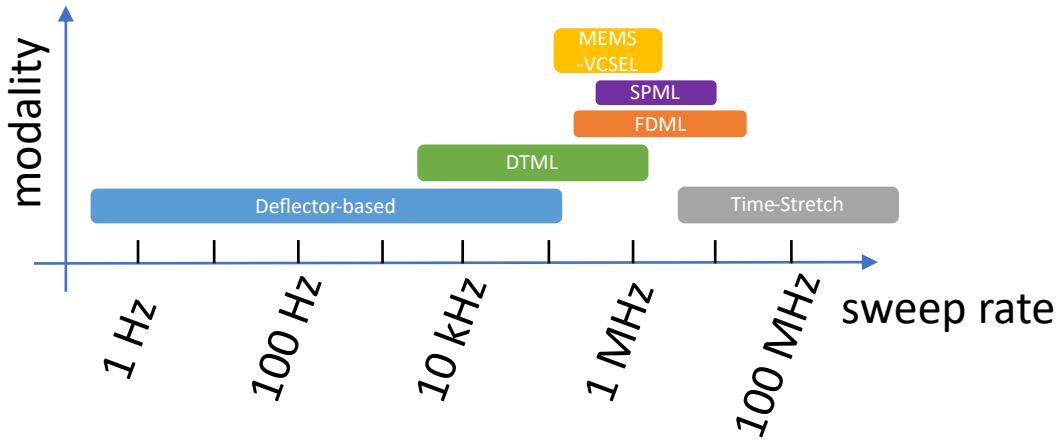

FIGURE 3.21: Swept source modalities in context with sweep rate.

Overall, for a longer axial range and higher axial resolution, two key parameters need to be optimized in the swept source development: bandwidth and linewidth. In the case of broadband swept sources (>100 nm), the bandwidth is ultimately limited by the gain medium, i.e. the SOA used. However, in some modalities, as in FDML, DTML, and SPML, the bandwidth might also be limited by the dispersion arrangement on the cavity. Typically, those mentioned modalities can achieve from 50 to 100 nm depending on the specific design. The development of semiconductor media will consequently have a high impact on the development of broader swept sources. Although strategies such as using more

than one SOA in the cavity have been explored, they do not seem to progress significantly [2]. In this sense, time-stretch allows implementation with supercontinuum generation or any other kind of pulse seed, which might alleviate the need for broadband SOAs, making this modality a fast-sweeping and high-resolution possible alternative. On the other hand, the linewidth, and therefore the axial range, of swept sources has increased from 1-2 mm with deflector-based sources to even a few-meter axial range [142]. In this direction, FDML and MEMS-VCSEL have been the two modalities that have advanced the linewidth the most. On those tuning modalities, the use of closed and high-finesse cavities improves the linewidth. Finally, FDML, SPML, DTML, and time-stretch use dispersion compensation devices such as cFBGs. Therefore, in the future, the development of cFBGs will clearly impact the growth of high-speed swept sources.

Chapter 4

Dispersion techniques and a swept source based on mode-locked laser and time-stretch

This chapter presents two novel dispersion measurement techniques, discussing their advantages and drawbacks. Furthermore, a pulsed fibre laser operating at 1550 nm is demonstrated. The laser uses nonlinear polarisation rotation (NPR) as the pulse generation technique. The chapter covers the cavity design, pulse regimes, and implementation. Finally, the laser is stretched and characterised for OCT.

Contents

4.1 Swept source laser based on NPR and time-stretch at 1550 nm

In recent years, OCT has witnessed a steady increase in repetition rates, potentially enhancing the imaging technique for high-speed applications. Since the introduction of time-stretch [157], interest in this modality has grown, demonstrating its effectiveness through two main seeds: supercontinuum and mode-locked based. Time-stretch enables high-speed repetition rates as the sweep is conducted in an akinetic manner, and the pulse repetition rate of the seed gives the sweep rate. Generating multi-MHz swept sources using time-stretch is more feasible than few-MHz sources, where the stretching element must undergo significant modifications.

In OCT, achieving fine axial resolution (1-5 μm) requires a source with a large bandwidth (>100 nm). This requirement has led only a few mode-locked techniques to opt for NPR as the best candidate [62, 142, 201]. NPR lasers can potentially generate broadband pulses if dispersion and polarisation conditions are met. A laser cavity is examined to study NPR operation. The telecommunications wavelength band, particularly 1550 nm, is the most advanced wavelength band in optical fibre and optoelectronic components. Fibres such as dispersion compensating fibre (DCF), equivalent to hundreds of kilometres, are ideal for time-stretching applications. In the following sections, we will explore the challenges of generating broadband mode-locked lasers at 1550 nm.

4.1.1 Mode-locked cavity design

A mode-locked cavity consists of at least three elements: a gain medium (such as a rare-earth-doped optical fibre, e.g., erbium- or ytterbium-doped fibre); a saturable absorber (SA) which can be either a physical component (e.g., a semiconductor saturable absorber mirror, SESAM) or an artificial effect (e.g., nonlinear

polarisation evolution or nonlinear optical loop mirror); and an output coupler. The gain medium, in this case a commercially available Erbium doped fibre amplfier, provides optical amplification by converting pump light into coherent light through stimulated emission. This amplification compensates for cavity losses and initiates the formation of a broadband optical spectrum. The NPR mechanism acts as an artificial saturable absorber, utilizing the intensity-dependent polarisation rotation of light as it propagates through the fibre. This effect is achieved by combining a polarisation controller and a polariser within the cavity: the polarisation controller adjusts the birefringence of the fibre, while the polariser selectively attenuates low-intensity light, allowing only high-intensity pulses to pass. This intensity-dependent filtering shapes the pulse and initiates mode-locking. Finally, the output coupler extracts a portion of the circulating pulse energy as the laser output, while the remainder continues to circulate within the cavity, maintaining the mode-locked operation. The interplay of these elements—gain, NPR, and output coupling—enables the generation of stable, short pulses with durations ranging from femtoseconds to picoseconds.

Although simple, such a configuration, in principle, allows for optimising many variants and parameters. The pumping power, the total length of the passive fibre, and the position of the polarisation controller might induce different regimes for pulse operation. Here, we examine these three parameters.

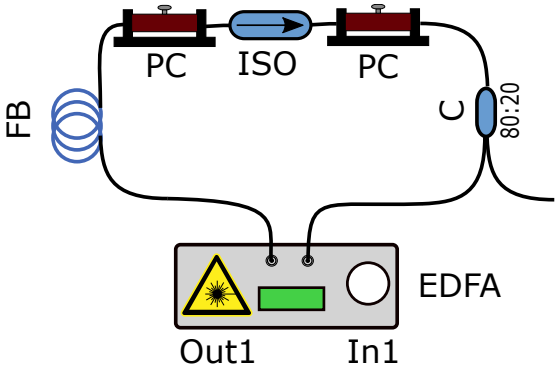

FIGURE 4.1: Nonlinear polarisation rotation cavity consisting of: PC1-2: Polarisation controllers, ISO: Isolator, C: Coupler, EDFA: Erbium Doped Fibre Amplifier.

The mode-locked laser is presented in Figure 4.1. The ring cavity presented here comprises of normal and anomalous dispersion fibre patchcords in the loop. The combination of the polarisation controllers, isolator, and fibre acts as a saturable absorber. A polarisation sensitive isolator (AFW, ISO-PS-15-B), ISO, with single mode fibre (SMF) patchcords, was used in the cavity. The selection of such an isolator is essential since the isolator implements a double function, ensures one-way operation, and acts as an artificial saturable absorber. The saturable operation has been described in previous works as follows [63, 90]: an initial long pulse generated by the mode-beating is linearly polarised, and the pulse is then made elliptical acting through a polarisation controller. The elliptically polarised light evolves through the fibre, and the polarisation over the peak pulse rotates more than the pulse wings. By actuating on the polarisation controller, the elliptical polarisation of the high-intensity part of the beam is converted into linear, leading to elliptical orientation in the wings and linear orientation on the central part. Then the linear polarisation will travel through the isolator, and the rest, i.e., the wing of the pulse, will be rejected. An effective artificial saturable absorber evolves the pulse into a steady state. Different mode-locking states are obtained by actuating on the polarisation controllers, PC1 and PC2, leading to spectral shapes of different bandwidths. The power strongly influences the spectrum stability and bandwidth in the cavity. During our research, several cavity designs have been studied. The dispersion inside the cavity should be measured to study the effects of changing the total cavity length. In that sense, we investigated two different techniques for dispersion assessment.

4.1.2 Dispersion assessment

The methods known for dispersion measurement [202] mostly employ either time of flight [203] or white light interferometry [204]. Common white light interferometry methods rely on acquiring the interferometric phase $\varphi(\lambda)$ for each wavelength and then computing the dispersion coefficient $D(\lambda)$. White light interferometry has shown reliable results for short group delay dispersion (GDD) measurements. However, such a method is unsuitable for measuring long patchcords due to the need for building large interferometers. Alternatively, rather than using the phase, the peaks in the interference spectrum are correlated in time and wavelength. In continuation, an experimental setup for the method mentioned is built. The set-up consists of a broadband mode-locked laser as a white light generator and an interferometer, see Figure 4.2.

The white light generated by the mode-locked laser is guided towards the interferometer. After the interferometer, the spectrum is modulated with a period defined by the optical path difference between the two arms. Then, the spectrum is recorded in time and wavelength. However, the time measurements require that the dispersion of the fibre under test must be large enough to spread optical modulation of the spectrum within the RF bandwidth of photodetectors. In this case, we use a 20 GHz oscilloscope (Lecroy Teledyne 820-ZiB) with a 23 GHz balanced photodetector (Optilab, BPR-23-M) and a spectrum analyzer (Yokogawa, AQ6373E). The mode-locked laser is the configuration number 5 of Table 5.1, the characteristics, optical spectrum and pulse are described further in the chapter. The dispersion is calculated then using the following:

$$D\left(\lambda\right) = \frac{1}{L}\frac{d\Delta\tau}{d\lambda}, \tag{4.1}$$

where $D(\lambda)$ is the dispersion coefficient in ps/nm/km, and L is the path length in km. The spectrum has been measured after the interferometer. Asymmetry in the laser spectrum is clearly depicted in Figure 4.3, which allows the matching

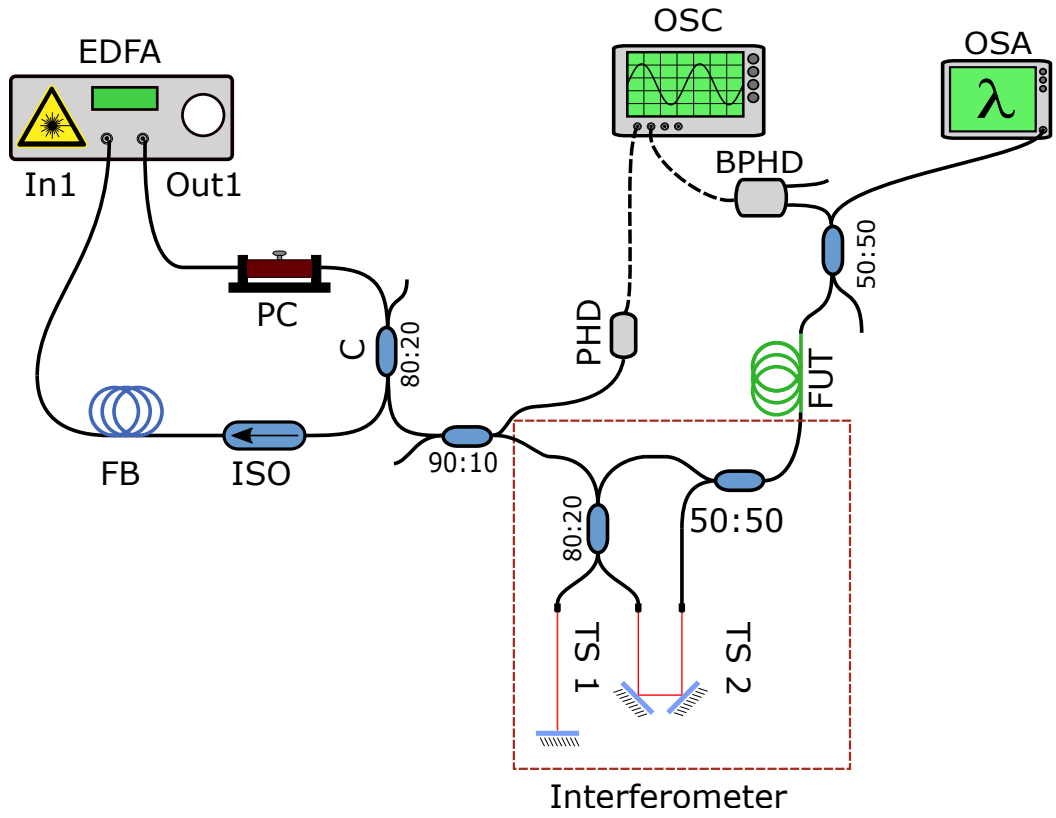

FIGURE 4.2: Mode-locked laser (EDFA: Erbium-doped fibre amplifier, PC: Polarisation Controller, FB: Fibre, ISO: Isolator), PHD: Photodetector, TS1,2: Translation Stages, FUT: Fibre Under Test, OSC: Oscilloscope, OSA: Optical Spectrum Analyser. We can differentiate three stages; on the left, we have a ring cavity for the NPR configuration. On the right, an Interferometer is shown with recirculation of the reference wave along the DL; in this case, the DL is used for frequency-time mapping in which we evaluate the delay of each wavelength.

of peaks between the left and right graphs in Fig. 4.3, i.e. between spectral and temporal evolution. Nominal values of dispersion are then calculated. Compared to the manufacturer specifications, the experimental data presented here has a 1.6% relative error, as shown in Figure 4.4.

The method may not be sensitive enough to predict small amounts of dispersion. In order to calculate the minimum detectable dispersion of this method for the devices used, we can use 4.1, assuming the 20 GHz photodetector, a time resolution of $\tau = 0.35/f$, then for the photodetector used $\tau =$ and 0.01 nm spectral resolution of the spectrometer, then $D(\lambda)L = \Delta\tau/\Delta\lambda = 50\text{ps}/0.01nm = 1,750\text{ps/nm}$. Furthermore, here, we are assuming that the dispersion of the other

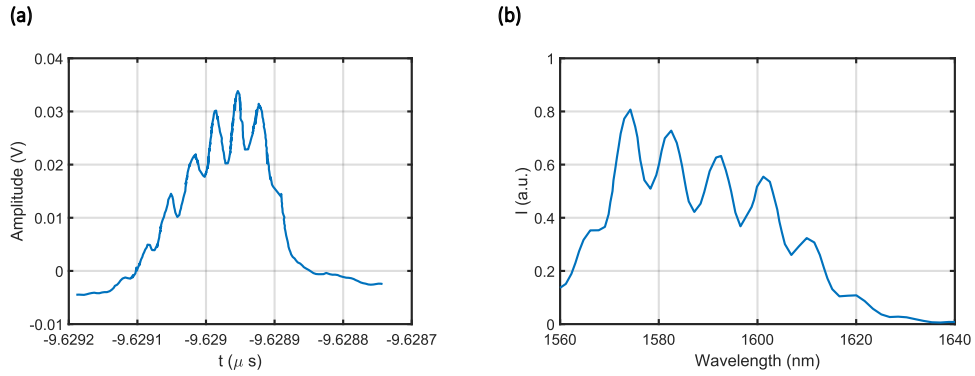

FIGURE 4.3: Experimental data recorded on the spectrometer and the oscilloscope. (a) Laser spectrum on time recorded from the OSC. (b) Laser spectrum on wavelength recorded from the OSA.

in-line components is negligible when compared with the dispersion of the FUT. However, this might not be true when using small patchcords of fibre, where this approximation won't be valid.

As the shorter wavelength is delayed more, this corresponds to normal dispersion. We tested the setup with different lengths. In the next case, a telecom fibre of 2.527 m length has been assessed. In order to identify the different peaks, more than 20 signals had to be averaged. However, averaging on the oscilloscope washed out the spectrum. Therefore, this was done offline. Taking the pulse as a reference, deviations due to laser jittering are corrected. Once corrected, the signal is averaged and filtered.

This technique, based on time of flight, is limited by the maximum frequency of the RF photodetector. However, it is insufficient for the length of our cavity laser, i.e. between 20 – 50 metres. Therefore, we propose an alternative method to assess the dispersion in the cavity. A novel method is presented, which enables accurate chromatic dispersion (CD) measurement in long fibre based on an electronic downconversion scheme. This overcomes the need for a high frequency digitiser and allows for inexpensive CD measurements.

Figure 4.5 shows the set-up used for measuring CD. This employs a tunable laser (Santec, TSL-210) TL, which emits a continuous wave (CW) towards an electro-optic intensity modulator, EOM. The EOM (Sumitomo Osaka Cement

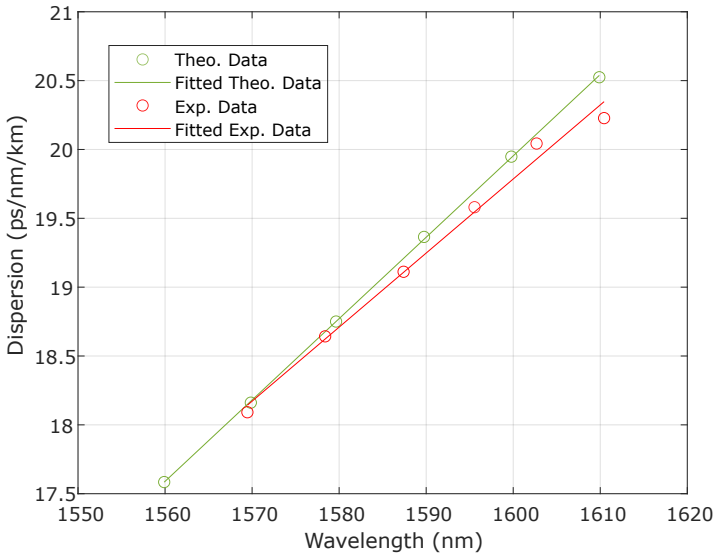

FIGURE 4.4: Dispersion measured in the OFS SMF-DK DCF @20km compared with theoretical values.

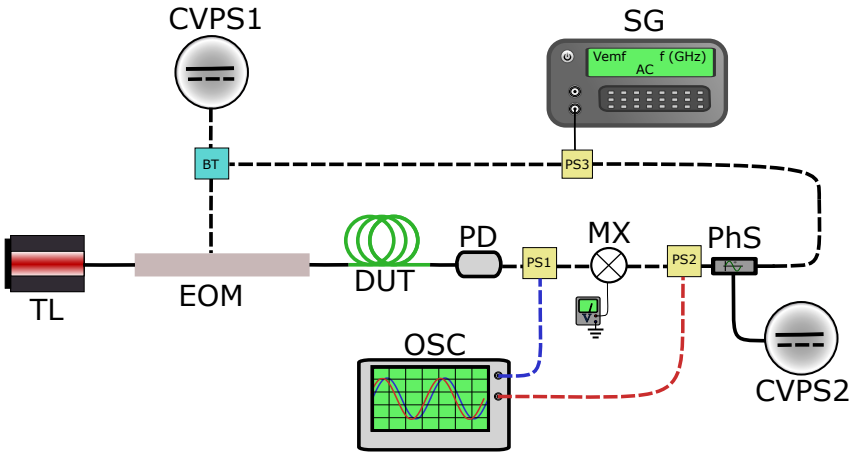

FIGURE 4.5: (a) Basic scheme for CD measurement. Solid line refers to fibre links and dashed line to electrical cables. TL: Tunable laser; EOM: Electro-optic modulator; DUT: Device under test; OSC: Oscilloscope; PS1-3: Power splitters; CVPS1-2: Control voltage power supply; BT: Bias tee; PhS: Phase shifter; BT: Bias tee; PD: Photodetector; MX: Mixer; SG: Signal generator.

Co., T-MZ 1.3-10) reaches frequencies up to 14 GHz; it is adjusted to operate at quadrature by using a voltage power supply, CVPS1, which delivers a DC component, and a signal generator (Keysight 8648B), SG, which delivers an AC component. The modulated optical signal travels along the device under test (DUT), and finally arrives at a photodetector, PD. The signal from the SG is split between the EOM and a phase shifter (ClearMicrowave, PA0102, 1-2 GHz), PhS, whose

phase φ_{PhS}(V) is controlled by a voltage power supply, CVPS2. The phase difference $\delta\varphi(\lambda)$ between the PD phase φ_{PD}(V) (λ) and the PhS phase φ_{PhS}(V) (V) is evaluated on an oscilloscope, OSC. For λ_{min}, by controlling the CVPS2 output, the phase difference is brought to zero, and as a consequence, the MX voltage at the mixer output. Then, the TL is tuned in steps of 2 nm over the tuning bandwidth. The phase difference between the two RF signals corresponding to two wavelengths spaced by $\Delta\lambda$ is related to the time delay according to Eq (4.2):

$$\Delta\tau(\lambda)[s] = -\frac{(\delta\phi\,(\lambda - \Delta\lambda/2) - \delta\phi\,(\lambda + \Delta\lambda/2))}{(360\ \times f_m[1/s]\,)} \times 10^{12}, \tag{4.2}$$

where f_m is the modulation frequency applied to the SG and $\Delta\tau(\lambda)$ is the relative group delay. For better accuracy, a smaller tuning interval can be chosen to fit better the dispersion variance curve, which can be used to determine the dispersion coefficient. As a low-cost alternative of using an oscilloscope, we propose using a mixer (Mini-circuits, ZEM-4300+). The mixer performs multiplication of the two input waves after PS1 and PS2 of a similar amplitude. The result is a superposition of signals pulsating at frequencies given by addition and subtraction of the original frequencies. As the frequency of the two signals at the mixer input is the same, a DC level results (the downconverted signal), whose amplitude depends on the phase difference. A low pass filter filters the signal pulsating at the summation of frequencies. Then, the phase difference $\delta\phi$ is extracted from the DC of the mixer output, and the dispersion is computed.

Moreover, for the calculations, the signal must be calibrated, considering the variations in wavelength of the electro-optic modulator. The electro-optical modulators are dependent on the wavelength used. Therefore, a voltage applied to them will affect the transmission differently. Here, we characterise the transmission to find the quadrature point for each wavelength; see Figure 4.6(a).

A set-up consisting of a power meter, a tunable laser and an electro-optic modulator was built to characterise the quadrature point. The results are shown in

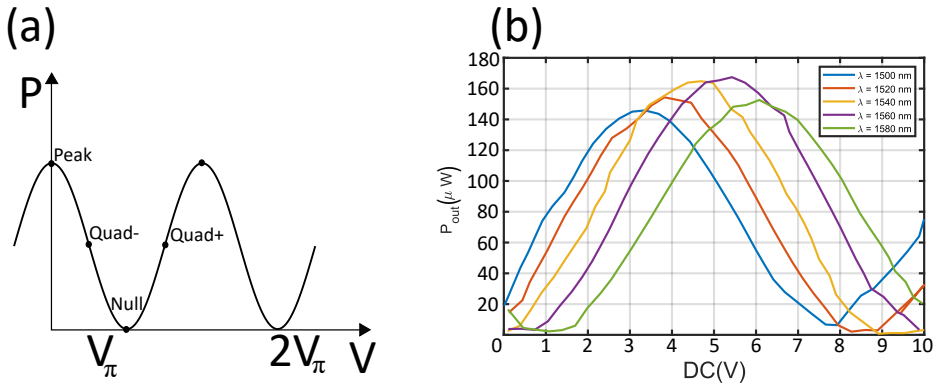

FIGURE 4.6: Quadrature point for the electro-optic modulator. (a) Concept of the quadrature point. (b) Experimental data for different wavelengths.

Figure 4.6 (b), where the tunable laser is set to five different wavelengths with a span of 10 nm, and the DC voltage is varied. As can be seen, the quadrature point differs from 5.5 V at 1500 nm to 8.5 V at 1580 nm, which has to be considered for the experiment. The optical signal is modulated at 1.5 GHz. The operations required to reach Eq. 4.5 are the following ones: In one of the inputs of the mixer, a sinusoidal wave from the signal generator is given, while in the other, the sinusoidal wave phase shifted from the fibre is received by the photodetector and coupled into the second input of the mixer. The mixer multiplies the two input signals, obtaining Eq. 4.3. Resulting in a superposition of two signals, pulsating at the sum and difference of frequencies of the two input signals. Using a low pass filter, the component with the addition of the two frequencies is eliminated, and Eq. 4.3 reduces into 4.4. Finally, as both signals have the same frequency, i.e. $\omega_1 = \omega_2$, then the equation is further reduced into Eq. 4.5. As a consequence, the output is proportional to the amplitude of the signals and the phase difference, which the latter can be measured with a simple voltmeter assuming A_{01} and A_{02} are stable in the process.

$$A_1 A_2 = \frac{A_{01} A_{02}}{2} \left[\cos\left((\omega_1 + \omega_2)t + (\phi_1 + \phi_2)\right) + \cos\left((\omega_2 - \omega_1)t + (\phi_2 + \phi_1)\right)\right] \quad (4.3)$$

$$A_1 A_2 = \frac{A_{01} A_{02}}{2} \left[\cos\left((\omega_2 - \omega_1)t + (\phi_2 - \phi_1)\right)\right] \quad (4.4)$$

$$A_1 A_2 = \frac{A_{01} A_{02}}{2} \left[\cos\left(\phi_2 - \phi_1\right)\right] \quad (4.5)$$

It is important to note that this technique may be unreliable when the photodetected signal is unstable, as changes in A_{01} or A_{02} could mislead the phase values when using a voltmeter to measure. In Figure 4.7 (a), the dispersion coefficient over the tuning bandwidth of the source for 50m of standard telecommunication single-mode fibre (SMF-28e+) was employed to test the set-up. A dispersion coefficient of 17 ps/nm/km at 1550nm is obtained in agreement with manufacturer data.

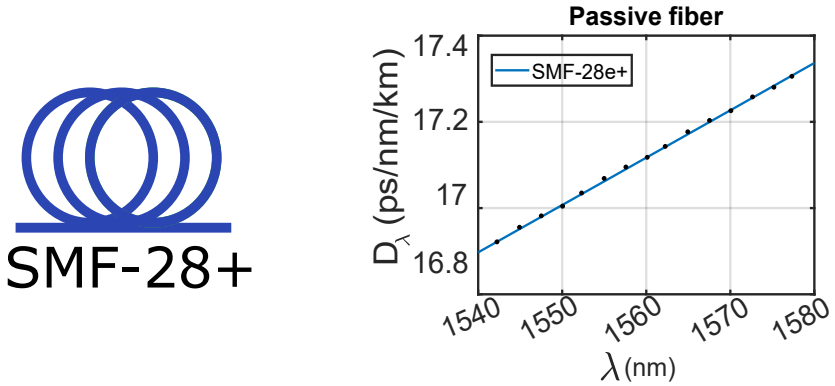

FIGURE 4.7: Experimental measurement of the dispersion coefficient calculated with the phase proposed method for a sample of passive fibre SMF-28e^{+}.

In this work, a modulation frequency of 1.5 GHz was used; the frequency chosen here is limited by the components available at the time in the AOG lab. Assuming that the time resolution is given by the photodetector used, then $\tau = 17.5$ ps, and the minimum phase detectable for a signal of 1.5 GHz $Phase = \left(\frac{t_r}{T_{signal}}\right) \times 360° = 9.45°$. If we now substitute the phase values into Eq. 4.2, $\Delta\tau(\lambda) = 110$ps, and therefore the minimum dispersion detectable is $D(\lambda)L = \Delta\tau(\lambda)/\Delta\lambda = 44$ps/nm. Of course, this is assuming no jitter noise in the system. In reality, the minimum dispersion values would be higher for both cases. Still, the accuracy of the dispersion measurement has been improved compared with the previous method. However, using this method for active fibre is not recommended since variations in the amplitude will be confused with phase changes. In the future, according to Eq.4.2, a higher modulation frequency applied to the intensity modulator will improve the accuracy of the measurement. However, the amplitude variations will remain, which might need to be compensated by a

constant measurement of the amplitude at each wavelength. Alternatively, other techniques based on white light interferometry can be used to obtain, in principle, a higher accuracy than the one reported here in the dispersion measurements [205]. However, when using active fibres, a calibration must be undertaken to compensate for the fluctuation they might cause. Additionally, while interferometric techniques could be effective when the OPD is less than l_c of the source, in scenarios where a cavity spanning hundreds of meters must be measured, the OPD will exceed the coherence length, resulting in no observable interferometric signal. Consequently, it's crucial to consider the maximum measurable length.

4.1.3 Pulse regime and characterisation

The pulse repetition rate (PRR) of the laser has been varied by adding fibre inside the ring loop, obtaining repetition rates of 0.9 MHz to 9.65 MHz. Table 4.1 shows the NPR operation for a wide range of cavity lengths in the laser cavity. For all cavity designs, mode-locking has been achieved. In general, when the broader spectrum is obtained, the temporal and spectral instabilities are more noticeable. All spectra are red-shifted from the fibre gain profile. Fluctuations are measured as the pulse-to-pulse peak intensity variation; no filter has been used for the noise measurements.

Config No.	Frequency [MHz]	FWHM [ps]	Bandwidth at 3 dB [nm]
1	0.91	801	53
2	3.51	265	46
3	6.61	371	33
4	7.94	206	67
5	9.65	170	45

TABLE 4.1: Parameters of the different cavity configurations used.

In Figure 4.8, configuration 5 was used, with a 30-metre cavity operating at 9.65 MHz PRR. A 24-hour optical power test was performed to assess the power stability, obtaining a standard deviation of 0.15 mW for the average power. Figure 4.8 (a) shows the laser spectrum before and after BOA amplification. The pulse

was measured using a single photodetector (EOT, ET3600, 20 GHz); a train of pulses can be seen in Fig.4.8 (b). In order to determine the pulse width, 10k pulses are acquired, and the FWHM is measured in each of them, calculating the average pulsewidth of the 10k pulses. A histogram of the FWHM is shown in Fig.4.8 (d). In the same way, jitter noise is shown in Fig.4.8 (c, e).

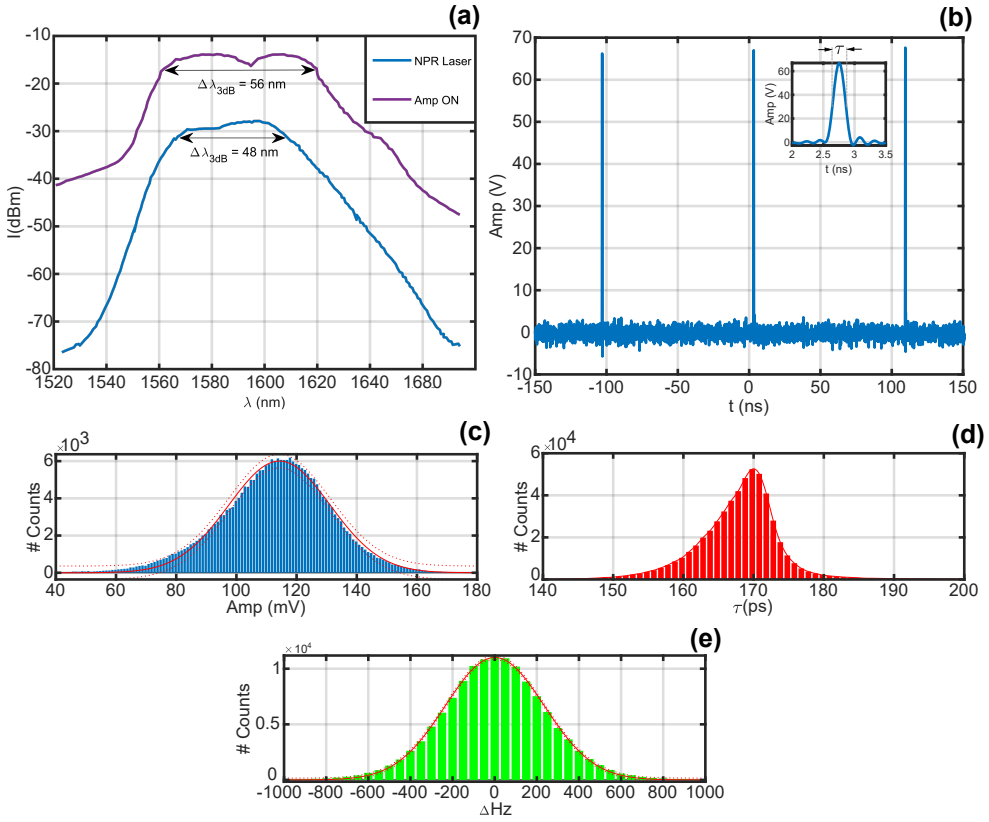

FIGURE 4.8: (a) Spectrum of the swept-source. (b) Train of pulses generated by the NPR cavity. (c) Histogram of maximum pulse voltage amplitude. (d) Pulse-width measurement over 10k pulses. (e) Jitter variation of the mode-locked repetition frequency.

4.1.4 Stretching element and OCT demonstration

On the sweeping stage, an optical delay line (DL) acts as a dispersive medium to stretch the pulses. Two configurations were studied, as shown in Figure 4.9. The ONE-WAY system consists of a spool of dispersion compensating fibre that creates an equivalent dispersion to that of a 100 km SMF at 1550 nm (SMFDK-S-100-03-02 by OFS), and another spool of 20 km (SMFDK-S-020-03-01 by OFS).

The total GVD achieved is 1.7 ns/nm at 1550 nm, generating a sweep time of 95ns with a duty cycle of 95%. The dispersed pulse after the delay line is then amplified up to 40 mW using a BOA. In addition, a TWO-WAY system performs a double time-stretch delay, consisting of a circulator, 60 km of SMF fibre and a Faraday mirror, contributing a delay equivalent to 120 km. A total loss of 6.4 dB and 17 dB was measured for the ONE-WAY and the TWO-WAY systems, respectively. The total GVD achieved in the TWO-WAY configuration is 4.08 ns/nm at 1550 nm. For OCT, the swept source should launch at least 20 mW input into the interferometer; therefore, an amplification stage is needed. An erbium-doped amplifier was used; however, the amplified spectrum is red-shifted, filtering the laser spectrum. Finally, a booster optical amplifier (Thorlabs, BOA18080S) based on a semiconductor chip was used, with the spectrum shifted to the L-Band. The output of the swept source is then launched into an interferometer that uses SMF-28 fibre. The light is guided towards an 80/20 coupler; 20% of the light goes to the sample and 80% towards the reference arm. The light from the reference and sample arm is then recombined in a 50/50 coupler.

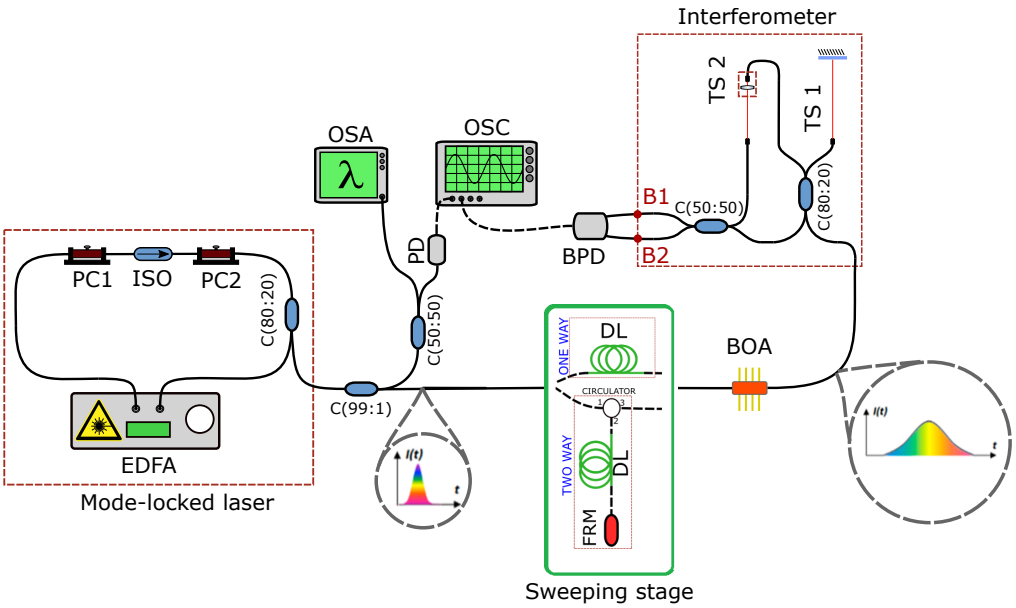

FIGURE 4.9: **Experimental set-up of the mode-locked laser.** Seed laser (EDFA: Erbium-doped fibre amplifier; PC1-2: Polarisation controllers; ISO: Isolator; C: Coupler). Sweeping stage (DL: Delay line; BOA: Booster optical amplifier, FRM: Faraday rotator mirror) Acquisition (OSC: Fast Oscilloscope, OSA: Optical spectrum analyser; PD: Photodetector, BPD: Balanced photodetector)

The channeled spectrum is then received by a 23 GHz balanced photodetector unit, and the electrical signal is acquired using a 20 GHz, 80 GSa/s, oscilloscope (Wavemaster 820Zi-b by Lecroy Teledyne). For the calibration, the CMS method, which has already been widely investigated, has been used [206]. Using a mirror in the sample arm, the channeled spectrum is acquired for 10 different values of the optical path difference. Then the phase of each channeled spectrum is extracted, subsequently $g(k)$ and $h(k)$ are obtained from a linear system of equations that can be described as:

$$\begin{aligned} \varphi_1 &= g(k)z_1 + h(k) \\ \varphi_2 &= g(k)z_2 + h(k) \end{aligned} \tag{4.6}$$

Using CMS in the postprocessing, A-scans are generated that exhibit similar axial resolution throughout the whole axial range. The phase of the interference signal can be written as:

$$\varphi\left(z,k\right) = g\left(k\right)z + h\left(k\right) + \varphi_{rand}, \tag{4.7}$$

where φ_{rand} is a random phase shift. Nonlinearities of sweeping and dispersion in the interferometer are respectively modelled by $g\left(k\right)$ and $h(k)$ functions. Figure 4.10 (a,b) displays these parameters for both systems. $g\left(k\right)$, blue in the chart, gives information about the linearity of the sweeping. In both cases, a linear regression of $g\left(k\right)$ is made, obtaining an R^2 of 0.999; this shows a linear sweep of the source. Thus if the Fourier transform is applied to the photodetected signal, then only the nonlinearities in the interferometer must be corrected. Furthermore, the linearity of the $g(k)$ function describes how the DCF fibre encodes the wavelength in time, and can be matched with the dispersion of this stretching element. On the other hand, $h(k)$ shown in Fig. 4.10 (a,b), referring to the uncompensated dispersion between reference and sample arm, suggests minimal mismatching

between both arms. Swept sources are typically characterized by measuring the

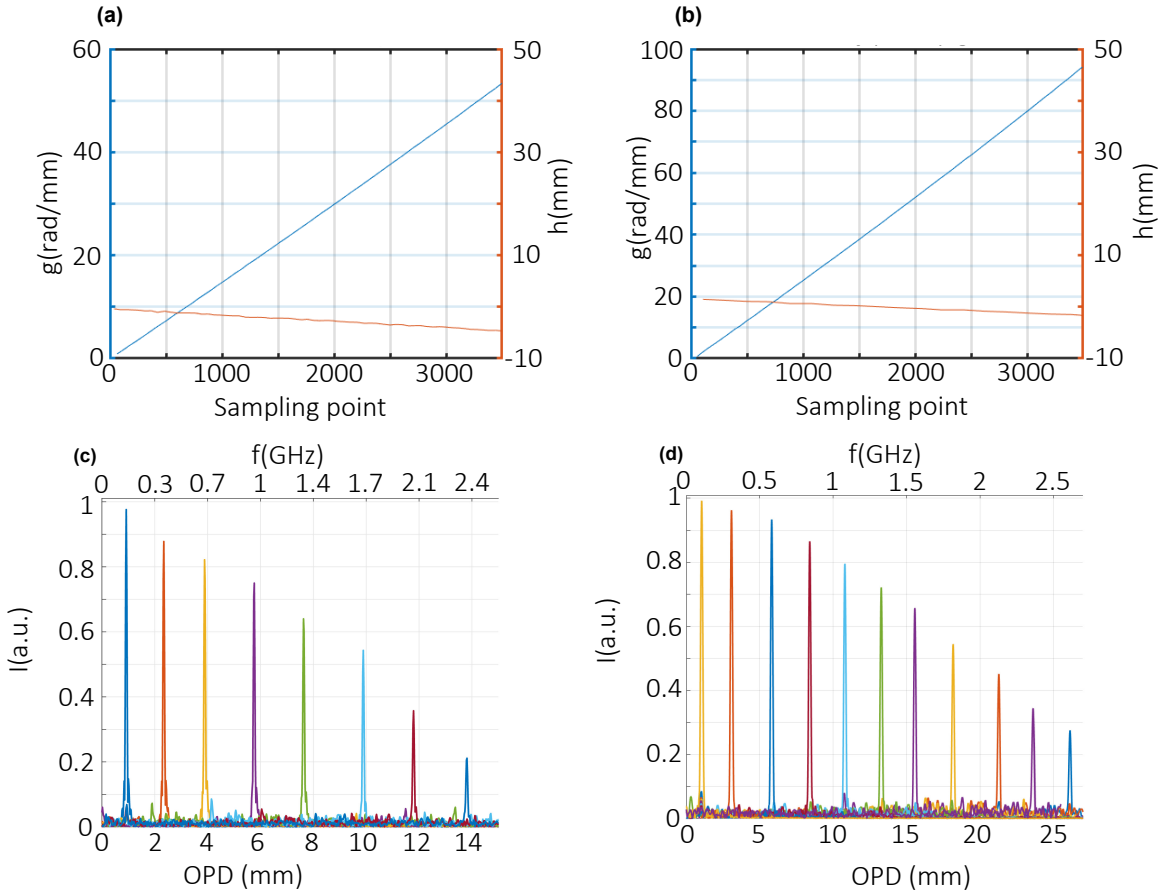

FIGURE 4.10: Functions $g(k)$ and $h(k)$ for (a) one-way and (b) two-way system. Roll-off for the (c) one-way spool system, and (d) two-way system.

axial resolution and axial range; for that, a graph with the roll-off is usually useful. The roll-off graph is created by acquiring the interferometric signal at different OPDs. Here, the OPD is varied by actuating during the translation stage of the collimator. Figure 4.10 (c,d) show the sensitivity roll-off for one-way and two-way systems, which is essential in determining the axial range. An axial resolution of $30\mu m$ is measured for both systems, in agreement with the theory as for $\Delta z = 0.64\lambda_0/\Delta\lambda = 29\mu m$, assuming a flat top, where the $1\mu m$ might arise from a difference in the spectral shape. An axial range at 6 dB of 13.7 and 26.3 mm is measured for one-way and two-way systems, respectively. Comparing the stretching stage, the two-way system allows the extraction of deeper information. For the same OPD value, the modulation frequency of the channelled spectrum is lower for wider stretching.

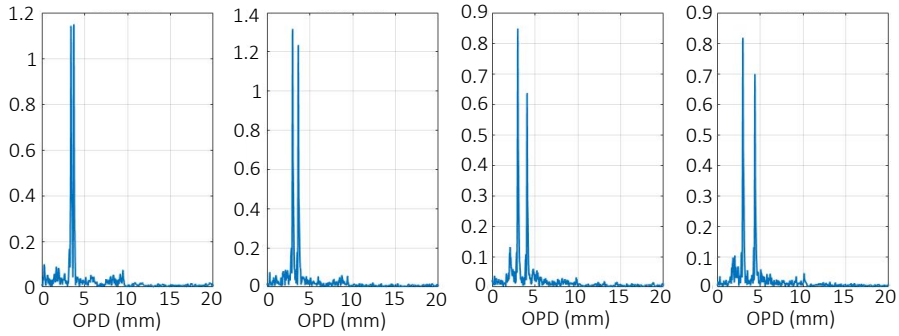

FIGURE 4.11: A-Scans obtained with different width glass plates in the reference arm. Two peaks regarding each surface are shown.

OCT capabilities are demonstrated using a glass plate in the reference arm. Four different glass plates of 0.35 mm, 0.7mm, 1mm, and 1.35 mm have been used to obtain the A-Scans through the intersection with the beam shown in Fig. 4.11. Two peaks from the glass-air interface can be seen, separated by the corresponding OPD of the glass thickness.

4.2 Conclusion

This chapter presents a swept source based on a mode-locked laser in addition to two dispersion measurement techniques. In order to build the mode-locked laser, two novel dispersion techniques have been presented to initially characterize the dispersion of the erbium-doped fibre used inside the laser. The methods have been useful for measuring the dispersion coefficient of SMF-28 fibre; although both have given experimental results in agreement with manufacturer data, they exhibit disadvantages worth mentioning. At first, the technique using the interferometric signal and making the difference between the peaks in the optical spectrum versus the time domain highly depends on the acquisition system. Its resolution can be improved by using high-speed photodetectors and high-precision optical spectrum analyzers, which might make it expensive for accurate measurement. The second dispersion measuring technique, a simpler and lower-cost alternative, uses a voltmeter as a measurement tool. This dispersion

measuring technique is able to sense lower dispersion coefficients as stated in Section 4.1.2, by applying high frequencies (order of few-GHz) to the intensity modulator. Specifically, in this work with the equipment used, the phase technique is $\simeq 40$ times more sensitive than the interferometric technique since the interferometric technique can sense $D(\lambda)L = 1,750$ ps/nm while the phase technique can sense $D(\lambda)L = 44$ ps/nm. On the other hand, the second dispersion measurement technique highly relies on the stability of the mixed signals; if both signals are stable in amplitude, then the change in the mixing output will only depend on the phase change. Otherwise, the phase measured will be distorted by the changes in amplitude. Overall, the two techniques presented are unreliable for measuring the dispersion in environments where either the dispersion coefficient is too low or the amplitude of the photodetected signal is unstable. However, they might seem useful when passive fibres are used. After further reviewing the literature, we decided that the dispersion added via the erbium-doped fibre might be negligible compared with SMF-28 fibre, and the mode-locked laser was built based on that.

The fibre laser was operating at a central wavelength of 1550 nm. This employed an Erbium-doped fibre amplifier, a polarisation-sensitive isolator, and a spool of SMF-28 fibre, whose length has been varied. Different repetition rates and bandwidths were achieved by adjusting the cavity length, ranging from 0.9 to 9.65 MHz and 33 nm to 67 nm bandwidth at 3 dB. However, the instabilities in the laser amplitude made it difficult to operate. Furthermore, the polarisation controllers were actuated each time the laser was started until mode-locking was found for specific power and total fibre length conditions. In practice, this starting operation mechanism is not practical since feedback is needed each time between the polarisation controller and the laser output. In the future, control tools should be added to the laser to ensure stability over time. Regardless of the starting mechanism, pulses were stretched using two different alternatives, resulting in durations of up to 240 ns in the best case, effectively yielding sweep

rates of 4 MHz (i.e. 9.65 MHz repetition of the seed laser with a 41% duty cycle). The significant stretching enabled an axial range of 25 mm, which was made feasible by employing DCF due to its high dispersion-to-loss ratio.

Chapter 5

Demonstration of fast scanning with multi-MHz swept sources

This chapter shows the use of a supercontinuum time-stretched swept source for OCT. As the repetition rates substantially increase from commercial devices, new challenges must be overcome for multi-MHz generation. Here, we present two assemblies capable of utilising lasers tuning at multi-MHz rates: (i) a set-up where characterisation of a fast moving object along the line of sight is performed and (ii) an OCT system where lateral scanning is achieved by driving an ultra fast electro-optic deflector based on a Potassium Tantalate Niobate (KTN) crystal. The challenges raised by polarisation effects combined with signal processing at GHz are presented and discussed.

Contents

5.1 Introduction

Ultrahigh-speed swept sources require new methods for acquiring and processing data in real-time. Once a multi-MHz swept source is made functional, there are several challenges to address in order to acquire and process the data. For instance, a multi-MHz swept source produces interferences of $f_{interf} = M \times f_{sweeprate}$, being M the number of cycles in the spectrum and $1/f_{sweeprate}$ the sweep time interval. As an example, for $1/f_{sweeprate} = 1\mu s$, assuming an OPD that gives $M > 1,000$, over 1 GHz signals are generated. A balanced photodetector unit with multi-GHz bandwidth is required in such cases. As the swept source presented here has a central wavelength of 1060 nm, the responsivity should be high around the central wavelength. However, no balanced photodetectors are reaching many GHz at 1060 nm. Hence, the balanced photodetector used, (based on InGaAs and optimised for 1550 nm by Optilab), may not have optimal responsivity at 1060 nm. Moreover, the real-time processing of such systems requires optimization for all the stages and elements involved: laser, triggering, sampling rate, etc. Even after optimisation, live streaming data at such high frequencies becomes difficult. Therefore, a new software that allows the generation of complete volumes in post-processing must be developed.

On the other hand, a multi-MHz swept source for OCT should fulfil the following requirements: (i) Relative intensity noise (RIN) lower than conventional supercontinuums which exhibit even more than 20% [207]; (ii) sufficient broadband spectrum (iii) phase stability for OCTA mechanisms; and (iv) multi-MHz repetition rate. In principle, low-noise supercontinuum sources should be able to fulfil all of the above. In a supercontinuum generation by coherent process [208], the intensity noise from the seed pulse is transferred to the intensity noise of the supercontinuum produced. Therefore, a low noise mode-locked laser will generate a low RIN supercontinuum. Production of low RIN supercontinuum sources are beneficial for OCT imaging, already subject to sensitivity limitation due to excess photon noise (EPN).

5.2 40 MHz Swept-Source

Author's Note: The work presented above is part of a collaboration with PhD Student Sacha Grelet from NKT Photonics, a partner in the NETLAS Consortium.

SG has designed, built, and done the initial characterisation of the swept source presented here. AMJ and SG have designed and built the interferometer. AMJ has developed the scripts for RIN, roll-off, and the procedure to generate images from the acquired interference using CMS. AMJ has characterized the swept source for OCT proposes. AMJ and SG have together integrated the swept source into the interferometer. AMJ and SG have acquired the images of the tape together with the chopper. AMJ built and optimized the KTN scanner. AMJ acquired and processed the volumetric images from the coin.

The work presented here is part of peer-reviewed papers [1,2] and a conference proceeding [2].

The swept-source used in this work is a supercontinuum followed by a time-stretcher. Figure 5.1 shows that a mode-locked laser pumps a highly nonlinear fibre (HNLF), generating a coherent supercontinuum. The supercontinuum is then stretched by a long dispersive fibre and amplified by pumping a ytterbium-doped fibre.

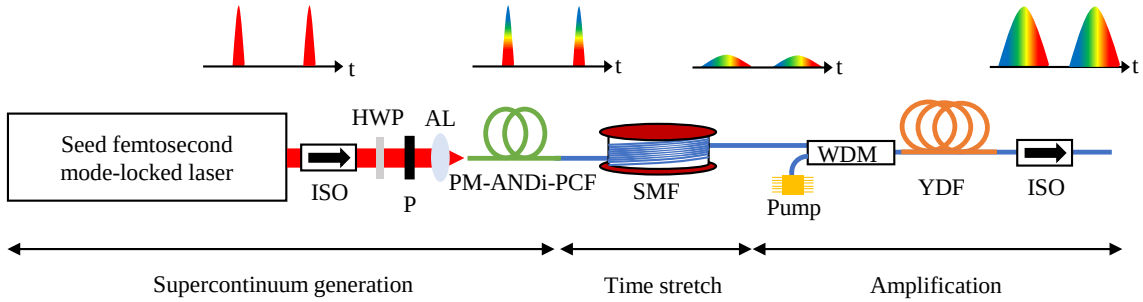

FIGURE 5.1: Schematic of the swept-source and depiction of pulse evolution throughout the system. ISO, isolator; HWP, half-wave plate; P, polariser; AL, aspheric lens; SM, single mode fibre; WDM, wavelength division multiplexer; YDF, Ytterbium doped fibre.

In this case, the HNLF is a photonic crystal fibre from NKT Photonics (NL-1050-NEG-1-PM, NKT Photonics). The fibre is PM with all normal dispersion over the pumping wavelength. The pulses used have a pulsewidth duration of about 180 fs. Once the supercontinuum is generated, a long single-mode fibre is used for stretching in time the spectral components generated. The initial low-noise mode-locked laser, an Origami 10 LP, had a repetition rate of 80 MHz, a central wavelength of 1030 nm, and 180 fs pulse duration. The amount of dispersion should be computed considering the period of the laser and the broadband spectrum generated in the supercontinuum process.

However, the Origami 10 LP failed after one month of use. Therefore, the laser was replaced with a similar Origami 10LP with a lower repetition rate and the same central wavelength. A total length of 2.7 km of 980XP fibre is used. The dispersion of the stretching fibre at 1060 nm is $D\,(\lambda = 1060\ nm) = -47.4\ \frac{\text{ps}}{(\text{nm}\cdot\text{km})}$ which after 2.7 km corresponds to a 10 ns stretch. The 2.7 km of stretching fibre leads to 6.5 dB losses in the middle of the spectrum and around 9 dB on the edges, with lower wavelengths suffering more losses than longer ones. Because of this, only 2.9 mW is left in the fibre. Therefore, output power must be amplified to compensate for further losses in the interferometer. An amplifier consisting of 50 cm of ytterbium-doped fibre and a pump diode of 100 mW at 980 nm is used. Due to the non-modulated pumping and the response time of the Ytterbium fibre, it is

expected to obtain excess noise. Moreover, the achievable bandwidth is reduced due to the limited bandwidth of the Ytterbium fibre. After the amplification stage, the swept source is ready to operate.

5.2.1 Swept-Source characterization

The excess photon noise on the OCT is directly linked to the RIN of the swept source. Therefore, the RIN is experimentally investigated for the swept-source built. Commonly, the RIN is obtained by measuring the intensity variations while filtering a part of the spectrum [176]. Since such filters were not available, we decided to perform an analogue measurement that recorded 1,000 consecutive channelled spectra using a mirror as a sample and then transferred from the time domain to the spectral domain via the time stretcher. A profile of the envelope of each channelled spectrum is obtained along each wavelength. Using these envelopes, the RIN is then calculated for each spectral point as follows:

$$\mathrm{RIN}\left(\lambda\right) = \sqrt{\left\langle \left(\left|\hat{A}\left(\lambda\right)\right|^2 - \left\langle \left|\hat{A}\left(\lambda\right)\right|^2 \right\rangle \right)^2 \right\rangle} / \left\langle \left|\hat{A}\left(\lambda\right)\right|^2 \right\rangle \tag{5.1}$$

It is worth noticing that the RIN measured here arises not only from the SCG but also from a combination of SCG, stretcher, and variations of the interferometer. In Figure 5.2, the RIN of the source is shown. A RIN of $\sim 3-4\%$ is obtained across the FWHM bandwidth, comparable with previous results of ANDi supercontinuum [176]. Compared with a conventional supercontinuum, based on anomalous dispersion [161], these results show the benefit of the new dynamics used. Moreover, the RIN spectrum does not exhibit characteristics of incoherent broadening mechanisms induced by Raman scattering or polarisation modulation instability [209, 210], and agrees with the theoretical results. It is, therefore, characteristic of low-noise ANDi supercontinuum dynamics, confirming that both the seed laser and nonlinear broadening process exhibit relatively low noise.

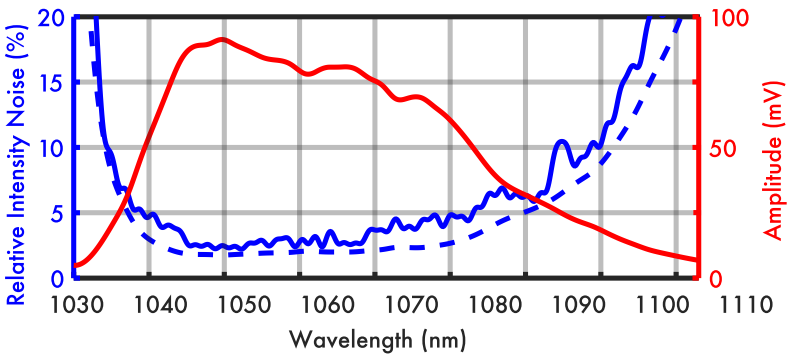

FIGURE 5.2: **RIN system characterization.** Experimentally measured relative intensity noise (in blue) for 1,000 consecutive channelled spectra with the detector limit (dotted blue) and the averaged channel spectrum envelope (red).

5.3 Complex Master Slave

CMS OCT, extensively described in [43, 206], was used to reconstruct the depth information. This method consists of two main stages: a calibration composed of three steps and OCT image production in a final step [43, 206, 211]. In the calibration, (i) a set of channelled spectra equidistant in OPD between them are acquired (minimum 2) within the axial range of the OCT imaging system. (ii) From this set of channelled spectra, the functions representing the nonlinearities, $g(k)$, and dispersion of the system, $h(k)$, are computed. (iii) Afterwards, a set of theoretically inferred channel spectra, also called here, "masks" are generated. These are, in fact, similar to those otherwise obtained by experiment at many other depths, i.e. this procedure infers channelled spectra modulation at any other depth of interest without the need to repeat their experimental acquisition.

Once the calibration is finished, the mirror is replaced with the sample under investigation, and the channelled spectra obtained are multiplied over the wavenumber by each of the masks previously generated, obtaining for each multiplication the amplitude of the A-Scan at the depth of the mask. This multiplication can be described by a product between a matrix M containing the masks,

and the vector $I(k)$ containing the channeled spectrum:

$$\begin{bmatrix} A(z_1) \\ \vdots \\ A(z_N) \end{bmatrix} = \begin{bmatrix} M(t_1, z_1) & \cdots & M(t_\tau,\ z_1) \\ \vdots & \ddots & \vdots \\ M(t_1, z_N) & \cdots & M(t_\tau, z_N) \end{bmatrix} \begin{bmatrix} I(t_1) \\ \vdots \\ I(t_\tau) \end{bmatrix} \tag{5.2}$$

with $A(z)$ the CMS-OCT signal corresponding to the depth z, N the number of synthesized masks and τ the number of sampled points over the channeled spectra, which depends on the acquisition sampling rate. This methodology has been applied on every configuration of this chapter.

5.4 Non-Scanning system

5.4.1 OCT Characterisation: Non-PM and symmetric configuration

As depicted in Figure 5.3, the system characterisation involves utilizing a reflective interface located at the sample position. Apodization is applied to the generated masks using a Hamming function. This setup yields an axial resolution of $12\mu m$ in air, approaching the limit of $10.3\mu m$ set by a spectrum width of 48.2 nm.

Due to considerable loss across the symmetric interferometer, the photodiode did not reach saturation, indicating that the measured signal-to-noise ratio (SNR) equals the system sensitivity. Using a theoretical model in which the sources of noises are shot noise, detector noise and excess photon noise [212], we found the theoretical maximum sensitivity in our setup to be 72 dB. Compared to OCT systems operating at hundreds of kHz to MHz sweep rates, which typically have a shot-noise limited sensitivity higher than 90 dB, the short integration time due to high-speed imaging poses a significant barrier [37, 71].

We determine the receiver noise to be 51 dB by measuring the balanced detector noise without optical power, as shown by the red line in Figure 5.3(a). The

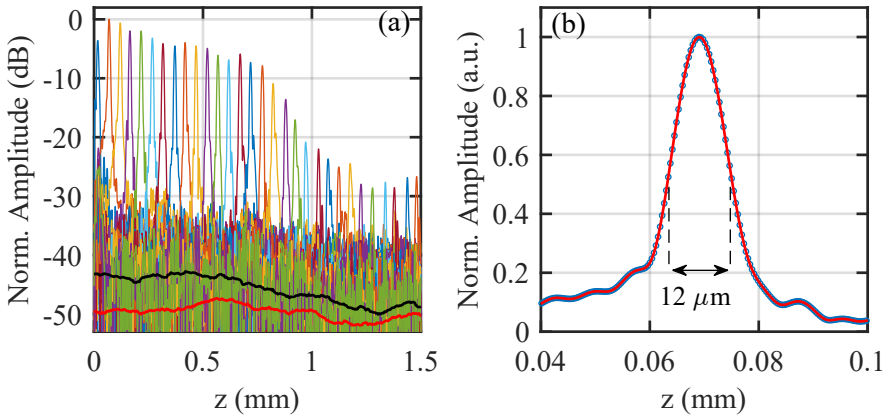

FIGURE 5.3: OCT system characterization. (a) A-scans for different OPD values. The bottom black and red lines are, respectively, measurements of the system noise floor and the detector noise. (b) A single A-scan showing an axial resolution at FWHM of $12\mu m$ in air.

noise floor increases to 41 dB when increasing the input optical power to the interferometer, illustrated by the black line in Figure 5.3(a), suggesting that receiver noise is not the primary noise factor. Furthermore, this value, below 72 dB, affirms that the system is not limited by shot noise. We, therefore, attribute the 41 dB sensitivity to excess noise generated by amplified spontaneous emission in the amplifier [108] and minor wavelength-dependent imbalance within the couplers, leading to inefficient noise cancellation at the balanced detection output. We note that noise from amplified spontaneous emission in the amplifier is an incoherent source that cannot be eliminated by balanced detection [213]. Figure 5.3 (a) shows the sensitivity roll-off, obtaining a -9 dB/mm ratio, with an axial range of -6 dB of 0.67 mm. The axial range obtained at -6 dB is calculated as:

$$z_{-6dB} = \frac{\ln(2)}{\pi} \frac{\lambda_0^2}{\delta\lambda} \tag{5.3}$$

where λ_0 is the central wavelength, $\delta\lambda$ is the spectral linewidth calculated as $\delta\lambda = 1/(|D|\, LB_{scope})$, with $|D|\, L$ the dispersion in the time stretch (respectively the fibre dispersion and length), the sampling rate B_{scope} [3, 214]. An axial range at -6 dB of 0.67 mm agrees with the experimental result.

5.4.2 Results on non-scanning OCT

In order to prove the benefit of using a fast laser, we decided first to obtain an A-scan from a fast-moving target. A symmetrical array consists of three couplers with a 50/50 ratio. The configuration can be used for balanced detection since two outputs preserve a π phase difference between them. As can be seen in the schematic of Figure 5.4(a), port A is used for the light source, port E is used for the reference arm, and port E' for the object arm, finally, the ports B and B' are used for the balanced photodetector. A 23 GHz balanced photodetector is used to capture the signal. Figure 5.4 (b) shows a picture of the sample arm configuration; a mirror behind the chopper is used to calibrate and obtain speed information about the chopper.

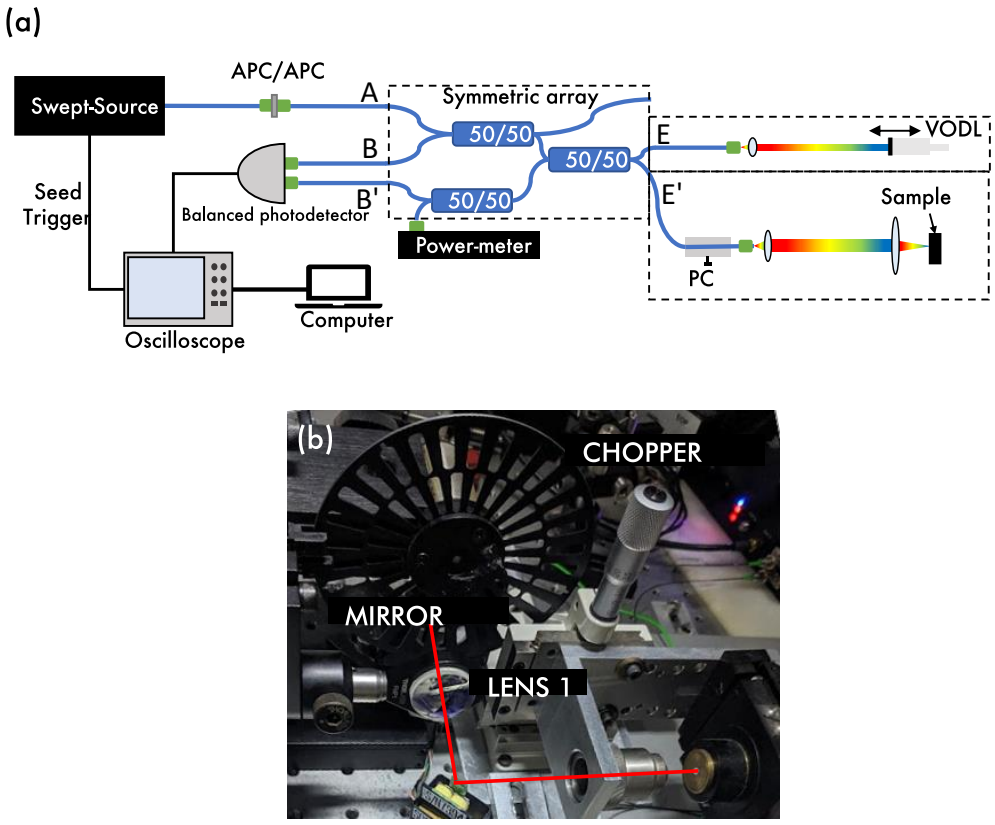

FIGURE 5.4: (a) Experimental set-up of the OCT system. APC angled polished physical contact fibre connectors; PC, polarisation controller; VODL, variable optical delay line. (b) Photo of the sample arm of the test system. Including a chopper with a mirror behind it. The focal length of the lens is 50 mm. The red line describes the beam path.

It should be noted that the amount of data in the experiment later described

makes real-time OCT processing complicated. Understanding real-time OCT as the time to transfer and compute the volumes less than the time of the sweep, i.e. $t_{sweep} < t_{transfer+processing}$. The data is stored in the oscilloscope and then transferred to a computer. The connection between the host computer and the scope is made by ethernet cables Cat 6, which allow for 1 Gbps transfer speed. However, writing the data on the hard drive and then reading the data in Matlab takes a few seconds. In this situation, i.e. post-acquisition, CMS processing presents similar performance with Fourier transform processing [43] with the benefit of being able to correct for dispersion.

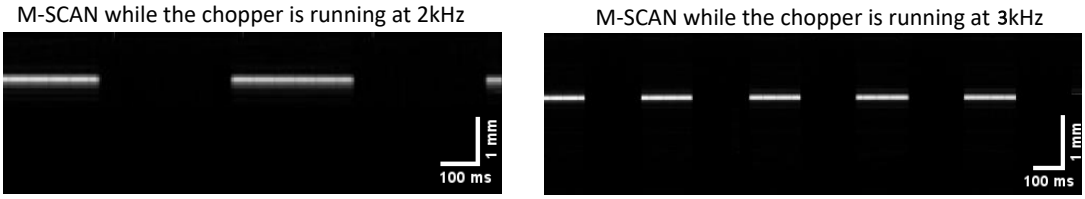

FIGURE 5.5: M-Scan of a mirror placed behind the chopper. (a) Chopper running at 2 kHz. (b) Chopper running at 3 kHz.

Before capturing the interferometric signal from multiple scattering objects, the speed of the chopper was characterized. In this configuration, the beam is not moving laterally; however, the mirror is placed behind the chopper disk. Figure 5.5 (a),(b) show the M-Scan of the chopper rotating at 2 kHz and 3 kHz. After the speed of the chopper is known, the sample is placed on top of the holes. Figure 5.6(a) shows that the sample comprises optical, crystal, and metallic wire. The bespoke design of the sample is determined by the need to demonstrate the depth capabilities of the system at high-speed moving objects.

Figure 5.6(b) shows 12,000 consecutive A-scans recorded in 0.3 ms. In the first and second areas marked by yellow and orange arrows, the optical tape is recognisable by the 3 interfaces between the air, the adhesive layer (1), the backing film (2) and air again. The respective thickness of the tapes is measured to be $69\mu m$ and $40\mu m$. This matches the expected equivalent distance in the air (calculated to be 61 μm and $43\mu m$) that considers the refractive index of these materials.

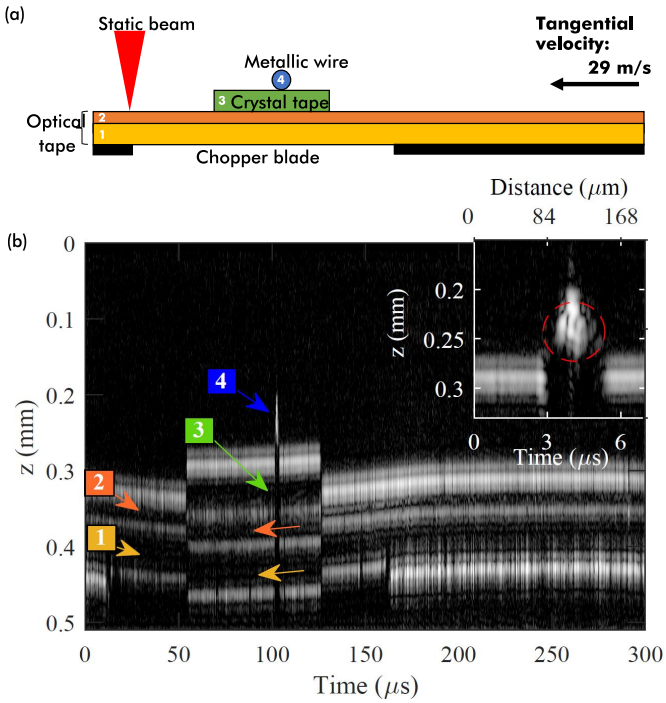

FIGURE 5.6: Imaging of fast-moving objects. (a) Representation of the sample used. Several objects are imaged: (1) an Adhesive layer and (2) a backing film of an optical tape covering the whole surface of a rotating chopper disk, (3) a Short piece of Crystal tape, (4) a $70\mu m$ metallic wire. (b) OCT image. The insert is a zoom on the area 4. A circle in red dots with a $70\mu m$ diameter is plotted for scale.

In the third area marked by the green arrow, one small piece of Crystal tape is measured, with a thickness of $67\mu m$ ($66\mu m$ calculated). The high sweep rate of the laser allows for the sharp detection of the edges of the fast-moving piece of tape while performing precise depth measurements of the four interfaces.

Finally, the metallic wire can be identified in the fourth area marked by the blue arrow and presented in the inset. Significantly, one can note that the $70\mu m$ metallic wire, measured over a $2.4\mu s$ range in the B-scan, contains 96 consecutive A-scans, indicating significant oversampling.

The experimentally implemented SS-OCT system presented here demonstrates the great potential of akinetic swept sources, and in particular, of those based on the method of spectrally broadened mode-locked lasers that use all-normal-dispersion supercontinuum dynamics. While this method is currently more expensive and bulkier compared to other solutions (FDML, MEMS-VECSEL), it

presents flexibility in allowing to precisely target the A-scan rate, axial resolution or axial range depending on the application.

Multiple possibilities can be investigated to overcome the current limitations. While a regenerative amplifier was needed in this case due to the low average power after stretching, new optical fibres with high normal dispersion could allow better compromise between losses and dispersion. Additionally, alternative stretching methods such as chirped fibre Bragg gratings can give less loss than optical fibre at $1\mu m$ and/or greater stretching, which combined with a lower repetition rate mode-locked laser, could lead to better sensitivity. Finally, further studies could benefit from a different interferometer design based on asymmetric configuration for better optical power management. The reasons above demonstrate high potential toward extending the capabilities of swept source technology.

5.5 Fast scanning system

Multi-MHz swept sources produce millions of pulses per second. However, to make use of these pulses, the scanning system must be fast enough to avoid high oversampling. One choice would be to use resonant scanners since they are faster than galvanometer scanners. However, their speed is still in the range of few kHz, which might be useful for few-MHz but insufficient for multi-MHz swept sources. For that reason, deflectors based on electro-optical means provide a faster alternative than resonant scanners. Some of the potential benefits are listed below:

a) The small single-volume acquisition time is beneficial for phase-sensitive OCT, in which tiny displacements are captured via the phase shift between consecutive channeled spectra. Therefore the phase of the source should be stable over the B-Scan integration time.

b) An exciting application of high-speed is 4D-OCT (3D + time), the continuous real-time visualization of the three-dimensional sample structure. First, this provides a means to accurately study the time-evolution of the sample structure, for instance in biology. Second, the real-time 3D coverage can have similar field-of-view and resolution as (scanning-laser) microscopy, while additionally providing views of layers inside the sample. Hence 4D-OCT may replace or augment existing microscopy solutions.

5.5.1 KTN crystal

OCT employing a few-MHz sweeping rate lasers have already raised the interest in ophthalmology due to their real-time applications: although multi-MHz still have some challenges to overcome. Here we have used a KTN crystal as a scanner. KTN crystal is an oxide crystal consisting of potassium (K), tantalum (Ta), and niobium (Nb).

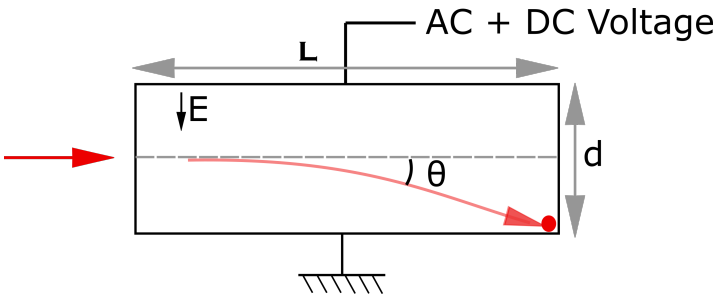

FIGURE 5.7: **KTN Crystal sketch**. L: Length of the crystal, E: Electric field applied, d: height of the crystal, θ: angle covered by the deflection of the beam.

A pair of firm electrodes are placed opposite in the crystal. The dimensions of the crystal, d for the height and L for the length, together with the voltage applied define the maximum deflecting angle that can be used [215], in our case $\theta = 62$mrad. The deflection of the beam is achieved by a non-uniform charge distribution along d. As explained in [216], the optical path length s of the crystal is modulated via the electro-optic index modulation of Δn, defined as:

$$\Delta s = \Delta n L = -\frac{1}{2} n_0^3 g \varepsilon^2 E^2 L \tag{5.4}$$

where n_0 is the original refractive index, ε is the permittivity and g is the second order electro-optic coefficient. If E is an electrical field spatially non-uniform, Δs is also non-uniform. Due to the variation of the refractive index along L, the deflection angle θ is expressed as:

$$\theta = \frac{d}{dx}(\Delta s) = -n_0^3 g \varepsilon^2 L E \frac{dE}{dx}. \tag{5.5}$$

Assuming that the electric field E and charge density ρ are related by Gauss's law as follow:

$$\frac{dE(x)}{dx} = \frac{\rho}{\varepsilon}, \tag{5.6}$$

then the deflection angle θ can be computed as follow:

$$\theta(x) = -n_0^3 g \varepsilon L E \rho \tag{5.7}$$

Therefore, θ is proportional to ρ; controlling the space charge is a fundamental technique for this deflector type. The space charge is formed by electrons injected into the KTN crystal through the electrode. Because the deflection direction depends on the polarisation of light, the KTN crystals are used with linear polarised light only. Hence when coupled to fibres, as in the current thesis, a PM fibre is used. This also determined employing a PM fibre array, as detailed in Section 5.5.2.

In previous reports, KTN scanners have been mainly used for multiple scanning experiments. Prior reports related to OCT can be classified into three main categories: (i) At first, swept-source that incorporates a KTN crystal into a spectral filter based on ray deflection; as explained in Chapter 3, a deflector with a diffraction grating can act as a wavelength selector. In [147, 217–219], deflectors at rates of 100 kHz have been reported. (ii) Secondly, the KTN scanner has also been used in the sample arm of time-domain systems [220–224]. 200 kHz deflection speed was reported by driving the KTN crystal via a resonant circuit at 100

kHz. This thesis uses a KTN crystal driven at 100 kHz to deflect the laser beam at 200 kHz. (iii) Finally, in order to employ such deflectors efficiently, it is important to be aware of their limitations in lateral scanning, lateral scanning nonlinearity, voltage applied, and polarisation effects. For these concerns, several papers refer to experiments on characterisation of stability and limitations [215, 216, 225, 226].

As detailed above, there is no report on using a KTN deflector in the sample arm of a swept-source OCT. Although there are publications on swept-source generation and on scanning a beam laterally, there is a gap in the literature on the combination of a fast swept source with a fast scanner in an OCT system. This gap appears due to the lack of multi-MHz swept sources allowing several points per B-Scan while fast scanning.

	Galvo-Scanner	**Resonant Scanner**	**KTN Scanner**
Model	Thorlabs, SS30X-AG	EOPC, SC-30	NTT, KTN
Max Stroke Angle (deg)	±20	±20	±3.45
Size Aperture [H x L mm]	30.7 mm x 22.2 mm	10 mm x 10 mm	Fibre coupled
B-Scan Rate	500 Hz	2 kHz	100 kHz
Assuming a lateral resolution	10 μm		
Size of the B-Scan	1 cm		
# resolvable points per B-Scan	200		
# points per B-Scan	80.000	20.000	400
Oversampling factor	400	100	1
Lateral distance between consecutive points	0.125 μm	0.05 μm	5 μm

TABLE 5.1: Comparison between (a) Galvo-Scanner, (b) Resonant scanner, (c) KTN Scanner used with a sweeping laser at 40 MHz.

However, when a real multi-MHz swept source is used, the need for a fast deflector becomes important to avoid oversampling. The system provided here sweeps at 40 MHz. A comparison of the number of points in a B-Scan using three different deflector speeds corresponding to a galvo, a resonant and a KTN, respectively, is presented in Table 5.1. For an optics arrangement of $20\mu m$ lateral resolution, 1 cm lateral size of the B-Scan, only 500 resolvable points are possible.

For the given configuration, a KTN scanner operating at a frequency of 200 kHz will achieve optimal results, i.e. resolvable points.

Oversampling is recommended for fine phase measurements. However, it becomes undesirable when the scanning rate approaches the duration of movement. Oversampling that much can be seen from different perspectives: first, oversampled points do not add extra information; second, transfer, processing and display of such volumes will take several minutes, and real-time imaging is not possible with current computing technology.

5.5.2 OCT Characterisation: PM and asymmetric configuration

Figure 5.8 shows the experimental set-up for the scanning system. The interferometer employs two fibre-based couplers of 25/75 and 50/50 coupling ratios. A total of 25% of the optical power is guided towards the sample via two lateral scanning devices: a KTN deflector (KTN by NTT Advanced Technology Corporation) for fast line scanning; and a galvanometer scanner (6210H by Cambridge Technology) for frame scanning. The deflection angle of the KTN scanner is proportional to the voltage applied by a high-voltage KTN driver (KPS1001CH-00 by NTT Advanced Technology Corporation). The maximum deflection angle is given by the 200 V applied to the crystal, corresponding to 120 mrad. This is fundamentally limited by the thickness of the crystal block [215, 216].

Due to the dependence of the deflection angle on the polarisation state, the manufacturer coupled the KTN crystal to a suitably oriented PM fibre. Therefore, the two couplers in Fig. 5.8 are also made of PM fibre (PANDA PM980 XP by Nufern). This reduces the losses between the interferometer and the KTN output, however the captured light back from the sample may be affected by the polarisation properties of the sample. A cylindrical concave lens compensates for the beam shape distortion; the manufacturer placed the cylindrical lens inside the KTN crystal (not shown in the diagram), which reduces astigmatism and produces a round beam of 1 mm in diameter. This cylindrical concave lens is

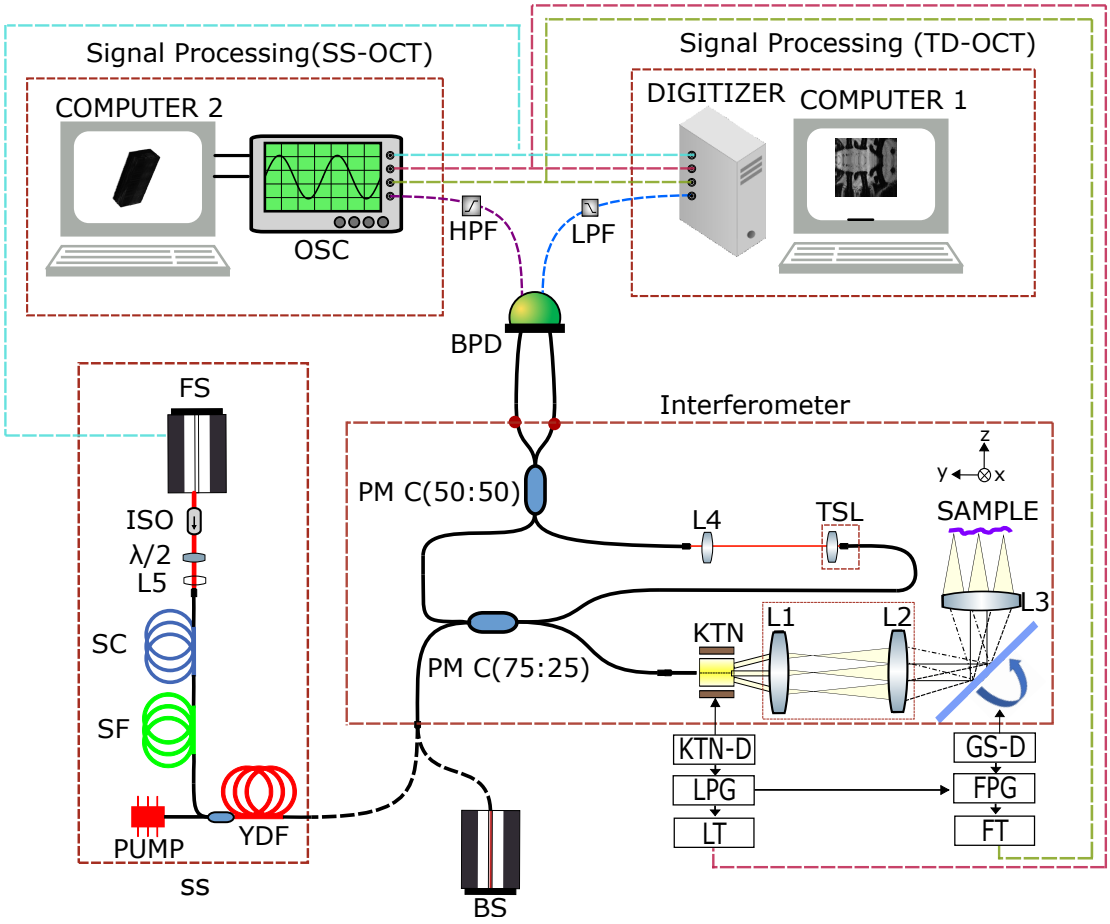

FIGURE 5.8: **Experimental set-up** SS: swept source; Interferometer (KTN: beam deflector using a KTN crystal, GS: galvanometer scanner, PM C: polarisation maintaining couplers, TSL: translation stage launcher); SP: signal processing block (BPD: balanced photodetector, PDS: Photodetected signal, HPF: High pass filter, OSC: oscilloscope, PC: Personal computer); Triggers (LT: line, FT: frame, PT: Optical pulse); Pulse generators (LPG: line, FPG: frame); Drivers (KTN-D: KTN, GS-D: galvanometer scanner). Lenses: L1, L2, L3, L4 and L5 of focal lengths 3 cm, 7.5 cm, 4.5 cm, 1.5 cm and 1.5 cm respectively. All lenses are achromat.

already incorporated in the package containing the crystal. In order to improve the transversal resolution, the beam is enlarged using a telescope made of two achromatic lenses of 30 mm (Thorlabs, AC254-030-A-ML) and 75 mm (Thorlabs, AC254-075-A-ML) focal length. Finally, a 45 mm (Thorlabs, AC254-045-A-ML) focal length lens focuses the fan of rays onto the sample.

Due to the PM interferometer used in the system, the object is excited with a linearly polarised state, which means that the polarisation state of the reflected

wave might come with an induced rotation. Over a sufficient depth in a birefringent target, this rotation can amount to up to 90 degrees, resulting in a lower signal. However, this case corresponds to a very particular orientation of the linear polarisation direction of the object beam with the optical axis of the sample, so in general, the signal should not be attenuated completely.

Polarisation effects can occur and imprint with a regular band structure over the image structure. However, this is equally true for non-polarisation sensitive OCT instruments, whose images are often disturbed by birefringence and display regular bands either in depth or in the *en-face* slice. Total signal cancellation is rare and depends on the coincidence of the appropriate orientation of the material optic axis and the exact depth for 90 degrees of rotation. Before assembling the PM fibre array, a fibre array based on non-PM HI1060 fibres was tested. However, the non-PM fibre array was discarded for the following reasons: i) a PM fibre only preserves the linear polarisation, and since the KTN is sensitive to the polarisation, when using non-PM array, the polarization was random, and more than 80% of the light was not deflected, obtaining at the output two beams from the KTN, one static with 80% of the optical power, and the deflected one with the rest of the optical power, ii) A double image may occur unless a single polarisation is selected.

The output optical signal was collected with a 23 GHz bandwidth balanced photodetector (BPR-23-M by Optilab), producing a photodetected signal (PDS), digitised by a 20 GHz bandwidth oscilloscope (Wavemaster 820Zi-b by Lecroy Teledyne). A high pass filter with a cut-off frequency of 300 MHz was used to eliminate laser pulsations at 40 MHz. Although this is not fully needed, the high-pass filter helps eliminate auto-correlation modulations close to 0 OPD at the cost of reducing the axial range. The oscilloscope data was collected at 40 GS/s and transferred to a PC for processing.

Figure 5.9 illustrates the depth resolution capabilities of the proposed instrument. On Fig. 5.9(a), a raw channel spectra is shown for an OPD=0.4mm. The

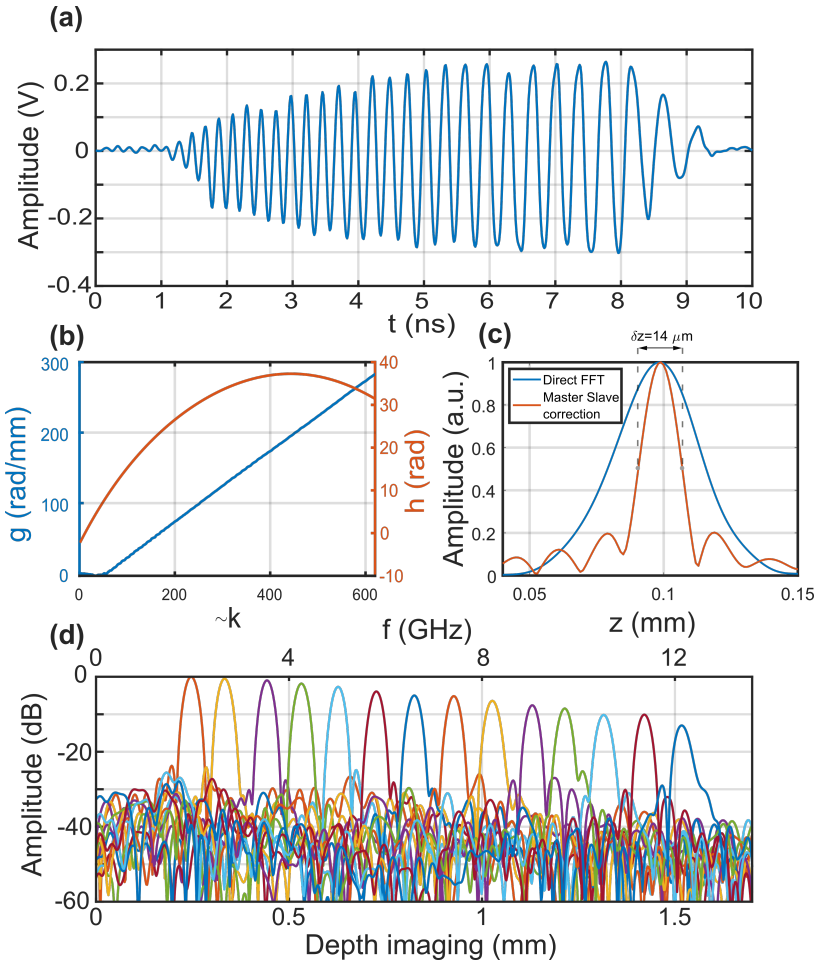

FIGURE 5.9: Calibration: (a) Photodetected signal corresponding to OPD≈ 0.4mm. (b) $g(k)$ and $h(z)$ calibration functions obtained using CMS algorithm. (c) Comparison between the FFT of the uncorrected photodetected signal (blue) and the corrected signal by CMS (red). (d) A-Scans obtained by CMS at 14 different depths.

calibration functions $g(k)$ and $h(k)$ are presented in Fig. 5.9(b). Figure 5.9(b) also shows that the chirp in the channelled spectrum modulation is mainly created by the dispersion, as the $g(k)$ function is almost linear. The axial resolution (see Fig. 5.9 (c)) is evaluated as $\Delta z = 14\mu m$ calculated for a $48nm$ Gaussian shape due to the spectrum shape of the booster. The side-lobes created by the shape of the spectrum are observed in Fig. 5.9 (c). Furthermore, the roll-off is shown in Figure 5.9 (d), which displays constant width across the entire axial range with a sensitivity profile decay rate of 8 dB/mm. Therefore, an attenuation of 6 dB is obtained for an axial range δz of $0.61mm$ in depth along the axial coordinate z. Near $OPD = 0$, a signal-to-noise ratio of $\simeq 45dB$ is achieved.

5.5.3 Acquisition procedure

Due to the difficulties of real-time processing, a new software had to be developed for post-processing. The interference signal should ideally be recorded at the maximum sampling rate. The 20 GHz oscilloscope has 4 inputs; however, in default mode, the 4 inputs can be used with a sampling of 40 GSa/s. Alternatively, 2 inputs can be combined into only 1 with a sampling rate of 80 GSa/s. In the case of this work, only three channels are available.

The process from acquiring the data follows three main steps, which have to be carefully adjusted: (i) At first, the whole volume is acquired at once using a trigger from the slow scanner, which consists of 3 channels, two at 40 GSa/s, and one at 80 GSa/s. As the photodetector has a bandwidth of 20 GHz, sampling at 40GSa/s is necessary. If all 3 inputs are digitised within a 12-bit range, a total of 12.6 GB of data is created. Therefore, the acquisition is followed by a long time saving for the local hard drive. In addition to sampling the photodetected signal, the other two channels are used for the fast and slow scanner triggers. To synchronise the display, triggers are also acquired for each lateral fast scan (hence in sync with the KTN scanner) and for each frame start (in sync with the slow scanner).

(ii) Once the data is transferred to an external computer, the numerical array containing the whole volume is cropped assuming a constant frequency of the swept source. However, this is not true, and jittering correction has to be applied, shifting the channel spectrum until all consecutive channel spectra match. Without the help of any external pulse trigger, this process is fully manual and might induce additional mismatches. Therefore, high-precision matching between acquired calibrated masks and experimental channeled spectra is not possible. (iii) Finally, after applying the shifting correction, each channel spectrum is inserted into a matrix to be used as per the CMS algorithm.

Time budget for each step

The laser system described here can generate sweeps every 12.5 ns, which, together with the scanning system, a raster consisting of 500x250 points, is doable in 2.5 ms. However, there is a cost associated with acquisition, saving, and post-processing. The acquisition time will depend on the density of points (i.e. sampling rate) and the strategy used for acquiring the data. In our case, we choose to acquire the 2.5 ms without interruption. This strategy is clearly different from the one used in real-time systems, where the data is acquired sweep by sweep, calculations are done, and the image is displayed without saving, unless it is requested. The acquisition and saving times together also depend on the format that the data is saved, here we used a format known as .trc, which is a binary format in 16 bits. This selection takes approximately 30 seconds to save 2.5 ms using the WaveMaster 8 Zi-B oscilloscope. Once the data is saved, it has to be transferred to the computer, which, using an Ethernet cable configuration and assuming a 1 Gbps connection speed and 4.5 GB of data size, will take 36 seconds. However, the worst bottleneck in this system occurs in the post-processing; large binary files are slow to open, and the custom script designed here takes an average of 15 minutes to open, crop and generate the volume from the raw data. Ideally, parallel processing and time-effective software should be designed for future occasions. However, the creation of this software is not part of the scope of this thesis. In summary, with the current setup, displaying a 2.5 ms volume takes approximately 17 minutes, which can be reduced significantly by hardware and software optimization.

Depending on how the system is used, one may consider showing only B-Scans for faster feedback. Only one B-Scan might be able to be displayed in just a few seconds. In many applications, the interest is given by the difference in consecutive B-Scans; therefore, no volume processing is needed. Alternatively, for topography scanning, the sampling rate could be lowered according to the desired

maximum axial range, making the datasets less dense and, therefore, smaller. The following section outlines a strategy for achieving real-time feedback through a TD-OCT complementary system.

5.5.4 Complementary TD-OCT for real-time operation

The configuration used for swept source detection allows for time domain detection with minor modifications, as seen in Figure 5.8. The swept source is replaced with a broadband continuous wave source (ALS-1050-S, Amonics). In order to create an image, the optical path difference (OPD) between the reference and sample arm must be zero, which means that the reference arm is adjusted to reach zero OPD. Dedicated software for the time domain is used to generate *en-face* images in real time. The images from the time domain system allow the correct alignment of the sample before switching back to the swept source. Due to the lack of real-time display in the SS-OCT, the *en-face* from TD-OCT provides sufficient guidance in positioning the sample before acquiring volumes later using the SS-OCT system. The lateral resolution is similar in TD to that obtained using the SS since it mainly depends on the optical design, and the emission bandwidth of the source is similar. Therefore, this is evaluated using *en-face* images of a USAF target in the TD-OCT regime.

Figure 5.10 shows an *en-face* of scanning a reflective USAF Target 1951 (R3L3S1PR, Thorlabs). Figure 5.10 (a) displays a resolved element where the bands are visible. On Figure 5.10 (b) an *en-face* from group 4, element 6 is shown. It can be noticed that the horizontal and vertical resolvable resolutions are different, which we accuse to the astigmatism created by using a cylindrical lens inside the KTN package. Figure 5.10 (c) and (d) show the profile for the vertical and horizontal yellow lines, respectively.

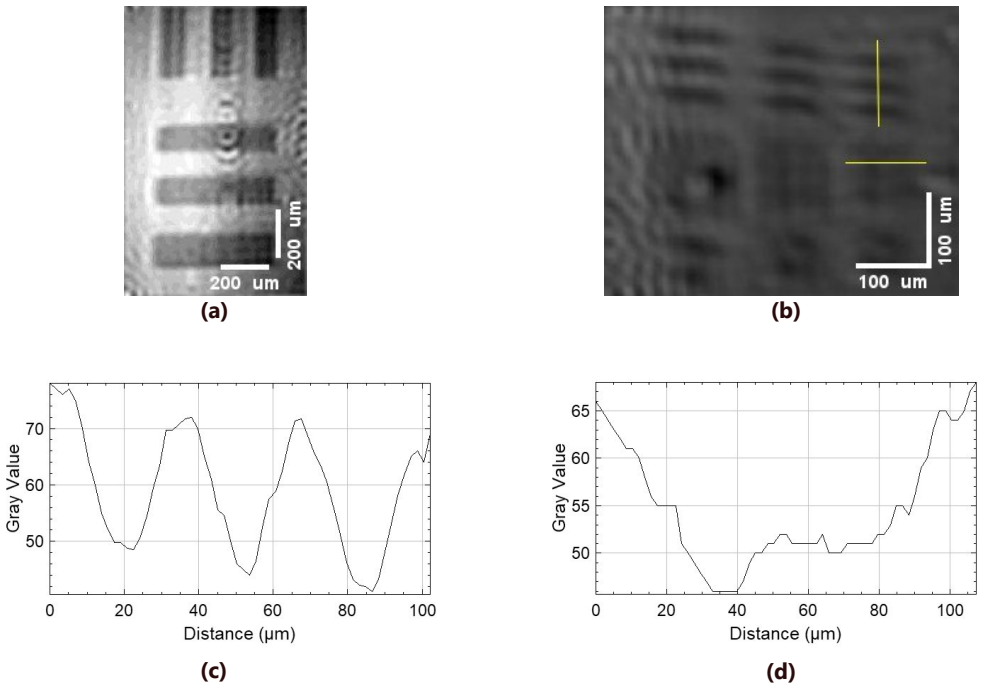

FIGURE 5.10: Reflective USAF Target (a) *En-face* image Group 1 Element 6. (b) *En-face* image, Group 4, Element 6. (c) Vertical yellow line profile from (b). (d) Horizontal yellow line profile from (b).

5.5.5 Results on fast-scanning OCT

Since the sensitivity is currently insufficient to produce images from biological scattering samples, the imaging capability is demonstrated on a coin.

To perform imaging, the KTN driver delivered 200 V amplitude sinusoidal driving voltage at 100 kHz, producing a full deflection angle of 124 mrad which covered 2.95 mm along $X-$direction. The raster formed by the two scanners comprises N_y lines, with each line consisting of N_x points. The lateral resolution, measured using a USAF target, is $23\mu m$ in the $x-$direction and $18\mu m$ along the $y-$direction. The different resolutions along the x and y axes are expected due to imperfect compensation of the beam astigmatism introduced by the KTN crystal, only partially reduced by the cylindrical lens installed by the manufacturer at the output of the KTN crystal. The wavefront in the sample is then not isoplanatic due to the scanning deflectors. As the resolution of the system is in the order of 15-20 μm, the isoplanatic condition is not strictly necessary as it could be in adaptive optics systems. These lateral resolutions are similar to those previously

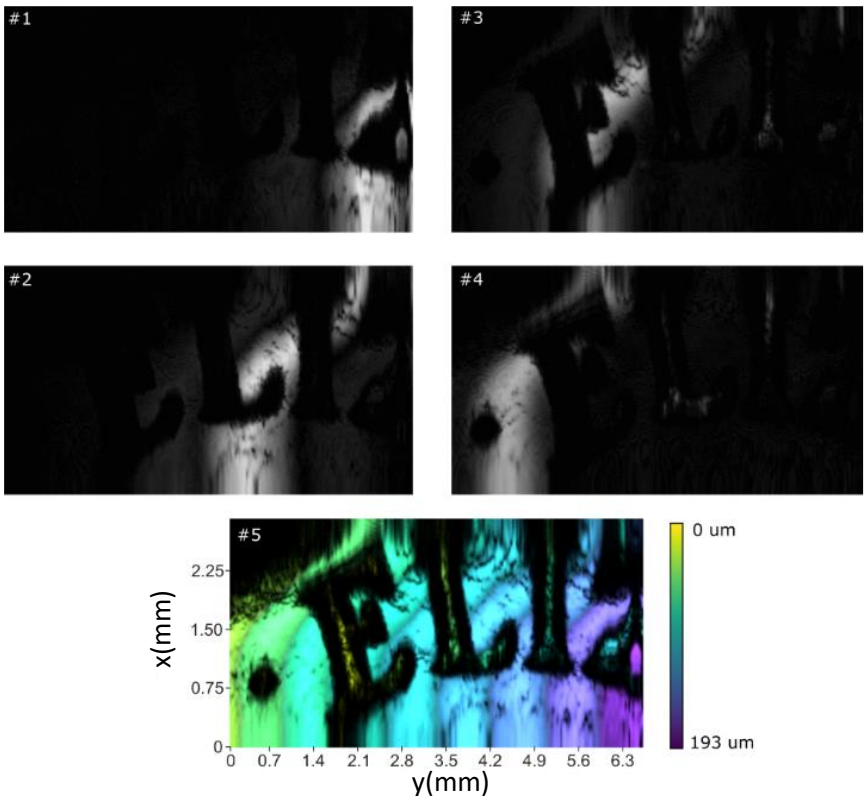

FIGURE 5.11: **Raw *en-face* OCT images.**(1-4) OCT images from different Z coordinate values separated by 40 μmm along the Z direction. (5) Superposition of 10 images separated by 10 μm along Z-direction, where the height position along Z is colour-coded. Black colour means no signal

reported using a KTN crystal for sample beam scanning [220, 221]. The image is limited along X due to the limited size created by the KTN deflector, hence to cover a larger area we increased the image size along Y to 6.6 mm by driving the frame galvoscanner with an amplitude of 2.5 Vpp. Driving the galvanometer-scanner with a sawtooth signal at 400 Hz gives a number of $N_y = 250$ lines in the *en-face* image. In the images presented in Figure 5.11, only half periods of the signal driving the KTN are used for simplicity. If both lateral scanning directions of the KTN scanner were used to assemble an *en-face* image, the frame rate could be doubled for the same number of lines.

Figure 5.11 shows *en-face* OCT images of a coin from $4z$ positions separated by $40\mu m$. The coin was slightly tilted, and therefore, the narrow axial resolution led to fragmented *en-face* OCT images. The 5th image underneath represents a summation of 10 en−face images separated $10\mu m$ into a single projection, where

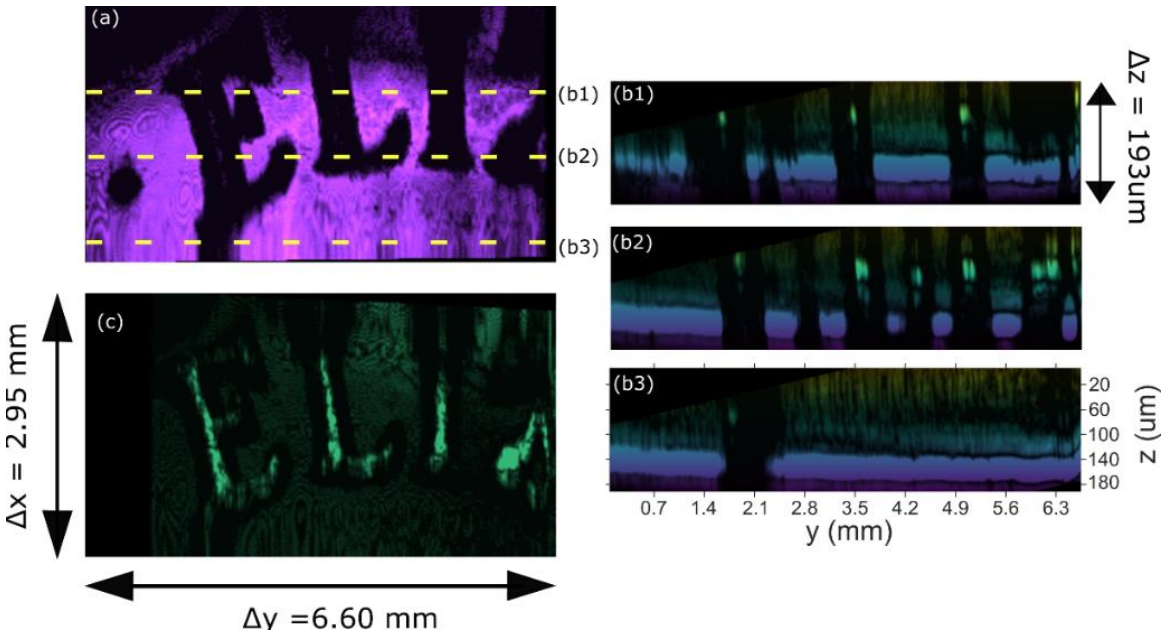

FIGURE 5.12: Tilt corrected OCT images. (a) *En-face* image of the bottom of the letters. (b1-3) B-scans at lateral positions as indicated by dashed yellow lines in (a). (c) *En-face* image of the top of the letters.

the height in Z of each image was colour-coded. The thickness of the bright patch in the *en-face* OCT images represents a projection of the axial resolution interval along the tilted surface of the coin. To widen the bright patch, the tilt of the coin in the volume of data acquired has been compensated manually using ImageJ and two such *en-face* cuts, corrected for tilt, corresponding to the Z-position of the coin base (a) and the top of the letters (c) are shown in Figure 5.12.

Figure 5.12 (b1-b3) show three B-scan OCT images. These are perpendicular to the *en-face* OCT image in Figure 5.12 (a) and oriented along the dashed lines superposed on the same image. The images in Figure 5.12 confirm that the axial range is sufficient to cover the tilt of the coin and the height of the letters on the coin.

The topography of the 3D volume generated is shown in Figure 5.13. Due to the sinusoidal shape of the signal driving the KTN deflector, the images present a nonlinear variation of pixel size along the $x-$ line in the raster. Therefore, margins were cropped to eliminate the regions of flyback and afterwards corrected along the $x-$ direction via linear interpolation. Considering the numerical values for

the axial range and axial resolution evaluated above, a number of points $N_z = \Delta z/\delta z = 53$ along the depth coordinate is obtained. Therefore, using one half of the KTN ramp, the displayed volume contains $200 \times 250 \times 53$ voxels.

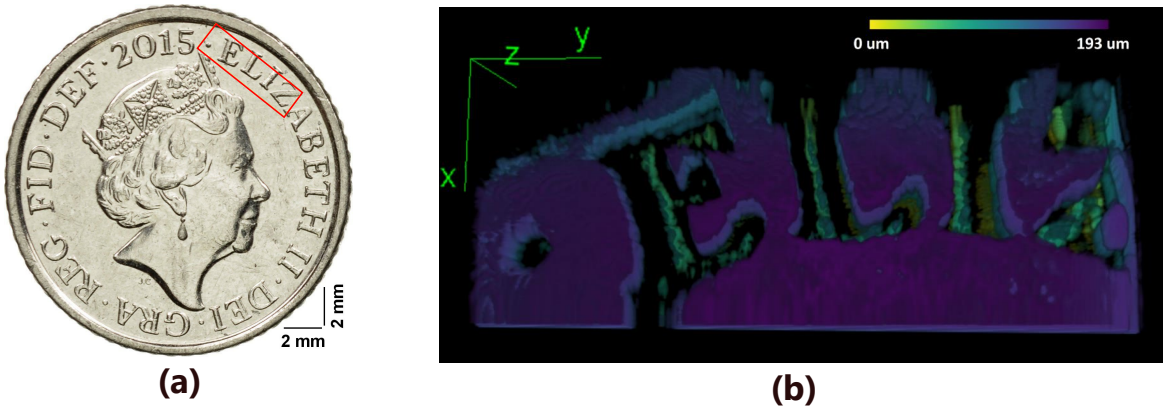

FIGURE 5.13: (a) Image of the Five Pence 2015 (Fifth Portrait) with a red overlay in the area scanned (b) Topographical representation of a 3D volume generated in a raster at 400 Hz from the coin, where the colour bar is used to illustrate the Z coordinate. Lateral size 2.95mm X 6.60mm.

5.6 Conclusions and discussions

This work responds to the progress in the high-sweeping speed of modern tuning lasers. Galvanometers and resonant scanners are widely used in OCT instruments; however, when paired with a fast-sweeping optical source, the distance between successive lateral pixels becomes smaller than the optical transversal resolution, which effectively turns into data oversampling with no effective increase in the volume acquisition rate. The effective scanning procedure using a fast KTN-based scanner shown in this report demonstrated a volume production rate of up to 400 Hz, which is superior to other reported values with OCT scanning systems operating in the $1\mu m$ band [227]. However, the volume rate of 400 Hz is only specific for 250 y-lines; depending on the desired requirements of the application, one could have volumes in shorter or longer amounts of time. In the case of this work, 400 Hz was selected to have a similar quantity of optical points in each direction, 200x250. As previously mentioned, galvanometer

scanners may suffer at frequencies higher than 1 kHz. Moreover, a limiting volume rate using a galvanometer scanner will be then at 1kHz, for which only 100 points will be generated. Furthermore, the amplitude achievable at 1 kHz using galvanometer scanners is also reduced compared to lower frequencies, obtaining more dense volumes. Alternatively, a KTN scanner could be paired with resonant scanners, allowing higher volume rates than 1 kHz instead of 400 Hz. Still, the resulting number of points will be minimal as it follows $N_y = f_{KTN}/f_{SlowScanner}$. Conversely, lower frequencies in the range of a few Hz might be achievable using galvanometer scanners; however, the acquisition might become a bottleneck. The real-time oscilloscope used here has a limited memory, being able to save a maximum of 512 Mpts per channel. Of course, this can be increased by adding more memory options to the device, which may increase the cost.

In the case of moving targets, the high-volume rate secures less distortion due to movement. This could benefit several applications such as phase-sensitive OCT, surgery guidance, and 4D-OCT [37]. However, increasing the sweeping speed comes at the expense of limited sensitivity. The sensitivity is affected by the noise of the source as well as the duration of the emission.

RIN of the source: The source presented here exhibited an average RIN of $\approx 4\%$ on the emitted spectra since the seed laser Origami 10LP had a 0.2% amplitude variation (manufacturer specification) originally, and the supercontinuum generated here has been previously demonstrated to exhibit a RIN of 0.54% [176]. Therefore, only the stretching element and the ytterbium amplifier could have caused the increase in the RIN. The stretching element is passive, only attenuating the input spectrum without influencing the noise. On the other hand, the ytterbium amplifier might induce noise since the response time of the ytterbium is lower than the repetition time from the seed laser; therefore, the amplifier acts on a continuous operation, which seems to impact the noise negatively. Overall, the performance of the source has been severely affected by the ytterbium

amplifier, first due to the noise and second due to bandwidth limitation. The supercontinuum community would expect a bandwidth of at least 200 nm and low noise ($RIN < 1\%$) to be delivered by those supercontinuum methods, which is feasible. On the other hand, OCT requires large powers of even 50 mW at the input of the interferometer. Those requirements can only be achieved by removing the ytterbium amplifier and using a higher average power laser (>1W) to seed the supercontinuum with a fibre with lower nonlinearities than the photonic crystal fibre used here. Note that a higher power seed with the same fibre for supercontinuum will only produce a large bandwidth, but the power spectral density will remain the same.

Duration of the emission: The $\sim 50\%$ duty cycle, while operating at 40 MHz repetition rate, corresponds to an equivalent sweeping at 80 MHz with 100% duty cycle. According to the estimated formula for sensitivity variation with the sweeping speed in [2], a 30 dB reduction is due to the increase in the sweeping rate from 1 MHz to 100 MHz. This comparison does not yet consider larger noise levels owing to an increase in the electronic bandwidth by 80 times when the sweeping rate is increased from 1 to 80 MHz. For instance, in a previous report [37], a sensitivity of 90 dB at a sweeping rate of 1 MHz was obtained. Therefore, by taking into account two corrections applied to a 90 dB sensitivity considered the norm: (i) suggested in [36] and (ii) due to the enlarged noise bandwidth, may lead to a much lower value, closer to that reported here. A modest improvement in sensitivity is possible by reducing the ratio of the first coupler, accompanied by a proportional increase in the optical power of the source for the same safety power limit delivered to the sample.

The data acquisition raises another limitation of the instrument reported. Although digital sampling acquisition can cope with tens of GHz, such high electrical bandwidths, when combined with a dynamic range of 12 bits, lead to large volumes of data (≈ 4 GB) for a time span of 2.5 ms. On this occasion, the acquisition time and the processing take an average of 17 minutes. This time can

substantially be improved by a specialized design of the hardware and software acquisition, which is out of the scope of this thesis. However, realistically, the processing time reduces the capabilities of this system for real-time use. Alternatively, smaller datasets of just one B-Scan can be sent and processed in pseudo-real-time. Here, we define real-time when $t_{processing} < t_{acquisition}$, with $t_{acquisition}$ being the $10\mu s$ that the B-Scan takes to be generated.

Chapter 6

In-vivo imaging of the human eye using ultrafast SS-OCT

A new generation of swept sources comes at the expense of new processing requirements. In this chapter, two novel sources that share the same characteristics, such as bidirectional sweeping and high-speed sweeping rates, are carefully studied. First, real-time operation is achieved using high-speed digitisers, producing retina images. Finally, imaging is made by a downconversion system, and the benefits of using such a system are studied. In fact, it reduces the bandwidth needed for the digitised source, diminishing the cost applicable to high-speed and bidirectional swept sources.

Contents

6.1 Introduction

Author's Note: All *in-vivo* images presented in this chapter were performed according to the protocol approved by the Human Participation Committee at the University of Kent, Ref 0191718 Nov. 2017.

In previous chapters, the use of multi-MHz swept sources for OCT has been described. However, multi-MHz swept sources are complicated to use in real-time, as described in Chapter 5. This chapter explores two novel mechanisms for swept sources with relatively high speeds: an 828 kHz FDML and a 1.6 MHz MEMS-VCSEL [109]. Both of them share similar characteristics, although their principle of operation is different. For instance, FDML lasers and MEMS-VCSEL both exhibit long axial ranges, which can exceed centimetres and reach even meters for the MEMS-VCSEL [142]. Moreover, as their principle of operation is based on a mechanical spectral filter, for fast operation, this is excited with a sinusoidal waveform applied to an actuator. Therefore, bidirectional behaviour is expected from both sources. In order to make the most of such sources, each sweep, forward and backwards, has to be analysed and characterised. This chapter is divided into two main sections: first, the work conducted to make use of the FDML source, with a brief description of the laser provided, and finally, the work using a MEMS-VCSEL. In the first part, the complex master slave is used and compared for both sweeps of the FDML. During the second part of the chapter, a downconversion set-up is presented that can enable real-time *en-face* display with just a low-speed digitizer of 5 MSa/s.

6.2 OCT with FDML at 840 nm

Author's Note: The work presented above is part of a collaboration with PhD Student Marie Klufts, from University of Lübeck, which is a partner of the NETLAS Consortium.

MK has designed and built the FDML and booster stage. AMJ and MK have together characterized the performance of the laser on OCT configurations. AMJ and MK have designed and built the interferometer. AMJ has acquired and conducted the phase stability study. AMJ and MK have acquired retinal OCT images together. AMJ and AB have developed the software for real-time processing.

The work shown here is part of the peer-reviewed paper [4].

FDML lasers have been extensively studied at different wavelength bands such as 1060 nm, 1300 nm and 1550 nm [54, 110, 111, 132]. However, shorter wavelength bands such as 850 nm exhibit benefits in terms of axial resolution; for example, a laser with a 40 nm bandwidth at 840 nm delivers a similar axial resolution to a 60 nm bandwidth laser at 1060 nm. Overall, better axial resolution can be obtained with the same bandwidth as in 1060 nm, shifting the central wavelength towards shorter wavelengths. Furthermore, 1060 nm is located in a local minimum of water absorption, which allows the use of 1060 nm as a central wavelength. However, the absorption increases by one order of magnitude towards 1100 nm and the same happens towards 980 nm[228]. Therefore, the usable FWHM is limited to 100 nm for a source with a Gaussian spectral shape. For those reasons, there is a need for new swept sources at 840 nm.

However, the development of semiconductor-based lasers depends on the evolution of SOA technology. Broad bandwidth and powerful SOAs at 840 nm have only been manufactured in recent years. Besides SOA developments, fibre technology, such as couplers, circulators, isolators, high chromatic dispersion, etc, has been a limiting factor. All of the aforementioned limiting factors are now challenged, and the first FDML at 840 nm is presented. Additionally, the use of complex master-slave for FDML sources is presented for the first time. The bidirectionality of the new laser is characterised, and images are produced utilising

both sweeps.

6.2.1 Laser characterisation

Figure 6.1 (a) illustrates the schematic diagram detailing the 840 nm FDML laser configuration. The cavity incorporates three chirped Fibre Bragg Gratings (cFBGs) to effectively compensate for chromatic dispersion across a wide bandwidth of 72 nm. Each cFBG addresses one-third of the total dispersion induced by the approximately 500 m fibre spool. Circulators facilitate the utilisation of cFBGs by directing the backscattered light, primarily from the cFBG with 90% reflectivity, to subsequent optical elements within the laser cavity. Polarisation controllers are strategically positioned at each circulator input to mitigate polarisation mode dispersion (PMD) and optimize optical power and bandwidth performance.

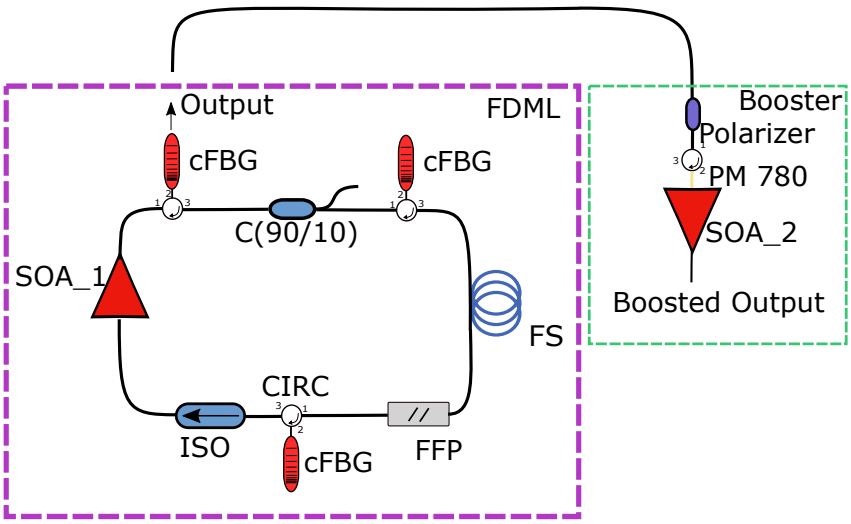

FIGURE 6.1: **Experimental set-up.** FDML laser set-up accompanied by its booster stage. SOA: semiconductor optical amplifier, PC: polarisation controller, cFBG: chirped fibre Bragg grating, ISO: isolator, FS: fibre spool, FFP: fibre Fabry-Pérot filter.

The setup employs a semiconductor optical amplifier (SOA_1) with a small signal gain of 22 dB as the gain medium (SOA-372-DBUT-SM, Superlum Ltd.). An isolator is introduced at the input of SOA_1 to prevent potential parasitic lasing resulting from low isolation loss of the final circulator. Additionally, a $90/10$ coupler serves as a monitoring port to supervise the circulating power within the

cavity and prevent surpassing the catastrophic optical damage (COD) threshold of SOA_1. Various components are spliced together to minimize overall losses within the laser cavity to 19 dB. The FFP is a custom-made product by the University of Lubeck. The Fabry-Perot filters are constructed from a non-confocal etalon, which consists of two mirrors of high reflectivity: one planar and the other spherical concave. The FFP feature is a piezoelectric transducer that adjusts the position of the etalon mirror, in which the separation allows the tuning of specific wavelengths transmitted. The piezo is synchronised with the round-trip time of the cavity. The laser output is directed towards a booster stage, elevating the output power from 1.7 mW to 17 mW. To counteract the PMD introduced by the booster stage, an in-line polariser followed by a PM−circulator is incorporated, considering the use of a Polarisation Maintaining Semiconductor Optical Amplifier (PM-SOA, SOA_2).

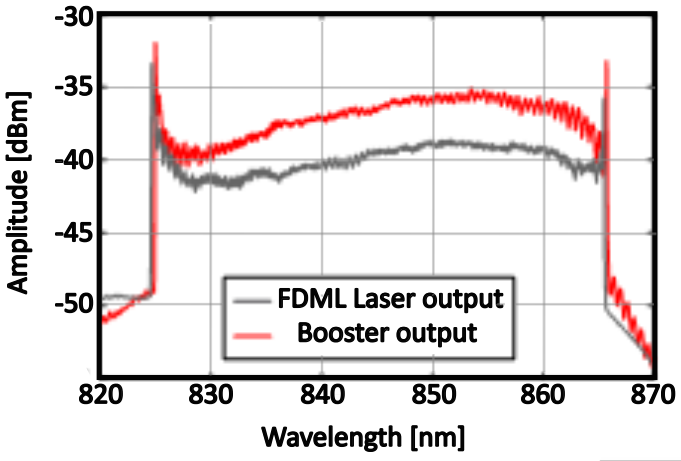

FIGURE 6.2: Spectra at the FDML laser output in grey and at the booster stage output in red after passing through an isolator and a coupler.

The spectrum characteristics at the output of both the 840 nm FDML laser and the booster stage are depicted in Figure 6.2. From Fig 6.2, it is clearly noticeable a peak on each of the edges. This can be explained by the fact that the FFP-TF is moved with a sinusoidal waveform, and therefore, the wavelengths on the edge remain longer time than the rest. In both cases, a tuning bandwidth of 40 nm full width at half maximum is achieved. However, it is noteworthy that while

a wider bandwidth is attainable, the gain shape of the SOA_2 within the booster section (Superlum Ltd., SOA$-372-$PM) is not as flat as the output laser spectrum. At the edges of the spectrum, the gain diminishes significantly, resulting in a narrower bandwidth achieved. The spectral profiles exhibit ripples, which are more pronounced in the output after the booster stage (red) than within the FDML cavity (grey), despite using PM components. The ripples observed here have been previously documented as the consequence of PMD in the circulators used at this wavelength [229]. The in-line polarisers' effectiveness in cancelling out the ripples across the entire range is limited due to the wavelength dependence of PMD. The boosted output from the FDML operates at an output power of 17 mW with a tuning bandwidth of 40 nm.

6.2.2 OCT Characterisation

FDML lasers feature bidirectional sweep operations facilitated by the sinusoidal drive of the fibre Fabry-Perot Tunable Filter (FFP-TF). Owing to their high similarity, both sweeps can be used for imaging. Consequently, a repetition rate of 828 kHz becomes feasible and is utilized in the subsequent section.

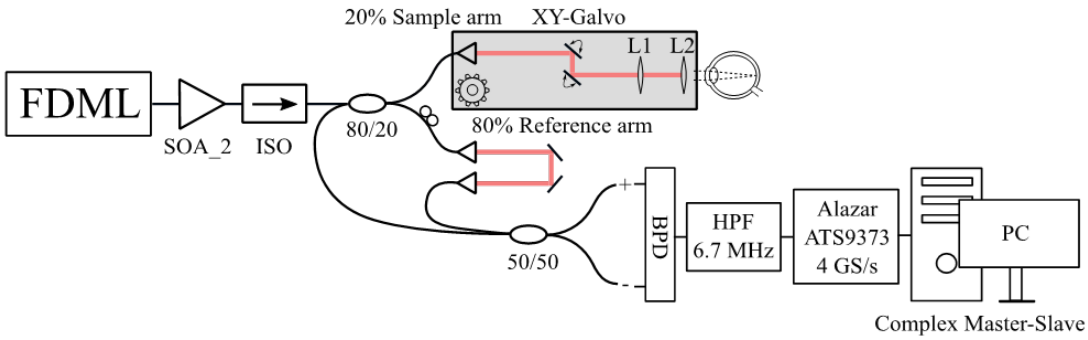

FIGURE 6.3: **Schematic whole OCT system, from the light source, FDML, the OCT interferometer and the acquisition system.** The light at the output of the booster enters the sample and reference arms, which are recombined by a 50/50 coupler. BPD: balanced photodetectors, HPF: high pass filter.

Figure 6.3 illustrates a schematic diagram of OCT instrument integrated with the FDML source. The light emitted by the FDML laser is guided towards an

80/20 fibre directional coupler, where 20% of the optical power is directed towards the sample arm. This light is then transitioned to free space using a fibre collimator (F220APC-850, Thorlabs), subsequently manipulated by two galvanometer scanner mirrors (Cambridge Technology, 6210H), and directed towards a telescope, producing a collimated beam with a diameter of 1.5 mm.

The remaining 80% of the light is routed towards the reference arm of the interferometer. The splitting ratio of the coupler ensures both a safe power level on the retina and efficient collection of light from the sample, with 80% allocated for the latter purpose. The interference of the backscattered light from both the sample and reference arms at the 50/50 coupler is detected by a custom-designed balanced silicon photodetector from Wieserlabs. Each photodiode exhibits a responsivity estimated at approximately 0.33 A/W at 850 nm and an electronic bandwidth of 600 MHz.

Subsequently, signals are acquired by a 12-bit waveform digitiser board operating at a rate of 4 GS/s (AlazarTech, ATS9373), followed by processing through the CMS procedure to generate images [43, 206]. An eye model consisting of a 19 mm focal length lens (AC127-019-B-ML, Thorlabs) and a flat mirror was utilised to acquire several channelled spectra for different optical path difference values in the interferometer. These were then employed to calculate two calibration functions, $g(k)$ and $h(k)$, describing unbalanced dispersion in the interferometer and sweeping non-linearity. To further confirm the similarities with the eye model, we inserted a 2cm water cuvette in the reference arm; however, no significant differences were seen. Furthermore, if needed, the calibration functions $g(k)$ and $h(k)$ can be fine-tuned for any specific image.

The interface optics within the sample arm are mounted on a motorised stage, with a chin rest at the end, facilitating pupil tracking via two cameras located at the bottom of L2. The pupil tracking gives feedback to the motorized translation stage to align the eye into a position where the eye is in the centre of the lens. The motorized translation stage can move in X, Y and Z directions. The movements

in X and Y allow the eye to be positioned correctly. Moreover, the length of the sample arm can be adjusted via computer using the Z stage to alter the focal point through the layers of the retina.

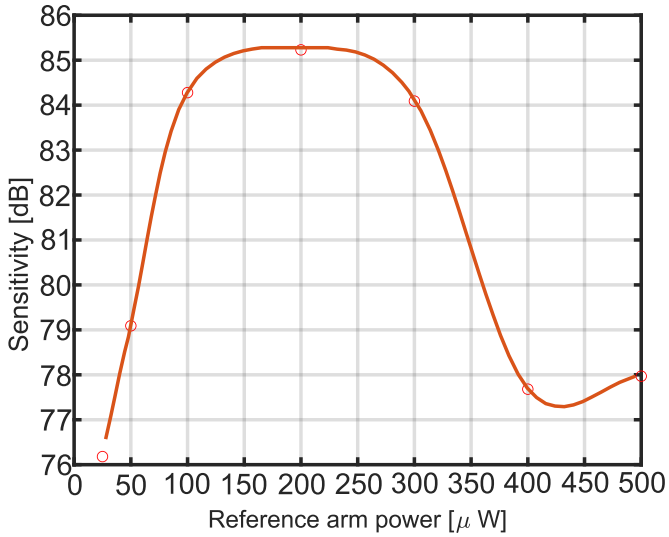

FIGURE 6.4: Sensitivity of the OCT system measured for different reference power values.

The measurement results lay along a plateau at approximately 84.6 dB for powers 100-300 μW, as illustrated in Figure 6.4. Rather than a distinct maximum, this plateau suggests performance limited by shot noise, as elaborated in reference [35]. Moreover, the plateau shown in 6.4 is a combined effect of two effects; in the first part, up to $100\mu W$, the system is dominated by the shot noise, then from $270\mu W$ onwards, the system is fully dominated by the excess noise, meanwhile in the plateau there is a combination of both, this effect has been reported in [40, 161]. According to calculations following reference [37], the theoretical sensitivity is estimated at 86.9 dB, considering the responsivity of the silicon detector at 850 nm of 0.3 A/W and a power of 1.2 mW on the sample. The 2.3 dB disparity between the measured sensitivity value and the theoretical sensitivity could stem from spectral shape deviations, power measurement inaccuracies in the assumed analogue detection bandwidth, or other parasitic effects. The MPE value for a stationary, collimated beam on the cornea, calculated using standards IEC 60825-1 and ANSI 136.1, is 0.8 mW for 840 nm [13, 230]. Due to continuous

scanning without interruptions during an examination, the retina can be exposed to a higher average power of 1.2 mW [231],

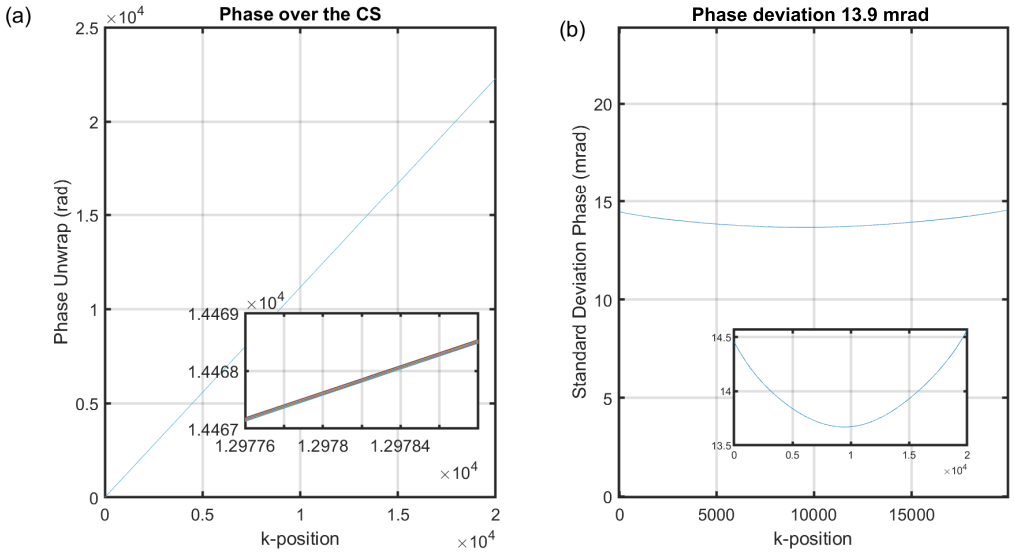

FIGURE 6.5: **Phase stability of the laser.** (a) Spectral phase for 1,000 forward sweeps, inset: zoom into its fluctuation. (b) The standard deviation for variation of phase among all 1,000 sweeps.

The phase stability of the laser was assessed over 1,000 consecutive forward channeled spectra in a common path configuration, utilising a glass plate with a thickness of $235\mu m$ introduced halfway through the reference path, as outlined in [232]. Before the measurement, two different glass thicknesses were employed to generate the masks utilised for signal processing [43, 206]. A 20 GHz oscilloscope (Lecroy Teledyne, Wavemaster 820Zi-b) captured 1,000 sweeps with a sampling rate of 80 GS/s in a single shot. Simultaneously, a trigger phase locked with the FDML filter was saved and later utilised in post-processing to separate each sweep. This approach was adopted to mitigate potential jitter noise that the trigger from the acquisition card could introduce. Upon cropping all forward sweeps, the CMS protocol was executed, interference noise was eliminated, and an inverse Fast Fourier Transform (iFFT) was applied to obtain the linearised signal. Subsequently, the phase was computed using a Hilbert transform (refer to Figure 6.5 (a)). The standard deviation of each point across the sweep was calculated following the method described in [232]. As depicted in Figure 6.5 (b), the

laser exhibited an average standard deviation of 14 mrad over the 1,000 sweeps.

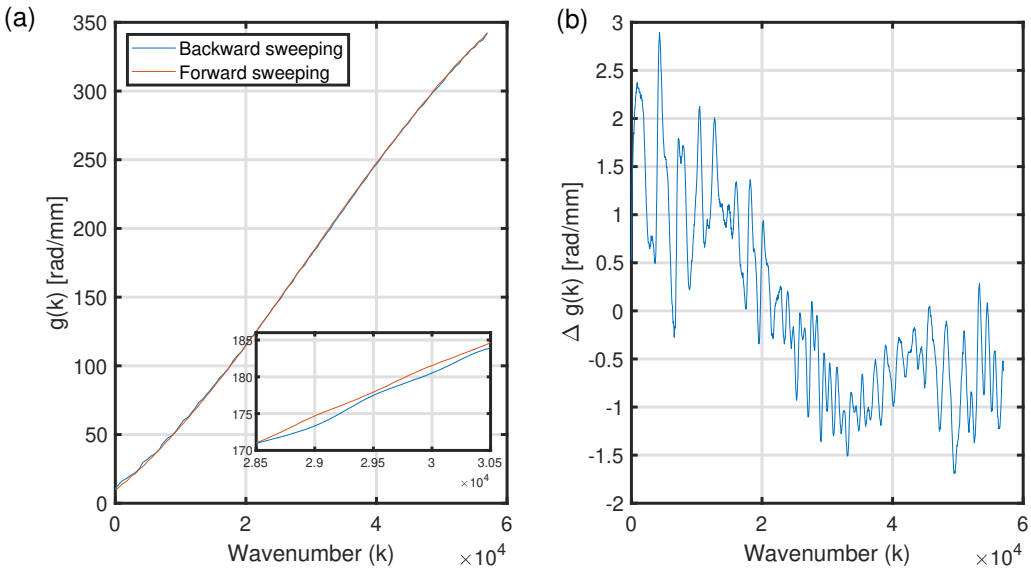

FIGURE 6.6: **Phase differences between backward and forward sweep.** (a) Comparison of the phase obtained from the CMS, used for recalibration of the forward and backward sweep. (b) Shows the $g(k)$ variation between the forward and backward sweep phases.

The inset in Figure 6.6 (a) illustrates the superposition of the calibration function represented by $g(k)$, along both the forward and backward sweeps. Linear fits applied to both curves yielded coefficients of determination exceeding 0.9983. These coefficients could be further improved towards 1.0 by modulating the laser and selecting a narrower, more linear segment of the driving signal of the FFP-TF. The $g(k)$ functions are compared, and the results are displayed in the inset of Figure 6.6 (b). It is evident that both sweeps can be utilised for imaging due to their similar power level and phase behaviour. However, to ensure correct imaging in depth, separate masks must be employed for each sweep. As demonstrated in Figure 6.7, A-scans employing the correct masks for each of the two sweeps exhibit good axial resolution, whereas using forward masks for the backward sweeps leads to a degradation in axial resolution and the height of the peaks. These differences between forward and backward sweep can be caused by many sources, such as uncompensated dispersion inside of the laser cavity, differences

in the FFP-TF movement, and the number of holes in the spectrum; more details analyzing the source of this problem can be found in [122, 126].

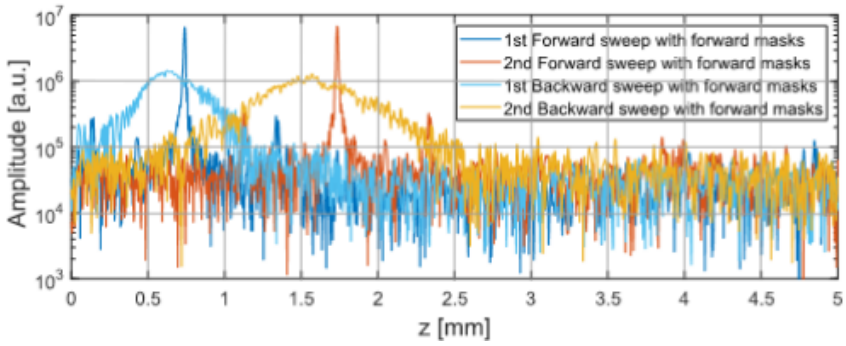

FIGURE 6.7: Four A-Scans were acquired using either a forward or a backward laser sweep. Each A-Scan acquired from the backward sweep is multiplied with a theoretical forward mask, while each A-Scan acquired from the forward sweep is multiplied with the right mask (i.e., theoretical forward masks).

The axial and lateral resolutions were evaluated and compared with theoretical values. Axial resolution was experimentally determined during imaging of the model eye. Seven B-Scans were acquired by adjusting the length of the reference arm in steps of 0.5 mm in OPD between consecutive scans. Figure 6.8 displays all peaks at various depths along with a Gaussian fit of the first and last peaks, revealing an evolution of axial resolution from $12.8\mu m$ to $12.5\mu m$. An average resolution of $13.16\mu m$ was calculated across the entire range. The theoretical calculation yielded an axial resolution of $10.58\mu m$ in air for a top-hat optical spectral shape centred around $840 \pm 20nm$ as per reference [26]. The observed difference of approximately $2.5\mu m$ arises due to the use of a Hanning window in the data processing, which slightly degrades the axial resolution. Regarding lateral resolution, a measurement of $17.54\mu m$ was obtained by imaging a 1951 USAF Resolution Target (Thorlabs, R1DS1P) using a fast scanner operating at 500 Hz driven by a triangular signal of 0.3V amplitude, and a slow scanner at 2.5 Hz driven by a sawtooth signal with 0.2V amplitude. It is important to note that this measurement may be better than that obtained on the retina, where aberrations introduced by the eye lens and cornea deteriorate the lateral resolution.

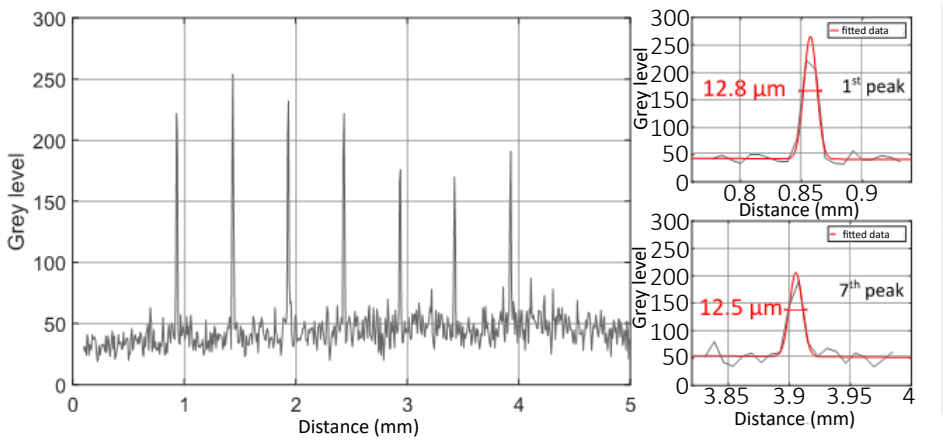

FIGURE 6.8: Axial resolution measured for 7 different depths, showing a quasi-constant $\sim 12.8\mu m$ resolution over the range.

Fig #	**Sweep acquisition**	**Oversampling**	**Galvo Frequency**	**FOV**	**Volume rate**
Fig. 6.9	Unidirectional	2	200 Hz	12 mm	n/a
Fig. 6.10	Unidirectional	1.6	200 Hz	15.5 mm	n/a
Fig. 6.10	Bidirectional	1	800 Hz	12 mm	n/a
Fig. 6.11	Unidirectional	2	200 Hz	7.8 mm	1 Hz
Fig. 6.11	Unidirectional	1	1 kHz	5 mm	10 Hz
Fig. 6.11	Unidirectional	5	200 Hz	3.2 mm	1 Hz
Fig. 6.11	Unidirectional	2.5	500 Hz	4 mm	1 Hz

TABLE 6.1: OCT Images acquisition configuration, scanning protocol and volume rate.

6.2.3 OCT Imaging results

Retinal images acquired with the 840 nm FDML laser are presented here; all imaging settings are shown in Table 6.1. All images were acquired on the same healthy volunteer with an optical power of 1.2 mW at the cornea. Two galvanometer scanners are used to acquire B-scans and volumes (set-up in Figure 6.3).

Retinal images captured using the 840 nm FDML laser are presented here, with all imaging parameters detailed in Table 6.1. B-scans and volumes were acquired using two galvanometer scanners, as depicted in the setup illustrated in Figure 6.3.

Figure 6.9 shows the macula region of the subject acquired using the unidirectional forward sweeping of the FDML laser, corresponding to a rate of 414,000 axial scans per second. The fast lateral scanner (horizontal) operated at 200 Hz with an amplitude of 2 V, resulting in a field of view of 12 mm with 1,000 points. With an estimated lateral resolution of 24 µm, an oversampling factor of approximately 2 was achieved. In Figure 6.9 (a), 20 consecutive frames were averaged, while in (c), 5 frames were averaged. In the non-averaged image (b), all three brighter layers beneath the external limiting membrane are visible. Although these layers are discernible without averaging, employing a 20-times average aids in enhancing contrast on the ganglion cell layer from the inner plexiform layer and facilitates visualisation of the external limiting membrane, as demonstrated in Figure 6.9 (a).

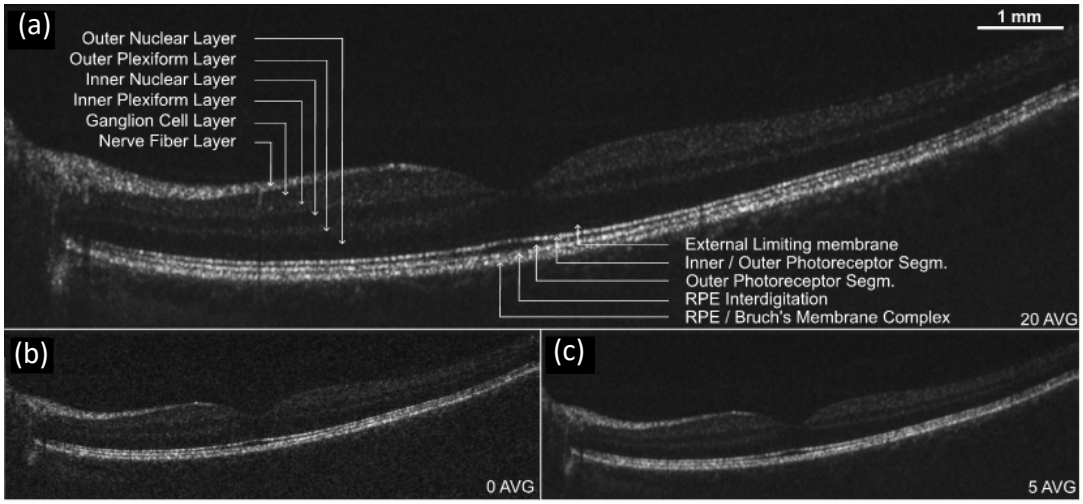

FIGURE 6.9: Retinal OCT imaging focused on the macula. (a) is 20 times averaged, (b) is obtained without average, and (c) is 5 times averaged. RPE: retinal pigment epithelium.

Wider B-scans were obtained by increasing the galvanometer scanner amplitude to 3 V at a frequency of 200 Hz, resulting in a reduced oversampling of 1.6 and an acquisition time of 5 ms. Consequently, both the fovea and the optic nerve are now accommodated within the same B-scan image, as depicted in Figure 6.10. Figure 6.10 (b) presents an unaveraged frame from the averaged image stack in (a), where the three brighter layers beneath the external limiting membrane, as

well as the choroid, are discernible. Figure 6.10 (c) and (d) were acquired using the bidirectional sweeping of the filter, corresponding to a rate of 2x 414 kHz, resulting in an A-scan rate of 828,000 per second. All layers observed in the previous images are still visible at this higher repetition rate. However, as mentioned in section 3.2, two sets of $g(k)$ and $h(k)$ were utilised, one for each sweep, leading to a slight frequency shift between the forward and backward A-scan. To mitigate this, a correction of 3 pixels is applied to each backward sweep, resulting in the images presented in (d) of Figure 6.10. The impact of image correction on the visibility of layers is minimal and not discernible. Figure 6.10 shows wide-angle retinal images of the optic nerve and the fovea. (a) and (b) were acquired at a rate of 414,000 axial scans per second, with 20-times average and non-average settings, respectively. (c) and (d) were acquired using the laser's bidirectional sweeping, resulting in a rate of 818,000 axial scans per second. (c) underwent 19-times averaging, while (d) remains non-averaged.

OCT aggregated *en-face* images, mean intensity projection images, as well as 3D images, are displayed in Figure 6.11. The mean intensity projection images are produced from the 3D volume, in which the value is calculated as the mean of all the depth values of a given X, Y pixel. The fundus images are generated by overlaying all *en-face* OCT images for all masks [49]. In Figure 6.11 (a), an average of 8 equivalent mean intensity projection images illustrates the optic nerve and the macula. Each of these volumes was acquired in 1 second, with the fast and slow scanners driven at frequencies of 200 Hz (triangular) and 1 Hz (sawtooth), respectively. The CMS approach employed in this study enabled real-time display of *en-face* OCT and mean intensity projection images. For example, Figure 6.11 (b) was captured in 100 milliseconds. Volumes in Figure 6.11 (b) and (d) have been flattened in post-processing to enhance rendering. They are presented with three *en-face* images separated by 10 frames each. In each image, both vessels and smaller capillaries are visible.

Figure 6.11 *en-face* OCT and mean intensity projection images of the optic

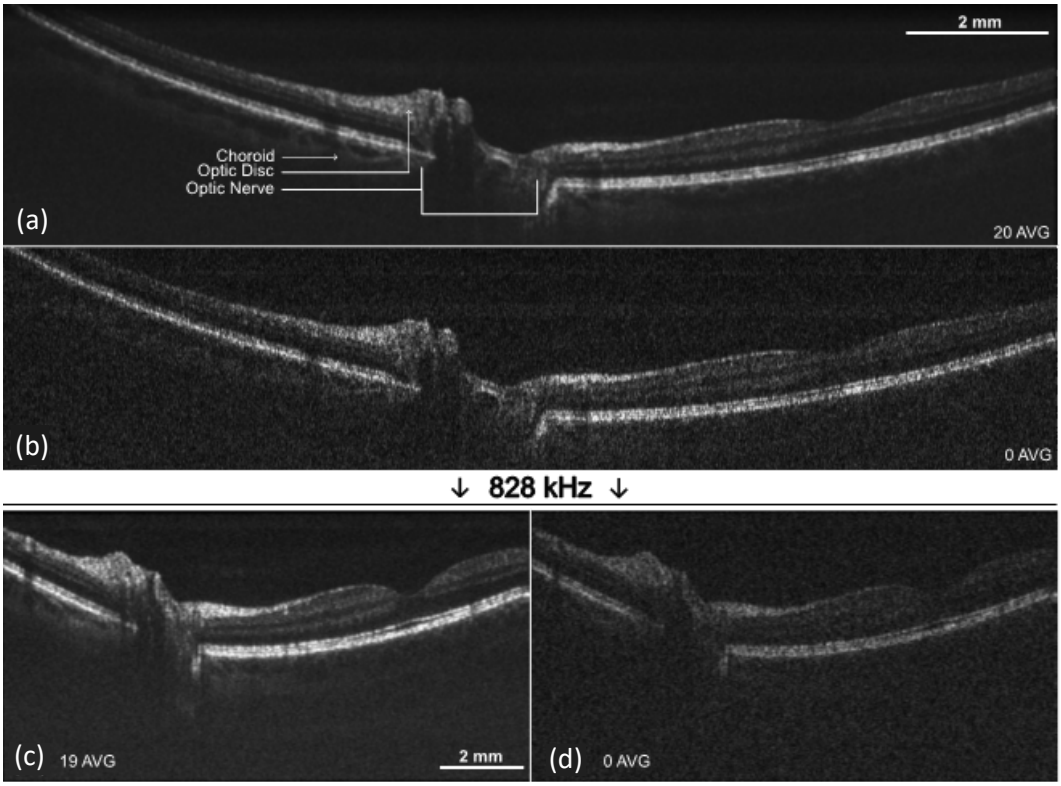

FIGURE 6.10: Wide-angle retinal images of the optic nerve and the fovea. (a) and (b) are acquired at a rate of 414,000 axial scans per second, 20 times average and non-average, respectively. (c) and (d) are acquired using the laser's bidirectional sweeping, leading to a rate of 818,000 axial scans per second. (c) is 19 times averaged, and (d) is non-averaged.

nerve and the macula regions acquired at a rate of 414,000 axial scans per second. (a) 8 times averaging of mean intensity projection images of the optic nerve and the macula. (b) flattened 3D of the optic nerve with 3 corresponding *en-face* spaced by 10 frames. (c) mean intensity projection images of the macula. (d) flattened 3D of the macula with 3 corresponding *en-face* spaced by 10 frames.

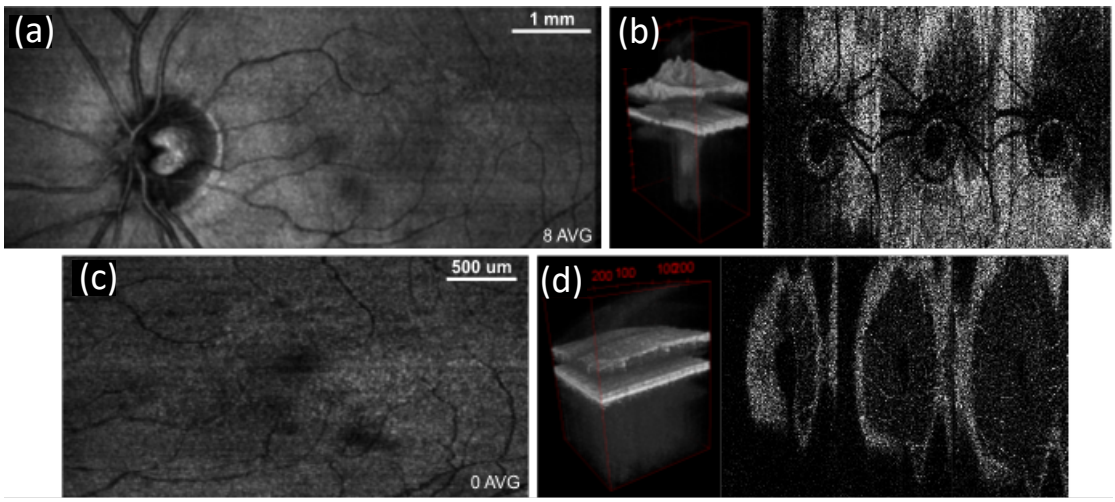

FIGURE 6.11: *En-face* OCT and mean intensity projection images of the optic nerve and the macula regions acquired at a rate of 414,000 axial scans per second. (a) 8 times averaging of mean intensity projection images of the optic nerve and the macula. (b) flattened 3D of the optic nerve with 3 corresponding *en-face* spaced by 10 frames. (c) mean intensity projection images of the macula. (d) flattened 3D of the macula with 3 corresponding *en-face* spaced by 10 frames.

6.3 OCT with MEMS-VCSEL at 1.6 MHz

Author's Note: The work presented above is part of a collaboration with PhD Student Esteban Andres Proano Grijalva from Technical University of Denmark - DTU, and OCTLight, which are partners on the NETLAS Consortium. As well as the Associate Researcher Dr. Ramona Cernat.

The MEMS-VCSEL presented here were fully designed and produced by OCTLight Aps. AMJ has developed the imaging software. AMJ has also built and designed the imaging interferometer. AMJ has conducted the OCT characterisation of the MEMS-VCSEL. AMJ has conducted the investigations on sweep instabilities. AMJ has produced the retinal images. AMJ, with RC, have built the downconversion system. AMJ and RC have together produced the retinal images with the downconversion system.

The work presented here is part of peer-reviewed paper [3], and conference proceeding [3,4].

Compared to other tunable sources, MEMS-VCSEL sources exhibit a short cavity. Their single-mode operation and narrow instantaneous linewidths enable long axial range in OCT imaging.

A swept source can sweep from red to blue or blue to red, i.e., forward or backward sweep, respectively. "Unidirectional sweeping" refers to the use of only one of the sweeps, as opposed to both. The majority of swept sources on the market are unidirectional, some with duty ratios less than 50%. Making the tuning bidirectional increases the duty ratio and doubles the tuning rates. However, high-speed swept sources and bidirectional multi-MHz MEMS-VCSELs provide two fundamental challenges that need to be addressed prior to imaging:

a) The ability to use forward and backward sweeping demands specific phase corrections to each sweep due to the asymmetry in the spectra [197]. Therefore, signal processing requires different phase corrections for forward and backward sweeping to be applied during each sweep [104].

b) Another problem for both unidirectional and bidirectional sweeping lasers is that the high sweeping rate demands high-speed photodetectors, digitisers, and complex software to display the image in real time. Due to the narrow linewidth of these sources, these sources exhibit a large coherence length, determining a large axial range that exceeds many cm. Therefore, a densely modulated channeled spectrum (CS) may be generated at the interferometer output. This can lead to a radio frequency spectrum of many tens of GHz of the photo-detected signal. The high-speed digitiser required to sample 2 GHz can exceed $\$10,000$. This increases the cost of fast-sweeping solutions, limiting fast OCT technology to research purposes only.

Yet another concern is instability in the tuning curve of the swept source, which requires frequent calibration. Using *k*-clocks can address the nonlinearity variation over time, but that is only possible if digitisers with input for *k*-clocks are used. Hence, new OCT protocols [45, 95, 233] are needed to address or alleviate the problems listed above.

Here, a solution is presented to address both challenges raised by the high sweep rates and those raised by bidirectional sweeping. Using a second interferometer for any depth of interest, the chirped characteristic signal required by the Master-Slave protocol is generated in real-time. By mixing the photo-detected signals from both interferometers, the dilemma of speed is addressed by electrical downconversion [234]. We refer to such a method as downconversion master-slave (DMS). The issue of specific processing required for forward and backward sweep is automatically addressed as the same swept source drives both interferometers. In order to present the DMS and illustrate the nonlinearities dependent on each sweep of the swept source, complex Master-Slave is used.

6.3.1 Complex Master Slave

The light source used in this work is a MEMS-VCSEL with a bidirectional sweeping rate of 1.6 MHz. The details of the source have been described in previous reports [235, 236]. To exploit the swept source full performance, both sweeps are used in this study. As tuning curves are different from forward to backward sweep, in order to obtain resolution-limited A-scans, a specific calibration must be applied for each sweep.

This problem is illustrated using the CMS protocol. As explained in previous reports [43], CMS is a method that looks into the spectrum modulation pattern and finds the amplitude of the modulation corresponding to the depth of interest. MS is a comparable method based on comparing the channeled spectrum by placing the sample in the sample arm with many modulation shapes, otherwise obtainable by placing a mirror in the sample arm at different OPD values corresponding to the depths of interest in the sample. MS involves a comparator for each such depth to produce A-scan peaks at all depths of interest. The comparison can be made in software, via calculators with stored versions of the channelled spectra, or in hardware where the modulation at any depth is generated in real-time with a supplementary interferometer (Master).

In the first part of this chapter, on the FDML, the software-based CMS protocol was used, which allowed the obtaining of A-scans from pre-calculated datasets of channelled spectra [43]. Here, we will demonstrate the hardware method. Conventional numerical procedures, such as phase calibration by dispersion compensation (PCDC), correct for nonlinearities in tuning and dispersion by resampling the data, i.e. the photodetected signal corresponding to the channelled spectrum. Conventional processing is based on the phase variation over the wavenumber, employed in a suitable resampling of data that leads to a linear in-phase CS. The resampled CS is then subject to FFT, obtaining an A-Scan. The CMS technique does not require a linear variation of the CS phase. Using a few experimental spectra (at least two), two functions are obtained: a function $g\left(k\right)$, which describes the nonlinear tuning, and a function $h(k)$, related to the unbalanced dispersion in the interferometer. In the next section, we will show that due to different nonlinearities in sweeping between the two consecutive sweeps, a bidirectional sweeping laser requires more sophisticated signal processing than unidirectional sweeping lasers. The function $g\left(k\right)$ is responsible for such differences. The $g\left(k\right)$ and $h(k)$ functions are obtained here using several channelled spectra (minimum 2), collected for several optical path difference (OPD) values, when a model eye, including a lens and a mirror, are used as the sample. Once functions $g\left(k\right)$ and $h(k)$ are obtained, then all other shapes of channelled spectra can be inferred for any OPD using the protocol described in reference [206]. These theoretically inferred spectra are called masks, they are top hat channeled spectra, which are chirped due to sweeping nonlinearities. The masks obtained are unique for each sweep; hence, they are calculated for both forward and backward sweeps. This protocol was used with the FDML, and it will be exemplified here again.

OCT Interferometer & Acquisition – Numerical generation of masks

The instrument, presented in Figure 6.12, is a balanced interferometer composed of an 80/20 directional coupler where 20% of the light is guided towards the sample arm, and 80% towards the reference arm. The back-scattered light from the sample interferes with light from the reference arm in a 50:50 directional coupler before reaching a balanced photodetector.

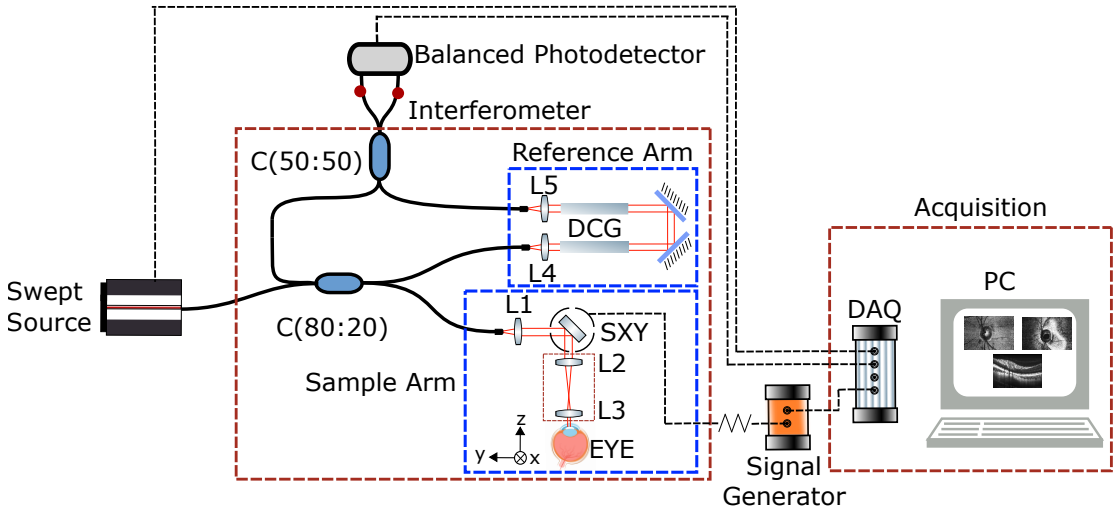

FIGURE 6.12: **Schematic of the SS-OCT system.** SS: MEMS-VCSEL swept source, Interferometer (C: couplers, TSL: translation stage launcher, DCG: dispersion compensating glass, SXY: 2-D Lateral scanning head, L1-5: lenses), Acquisition (DAQ: digitiser, BPD: balanced photodetector, PC: Computer); SG: Dual signal generator.

The output of the light source (OCTLight Aps, experimental version) includes a built-in booster that can deliver optical powers ranging from 20 mW to 40 mW. All the lenses used in the system are achromats with AR from 1050nm to 1600 nm. On the reference arm, the two lenses L4 and L5 are aspheric objective lenses with 15.6 mm focal length (Newport, 5726-C-H). On the sample arm, lens L1 is part of a fibre collimator (Thorlabs, F220APC-1064) that has an aspheric lens with a focal length of 11.16 mm, then lenses L2 and L3 are 2-inch lenses with 15 cm and 8 cm focal lengths, respectively. In the first experiment, the source was set to 20 mW. A system sensitivity of -90 dB was measured when the optical power on the sample was 1.9 mW. The light is conveyed via a galvanometer scanning head composed

of 2-D orthogonal scanners in the sample arm. For long axial range measurements, a high-speed oscilloscope (Teledyne Lecroy, WaveMaster 820Zi-B) was used for digitising the signal at the output, together with a 23 GHz bandwidth balanced photodetector (Optilab, BPR-23-M). For real-time imaging, the photodetected signal was digitised at 4 GS/s using an acquisition card (AlazarTech, ATS9373). Furthermore, the 23 GHz balanced photodetector was manually replaced with a balanced photodetector with lower noise, and higher gain was employed (Thorlabs, PDB482C-AC, 1 GHz). Real-time OCT imaging with this source does not need to capture multi-GHz signals. This can be understood in two ways: first, the penetration depth limits the axial range, i.e., objects will be placed near 0 OPD, and the total axial range will be the starting position of the sample plus the penetration depth, and second, the real-time digitised used here can only capture up to 2 GHz signals; therefore the noise captured at higher frequencies will only contribute to aliased noise which is not beneficial in this case. A LabVIEW software was created to enable real-time display of the OCT images using the CMS approach. The software simultaneously displays three images: a mean intensity projection, an *en-face* OCT image (C-scan), and a cross-section OCT image (B-Scan). To ensure synchronisation, the swept source triggers the acquisition card using a TTL signal, which operates in synchronism with the signal driving the galvanometer scanners.

6.3.2 Complex Master Slave Results

Two sets of 5 calibration channeled spectra are acquired, shifting the trigger delay from the λ-trigger to match the forward and backward sweeping. From the calibration spectra, the functions $g\left(k\right)$ for the forward and the backward sweep are obtained. As it can be seen in Figure 6.13(a) and Figure 6.13(b), the relative differences between the $g\left(k\right)$ functions corresponding to the two sweeps are very small, less than 1%. Figure 6.13(c) presents the output spectrum of the swept source. Although the differences between forward and backward calibration functions are

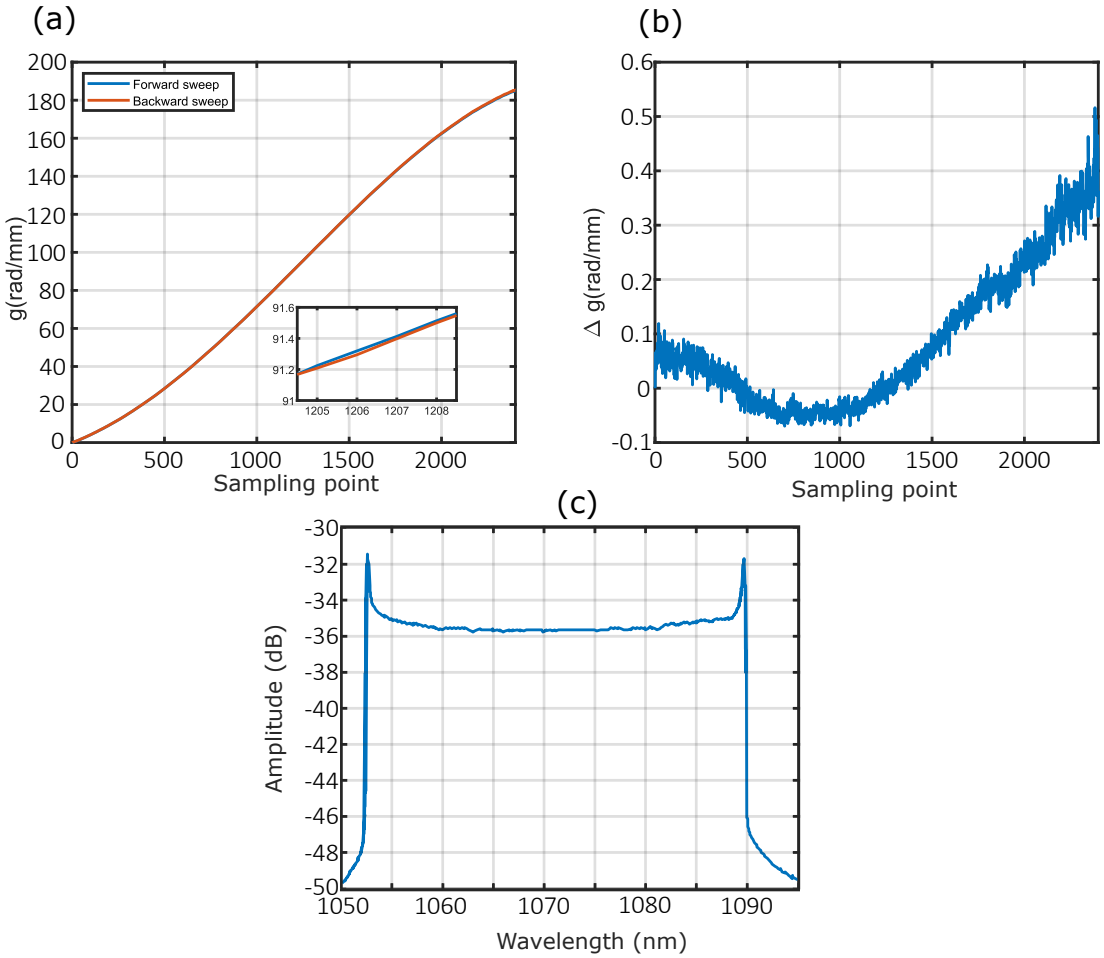

FIGURE 6.13: **Comparison forward and backward sweep.** (a) Forward and backward nonlinearities $g(k)$. (b) Differences on the $g(k)$ function between forward and backward sweep. (c) Output spectrum of the swept source.

small, the A-scans and B-scans obtained with a mirror are corrupted if the wrong masks are used, as demonstrated in Figure 6.14. In Figure 6.14 (a), the A-scan profiles are affected in shape and position. Even at a relatively small OPD, the resulting axial resolution is degraded by a factor of >3 when the incorrect set of masks is employed. When using the wrong masks, the experimental axial resolution worsens from $\sim 20\mu m$ to $\sim 70\mu m$ on the backwards sweep. This difference might increase noticeably at larger OPD values.

The coherence length of the MEMS-VCSEL used in this work can reach over 9 cm. Thus, processing the signal is crucial to match the axial range value with that of the coherence length. Figure 6.14(b) shows that the T-scan corresponding to the mirror surface is represented by two sets of small stripes of different extensions.

This demonstrates the need to perform separate signal processing on each sweep to use both sweep directions.

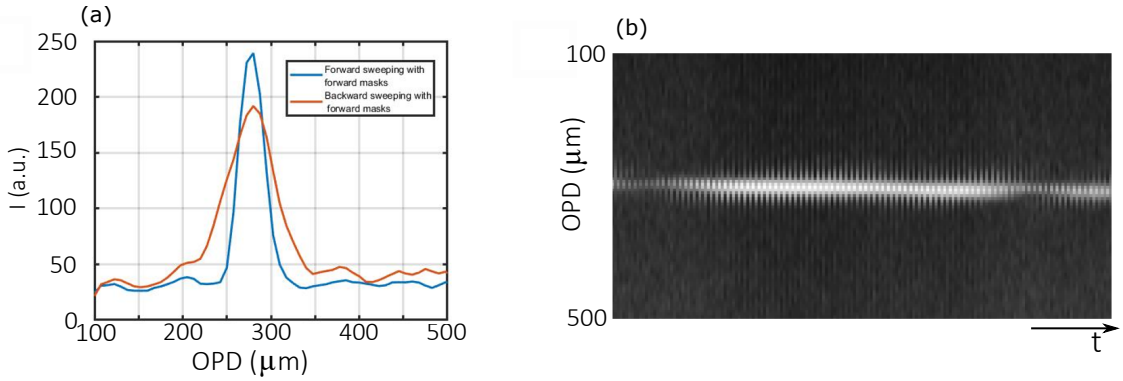

FIGURE 6.14: **Comparison forward sweep with backward sweep through A-scans using forward masks.** (a) A-Scan plots of consecutive sweeps, the forward (blue) and backward (red) sweep. (b) T-Scan, in which the masks of the forward sweep are used.

It was observed that once $g\,(k)$ and $h(k)$ is obtained and masks calculated, the calibration obtained does not guarantee good image processing over time. In less than 10 minutes, the thickness of the T-Scan increases. As a consequence of these sweep-to-sweep variations, the output peak as a result of the initial calibration differs, as shown in Figure 6.15. A mirror is placed in the sample arm to obtain a sharp peak for forward sweeping with the initial calibration, and channeled spectra are obtained every two minutes fora total of 10 minutes. Figure 6.15 shows the peak degradation over time; right after calibration, the FWHM of the peak is $\sim 20\mu m$, and after 10 minutes, the FWHM evolves to $\sim 45\mu m$. Although the reason behind the degradation is unknown, we expect this kind of behaviour from a mechanical swept source where temperature fluctuations can interfere with the position of the mirrors in the MEMS-VCSEL structure. Moreover, the peak height drops to half, hence the sensitivity of the system falls. After the first 10 minutes, the variations are less noticeable, and the axial resolution can be restored to $20\mu m$ if calibration is redone. Therefore, if OCT imaging based on CMS is to be performed, it would be recommended to wait for mask collection until the transit time is finished. Once the transit time is finished, the roll-off of the OCT system is

measured using the Teledyne high-speed scope that allows measurements in the GHz range.

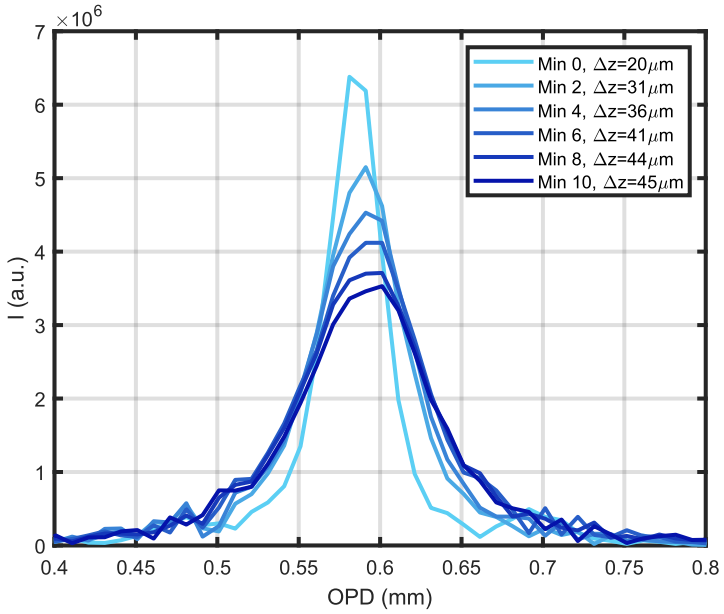

FIGURE 6.15: **A-Scan over time.** A-Scans produced by CMS with the same calibration files over 10 minutes from powering up the source.

Figure 6.16 depicts the calibration masks $g(k)$ and $h(k)$ used to generate the OCT images. Furthermore, Figure 6.16 (b) displays multiple A-Scans with the mirror at different OPDs. A decay in the peak of 0.06 dB/mm was observed within the first 10 mm displacement in OPD. Consequently, the estimated axial range at -6 dB of the source is obtained at 90 mm. From the digitisers perspective, there is almost no decay along the first 10 mm, which makes it ideal for long range applications, such as the anterior segment of the eye.

At first, to test the depth capabilities of the source, the OCT is adapted for retinal imaging. Figure 6.17(a) shows the mean intensity projection image obtained simultaneously with the *en-face* and B-scans. Figure 6.17(b) shows an averaged B-scan composed of 200 B-scans, continuously acquired at a line rate of 1 kHz. The montage presented in Figure 6.17(c) is composed of 36 *en-face* images recorded sequentially in real-time at a rate of 4 Hz (0.2 s to acquire the volumetric data and 50 ms to process it). To produce it, the axial position of the eye was fixed, while the selection of the axial position where the *en-face* was produced, performed by the

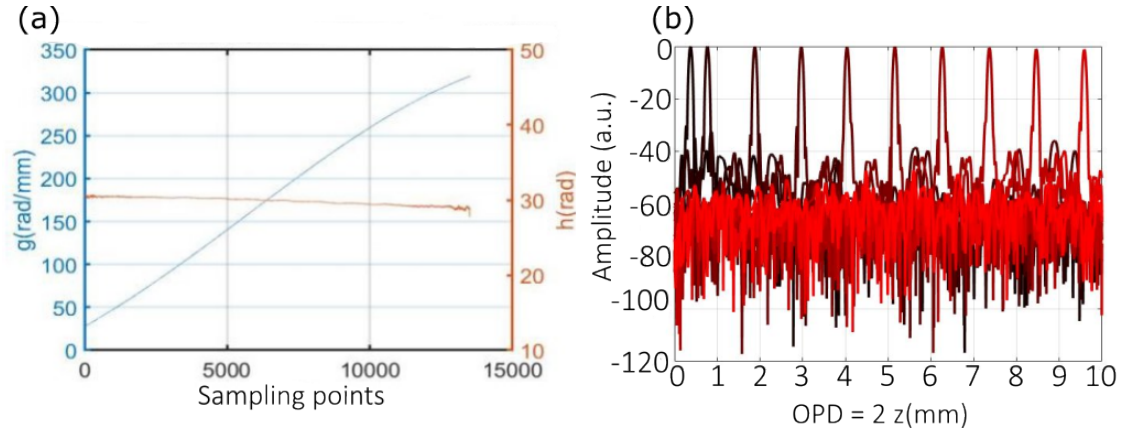

FIGURE 6.16: **Long range performance of the MEMS-VCSEL:** (a) Dispersion and nonlinearities functions $g(k)$ and $h(k)$ from a set of 10 masks. (b) Roll-off of the source in logarithmic scale, composed of multiple single A-Scans at different depths from 0.2 mm to 9.6 mm OPD.

CMS processing, was varied from OPD = 0.1 mm up to 1.6 mm by changing the mask. For the lateral x-direction, the line (fast) lateral scanner is driven with a triangular shape at 1 kHz and an amplitude of 1.5 V. The corresponding lateral size covers approximately 3.7 mm on the retina. In the y-direction, 200 points were used, corresponding to an amplitude of 0.85 V applied to the frame galvanometer scanner, corresponding to 1.8 mm. Figure 6.17(d) is a depth colour-coded image projection of all *en-face* images generated in a 3D volume acquired at 4 Hz.

By the time these images were obtained, a digitiser of only 500 MSa/s was in use (AlazarTech, ATS9350). This limited the maximum axial range that was possible to acquire during imaging. A continuation of this work utilised a different acquisition card within the same computer, with a sampling rate of 4 GSa/s (AlazarTech, ATS9373) and therefore extending the maximum axial range to more than 10 mm. Figure 6.18 shows a new set of images acquired with the latest acquisition card. In this new version, the display is done using a single ramp. However, the display image was used only for guidance; the data was acquired and composed in an external software using both ramps. The LabView software for image display allows the addition of a delay from the electronic trigger to the captured CS. Before the image session, a set of calibration masks is obtained with the forward sweep. Afterwards, the trigger delay is shifted to accommodate the

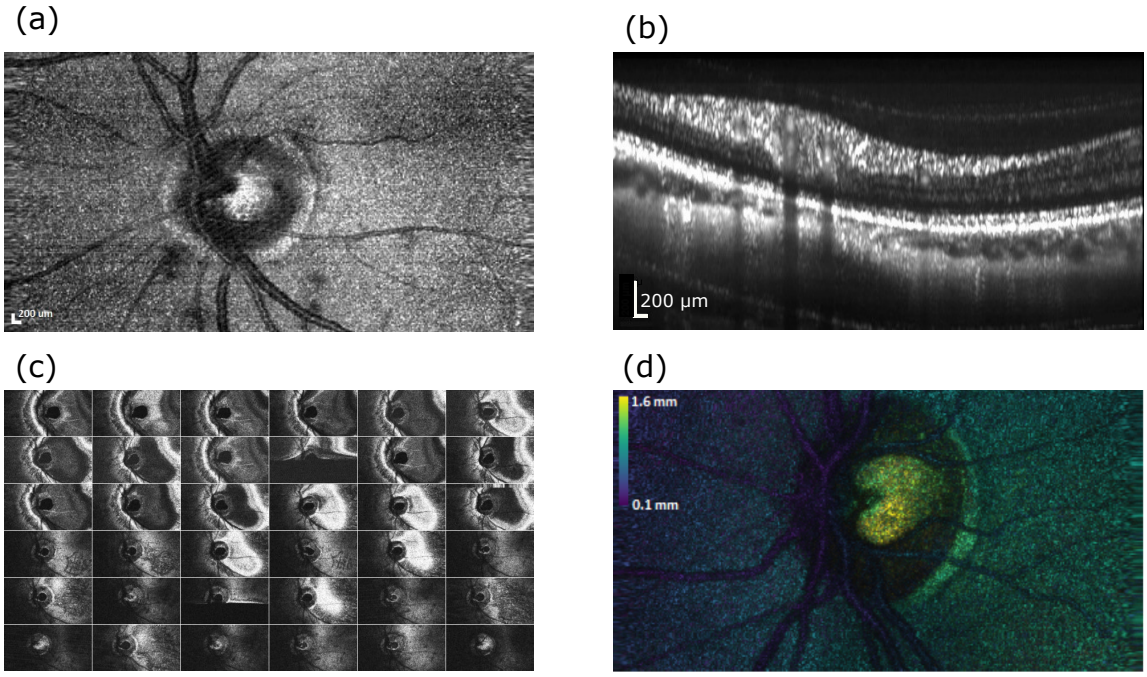

FIGURE 6.17: **Retinal OCT images using a 500 MSa/s digitiser.**(a) Mean intensity projection Image from the optic nerve. (b) B-Scan image from the surrounding areas of the optic nerve. (c) Montage of 36 *en-face* scrolled axially in real-time. (d) Depth colour-coded display of a volume.

backward sweep, and another set of masks is acquired. Once both sets of masks are acquired, the functions $g(k)$ and $h(k)$ are calculated. These functions allow the generation of any number of masks. Once these are produced, everything is set for the imaging session to start. The volunteer is asked to place his head on the chin rest, and images are collected at different scanning speeds and image sizes.

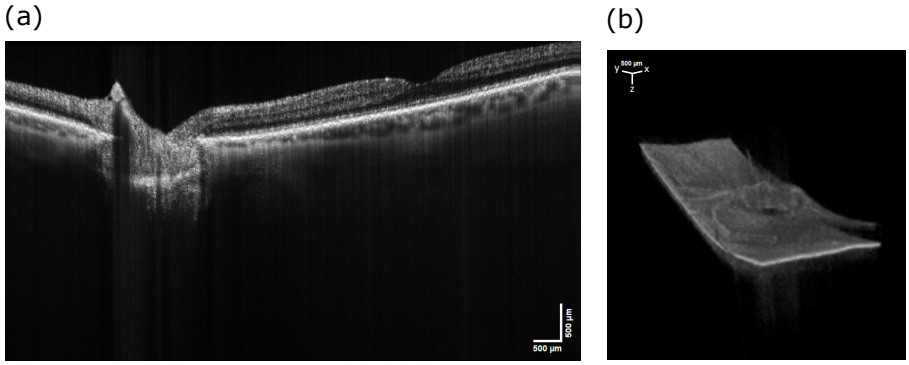

FIGURE 6.18: **Retinal OCT images using a 4GSa/s digitiser.** (a) B-Scan of the retina where at 800 Hz using 2 V using forward and backward sweep. (b) Volume of the retina for the optic nerve area using 800 x 500 x 300 resolvable points using and both sweeps.

Figure 6.18(a) presents 8 times averaged B-Scan computed with both ramps,

2V applied to the scanners and a line rate of 800 Hz. Two key elements should be noted here: (i) the resolution of the source is sufficient to be able to distinguish multiple layers in the retina structure, with the brightest being the RPE layer, and (ii) the long axial range and depth penetration of the source allows good penetration in the choroid. In Figure 6.18(b), an OCT volume is captured from the optic nerve region, composed of both ramps of the swept source.

The long axial range of the swept source allows for retinal imaging and exploration of anterior segment features. As shown in Figure 6.19 (a), the sample arm is slightly modified, adding a lens L4 of 19 mm focal length, focusing the scanned beam on the cornea. The B-Scans shown in Figure 6.19 (b),(c) and the *en-face* on Figure 6.19 (d) are produced with both sweeps of the swept source.

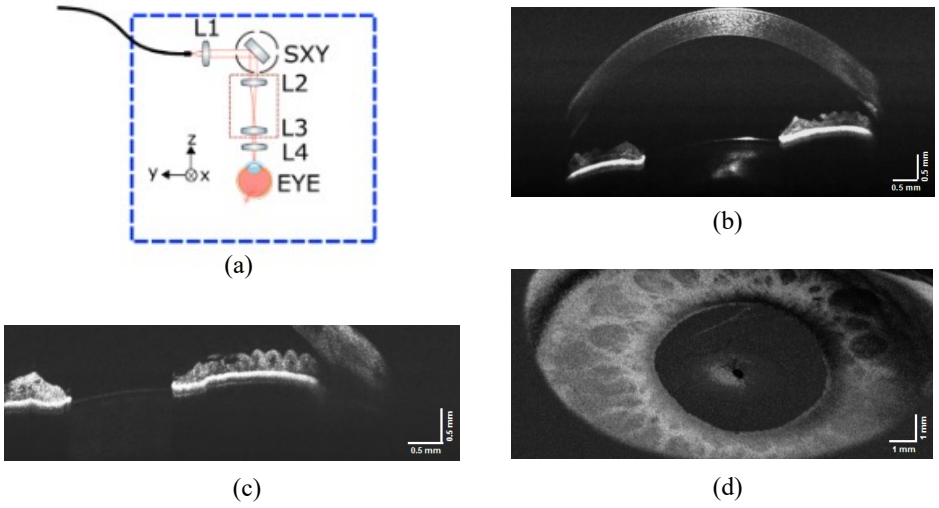

FIGURE 6.19: **OCT images of the posterior segment.** (a) Sample arm arrangement. (b) B-Scan of the anterior segment, corneal image. (c) B-Scan of the anterior segment focused on the iris and trabecular meshwork. (d) *En-face* image on the iris.

6.3.3 Downconversion Master Slave

The method proposed here is inspired by the Master Slave protocol [49], where the mask is generated in real time using another interferometer, called the Master. In principle, many Master interferometers can be used, or a single Master interferometer can be used sequentially on producing masks corresponding to

different OPD values. The photodetected signal obtained due to the modulation of the CS from the interferometer containing the sample (Slave interferometer) is then multiplied with the mask (delivered in real time by the Master interferometer), followed by integration over the whole sweep, obtaining an OCT signal for the depth corresponding to the OPD used to infer the mask. The strength of the result of such integration is nothing else but the amplitude of the A-scans for the depth in the sample selected by the OPD value of the mask.

In practice, the integration of the product of two CSs is performed using a RF analogue mixer. An analogue mixer produces the product of the two RF signals, obtaining signals pulsating at the addition and subtraction of the frequencies of the two RF signals. The subtraction signal is called a downconverted signal. Hence, the method is referred to as downconversion Master-Slave OCT. The interferometer shown in Figure 6.4 is now employed as the Slave interferometer, and a second interferometer acts as a Master interferometer, as initially described in reference [206]. The downconverted signal can be expressed as:

$$CS_1 = r_1 \sin[g(k)z_1 + h_1 k] \leftrightarrow CS_2 = \sum_{i=1}^{N} r_i \sin[g(k)z_i + h_2 k] \tag{6.1}$$

$$DMS\,(z_1 = z_i) = filter\,(CS_1 \times CS_2) = r_1^2\,\cos\left(\Delta h\,(k) + \phi_{rand}\right) \tag{6.2}$$

Here, DMS is the downconverted signal, $g\,(k)$ the nonlinearity due to tuning and $h_i(k)$ uncompensated dispersion in each interferometer. As a result, when both signals exhibit the same modulation periodicity, i.e. they are obtained for the same imaging depth $z_1 = z_2$, the output signal is at its main peak. A low-pass filter is used after the mixing to eliminate the signals oscillating at the sum of frequencies.

Figure 6.20 was produced by simulating the channelled spectrum in Matlab using a source with a central wavelength of 1060 nm and 90 nm bandwidth. The simulation code is shown in Appendix C. A Gaussian shape was used for the spectrum envelope. Nonlinearities in sweeping are introduced by a cosine

function in k. The same reflectivity value has been considered for two scattering centres in the object, determining OPDs of z_1 and z_2. In Figure 6.20, the photodetected signal obtained due to the modulation of the CS at the Slave interferometer output delivered by BPD1 is shown in the first row, either for a mirror placed at a distance that determines z_1 in the first column, or larger z_2 in the second column, the plots have been normalized. The balanced signal is simulated, creating a positive and a negative copy with a phase shift of the interference signal. Then, the third column shows the slave signal in the case of an object composed of two interfaces at z_1 and z_2. This is obtained by the simple addition of channelled spectra modulations according to (1). In the second row, the signal mask delivered at the output of BPD2 by the master interferometer (2) is shown for an OPD in the master interferometer chosen to match the OPD in the slave interferometer, i.e. $z_M = z_1$. Their multiplication is demonstrated by the mixed signal (3), in the third row. The integral values of oscillations during the sweeping interval, τ, are shown at (4). In the simulation, the integral value is calculated as:

$$\text{Integral Value} = \int_{k_0-\Delta k/2}^{k_0+\Delta k/2} \frac{I_D(z_1,k)I_D(z_1,k)}{\max\{I_D(z_1,k)I_D(z_1,k)\}}dk \tag{6.3}$$

for the case of the channelled spectrum at two different depths z_1 and z_2, i.e. $I_D(z_1,k)$ and $I_D(z_2,k)$. As the integral from Eq. 6.3.3 is proportional to the area of the multiplied interferograms, which are each expressed in volts, then the units of the integral are $[\text{V}^2/nm]$. The multiplied result in the third row for the same OPD in both interferometers is shown in column 1, displaying a large DC value and the integration from the simulation result of 277.5 $[\text{V}^2/nm]$. The DMS operation recognizes in this way the existence of modulation in the channelled spectrum from the Slave interferometer, similar to that selected by the OPD in the Master interferometer. If in the Slave interferometer, the interface is moved to z_2, i.e. for the case in column 2, then the multiplied result exhibits oscillations with areas

above the axis and areas below the axis, leading to much lower integration results than 0.2 $[V^2/nm]$. This low value means that in the channelled spectrum at the Slave interferometer output, there is no component pulsating with the same modulation rate in the channelled spectrum of the Master interferometer, determined by z_1. In the last column, 3, third row, again, DMS recognizes the existence of modulation for OPD selected in the Master interferometer for an object consisting of two interfaces, at z_1 and z_2, by a large value of the integration calculation of 181.6 $[V^2/nm]$.

A low-pass filter cleans the signal. Its cut-off frequency should be according to Nyquist $2/\tau$ to conserve the bandwidth of lateral scanning over each pixel [237]. DMS delivers significant DC components only for mixing signals that differ in frequency by less than the bandwidth of the low-pass filter, i.e. favouring signal from the depth corresponding to the OPD used to infer the mask. The strength of the result of such an integration is nothing but the amplitude of the A-scan for the depth in the sample selected by the OPD value of the mask.

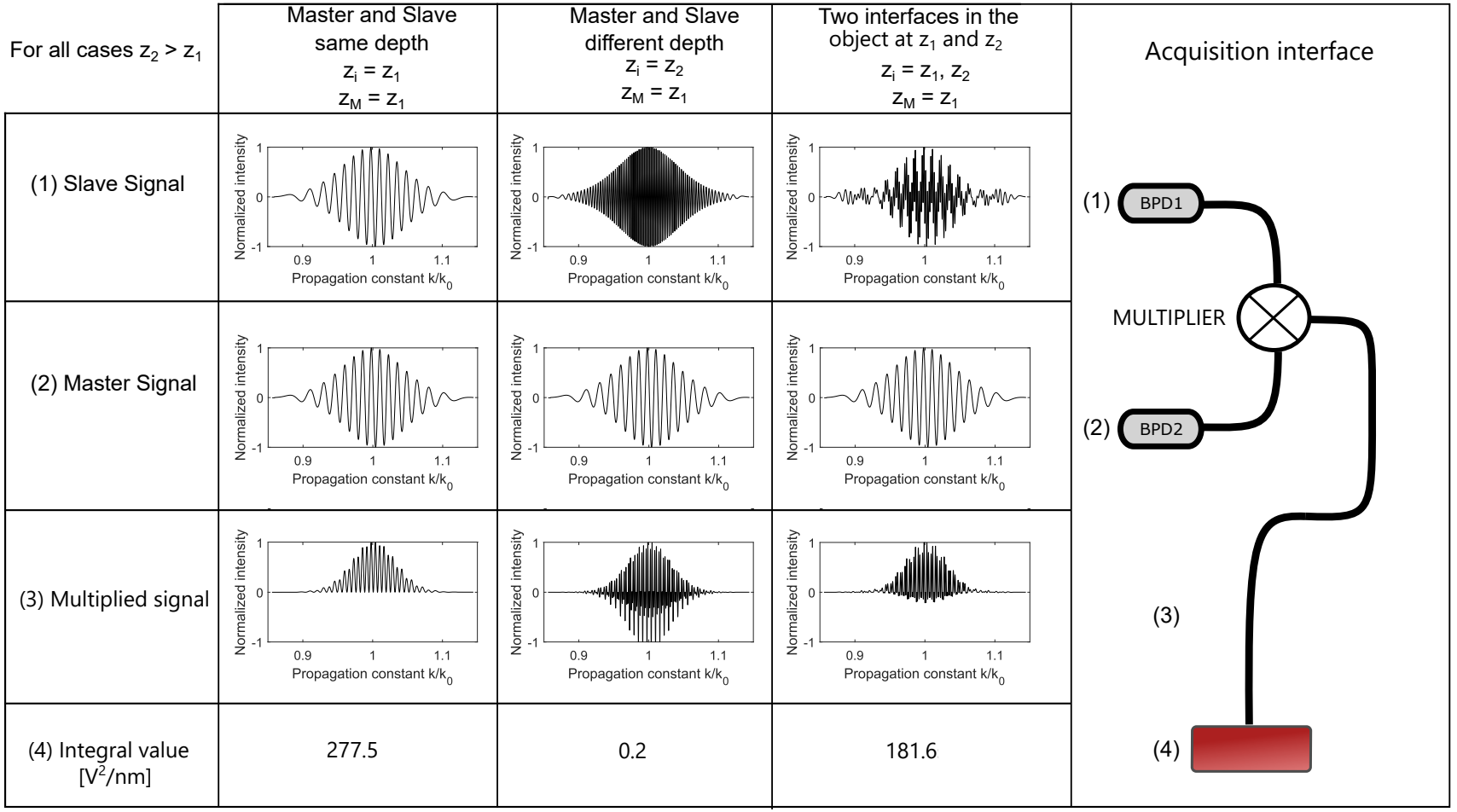

FIGURE 6.20: Signal evolution from the two photodetectors blocks through multiplication and integration. (1) and (2) BPD1.2: Balanced photodetectors. (3) Multiplier. (4) Computer, signal integrator.

OCT Interferometers & Display – Real-time generation of masks

The output power from the swept source is split with a broadband 95/5 coupler to the Master and Slave interferometer, with larger power to the slave interferometer. As seen in Figure 6.21, both interferometers employ a broadband directional coupler, 20/80. In both interferometers, 80% is sent to the recirculating reference path. The light from the two arms is then recombined in a 50/50 coupler, whose outputs are connected to balanced photodetectors, BPD1 (Thorlabs, PDB482C-AC, 1 GHz). The two interferometers are similar, with the only difference being that of a lateral 2D scanner, which consists of two orthogonal galvo-scanners in the object arm of the Slave interferometers. Lens L1 is a 3 cm focal length (Thorlabs, AC254-030-B), and L2-L7 are aspheric objective lenses (Newport, 5724-C-H). In order to couple the light into the fibres, as shown in the reference arms of both interferometers of Fig. 6.21, a 3D stage is attached to a fibre optic positioner mount (FPR2-C1A, Newport), and the lens are placed in front of the mount. Glass rods minimise the unbalanced dispersion between the two interferometers. The RF electrical signals from BPD1, the Master, and BPD2, the Slave, are sent towards the local oscillator (LO) and radio frequency (RF) inputs, respectively, of a double-balanced passive mixer (Minicircuits, ZFM-4-S+). The output signal is then amplified and filtered using a filtered preamplifier, S&F (Stanford Research, SR560). The output signal from S&F is then digitised with a slow digitiser (NI PCI 6132, 2.5 MSa/s) and the low-frequency signal is displayed in the form of an *en-face* OCT image. A custom software delivers a real-time *en-face* image, where the number of lines in the frame, speed of the scanners and gain in the images can be modified.

When using an FFT processor, the signal from the OCT interferometer is multiplied numerically with that of harmonics; here, the multiplication is done using an RF mixer, and the role of each harmonic is replaced by the chirped signal generated by a Master interferometer.

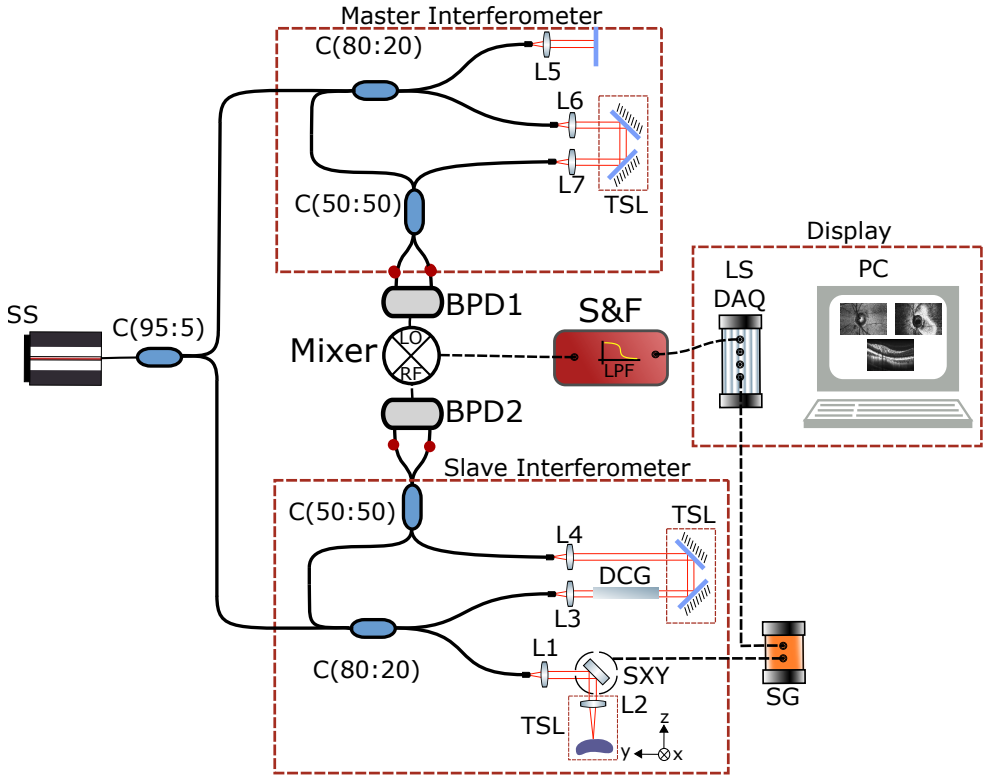

FIGURE 6.21: **Schematic of the DMS-OCT system.** SS: MEMS-VCSEL swept source, Interferometers (C: Couplers, TSL: Translation stage launcher, DCG: dispersion compensating glass, SXY: 2-D Lateral Scanning head, L1-8: lenses), Display (LS DAQ: Low speed digitised, BPD: balanced photodetector, PC: Computer, S&F: signal amplifier and filter); SG: Dual signal generator.

6.3.4 Downconversion Master Slave results

With the Master interferometer set at a chosen OPD value, the axial resolution can be estimated by changing the OPD in the Slave interferometer when the object is a single surface reflector (mirror). This procedure is different from Figure 6.14, where the axial resolution is obtained from the FFT or MS protocol, giving an A-scan peak whose width along the axial extension of the A-scan is measured. Two measurements are presented:

In the first method, the axial resolution was measured from the RF spectrum analyser of the mixer signal, close to $|\text{OPD}_M - \text{OPD}_S| = 0$. For this, the lateral scanning was stopped, and we first identified the relation between OPD and frequency, corresponding to $12.8\mu m/MHz$. From this conversion, the width of the peak generated from the mixer is measured to be 5 MHz, corresponding to $32\mu m$

axial resolution along the depth, as shown in Fig. 6.22. In order to evaluate the sweep-to-sweep variations, the RF signal at the mixer output was recorded in intervals of two minutes during a total span of ten minutes, as in CMS. As in Fig. 6.15, if the sweep-to-sweep variations are not corrected, we would expect 6.22 to exhibit similar behaviour on the width of the peaks. The curve presented in Fig. 6.22 has been smoothed over the maxima of multiple peaks for proper visualisation. In Figure 6.22, no significant variation of the width peak is observed, as shown by consistent axial resolution over time, even during the initial time interval of the laser thermal stabilization.

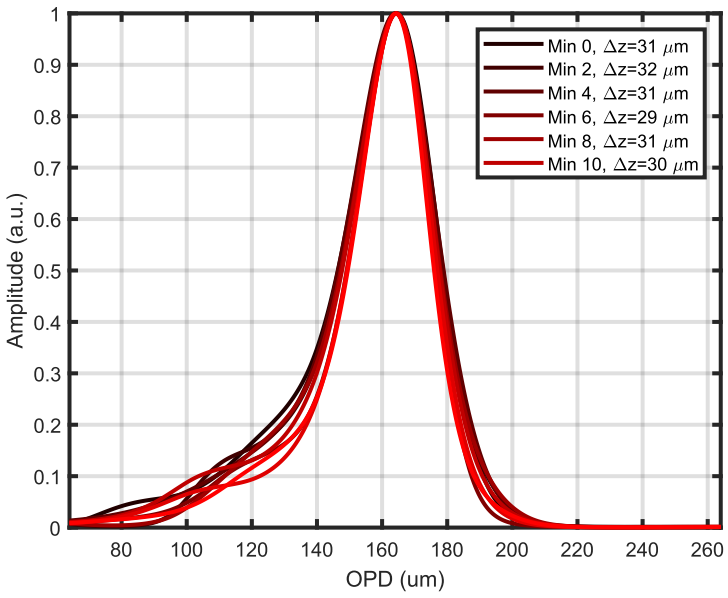

FIGURE 6.22: **Stability of the axial resolution.**Output of the beating signal measured through an RF analyzer. 6 graphs superposed, acquired at a 2-minute interval between them.

In the 2nd method, the axial resolution is inferred from the projection of the coherence gate over the *en-face* OCT image of a tilted single surface object. Figure 6.23 (a) shows the *en-face* OCT image of a coin. A plain section on the coin surface was used. The coherence gate width was evaluated along the yellow line displayed on the image. The brightness variation along the yellow line in the OCT *en-face* in Figure 6.23 (a) is represented in Figure 6.23 (b). A set of 6 consecutive

images have been acquired every 2 minutes over a period of 10 minutes. Overall, the axial resolution measured by the system is $\Delta z = 32\mu m$ on average.

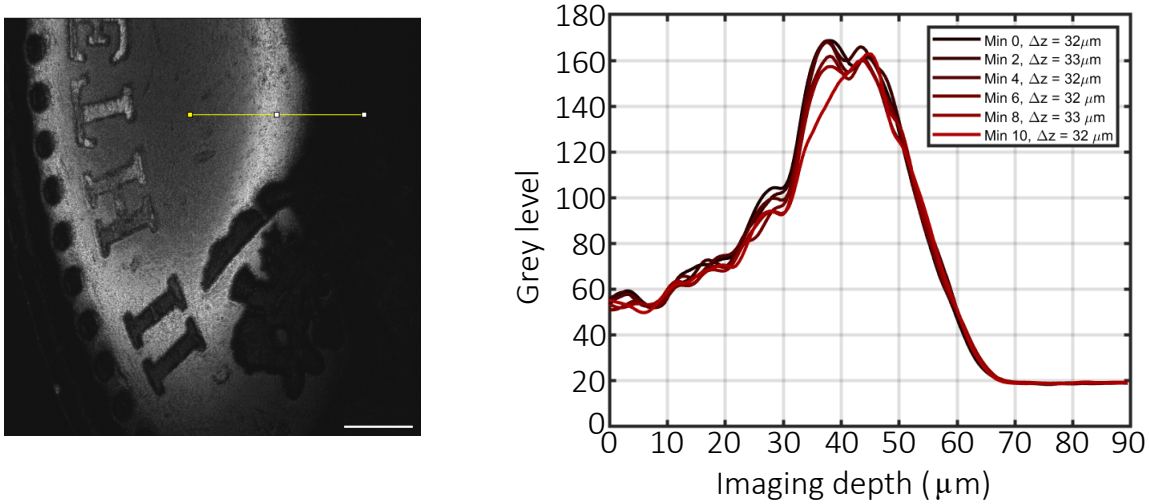

FIGURE 6.23: **Indirect evaluation of the DMS system axial resolution via *en-face* OCT imaging** (a) *En-face* image of a coin, scale bar 1 mm, image size 6.09 mm $\times$ 6.09 mm. (b) Signal strength along the horizontal yellow line over the image in (a), made from average of 10 acquisitions, separated by 2 minutes intervals.

In both experiments, it can be highlighted that the variations of the tuning curves from sweep to sweep do not alter the resolution. The axial resolution in the DMS system drops slightly below the bandwidth-limited resolution of the source. In fact, the unmatched uncompensated dispersion between the master and slave interferometer degrades the resolution, which is a disadvantage of the DMS method. We define here the unmatched uncompensated dispersion as the following: each interferometer is composed of a reference and a sample arm, which might have slightly different optics or fibres in place; therefore, even though the OPD is the same, the dispersion might be different, which is later calibrated with the $h(k)$ function in CMS. However, in DMS, we have two interferometers, and therefore there are two different $h(k)$ functions, which brings the unmatched uncompensated dispersion as the difference between them, $h_{master}(k) - h_{slave}(k)$, where $h_{master}(k)$ is the uncompensated dispersion from the master interferometer, and $h_{slave}(k)$ is the uncompensated dispersion from the slave interferometer. Hereby, the differences between the theoretical and experimental values

strongly depend on the mismatch. The sensitivity was measured with 1.9 mW in the sample arm, obtaining 72 dB. Fig. 6.23 illustrates the possibility of evaluating the coherence gate width employing a single *en-face* OCT image of a flat tilted surface. If the flat surface is oriented exactly normal to the axis, all its points are within the coherence gate and all would be bright or dark when moving the OPD in the Master interferometer. In case the surface is tilted by an angle α, then the coherence gate is projected over the *en-face* map in a stripe of width e. Considering the coherence gate of thickness δ along depth, the lateral extension e is:

$$e = \delta / \tan \alpha \tag{6.4}$$

In the image in Fig.6.23(a), $\alpha = 20$ and using $e = 1$mm, leading to an axial resolution of $\delta \sim 35\mu$m.

The curve in Fig. 6.23 represents the profile of the coherence gate. This shows in real time the capability of the downconversion OCT to select scattering centres in depth. Apart from the possibility to evaluate the axial resolution achievable via the FWHM measured on such a profile, we also note its asymmetry. This may be the result of some mismatch in the delay of photodetected signals from the photodetectors in the two interferometers, up to the mixer inputs. A justification along these lines is presented in Appendix D.

The functionality of the system is demonstrated with images of a coin, shown in Figure 6.24. The fast galvanometer scanner is driven at 500 Hz and 7.8 Vpp with a triangular signal. This means that each T-scan is obtained at 1 kHz. The slow scanner moves through 512 points in the orthogonal direction, driven by a sawtooth signal. The voltage applied is equivalent to a lateral size of 6.10 mm using a 3 cm focal length lens. Both ramps of the fast scanners are used; together, the fast and slow scanners form a square image. The following images are generated with 1.9 mW on the sample. Figure 6.24 shows 4 *en-face* images for different

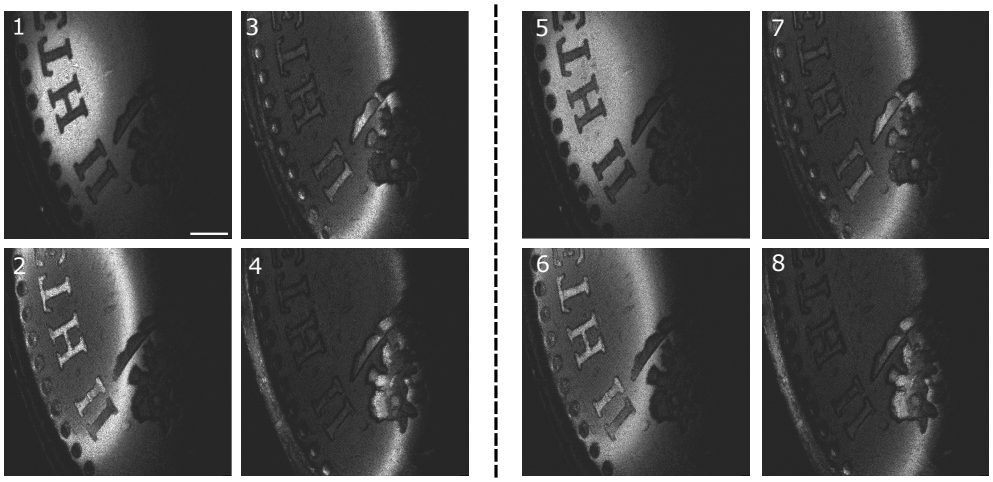

FIGURE 6.24: *En-face* images generated by DMS. Each set of *en-face* OCT images was collected at 4 different OPD values in the master interferometer. (1)-(4) *En-face* images at $f_{modulation} = 300$ MHz in the Master interferometer, i.e. OPD =3.84 mm, (5)-(8) *en-face* images at $f_{modulation} = 600$ MHz in the slave interferometer, OPD = 7.68 mm. Scale bar 1 mm, applies for all images, image size 6.09 mm $\times$ 6.09 mm.

values of the OPD in the Master interferometer, stepped at 100 microns in panels (1)-(4), acquired from a starting point of $f_{modulation} = 300$ MHz corresponding to an OPD=3.84 mm, in both interferometers. Initially, the reference arm of the slave interferometer is actuated until the $f_{modulation} = 300$ MHz is reached, then the reference arm of the master interferometer is placed at the same frequency, and finally the translation stage is actuated in steps of $100\mu m$. In panels (5)-(8), the images are repeated at the same step of 100 microns from a starting frequency of 600 MHz, which corresponds to an OPD of 7.68 mm. The coherence gate, as the area where both interferometers coincide, is visible in both sets of images, being the bright white area on the images. During the imaging process, the position of the translation stage in the reference arm of the master interferometer was manually adjusted.

In order to demonstrate the capabilities of our system against moving objects, we imaged a human thumb. The power of the swept source was increased to the point where the sample plane received 2.9 mW. The scanning speed was increased to 1 kHz for the fast scanner while preserving the same number of lines. As a consequence, the frame rate was doubled to 10 Hz. The image size remained

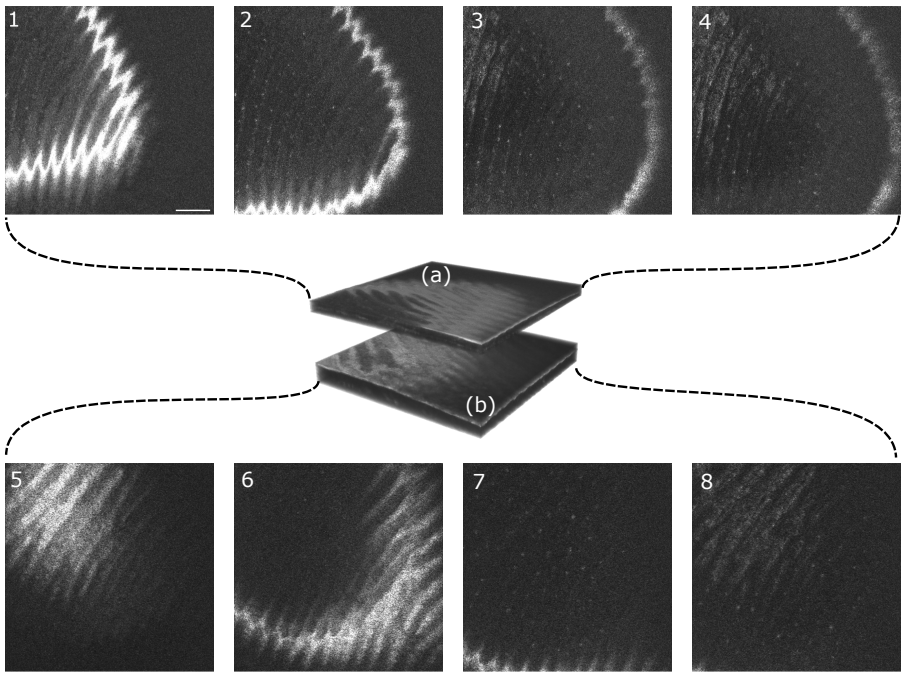

FIGURE 6.25: **In-vivo *en-face*** images generated by DMS. Each row represents a set of images acquired at significantly different OPDs of the master interferometer, 3.84 mm and 12.8mm, respectively. (1)-(4) *En-face* images generated at an OPD correspondent to 3.84 mm and $f_{modulation} = 300$ MHz (a) Volume representation of the consecutive *en-face* images acquired around 3.84 mm OPD. (5)-(8) *En-face* images generated at OPD $= 12.8$ mm and $f_{modulation} = 1,000$ MHz. (b) Volume representation of the consecutive *en-face* images acquired around 12.8 mm OPD. Scale bar 1 mm, applies for all images, image size 6.09 mm $\times$ 6.09 mm.

constant during the imaging session with 7.8 Vpp. Since both ramps of the galvo scanners are used, an effective T-Scan is produced at 2 kHz. The first set shown in Figure 6.25 (1)-(4) is generated at $f = 300$ MHz, and the second set (5)-(8) at $f = 1,000$ MHz. Those two sets were acquired at different times. The white band seen in Figure 6.25 (1) corresponds to the coherence gate through the fingerprint, sampling the stratum corneum. As the OPD is varied in the Master interferometer, the coherence gate moves through the finger, in Figure 6.25 (2) the sweat ducts are visible on the left side of the image. At a deeper layer, the epidermis can be observed on the left side of Figure 6.25 (4). The volume represented in Figure 6.25 (a)-(b), is an illustration of volumes reconstructed after scrolling through the reference stage in the master interferometer, with both sets at different OPDs. Volume reconstruction is done post-processing, where the images are registered

axially. Although the source allows for larger OPD, the photodetector used here limits the maximum axial range for the system. A higher frequency balanced photodetector may extend the capabilities of this system.

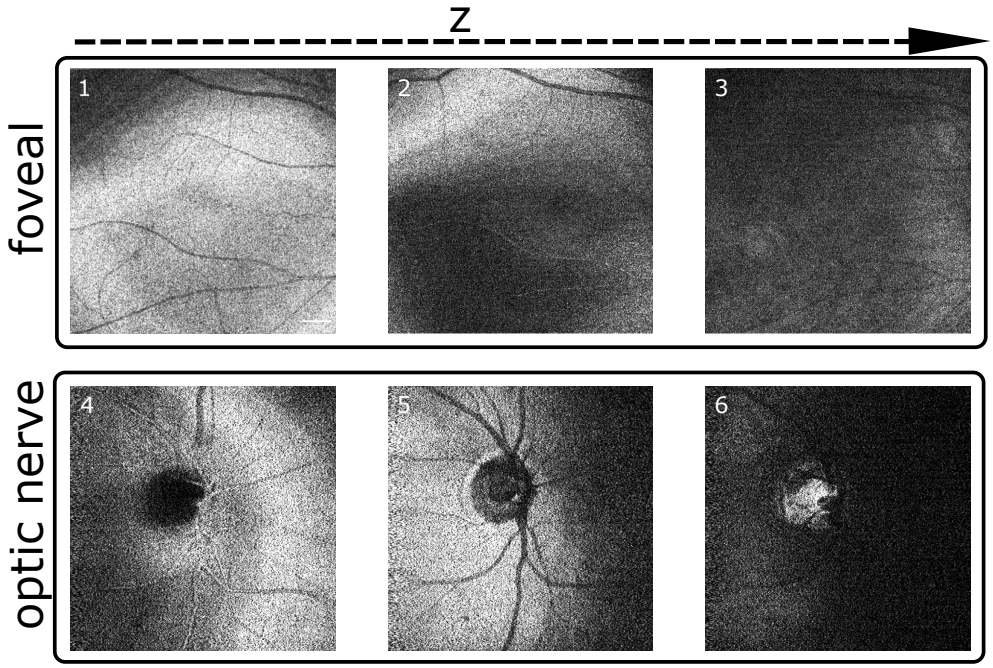

FIGURE 6.26: In-vivo *en-face* eye images generated by DMS. (1)-(3) *En-face* images of the foveal area, generated at an OPD corresponding to 1.92 mm and $f_{modulation} = 150$ MHz (4)-(6) *En-face* images of the optic nerve area, generated at an OPD correspondent to 1.92 mm and $f_{modulation} = 150$ MHz. Scale bar 1 mm, image size 9.3mm $\times$ 9.3mm.

Moreover, the slave interferometer is adapted for eye imaging; in fact, the interferometer in Figure 6.12 is used as a Slave with the Master interferometer of Figure 6.21. The same chin rest is used as that in Figure 6.3 to stabilize the patient's head and limit head movement. The fast galvo runs at 1 kHz and the slow scanner at 4 Hz, both driven by 3.4 Vpp. These voltages determine a square image of 9.3 mm × 9.3 mm lateral size. For this measurement, the Master interferometer was set to $f = 150$ MHz, corresponding to an OPD of 1.92 mm. In Figure 6.26 (1)-(3), three different *en-face* images of the foveal area are presented at various depths. The same occurs in the consecutive images in depth in Figure 6.26 (4)-(6) from the optic nerve. The coherence gate is moved axially by actuating the reference arm of the slave interferometer. In this way, the visualisation of deeper

layers is possible. This can be seen in Figure 6.26 (4) and (6), while in (6), the lamina cribosa is seen bright. In Figure 6.26 (6), the other pixels are closer to the anterior part of the eye, well outside the depth of the lamina; hence, they appear dark.

6.3.5 Comparing numerical procedures with DMS

Figure 6.27 provides a comparative flow chart graphical representation of the two methods under consideration, namely the conventional numerical protocol (CNP) and DMS.

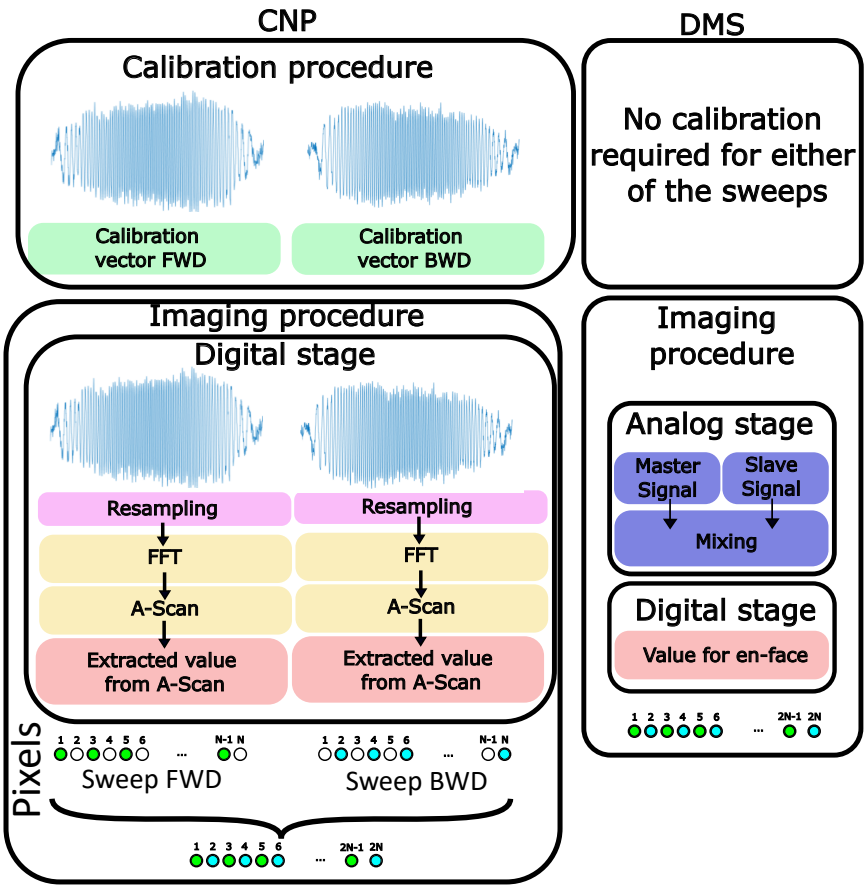

FIGURE 6.27: Comparison of conventional numerical protocol (left) and down-conversion (right).

On the left of Figure 6.27, conventional numerical procedures (FFT or CMS) are shown; the two columns of steps illustrate the need for separate processing

steps for each sweep. When using FFT, calibration handles a separate vector of data for backward and forward sweeping. In FFT, the calibration vector contains data resampled according to each sweep. Only after data is resampled can an FFT be computed. For CMS, this may mean different masks. CMS uses the raw data but requires masks to perform the CMS protocol on each sweep.

A major challenge when utilising computational phase compensation methods is their inability to correct for sweeping changes over time. This is because the calibration masks are obtained only once during the process, and if the phase alters for any reason, the acquired masks will not account for these fluctuations. Thus, sweeping stabilisation is typically necessary when utilising computational phase methods. However, in the case of downconversion Master-Slave, the sweep changes take place in both interferometers at the same time, resulting in no degradation of their mixing over time due to sweep variations. This means the "masks" are generated in real-time for each *en-face* image, enhancing the system's tolerance to sweep-to-sweep variances.

Digitisers are available for several MHz (up to 12 GSa/s, the fastest in the market, and 10GB per second data throughput) swept sources, and processed data may still be produced with a maximum delay of one lateral scan or one volume, i.e. quasi-real-time and acceptable if the time lag is not too high. For larger than a few MHz sweeping rates, digital oscilloscopes are needed, where data is sampled at a much higher speed (100 GSa/s for the fastest oscilloscopes), but data obtained is stored locally [71, 238]. This precludes any chance of real-time processing, as data transfer may require a few minutes. Even if the system is perfectly designed with zero dispersion and fully linear, where no operation apart from an FFT is required, such as in *k*-clock systems, the signal still requires digitisation. In fact, those mentioned are only technological limits which, in the future, is reasonable to think that higher data-transfer rates (1TB per second data throughput) and higher computational power with more efficient algorithms will be possible.

On the left of Figure 6.27, N pixels are along the lateral direction, $N = T/(2\tau)$, where τ is the sweep time, with period of sweeping 2τ and period of lateral scanning $2T$. Each image has M pixels. To produce an image with both sweeps, the conventional procedure on the left requires interlacing of the two images, with an image for each sweep. The raw signal is used using the DMS, as shown in Figure 6.27 right, like in CMS with numerical production of masks. The difference is that the masks are generated in real time.

The DMS proceeds on both sweeps continuously, and lateral pixels are created in the T-scan as the lateral scanner progresses, i.e., in the image, there will be alternative pixels due to each sweep. Interlacing the two T-scans or frames for each sweep to create an image based on alternate sweeps is not necessary when performing DMS. The DMS produces an *en-face* view with $2M$ pixels straight away, i.e. the image generated contains both sweeps (with no need for an extra operation of interlacing).

6.3.6 Discussions

Recent developments of fast-swept sources with long coherence lengths (a few cm) demand digitizers able to acquire tens of GHz. The dilemma of high-speed digitization to be used specifically in each sweeping direction is addressed by employing analogue mixing. Instead of sampling photodetected signals at the GHz rate, the digitizer needs to sample at a much lower rate (on the kHz range) than that of the sweeping rate.

In respect of using a digitizer to produce images corresponding to an axial range exceeding that determined by its sampling rate, there are already reports in the OCT literature. A two-input digitizer, with a limited sampling rate, was used to extend the axial range of a swept source OCT system by engaging two inputs in sampling a 0 and 90 degrees shifted replica of the photodetected signal [239]. Optical subsampling was proposed for objects of limited extension in

depth that can produce correct cross-section images of the object even if the object is placed at distances several times larger than its axial extension [240]. Using frequency combs, circular ranging was reported to image single-layer extended objects [185].

It is, therefore, interesting to place the DMS reported here in the landscape of other OCT methods that address the high sampling rates needed. Compared with other techniques that reduce the digitization burden, such as optical subsampling, DMS can correctly generate *en-face* images with no superposition from any other depth of an extended object. The object can be as extended in depth as the axial range determined by the instantaneous spectral linewidth [47, 234, 241]. In opposition, the optical subsampling will lead to an *en-face* slice with backscattered light from multiple depths outside that of interest. An *en-face* OCT image from any depth can be obtained with MS by simply changing the mask file (pre-stored from an experimentally collected channeled spectrum in [46] or from a pre-calculated mask [158]) or with DMS [234] by simply changing the optical path difference in the Master interferometer. Any depth means from the whole axial range determined by the spectral linewidth of the swept source [47, 241] and not restricted to a stripe in-depth as in optical subsampling. Furthermore, it is worth comparing the MS principle with frequency scanning interferometry (FSI), an existing technology widely used for large distance measurement [242–244]. In a typical FSI system, two interferometers are used, a reference interferometer and a measuring interferometer, both driven by a tunable laser. The MS, in its digital signal processing version, widely used by the Applied Optics Group in Kent, as well as the downconversion version, DMS, employ in principle two interferometers. The digital signal processing version utilises a single interferometer but in two steps. Therefore, the MS and FSI structurally use 3 similar blocks, a tunable laser and two interferometers. However, the principles and applications so far are different. In FSI, distances are measured based on the ratio of

two-phase measurements, where the two phases are determined by the OPD values in the two interferometers. This means that from the start, FSI cannot perform measurements on multi-layer objects; both interferometers need single-layer reflectors. FSI can cover by phase measurements a large range of OPD variation in the measurement interferometer but cannot be used to determine the distance between two reflectors along the measurement ray, as the phase would be scrambled. However, the same distance can be measured by the FSI if a single reflector is placed sequentially in the two positions. Because a ratio of phases gives the result in FSI, FSI does not suffer from nonlinearities in tuning. This is a problem for the digital version of the MS, the CMS, but not a problem for the DMS, as expected. This will make DMS closer in performance to the FSI. However, DMS can select from the many depths present in the spectrum by different modulations, the modulation that is similar to the modulation determined by the OPD in the Master interferometer. In other words, DMS involves the orthogonality of masks, which is characteristic of the MS method, i.e., spectra from OPDs that are different by more than an axial resolution interval satisfy the orthogonality condition. The integration over the wavenumber of the product of the two spectra leads to zero if the OPDs are different. FSI does not calculate any integral over the spectrum; only the phase is inferred. In doing so, being sensitive to phase, FSI can achieve, like in usual interferometry, sensitivity to subwavelength in relative measurements from a position in depth. In MS and DMS, axial resolution is determined by the tuning bandwidth exceeding several microns. However, the comparison can be pushed into the other direction. It cannot be said that MS ignores the phase. So far, the CMS phase has been discarded. Still, there are already studies in the Applied Optics Group to make use of the phase values of the masks and to compare them with the phases of the clock signal of the tunable laser, in order to eliminate the effect of tuning instabilities of the laser from one sweep to the next. As another example where subwavelength relative variation in depth was already obtained using MS and CMS, it was in the *en-face*

imaging of single-layer objects (unpublished results, research ongoing). In this case, it is not the intensity being displayed but the phase across the *en-face* view. In conclusion, there are similarities in structure, However, there are differences in both the method and objectives. The MS method is based on calculating an integral over the wavenumber of spectra obtained, multiplied by masks that reproduce the spectra themselves. The FSI method is based on the calculation of ratios of phases. In terms of objectives, the MS was created to provide an alternative avenue to both spectrometer based OCT and swept source based OCT, in: (i) producing an *en-face* view without assembly of A-scans in a volume and (ii) in producing equivalent information along the A-scans but without a FFT that suffers because of chirp. FSI was created to measure distances only. MS operates with scattering structures, collecting depth-resolved images from the volumes of the objects. FSI operate with single layer objects, mirrors. FSI may be used, if equipped with lateral scanners, to produce an *en-face* view from a single layer object (in which case there is no difference to DMS) but cannot be used to produce A-scans. MS and DMS use the data as it is, affected by the chirp. FSI also uses the data as it is; the phase ratio measurement is tolerant to chirp as well. Therefore, FSI does not need resampling, practised by the OCT community employing FFT. So both FSI and MS use the data as provided by tuning, while conventional spectral processing methods resample the data before FFT.

Overall, although both techniques employ a frequency-swept laser and interferometry, their aims and implementations vary significantly, rendering them suitable for distinct applications.

We anticipate that DMS may become more useful for sweeping rates exceeding 10 MHz, where only digital scopes can be used to sample the multi-GHz signal (>4 GHz), in which case the data acquired is stored and processed offline later [238, 245]. In such cases, the DMS may find a useful niche in providing real time information on the imaged sample. Overall, DMS is able to produce *en-face*

images without heavy computation and with low-bandwidth electronics. In practice, there are also losses, but not due to the principle, which has more to do with the device employed for producing the multiplication effect. As such, the passive Minicircuits, ZFM-4-S+ mixer, have a 7 dB conversion loss. There is also cross-talk between the inputs, RF, and LO signals on one side and the output on the other side. Perfecting the MS in a single interferometer, i.e. CMS using pre-calculated masks and performing calculations with a digitizer, leads to a sensitivity of 90 dB. Using the downconversion 72 dB was obtained. Most of the difference in sensitivity is attributed to uncompensated dispersion mismatch between interferometers. For future system designs, these issues can be amended by careful dispersion compensation, and use of electronics with lower figure noise.

However, there is a degrading factor: If deterministic oscillations (for example, reflections from the fibre outputs, a doublet used in the optics arrangement, PMD in the system) pulsate similarly in the two interferometers, these determine an extra noise source. When using FFT, the harmonics are clean. As well, when using CMS the masks are also clean (which employs pre-calculated masks). However, in DMS, pulsations seen in the two interferometers in a single arm create noise through the process of multiplication.

6.4 Conclusions

During this chapter, key challenges associated with swept sources that produce bidirectional sweeping have been addressed. In the first part, using the FDML source at 840 nm, the capabilities to produce high-quality images using both sweeps calibrated by CMS are investigated. CMS uses masks obtained by employing the same interferometer for both calibration and imaging. Once masks are generated, A-scans, B-scans, and C-scans can be obtained, similar to using the FFT-based method. Using bidirectional sweeping lasers, we demonstrate here that even minor variations in sweep between forward and backward scans can

substantially degrade the image quality, hence the need for separate processing of the signal obtained from each sweep direction. The results shown here prove the benefit of using different calibration procedures for each sweep, obtaining double the points in a B-Scan.

In the second part of the chapter, using the MEMS-VCSEL, two alternative imaging approaches are used, CMS and DMS, both based on the MS protocol. In addition, CMS or FFT-based methods often require calibration if sweeping parameters vary over time. Such an instability problem is addressed using the DMS-OCT procedure. In addition, the masks generated by DMS contain both sweeps straight away, eliminating the need for the interlacing steps required by both FFT-based and CMS-based methods. Tolerance of instabilities in $g\left(k\right)$ comes from the real-time generation of a chirped channelled spectrum in a Master interferometer driven by the same swept source. This means that the nonlinearity is the same in the Slave and Master interferometers, hence tolerance to g variation along the k coordinate. Therefore, mixing in DMS takes place between two photodetected signals suffering from similar chirp.

In terms of digitisation demands, CMS requires a digitiser to be able to cope with high-frequency modulation from the maximum OPD, i.e. when the OPD is at the maximum limit (axial range). If the coherence length of the swept source enables N cycles of modulation, then for sweeping at f, the maximum frequency is Nf, and according to Nyquist, the sampling rate should be at least $2Nf$. Irrespective of the frequency of the signal downconverted, DMS processes the signal at the rate of sweeping, i.e. f_s. Hence the reduction in digitisation demands is of the order of N.

Hence, an important advantage of the DMS is that the signal to be processed after the analogue mixer has a much lower bandwidth (i.e., downconverted in frequency, kHz range). In the case of this work, a 5 MSa/s digitiser was used with the DMS to acquire *en-face* images at an OPD=12.8 mm (equivalent to a modulation frequency of $\simeq$ 1 GHz) while using an FFT, a digitiser of at least 2

GSa/s is needed. Assuming the 2 GSa/s needed for numerical procedures while a 5 MSa/s is used, it represents a reduction of 400 times in the requirement of digitised bandwidth. In fact, a digitised with a sampling rate of only twice the sweeping rate would be sufficient. However, this is just a particular example of a given OPD. In theory, assuming the extreme cases, i.e. the downconverted signal is sampled by just the minimum frequency dictated by Nyquist and the maximum axial range, then we can compute the reduction as:

$$Reduction = \frac{f_{modulation}}{f_{downconverted}} = \frac{f_{SweepRate}\frac{OPD}{\lambda^2/\Delta\lambda^2}}{f_{SweepRate}/2} = 2\frac{OPD}{\lambda^2/\Delta\lambda} = 2\frac{\frac{2\ln 2}{\pi}\frac{\lambda^2}{\delta\lambda}}{\lambda^2/\Delta\lambda^2} = \frac{4\ln 2}{\pi}\frac{\Delta\lambda}{\delta\lambda} \tag{6.5}$$

which is approximately N. In Eq. 6.5, OPD reached the maximum axial range z_{-6dB}, $\delta\lambda$ is the instantaneous linewidth of the source, and $\Delta\lambda$ is the tunning bandwidth. Therefore, the reduction in digitising bandwidth is given by the maximum number of cycles in the channelled spectrum, approximately given by the ratio of tunning bandwidth and the instantaneous linewidth.

DMS presents a promising solution for bidirectional sweeping lasers thanks to its processing simplicity. This approach eliminates the need for separate resampling, additional calibration, or processing of the two separate sweeps. Moreover, it offers a cost-effective implementation by simplifying the digitisation process. Despite its limitations, such as a single depth per interferometer and potential dispersion mismatches between the Slave and Master interferometers impacting axial resolution, DMS presents advantages not matched by any other method, such as real-time delivery of *en-face* images at lower computational cost. Furthermore, several master interferometers can be utilized in practice with careful interferometric design. Nevertheless, the DMS capability can easily be attached as an add-on to any existing OCT system with minimal modifications to a functional setup.

Chapter 7

Conclusions

Over the last three decades, OCT has become a major biomedical imaging technique for the eye. Since its early start, the axial scan rate has increased from a few Hz to a few MHz. This speed improvement came with a series of challenges that needed to be addressed. Those challenges range from building the source to examining a new scanning deflector that can cope with the A-rate to, finally, the acquisition methods. However, it is important to mention the limitations and possible new lines of those systems presented in this thesis.

During Chapter 4, i.e. the first experimental chapter, it has been shown how a commercially available Erbium-doped amplifier can be used with minimal components to build a swept source. However, selecting those components is not trivial, and the outcome may vary significantly depending on the fibre chosen and its layout. Although mode-locking is achieved in all configurations, the output pulses' stability in terms of pulsewidth is seriously compromised depending on the action of the polarisation controller. Even though the pulsewidth does not impact the stretched pulse after the dispersive element, the amplitude variations do affect the outcome of the swept source. Such amplitude can be translated into high RIN, which is linked to the excess photon noise on the interferometer. Nevertheless, A-Scans of a glass plate as an OCT demonstration have been shown. Ideally, those instabilities should be tackled in the future to generate a reliable swept source. Different ways exist to overcome this issue: using environmentally stable lasers, as shown in the work carried out by P. Bowen [189]. As

in Ref [189], the mode-locking process eventually achieves low relative intensity noise outputs using PM fibres inside the cavity. Furthermore, clear dispersion compensation methods should be implemented to simulate the source dynamics. Regarding the dispersion measurements, two techniques are presented: stretching the interference in time, and mixing a calibrated signal with a photodetected one, which, as stated in the chapter, are not useful to assess the dispersion of small patchcords of active fibre. In particular, the technique of stretching in time the interference is limited by the minimum cycle that can be measured. Since the interference must be measured in time and wavelength, both acquisition systems must be optimized. Although this is possible, in the work presented here, the measurements were limited by the instrumentation available, which is 0.01 nm in wavelength and 17.5 ps in time. Finer separation in wavelength and time can be achieved by high-precision instrumentation nowadays. On the other hand, measuring the dispersion by mixing a calibrated signal with a photodetected one is an alternative that reduces the requirements of the measuring devices. However, this technique has some limitations; now, the requirements are shifted towards a high-frequency (multi-MHz) waveform generator. While a <10 ps/nm dispersion coefficient can be obtained using commercially available high-frequency (up to 40 GHz) signal generators, the technique is still subject to the stability of the input signals. Consequently, alternative solutions that facilitate the measurement of small dispersion coefficients and are not sensitive to active fibre remain under investigation. In this sense, techniques that involve white-light interferometry might overcome this issue in the future since they can sense small dispersion coefficients. However, more work has to be done to compensate for the intensity fluctuations of the active fibre.

In Chapter 5, the laser, a 40 MHz swept source based on supercontinuum generation along time stretch, has successfully demonstrated lower noise than conventional supercontinuum while preserving at least 40 nm bandwidth. Perhaps

the expectation from a supercontinuum source was to generate a broader bandwidth; however, the losses in the stretching element have complicated the benefit of supercontinuum. Supercontinuum generation is often associated with the ability to create broad spectrums, hundreds of nm. Still, the stretching element and the ytterbium amplifier could not preserve the original bandwidth in this work. One could think that an easy solution would be to increase the pump power of the laser used to seed the supercontinuum; however, this is not as straightforward. Increasing the pump power will mostly generate a larger bandwidth without increasing the power spectral density. Ideally, the ytterbium amplifier should be removed from the setup since it causes two main issues: first, an increase in the overall RIN noise of the system, and second, the ytterbium fibre cannot cope with the broadband bandwidth of the supercontinuum. In order to counterbalance the increasing bandwidth with the rising power, an alternative is to use passive fibres with a lower nonlinear coefficient (lower than the photonic crystal fibre used here), which would effectively increase the power spectral density while preserving a broadband spectrum. Overall, still obtaining a broad bandwidth at high repetition rates with supercontinuum and time stretch remains challenging, and special attention must be given to the output power of the supercontinuum source.

On the other hand, the OCT system with the KTN scanner is presented in Chapter 5. The KTN electro-optic deflector has been successfully used here for the first time in the sample arm of an SS-OCT system. Combining the 40 MHz swept source with the electro-optic deflector, B-Scans were produced at a rate of 100 kHz, which, paired with a galvoscanner, produced volumes at a rate of 400 Hz, selected by the galvoscanner. Nevertheless, this achievement came with a series of trade-offs, which can be grouped into three categories: i) processing bottleneck, ii) issues in adapting the KTN scanner since the crystal needs PM fibre, and iii) sensitivity from a high-speed swept-source. First of all, the SS-OCT system presented here presents several limitations in order to process the data in real

time. As stated in chapter 5, a high-speed oscilloscope is used to acquire the data, severely limiting the real-time capabilities. Those oscilloscopes are designed to display and analyze single events but are not ideal for quickly transferring data to a different computer. In that sense, just acquiring and storing the data in the oscilloscope was a task that required a much longer time (a few seconds) than the time needed to scan the whole sample. In this work, the oscilloscope was proposed as a proof of concept; the KTN with a high-sweeping rate source is possible, but data throughput must be severely enhanced to become useful. In order to alleviate that necessity, we built a secondary sub-system with a ytterbium source. Although the sub-system is useful for alignment purposes since real-time feedback is obtained, there is no other benefit to the sub-system apart from alignment. In the future, high-speed oscilloscopes should be avoided; this technological limitation might be sorted out by incorporating high-speed acquisition cards (more than 20 GSa/s) in a few years. However, the second issue faced here, the sensitivity, acts as a fundamental limit of the system. The sensitivity of high-speed OCT decays below the clinical levels needed of 95 dB [246] for eye imaging, as mentioned in different reports. A few solutions can be taken to improve the sensitivity: volume averaging or increasing the power in the reference arm. However, those solutions are also not straightforward; in the case of volume averaging, first, the effective volume rate will be considerably reduced, and secondly, to successfully average volumes, there is a need to register them, which will delay the possibility of real-time. The other solution is increasing the power sent to the reference arm; this would only work if the noise of the system is dominated by shot noise. As demonstrated in Chapter 6, an increase in the reference power does not necessarily improve the sensitivity, so a low-noise source has to be used in that case. Meanwhile those problems are sorted, only applications where there is no limit on the power applied to the sample will be seen. Finally, it is worth mentioning the limitations of using an optical deflector sensitive to polarisation. The KTN deflector comes equipped with a PM fibre and only deflects

the light from linear polarisation; this imposes a limit that has to be overcome when building the interferometer. Most common swept sources are randomly polarized, and PM stability is not ensured. Therefore, a linear polariser has to be placed at the entrance of the interferometer, meaning that all the light that is not linearly polarized will be rejected. Although this is only a technological issue since a booster can be added, it is definitely a drawback worth mentioning. Furthermore, the output from the deflector is also polarized, which, together with a highly polarizing sample, will attenuate the final image. KTN, as a beam deflector for OCT, might become popular in the future because of its ability to cope with high repetition rates. However, due to the high cost of the crystal and driver, and the difficult implementation in imaging systems, it seems hard nowadays to become popular in commercial devices where the price is a limiting factor.

In the following Chapter 6, two swept source lasers whose tuning mechanism is based on movable mirrors, the MEMS-VCSEL and the FDML, have been successfully used with complex master slave. Both sources, at a sweeping rate of 1.6 MHz and 828 kHz, respectively, have bidirectional sweeping. At first, the FDML source was characterized by CMS, sensitivity, axial range, and imaging capabilities. In the same way, a similar characterisation is achieved with a MEMS-VCSEL. CMS is a protocol based on a calibration stage by which two calibration functions are acquired. Those calibration functions are acquired once, and after that, they are used to generate a series of theoretical "masks" needed to build the OCT images. However, if those functions change while imaging, the calibration will no longer be valid; this is one of the main limitations of numerical processing methods such as CMS. Nevertheless, this limitation can be overcome by additional numerical means. In fact, this might become an optimization problem, where the calibration functions are the input that needs to be optimized for a high-resolution image. In that sense, actual AIs could be used with the OCT images and calibration functions to maximize the axial resolution. Because, in fact, for both sources, the data shows that minimal changes in the calibration highly

impact the sensitivity and resolution.

Finally, still in Chapter 6, a downconversion setup was presented to alleviate the required specifications of the acquisition system. For the downconversion system, the photodetected signal from a measuring interferometer (slave) is mixed with a reference interferometer (master), producing a signal with the amplitude information of the original signal at a much lower frequency. In theory, this reduction in frequency depends on the characteristics of the laser, depending on the fraction between $\Delta\lambda/\delta\lambda$. However, the reduction of electronic bandwidth comes at the cost of losing the capability to produce all the A-Scan depth points at once. Since only the depth at the OPD of the master interferometer is interrogated each time. In this sense, downconversion exhibits the prominent benefit of generating *en-face* OCT images quickly but loses the B-Scan generality. In order to produce B-Scans, one would have to interrogate at all depths, which can be done either by moving the translation stage in reference to the master interferometer or by having multiple interferometers. In the future, it is reasonable to think that downconversion could benefit from the use of photonic integrated circuits where one could input the swept source emission on one side while obtaining the interference signal at a fixed OPD at the output. Furthermore, it is worth mentioning the measured loss in sensitivity. As commented during the Chapter 6, the sensitivity obtained using standard numerical procedures is not recovered when using DMS. We blame this difference in sensitivity on two main elements: i) the unmatched uncompensated dispersion, i.e. the uncompensated dispersion between both the master and slave interferometers, might be different. This issue, in principle, can be solved by using the exact same components for both interferometers, but it is not ideal. In fact, the only thing that is needed is to replicate the interferometric signal from the slave interferometer. One possibility to explore is the use of arbitrary waveform generators that could electrically replicate the masks obtained from CMS at different depths. In this way, one could potentially have many mixers, one per depth. Since the masks already have the dispersion

and nonlinearities of the slave interferometer, the sensitivity should, in principle, remain equal to the numerical procedures. Secondly, ii) the insertion loss and potential noise added from the electronics used for the mixing process, it is known and documented here that the mixers attenuate the signal from the slave interferometer; this is, in fact, a technological limitation that further low-noise mixers and low-noise amplifiers could optimize. Furthermore, the performance of DMS could deteriorate severely due to fixed noise from the laser. Sometimes, swept sources exhibit fixed modulation in their spectra, translating into fixed noise on the photodetected signal. Those modulations, which might come from back reflections in the interferometer, polarisation mode beating or many others, might be mixed with the interferometric signal, producing artefacts on the image. For this issue, it is important to filter the electrical signal with low and high-pass filters. As well, back reflections from the interferometer can be reduced using appropriate coatings in the optics used, angle-polished fibres, etc.

Beyond the solution proven in this thesis, high-performance and highly specialized software might reduce the lag between acquisition and real-time display to a reasonable time usable for 4D applications. However, multi-MHz still seems far from real-time display by conventional procedures; therefore, alternative protocols such as circular ranging [185] and downconversion might become desired in the future.

The future of high-speed SS-OCT relies on developing new opto-electronics components and more data-efficient algorithms. From semiconductor optical amplifiers and enhanced balanced photodetectors to faster electro-optical deflectors. The progress in these technologies will open the way for accessing new wavelength bands, improving sensitivity, and enabling faster scans. Nowadays, the majority of applications of high-speed OCT are in the medical industry, such as 4D imaging [131, 247]. However, the real benefits of high-speed systems might be about to be explored with industrial applications; for instance, in large-area scanning applications, as already demonstrated [110, 111], also could be used on

security checks [248], crack inspection [163], etc.

Appendix A

Peer-reviewed articles published during the course of the doctoral programme

Peer-reviewed papers in golden open access journals

1. **Alejandro Martinez Jimenez**, Sacha Grelet, Veronika Tsautorian, Patrick Bowen Montague, Adrian Bradu, and Adrian Podoleanu "400 Hz volume rate swept-source optical coherence tomography at 1060 nm using a KTN deflector", *IEEE Photonics Technology Letters*, Vol 34, Issue 23, Dec. 2022. DOI: https://doi.org/10.1109/LPT.2022.3212015

2. Sacha Grelet, **Alejandro Martinez Jimenez**, Rasmus Dybbro, Patrick Bowen Montague, and Adrian Podoleanu "40 MHz swept-source optical coherence tomography at 1060 nm using a time-stretch and supercontinuum spectral broadening dynamics", *IEEE Photonics Journal*, Vol 14, Issue 6, Dec 2022. DOI: https://doi.org/10.1109/JPHOT.2022.3226820

3. **Alejandro Martinez Jimenez**, Ramona Cernat, Adrian Bradu, Rene Riha, E. A. Proano Grijalva, B. O. Meyer, T. Ansbaek, K. Yvind, and Adrian Podoleanu "Downconversion master slave OCT with a bidirectional sweeping laser" *Journal of Biophotonics* https://doi.org/10.1002/jbio.202400201, e202400201

4. Marie Klufts, **Alejandro Martinez Jimenez**, Simon Lotz, Muhammad Asim Bashir, Tom Pfeiffer, Alexander Mlynek, Wolfgang Wieser, Alexander Chamorovskiy, Adrian Bradu, Adrian Podoleanu, and Robert Huber, "828 kHz retinal imaging with an 840 nm Fourier domain mode locked laser", *Biomed. Opt. Express* Vol. 14, Issue 12, pp 6493-6508 (2023). DOI: https://doi.org/10.1364/BOE.504302

5. R. Riha, **A. Martinez Jimenez**, G. Venugopal, M. Klufts, R. Huber and A. Podoleanu, "Dispersion-Tuned Mode-Locked Laser for Swept Source OCT at 850 nm Using a cFBG and the Pulse Modulation Technique," in *IEEE Photonics Journal*, Vol. 16, Issue. 4, pp. 1-5, Aug. 2024, Art no. 1502205, doi: https://doi.org/10.1109/JPHOT.2024.3417829

6. Ramona Cernat, **Alejandro Martinez Jimenez**, Adrian Podoleanu "Down-conversion Master Slave Optical Coherence Tomography for simultaneous *en-face* imaging at two depths", *Optics Express*, Vol. 32, Iss 17, Aug 2024 https://doi.org/10.1364/OE.530325

7. Sacha Grelet, **Alejandro Martinez Jimenez**, Patrick Bowen, and Adrian Podoleanu "Shot-noise limited, 10 MHz swept-source optical coherence tomography for retinal imaging", in *IEEE Photonics Journal*, Vol 17, Issue 2, Jan 2025 https://doi.org/10.1109/JPHOT.2025.3534424

Conference proceedings

1. **A. Martinez Jimenez**, M. Spacek, M. Waker, R. Huber, and A. Podoleanu. "MHz time stretch swept source using a commercial erbium-doped amplifier" Proc. SPIE 12367, Optical Coherence Tomography and Coherence Domain Optical Methods in Biomedicine XXVII, 1236706 (8 March 2023); https://doi.org/10.1117/12.2651127

2. **A. Martinez Jimenez**, Sacha Grelet, Patrick Bowen Montague, Adrian Bradu, Adrian Podoleanu, "Dual ultrahigh speed swept-source and time domain optical coherence tomography system using a time stretch laser and a KTN deflector," Proc. SPIE 12632, Optical Coherence Imaging Techniques and Imaging in Scattering Media V, 126320B (11 August 2023); https://doi.org/10.1117/12.2670440

3. **A. Martinez Jimenez**, E. A. Proano Grijalva, A. Bradu, B. Meyer, T. Ansbaek, K. Yvind, A. Podoleanu, "Using complex master-slave protocol for OCT with bidirectional sweeping laser," Proc. SPIE PC12830, Optical Coherence Tomography and Coherence Domain Optical Methods in Biomedicine XXVIII, PC128301I (13 March 2024); https://doi.org/10.1117/12.3005674

4. E. A. Proano Grijalva, **A. Martinez Jimenez**, A. Bradu, A. Fernandez, B.O. Meyer, A. Jensens, E. Semenova, T. Ansbaek, K. Yvind, and A. Podoleanu. "Novel 1.6 MHz swept source for real-time OCT imaging of the human retina" Proc. SPIE 12367, Optical Coherence Domain Optical Methods in Biomedicine XXVII, 1236704 (8 March 2023); https://doi.org/10.1117/12.2649142

5. I. Lamoso Rodriguez, **A. Martinez Jimenez**, J. Cesar, S. Preu, and A. Podoleanu. "Characterization of SiN/SiO2 based MEMS-VCSEL at 1550 nm for optical coherence tomography" Proc. SPIE 12367, Optical Coherence Tomography

and Coherence Domain Optical Methods in Biomedicine XXVII, 1236716 (8 March 2023); https://doi.org/10.1117/12.2652961

Appendix B

Table swept-sources

TABLE B.1: Table swept-sources, Fig. 3.7

Name & Link	Sweep Rate [kHz]	Year	λ_c[nm]	$\Delta\lambda$[nm]
J-L Wu et al.	80000	2017	700	5
T. Yoshimura, et al.	0.0002	1998	800	13
U. Haberland, et al.	0.2	1998	800	20
S.R.Chinn, et al.	0.001	1997	850	25
Lim et al.	43.2	2006	850	55
S-W. Lee et al.	0.2	2007	850	48
Srinivasan et al.	16	2007	850	35
Goda et al.	90900	2012	850	14
Cho et al.	1	2014	850	40
John et al.	430	2016	850	37.7
Toadere et al.	1000	2017	850	4
M. Kendrisic, et al.	2	2023	850	5
M. Klufts, et al.	828	2023	850	40
X. Wei, et al.	7600	2016	900	7.2
B. Potsaid, et al.	400	2010	1050	100
C. Chango, et al.	2.5	2009	1060	18
E. C. W. Lee, et al.	18.8	2009	1060	62
C. M. Eigenwillig, et al.	340	2011	1060	70
T. Klein, et al.	1370	2011	1060	43
I. Grulkowski, et al.	580	2012	1060	3
T.T. W. Wong et al.	10000	2012	1060	60
T. Klein, et al.	6600	2013	1060	70
W. Wieser, et al.	3200	2014	1060	70
A. K. Lau	20000	2014	1060	40
J. P. Kolb, et al.	1600	2015	1060	70
X. Wei, et al.	28000	2015	1060	63
X. Wei, et al.	8700	2016	1060	73
S. Tan, et al.	19000	2018	1060	7.1
H.D. Lee, et al.	200	2019	1060	40
S. Grelet et al.	40000	2022	1060	50
E. A. Proano, et al.	1600	2023	1060	30

Name & Link	Sweep Rate [kHz]	Year	λ_c[nm]	$\Delta\lambda$[nm]
G.H. Kim, et al.	5000	2023	1060	97
S. H. Yun, et al.	15.7	2003	1300	73
M. A. Choma, et al.	0.25	2005	1300	130
R. Huber, et al.	20	2005	1300	120
Y. Yasuno, et al.	20	2005	1300	110
W. Y. Oh, et al.	115	2005	1300	80
S. Yamashita, et al.	200	2006	1300	100
R. Huber, et al.	232	2006	1300	105
R. Huber, et al.	370	2006	1300	100
D. C. Adler, et al.	100	2007	1300	160
W-Y. Oh, et al.	403	2010	1300	104
W. Wieser, et al.	5200	2010	1300	80
Y. Okabe, et al.	200	2012	1300	80
W. Wieser, et al.	1600	2012	1300	100
V. Jayaraman, et al.	1000	2013	1300	107
M. Bonesi, et al.	102	2014	1300	30
S. Song, et al.	100	2016	1300	100
C. Jun, et al.	240	2016	1300	125
T. S. Kim, et al.	9400	2020	1300	100
I. Akkaya, et al.	7630	2021	1300	90
J-Y. Joo, et al.	10000	2022	1300	90
Y. Takubo, et al.	100	2013	1500	60
Z. He, et al.	0.095	1999	1550	32
S. Moon, et al.	5000	2006	1550	150
B. R. Biedermann, et al.	110	2009	1550	115
M. Bonesi, et al.	200	2014	1550	40
S. Tozburun et al.	9000	2014	1550	94
X. Wei, et al.	115000	2014	1550	58
J. Xu, et al.	11500	2015	1550	56
B. Li, et al.	109000	2015	1550	5

Appendix C

Interferogram simulation with downconversion

```
clc, clear all, close all

lambda0 = 1060E-9;    % [m] Center wavelength of the source
dlambda = 90E-9;      % [m] FWHM wavelength bandwidth of
   source
ns = 1.38;

ls1 = 20E-6;    % Location of backscatterer 1
ls2 = 100E-6;   % Location of backscatterer 2

rs1 = 0.5;      % Reflectivity of backscatterer 1
rs2 = 0.5;      % Reflectivity of backscatterer 2

k0 = 2*pi/lambda0;     % Central wavenumber
delta_k = 2*pi*dlambda/lambda0^2;    % FWHM bandwidth of k
sigma_k = delta_k/sqrt(2*log(2));    % standard deviation of
    k

N= 2^11;     % Number of sampling points
nsigma= 2;   % Number of standard deviations to plot on each
    side of k0

k = k0+ sigma_k*nonLinspace(-nsigma,nsigma,N,"cos");
k1 = k0+ sigma_k*linspace(-nsigma,nsigma,N);

S_k = exp(-(1/2*(k-k0).^2/sigma_k.^2));      % Gaussian
   source PSD

E_s1 = rs1*exp(1i*2*k*ns*ls1);      % Electric field from
   backscatter 1
E_s2 = rs2*exp(1i*2*k*ns*ls2);      % Electric field from
   backscatter 2

I_k2_positive = S_k.*abs(1+E_s2).^2; % Positive photodiode
```

```
29 I_k2_negative = -circshift(I_k2_positive,5);  % Negative
      photodiode, signal is phase shifted
30 I_bpd_2 = I_k2_positive + I_k2_negative; % Balanced signal
31
32
33 I_k1_positive = S_k.*abs(1+E_s1).^2;  % Positive photodiode
34 I_k1_negative = -circshift(I_k1_positive,26);  % Negative
      photodiode, signal is phase shifted
35 I_bpd_1 = I_k1_positive + I_k1_negative; % Balanced signal
36
37
38 I_k3_positive = S_k.*abs(1+E_s1+E_s2).^2; % Positive
      photodiode
39 I_k3_negative = -circshift(I_k3_positive,19);   % Negative
      photodiode, signal is phase shifted
40 I_bpd_3 = I_k3_positive + I_k3_negative;  % Balanced signal
41 xlim([0.85 1.15])
42
43 figure(3)
44 movegui('northwest')
45 subplot(3,3,1)
46 plot(k1/k0,I_bpd_1/max(I_bpd_1),'k'), ylim([-1 1])
47 title('Slave Interferogram at z1')
48 xlabel('Propagation constant k/k_0'), ylabel('Normalized
      intensity')
49
50 subplot(3,3,2)
51 plot(k1/k0,I_bpd_2/max(I_bpd_2),'k'), ylim([-1 1])
52 title('Slave Interferogram at z2')
53 xlabel('Propagation constant k/k_0'), ylabel('Normalized
      intensity')
54
55 subplot(3,3,3)
56 plot(k1/k0,I_bpd_3/max(I_bpd_3),'k'), ylim([-1 1])
57 title('Slave Interferogram with 2 layers z1 and z2')
58 xlabel('Propagation constant k/k_0'), ylabel('Normalized
      intensity')
59
60 subplot(3,3,4)
61 plot(k1/k0,I_bpd_1/max(I_bpd_1),'k'), ylim([-1 1])
62 title('Master Interferogram at z1')
63 xlabel('Propagation constant k/k_0'), ylabel('Normalized
      intensity')
64
65 subplot(3,3,5)
66 plot(k1/k0,I_bpd_1/max(I_bpd_1),'k'), ylim([-1 1])
67 title('Master Interferogram at z1')
```

```
68 xlabel('Propagation constant k/k_0'), ylabel('Normalized
      intensity')
69
70 subplot(3,3,6)
71 plot(k1/k0,I_bpd_1/max(I_bpd_1),'k'), ylim([-1 1])
72 title('Master Interferogram at z1')
73 xlabel('Propagation constant k/k_0'), ylabel('Normalized
      intensity')
74
75 subplot(3,3,7)
76 plot(k1/k0,I_bpd_1.*I_bpd_1./max(I_bpd_1.*I_bpd_1),'k'),
      ylim([-1 1])
77 int_value_11 = sum(I_bpd_1.*I_bpd_1./max(I_bpd_1.*I_bpd_1))
      ;
78 title(['Multiplication of I1 and I1, integral value:',
      num2str(int_value_11)])
79 xlabel('Propagation constant k/k_0'), ylabel('Normalized
      intensity')
80
81 subplot(3,3,8)
82 plot(k1/k0,I_bpd_1.*I_bpd_2./max(I_bpd_1.*I_bpd_2),'k'),
      ylim([-1 1])
83 int_value_12 = sum(I_bpd_1.*I_bpd_2./max(I_bpd_1.*I_bpd_2))
      ;
84 title(['Multiplication of I1 and I2, integral value:',
      num2str(int_value_12)])
85 xlabel('Propagation constant k/k_0'), ylabel('Normalized
      intensity')
86
87 subplot(3,3,9)
88 plot(k1/k0,I_bpd_1.*I_bpd_3./max(I_bpd_1.*I_bpd_3),'k'),
      ylim([-1 1])
89 int_value_13 = sum(I_bpd_1.*I_bpd_3./max(I_bpd_1.*I_bpd_3))
      ;
90 title(['Multiplication of I1 and I3, integral value:',
      num2str(int_value_13)])
91 xlabel('Propagation constant k/k_0'), ylabel('Normalized
      intensity')
```

Appendix D

Asymmetry

The research described in Section 6.3.4 was performed during the collaboration with DTU and OCTLight Aps., part of the ITN that supported this PhD. This company enabled access to the laser for a limited time. I presented here the results obtained with such a laser and replicated the coherence gate profile from the paper published [249]. After the experiments described above and after the publication of the paper [250], we continued to perform downconversion. During these experiments, we noticed that it is essential for resolution-limited downconversion for the two photodetected signals transducing the channeled spectra in the two interferometers to be perfectly aligned in time. Slight misalignment leads to asymmetry in the coherence gate profile as shown in Fig. 6.23. There are long fibres in the two fibre arrays used in the downconversion experiment, plus several meters of cables connecting the photodetectors and switches. Therefore, the delay between the two interferometers must be adjusted prior to any measurement. By the time of the experiment, this was done using a 4 GS/s oscilloscope. Later, during experiments on downconversion, we improved the precision in adjusting the overlap of the two spectra using an FBG [249]. It was realised that simple visual inspection of spectra on the scope to adjust the delay mismatch was not sufficiently accurate. Not having access to the same laser, we performed similar experiments here using a swept commercial laser at 100 kHz (Axsun, Excelitas 1060 nm, 100 kHz) to show how mismatch of delays affects the profile of the coherence gate. Fig. D.1 represents the coherence gate with 5 different time delays, from -20 ns to +70 ns. Fig. D.1 indicates that even a 4 m cable extra mismatch, corresponding to $\simeq 20ns$, produces an enlargement and asymmetry in the coherence gate profile in the shape of the asymmetry seen in Fig. 6.23. The sweeping rate of the laser in the experiment above was at 1.6 MHz, 16 times faster than for the laser used to produce the coherence gate shown here, which would have required an even better precision in delay mismatch adjustment.

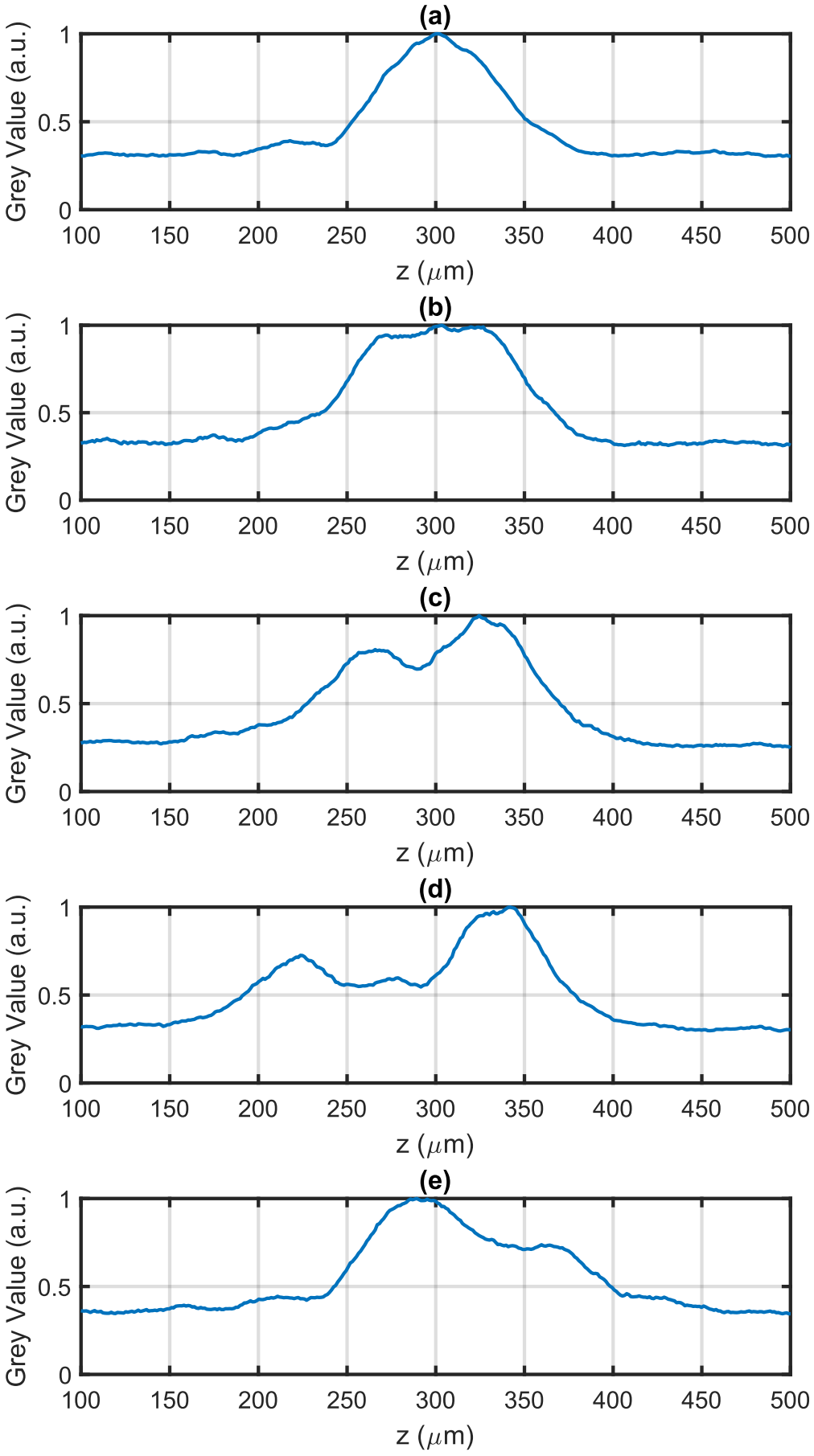

FIGURE D.1: Coherence gate with (a) no delay, (b) +20 ns delay, (c) +35 ns delay, (d) 70 ns delay, and (e) -20 ns delay between RF and LO inputs of the mixer.

Bibliography

[1] D. Huang, E. A. Swanson, C. P. Lin, J. S. Schuman, W. G. Stinson, W. Chang, M. R. Hee, T. Flotire, K. Gregory, C. A. Puliafito, and J. G. Fujimoto, "Optical Coherence Tomography," *Science*, vol. 254, pp. 1178–1181, 5035 Nov. 1991. DOI: 10.1126/science.1957169.

[2] J. F. de Boer, R. Leitgeb, and M. Wojtkowski, "Twenty-five years of optical coherence tomography: The paradigm shift in sensitivity and speed provided by fourier domain OCT [Invited]," *Biomedical Optics Express*, vol. 8, p. 3248, 7 Jul. 2017, ISSN: 2156-7085. DOI: 10.1364/boe.8.003248.

[3] W. Drexler and J. G. Fujimoto, *Optical Coherence Tomography*, W. Drexler and J. G. Fujimoto, Eds. Springer International Publishing, 2015, ISBN: 978-3-319-06418-5. DOI: 10.1007/978-3-319-06419-2.

[4] M. A. Duguay and A. T. Mattick, "Ultrahigh speed photography of picosecond light pulses and echoes," *Applied Optics*, vol. 10, 9 1971, ISSN: 0003-6935. DOI: 10.1364/ao.10.002162.

[5] J. G. Fujimoto, C. A. Puliafito, R. Margolis, A. Oseroff, S. D. Silvestri, and E. P. Ippen, "Femtosecond optical ranging in biological systems," *Optics Letters*, vol. 11, p. 150, 3 Mar. 1986, ISSN: 0146-9592. DOI: 10.1364/OL.11.000150.

[6] E. Hecht and A. Ganesan, *Optics (4th ed.)* Pearson, 2001.

[7] B. D. Guenther and D. G. Steel, *Encyclopedia of modern optics*. 2018, vol. 1-5. DOI: 10.5860/choice.43-0036.

[8] A. G. Podoleanu, M. Seeger, G. M. Dobre, D. J. Webb, D. A. Jackson, and F. W. Fitzke, "Transversal and longitudinal images from the retina of the living eye using low coherence reflectometry," *Journal of Biomedical Optics*, 1998. DOI: 10.1117/1.429859.

[9] A. G. Podoleanu, J. A. Rogers, D. A. Jackson, and S. Dunne, "Three dimensional oct images from retina and skin," *Optics Express*, vol. 7, 9 2000, ISSN: 10944087. DOI: 10.1364/oe.7.000292.

[10] A. G. Podoleanu, "Unbalanced versus balanced operation in an optical coherence tomography system," *Applied Optics*, vol. 39, 1 2000, ISSN: 0003-6935. DOI: 10.1364/ao.39.000173.

[11] R. K. Tyson, *Principles and applications of fourier optics*. 2014. DOI: 10.1088/978-0-750-31056-7.

[12] L. M. Smith and C. C. Dobson, "Absolute displacement measurements using modulation of the spectrum of white light in a michelson interferometer," *Applied Optics*, vol. 28, 16 1989, ISSN: 0003-6935. DOI: 10.1364/ao.28.003339.

[13] ANSI, "American national standard for safe use of lasers.," *Laser Institute of America*, 2007.

[14] M. Maria, "Supercontinuum in the practice of optical coherence tomography with emphasis on noise effects," Ph.D. dissertation, University of Kent, 2018.

[15] N. M. Israelsen, C. R. Petersen, A. Barh, D. Jain, M. Jensen, G. Hannesschläger, P. Tidemand-Lichtenberg, C. Pedersen, A. Podoleanu, and O. Bang, "Real-time high-resolution mid-infrared optical coherence tomography," *Light: Science and Applications*, vol. 8, 1 2019, ISSN: 20477538. DOI: 10.1038/s41377-019-0122-5.

[16] "Imaging ex vivo healthy and pathological human brain tissue with ultra-high-resolution optical coherence tomography," *Journal of Biomedical Optics*, vol. 10, 1 2005, ISSN: 10833668. DOI: 10.1117/1.1851513.

[17] F. Spöler, S. Kray, P. Grychtol, B. Hermes, J. Bornemann, M. Först, and H. Kurz, "Simultaneous dual-band ultra-high resolution optical coherence tomography," *Optics Express*, vol. 15, 17 2007, ISSN: 10944087. DOI: 10.1364/oe.15.010832.

[18] D. Woods and A. Podoleanu, "Controlling the shape of talbot bands' visibility," *Optics Express*, vol. 16, 13 2008, ISSN: 10944087. DOI: 10.1364/oe.16.009654.

[19] D. Woods, "Selection in depth in Fourier domain optical coherence tomography," Ph.D. dissertation, University of Kent, Mar. 2008.

[20] Z. Hu, Y. Pan, and A. M. Rollins, "Analytical model of spectrometer-based two-beam spectral interferometry," *Applied Optics*, vol. 46, 35 2007, ISSN: 15394522. DOI: 10.1364/AO.46.008499.

[21] Y. Chen, D. M. de Bruin, C. Kerbage, and J. F. de Boer, "Spectrally balanced detection for optical frequency domain imaging," *Optics Express*, vol. 15, 25 2007, ISSN: 10944087. DOI: 10.1364/oe.15.016390.

[22] W.-C. Kuo, C.-M. Lai, Y.-S. Huang, C.-Y. Chang, and Y.-M. Kuo, "Balanced detection for spectral domain optical coherence tomography," *Optics Express*, vol. 21, 16 2013, ISSN: 10944087. DOI: 10.1364/oe.21.019280.

[23] A. Bradu and A. G. Podoleanu, "Fourier domain optical coherence tomography system with balance detection," *Opt. Express*, vol. 20, no. 16, pp. 17 522–17 538, Jul. 2012. DOI: 10.1364/OE.20.017522.

[24] I. Rubinoff, D. A. Miller, R. Kuranov, Y. Wang, R. Fang, N. J. Volpe, and H. F. Zhang, "High-speed balanced-detection visible-light optical coherence tomography in the human retina using subpixel spectrometer calibration," *IEEE Transactions on Medical Imaging*, vol. 41, pp. 1724–1734, 7 Jul. 2022, ISSN: 1558254X. DOI: 10.1109/TMI.2022.3147497.

[25] O. P. Kocaoglu, T. L. Turner, Z. Liu, and D. T. Miller, "Adaptive optics optical coherence tomography at 1 MHz," *Biomedical Optics Express*, vol. 5, 12 2014, ISSN: 2156-7085. DOI: 10.1364/boe.5.004186.

[26] J. P. Fingler, "Motion contrast using optical coherence tomography," Ph.D. dissertation, California Institute of Technology, May 2007.

[27] J. Pawley, *Handbook of biological confocal microscopy*. Springer Science & Business Media, 2006, vol. 236.

[28] G. S. Kino and T. R. Corle, *Confocal scanning optical microscopy and related imaging systems*. Academic Press, 1996.

[29] M. Hughes and A. G. Podoleanu, "Simplified dynamic focus method for time domain oct," *Electronics letters*, vol. 45, no. 12, pp. 623–624, 2009.

[30] R. Cernat, A. Bradu, N. M. Israelsen, O. Bang, S. Rivet, P. A. Keane, D.-G. Heath, R. Rajendram, and A. Podoleanu, "Gabor fusion master slave optical coherence tomography," *Biomedical optics express*, vol. 8, no. 2, pp. 813–827, 2017.

[31] B. Hermann, E. Fernández, A. Unterhuber, H. Sattmann, A. Fercher, W. Drexler, P. Prieto, and P. Artal, "Adaptive-optics ultrahigh-resolution optical coherence tomography," *Optics letters*, vol. 29, no. 18, pp. 2142–2144, 2004.

[32] A. G. Podoleanu and D. A. Jackson, "Noise analysis of a combined optical coherence tomograph and a confocal scanning ophthalmoscope," *Applied Optics*, vol. 38, 10 1999, ISSN: 0003-6935. DOI: 10.1364/ao.38.002116.

[33] T. Mitsui, "Dynamic range of optical reflectometry with spectral interferometry," *Japanese Journal of Applied Physics, Part 1: Regular Papers and Short Notes and Review Papers*, vol. 38, 10 1999, ISSN: 00214922. DOI: 10.1143/jjap.38.6133.

[34] M. Choma, M. Sarunic, C. Yang, and J. Izatt, "Sensitivity advantage of swept source and Fourier domain optical coherence tomography," *Optics Express*, vol. 11, 18 2003, ISSN: 1094-4087. DOI: 10.1364/oe.11.002183.

[35] R. Leitgeb, C. Hitzenberger, and A. Fercher, "Performance of Fourier domain vs time domain optical coherence tomography," *Optics Express*, vol. 11, 8 2003, ISSN: 1094-4087. DOI: 10.1364/oe.11.000889.

[36] J. F. D. Boer, B. Cense, B. H. Park, M. C. Pierce, G. J. Tearney, and B. E. Bouma, "Improved signal-to-noise ratio in spectral-domain compared with time-domain optical coherence tomography," vol. 28, 2003. DOI: 10.1364/OL.28.002067.

[37] T. Klein, W. Wieser, L. Reznicek, A. Neubauer, A. Kampik, and R. Huber, "Multi-MHz retinal OCT," *Biomedical Optics Express*, vol. 4, p. 1890, 10 Oct. 2013, ISSN: 2156-7085. DOI: 10.1364/boe.4.001890.

[38] A. G. Podoleanu, "Optical coherence tomography," *Journal of Microscopy*, vol. 247, pp. 209–219, 3 Sep. 2012, ISSN: 00222720. DOI: 10.1111/j.1365-2818.2012.03619.x.

[39] G. P. Agrawal, *Applications of nonlinear fiber optics*. Academic press, 2008, vol. 10.

[40] A. M. Rollins and J. A. Izatt, "Optimal interferometer designs for optical coherence tomography," *Optics Letters*, vol. 24, 21 1999, ISSN: 0146-9592. DOI: 10.1364/ol.24.001484.

[41] A. Bradu, S. Rivet, and A. Podoleanu, "Master/slave interferometry – ideal tool for coherence revival swept source optical coherence tomography," *Biomedical Optics Express*, vol. 7, p. 2453, 7 Jul. 2016, ISSN: 2156-7085. DOI: 10.1364/boe.7.002453.

[42] D. Hillmann, T. Bonin, C. L. ¨. Uhrs, G. Franke, M. Hagen-Eggert, P. Koch, G. H. ¨. Uttmann, .-S. Lee, J. P. Rolland, J. M. Zavislan, J. V. Aquavella, and G. Yoon, "Common approach for compensation of axial motion artifacts in swept-source oct and dispersion in fourier-domain oct," *Optics Express*, vol. 12, pp. 2977–2998, 2004.

[43] A. Bradu, N. M. Israelsen, M. Maria, M. J. Marques, S. Rivet, T. Feuchter, O. Bang, and A. Podoleanu, "Recovering distance information in spectral domain interferometry," *Scientific Reports*, vol. 8, 1 Dec. 2018, ISSN: 20452322. DOI: 10.1038/s41598-018-33821-0.

[44] D. Hillmann, C. Lührs, T. Bonin, P. Koch, A. Vogel, and G. Hüttmann, "Holoscopy: Holographic optical coherence tomography," R. A. Leitgeb and B. E. Bouma, Eds., Jun. 2011, 80911H. DOI: 10.1117/12.889485. [Online]. Available: http://proceedings.spiedigitallibrary.org/proceeding.aspx?doi=10.1117/12.889485.

[45] X. Attendu and R. M. Ruis, "Simple and robust calibration procedure for k-linearization and dispersion compensation in optical coherence tomography," *Journal of Biomedical Optics*, vol. 24, p. 1, 05 May 2019, ISSN: 15602281. DOI: 10.1117/1.jbo.24.5.056001.

[46] A. G. Podoleanu and A. Bradu, "Master–slave interferometry for parallel spectral domain interferometry sensing and versatile 3d optical coherence tomography," *Optics Express*, vol. 21, p. 19 324, 16 Aug. 2013, ISSN: 1094-4087. DOI: 10.1364/oe.21.019324.

[47] M. J. Marques, S. Rivet, A. Bradu, and A. Podoleanu, "Complex master-slave for long axial range swept-source optical coherence tomography," *OSA Continuum*, vol. 1, p. 1251, 4 Dec. 2018, ISSN: 2578-7519. DOI: 10.1364/osac.1.001251.

[48] S. Rivet, A. Bradu, F. Bairstow, H. Forrière, and A. Podoleanu, "Group refractive index and group velocity dispersion measurement by complex master slave interferometry," *Optics Express*, vol. 26, p. 21 831, 17 Aug. 2018, ISSN: 1094-4087. DOI: 10.1364/oe.26.021831.

[49] A. Bradu, K. Kapinchev, F. Barnes, and A. Podoleanu, "Master slave en-face oct/slo," *Biomedical Optics Express*, vol. 6, p. 3655, 9 Sep. 2015, ISSN: 2156-7085. DOI: 10.1364/boe.6.003655.

[50] V.-F. Duma, J. P. Rolland, and A. G. Podoleanu, "Perspectives of optical scanning in oct," vol. 7556, SPIE, Feb. 2010, 75560B, ISBN: 9780819479525. DOI: 10.1117/12.840718.

[51] J. P. Kolb, J. Klee, T. Pfeiffer, and R. Huber, "1060 nm FDML laser with centimeter coherence length and 1.67 MHz sweep rate for full eye length and retinal ultra-widefield OCT," in *Optics InfoBase Conference Papers*, vol. Part F61-ECBO 2017, OSA - The Optical Society, 2017, ISBN: 9781557528209. DOI: 10.1117/12.2286854.

[52] S. Ni, X. Wei, R. Ng, S. Ostmo, M. F. Chiang, D. Huang, Y. Jia, J. P. Campbell, and Y. Jian, "High-speed and widefield handheld swept-source OCT angiography with a VCSEL light source," *Biomedical Optics Express*, vol. 12, 6 2021, ISSN: 2156-7085. DOI: 10.1364/boe.425411.

[53] P. Zang, G. Liu, M. Zhang, C. Dongye, J. Wang, A. D. Pechauer, T. S. Hwang, D. J. Wilson, D. Huang, D. Li, and Y. Jia, "Automated motion correction using parallel-strip registration for wide-field en face oct angiogram," *Biomedical Optics Express*, vol. 7, 7 2016, ISSN: 2156-7085. DOI: 10.1364/boe.7.002823.

[54] J. P. Kolb, T. Klein, C. L. Kufner, W. Wieser, A. S. Neubauer, and R. Huber, "Ultra-widefield retinal mhz-oct imaging with up to 100 degrees viewing angle," *Biomedical Optics Express*, vol. 6, 5 2015, ISSN: 2156-7085. DOI: 10.1364/boe.6.001534.

[55] V.-F. Duma, "Optimal scanning function of a galvanometer scanner for an increased duty cycle," *Optical Engineering*, vol. 49, p. 103 001, 10 Oct. 2010, ISSN: 0091-3286. DOI: 10.1117/1.3497570.

[56] B. A. Lengyel, "Lasers; generation of light by stimulated emission.," *John Wiley & Sons*, vol. 184, 5 1963, ISSN: 0098-7484. DOI: 10.1001/jama.1963.03700180158032.

[57] F. J. McClung and R. W. Hellwarth, "Giant optical pulsations from ruby," *Journal of Applied Physics*, vol. 33, 3 1962, ISSN: 00218979. DOI: 10.1063/1.1777174.

[58] J. Stone and C. A. Burrus, "Neodymium-doped silica lasers in end-pumped fiber geometry," *Applied Physics Letters*, vol. 23, 7 1973, ISSN: 00036951. DOI: 10.1063/1.1654929.

[59] A. Tuennermann, "High-power Nd double-clad fiber lasers," *Conference Proceedings - Lasers and Electro-Optics Society Annual Meeting-LEOS*, 1996, ISSN: 10928081.

[60] M. J. Digonnet, "Theory of superfluorescent fiber lasers.," *Journal of Lightwave Technology*, vol. LT-4, 11 1986, ISSN: 07338724. DOI: 10.1109/jlt.1986.1074661.

[61] K. Liu, M. Digonnet, K. Fesler, B. Y. Kim, and H. J. Shaw, "Broadband diode-pumped fibre laser," *Electronics Letters*, vol. 24, 14 1988, ISSN: 00135194. DOI: 10.1049/el:19880570.

[62] G. Chang and Z. Wei, "Ultrafast fiber lasers: An expanding versatile toolbox," *ISCIENCE*, vol. 23, p. 101 101, 2020. DOI: 10.1016/j.isci. [Online]. Available: https://doi.org/10.1016/j.isci..

[63] V. J. Matsas, D. J. Richardson, T. P. Newson, and D. N. Payne, "Characterization of a self-starting, passively mode-locked fiber ring laser that exploits nonlinear polarization evolution," *Optics Letters*, vol. 18, 5 1993.

[64] Y. Song, X. Shi, C. Wu, D. Tang, and H. Zhang, "Recent progress of study on optical solitons in fiber lasers," *Applied Physics Reviews*, vol. 6, 2 Jun. 2019, ISSN: 19319401. DOI: 10.1063/1.5091811.

[65] F. X. Kärtner, I. D. Jung, and U. Keller, "Soliton mode-locking with saturable absorbers," *IEEE Journal of selected topics in quantum electronics*, vol. 2, 3 1996. DOI: 10.1109/2944.571754.

[66] J. P. Gordon, "Theory of the soliton self-frequency shift," *Optics Letters*, vol. 11, 10 1986. DOI: doi.org/10.1364/OL.11.000662.

[67] H. A. Haus, "Mode-locking of lasers," *IEEE Journal on selected topics in quantum electronics*, vol. 6, 6 2000. DOI: 10.1109/2944.902165.

[68] U. Keller, K. J. Weingarten, F. X. Kärtner, D. Kopf, B. Braun, I. D. Jung, R. Fluck, C. Hönninger, N. Matuschek, and J. A. D. Au, "Semiconductor saturable absorber mirrors (sesam's) for femtosecond to nanosecond pulse generation in solid-state lasers," *IEEE Journal on Selected Topics in Quantum Electronics*, vol. 2, 3 1996, ISSN: 1077260X. DOI: 10.1109/2944.571743.

[69] U. Keller, *Recent developments in compact ultrafast lasers*, 2003. DOI: 10.1038/nature01938.

[70] N. Ming, S. Tao, W. Yang, Q. Chen, R. Sun, C. Wang, S. Wang, B. Man, and H. Zhang, "Mode-locked er-doped fiber laser based on pbs/cds core/shell quantum dots as saturable absorber," *Optics Express*, vol. 26, 7 2018, ISSN: 10944087. DOI: 10.1364/oe.26.009017.

[71] L. Huang, Y. Zhang, and X. Liu, *Dynamics of carbon nanotube-based mode-locking fiber lasers*, 2020. DOI: 10.1515/nanoph-2020-0269.

[72] C. Aguergaray, N. G. R. Broderick, M. Erkintalo, J. S. Y. Chen, and V. Kruglov, "Mode-locked femtosecond all-normal all-pm yb-doped fiber laser using a nonlinear amplifying loop mirror," *Optics Express*, vol. 20, 10 2012, ISSN: 1094-4087. DOI: 10.1364/oe.20.010545.

[73] I. N. Duling, "All-fiber ring soliton laser mode locked with a nonlinear mirror," *Optics Letters*, vol. 16, 8 1991, ISSN: 0146-9592. DOI: 10.1364/ol.16.000539.

[74] J. Szczepanek, T. M. Kardaś, M. Michalska, C. Radzewicz, and Y. Stepanenko, "Simple all-pm-fiber laser mode-locked with a nonlinear loop mirror," *Optics Letters*, vol. 40, 15 2015, ISSN: 0146-9592. DOI: 10.1364/ol.40.003500.

[75] M. E. Fermann, M. J. Andrejco, M. L. Stock,) Y. Silberberg, and A. M. Weiner, *Passive mode locking in erbium fiber lasers with negative group delay*, 1993. DOI: 10.1063/1.108516.

[76] J. Wang, "Theory of passive additive-pulse mode locking," *Optics Letters*, vol. 16, 14 1991, ISSN: 0146-9592. DOI: 10.1364/ol.16.001104.

[77] C. Spielmann, F. Krausz, E. Wintner, and A. J. Schmidt, "Self-starting additive pulse mode-locking of a nd:glass laser," Optica Publishing Group, 1990, PDP10. DOI: 10.1364/UP.1990.PDP10. [Online]. Available: https://opg.optica.org/abstract.cfm?URI=UP-1990-PDP10.

[78] H. A. Haus, K. Tamura, L. E. Nelson, and E. P. Ippen, "Stretched-pulse additive pulse mode-locking in fiber ring lasers: Theory and experiment," *IEEE Journal of Quantum Electronics*, vol. 31, 3 1995, ISSN: 15581713. DOI: 10.1109/3.364417.

[79] H. A. Haus, J. G. Fujimoto, and E. P. Ippen, "Structures for additive pulse mode locking," *Journal of the Optical Society of America B*, vol. 8, 10 1991, ISSN: 0740-3224. DOI: 10.1364/josab.8.002068.

[80] K. Okamoto, *Fundamentals of Optical Waveguides, Second Edition*. 2005. DOI: 10.1016/B978-0-12-525096-2.X5000-4.

[81] A. Einstein, "Strahlungs-emission und absorption nach der quantentheorie," *Verh. d. Deutsche Physik. Ges.*, vol. 18, pp. 318–328, 1916.

[82] J. R. Kraus, "Collected papers of albert einstein," *The Charleston Advisor*, vol. 23, 3 2022, ISSN: 1525-4011. DOI: 10.5260/chara.23.3.17.

[83] E. Fermi, "Quantum theory of radiation," *Reviews of Modern Physics*, vol. 4, 1 1932, ISSN: 00346861. DOI: 10.1103/RevModPhys.4.87.

[84] P. M. Becker, A. A. Olsson, and J. R. Simpson, *Erbium- Doped Fiber Amplifiers: Fundamentals and Technology (Optics and Photonics)*. Elsevier, 1999.

[85] R. Paschotta, J. Nilsson, A. C. Tropper, and D. C. Hanna, "Ytterbium-doped fiber amplifiers," *IEEE Journal of Quantum Electronics*, vol. 33, 7 1997, ISSN: 00189197. DOI: 10.1109/3.594865.

[86] N. Simakov, Z. Li, Y. Jung, J. M. O. Daniel, P. Barua, P. C. Shardlow, S. Liang, J. K. Sahu, A. Hemming, W. A. Clarkson, S.-U. Alam, and D. J. Richardson, "High gain holmium-doped fibre amplifiers," *Optics Express*, vol. 24, 13 2016, ISSN: 10944087. DOI: 10.1364/oe.24.013946.

[87] S. Chen, Y. Jung, S.-u. Alam, D. J. Richardson, R. Sidharthan, D. Ho, S. Yoo, and J. M. O. Daniel, "Ultra-short wavelength operation of thulium-doped fiber amplifiers and lasers," *Optics Express*, vol. 27, 25 2019, ISSN: 10944087. DOI: 10.1364/oe.27.036699.

[88] R. Leonhardt, B. R. Biedermann, W. Wieser, and R. Huber, "Nonlinear optical frequency conversion of an amplified fourier domain mode locked (fdml) laser," *Optics Express*, vol. 17, 19 2009, ISSN: 10944087. DOI: 10.1364/oe.17.016801.

[89] T. Klein, W. Wieser, C. M. Eigenwillig, B. R. Biedermann, and R. Huber, "Megahertz OCT for ultrawide-field retinal imaging with a 1050nm Fourier domain mode-locked laser," *Optics Express*, vol. 19, 4 2011, ISSN: 1094-4087. DOI: 10.1364/oe.19.003044.

[90] K. Tamura, L. E. Nelson, H. A. Haus, and E. P. Ippen, "Soliton versus nonsoliton operation of fiber ring lasers," *Applied Physics Letters*, vol. 64, pp. 149–151, 2 1994, ISSN: 00036951. DOI: 10.1063/1.111547.

[91] E. Ding, W. H. Renninger, F. W. Wise, P. Grelu, E. Shlizerman, and J. N. Kutz, "High-energy passive mode-locking of fiber lasers," *International Journal of Optics*, vol. 2012, 2012, ISSN: 16879384. DOI: 10.1155/2012/354156.

[92] T. K. Robert, "Additive pulse mode-locked erbium-doped fiber lasers," Ph.D. dissertation, Massachusetts Institute of Technology, Oct. 1994.

[93] L. Zhou, Y. Liu, G. Xie, W. Zhang, Z. Zhu, C. Ouyang, C. Gu, and W. Li, "Generation of stretched pulses from an all-polarization-maintaining Er-doped mode-locked fiber laser using nonlinear polarization evolution," *Applied Physics Express*, vol. 12, 5 May 2019, ISSN: 18820786. DOI: 10.7567/1882-0786/ab15c0.

[94] H. E. Ibarra-Villalon, O. Pottiez, A. Gómez-Vieyra, J. P. Lauterio-Cruz, and Y. E. Bracamontes-Rodriguez, "Numerical study of polarization evolution governed by linear birefringence, twist-induced circular birefringence and nonlinear birefringence in a single-mode optical fiber," *Journal of Optics (United Kingdom)*, vol. 23, 12 Dec. 2021, ISSN: 20408986. DOI: 10.1088/2040-8986/ac2eaa.

[95] H. Chen, Y. Li, D. Huang, Y. Shi, F. Li, C. Lu, and P. K. A. Wai, "Highly coherent, flat, and broadband time-stretched swept source based on extra-cavity spectral shaping assisted by a booster semiconductor optical amplifier," *Optics Express*, vol. 30, p. 33 708, 19 Sep. 2022, ISSN: 10944087. DOI: 10.1364/oe.468042.

[96] D. Huang, F. Li, Z. He, Z. Cheng, C. Shang, and P. K. A. Wai, "400 mhz ultrafast optical coherence tomography," *Optics Letters*, vol. 45, p. 6675, 24 Dec. 2020, ISSN: 0146-9592. DOI: 10.1364/ol.409607.

[97] S. R. Chinn, E. A. Swanson, and J. G. Fujimoto, "Optical coherence tomography using a frequency-tunable optical source," *Optics Letters*, vol. 22, 5 1997. DOI: 10.1364/OL.22.000340.

[98] Z. He and K. Hotate, "Synthesized optical coherence tomography for imaging of scattering objects by use of a stepwise frequency-modulated tunable laser diode," *Optics Letters*, vol. 24, 21 1999, ISSN: 0146-9592. DOI: 10.1364/ol.24.001502.

[99] U. H. P. Haberland, V. Blazek, and H. J. Schmitt, "Chirp optical coherence tomography of layered scattering media," *Journal of Biomedical Optics*, vol. 3, pp. 259–266, 3 1998. DOI: 10.1117/1.429889.

[100] R. Leitgeb, M. Wojtkowski, A. Kowalczyk, C. K. Hitzenberger, M. Sticker, and A. F. Fercher, "Spectral measurement of absorption by spectroscopic frequency-domain optical coherence tomography," *Optics Letters*, vol. 25, 11 2000, ISSN: 0146-9592. DOI: 10.1364/ol.25.000820.

[101] J. J. Kałuzny, M. Wojtkowski, and A. Kowalczyk, "Imaging of the anterior segment of the eye by spectral optical coherence tomography," *Optica Applicata*, vol. 32, 4 2003, ISSN: 00785466.

[102] M. Wojtkowski, R. Leitgeb, A. Kowalczyk, T. Bajraszewski, and A. F. Fercher, "In vivo human retinal imaging by fourier domain optical coherence tomography," *Journal of Biomedical Optics*, vol. 7, 3 2002, ISSN: 10833668. DOI: 10.1117/1.1482379.

[103] E. A. Swanson and J. G. Fujimoto, "The ecosystem that powered the translation of OCT from fundamental research to clinical and commercial impact [Invited]," *Biomedical Optics Express*, vol. 8, 3 2017, ISSN: 2156-7085. DOI: 10.1364/boe.8.001638.

[104] M. Klufts, S. Lotz, M. A. Bashir, T. Pfeiffer, A. Mlynek, W. Wieser, A. Chamorovskiy, V. R. Shidlovski, and R. A. Huber, "850 nm fdml: Performance and challenges," in *Optical Coherence Tomography and Coherence Domain Optical Methods in Biomedicine XXVII*, J. A. Izatt and J. G. Fujimoto, Eds., SPIE, Mar. 2023, p. 9, ISBN: 9781510658394. DOI: 10.1117/12.2649646.

[105] M. Glick, L. Liao, and K. Schmidtke, *Integrated Photonics for Data Communication Applications*. Elsevier, 2023.

[106] M. Kendrisic, V. Agafonov, M. Salas, L. Ferrara, M. Niederleithner, H. Resch, S. Steiner, C. Vass, W. Drexler, and R. A. Leitgeb, "Thermally tuned VCSEL at 850 nm as a low-cost alternative source for full-eye SS-OCT," *Optics Letters*, vol. 48, 11 2023, ISSN: 0146-9592. DOI: 10.1364/ol.489050.

[107] J. S. Heier, Y. Liu, N. M. Holekamp, M. H. Ali, K. Astafurov, K. J. Blinder, M. A. Busquets, M. A. Chica, M. J. Elman, J. G. Fein, *et al.*, "Clinical use of home oct data to manage neovascular age-related macular degeneration," *Journal of VitreoRetinal Diseases*, p. 24 741 264 241 302 858, 2024.

[108] J. Xu, C. Zhang, J. Xu, K. K. Y. Wong, and K. K. Tsia, "Megahertz all-optical swept-source optical coherence tomography based on broadband amplified optical time-stretch," *Optics Letters*, vol. 39, p. 622, 3 Feb. 2014, ISSN: 0146-9592. DOI: 10.1364/ol.39.000622.

[109] T. Klein and R. Huber, "High-speed OCT light sources and systems [Invited]," *Biomedical Optics Express*, vol. 8, p. 828, 2 Feb. 2017, ISSN: 2156-7085. DOI: 10.1364/boe.8.000828.

[110] M. Göb, S. Lotz, L. Ha-Wissel, S. Burhan, S. Böttger, F. Ernst, J. Hundt, and R. A. Huber, "Large area robotically assisted optical coherence tomography (LARA-OCT) for skin imaging with MHz-OCT surface tracking," J. A. Izatt and J. G. Fujimoto, Eds., SPIE, Mar. 2023, p. 29, ISBN: 9781510658394. DOI: 10.1117/12.2652616.

[111] M. Göb, T. Pfeiffer, W. Draxinger, S. Lotz, J. P. Kolb, and R. Huber, "Continuous spectral zooming for in vivo live 4D-OCT with MHz A-scan rates and long coherence," *Biomedical Optics Express*, vol. 13, p. 713, 2 Feb. 2022, ISSN: 2156-7085. DOI: 10.1364/boe.448353.

[112] R. K. Meleppat, D. Valente, E. Pijewska, S. Lee, R. S. Jonnal, N. P. Doble, and R. J. Zawadzki, "Progress on the development of FF-SS-OCT system for functional retinal imaging," SPIE-Intl Soc Optical Eng, Mar. 2023, p. 72, ISBN: 9781510658257. DOI: 10.1117/12.2650676.

[113] B. S. Wang and E. W. Mies, "Advanced topics on fusion splicing of specialty fibers and devices," vol. 6781, SPIE, Nov. 2007, p. 678 130, ISBN: 9780819469441. DOI: 10.1117/12.745625.

[114] S. W. Lee and B. M. Kim, "Line-field optical coherence tomography using frequency-sweeping source," *IEEE Journal on Selected Topics in Quantum Electronics*, vol. 14, pp. 50–55, 1 Jan. 2008, ISSN: 1077260X. DOI: 10.1109/JSTQE.2007.914046.

[115] C. Ruini, S. Schuh, E. Sattler, and J. Welzel, "Line-field confocal optical coherence tomography—practical applications in dermatology and comparison with established imaging methods," *Skin Research and Technology*, vol. 27, pp. 340–352, 3 May 2021, ISSN: 16000846. DOI: 10.1111/srt.12949.

[116] E. Auksorius, K. Adomavičius, D. Borycki, P. Węgrzyn, S. Tomczewski, K. Liżewski, I. Žičkienė, and M. Wojtkowski, "Spatio-temporal optical coherence tomography with optimized light source for in vivo imaging of chorioretinal complex," in *Biophotonics Congress: Optics in the Life Sciences 2023 (OMA, NTM, BODA, OMP, BRAIN)*, Optica Publishing Group, 2023, DTh2A.5, ISBN: 978-1-957171-21-0. DOI: 10.1364/BODA.2023.DTh2A.5.

[117] S. Tomczewski, P. Węgrzyn, D. Borycki, E. Auksorius, M. Wojtkowski, and A. Curatolo, "Light-adapted flicker optoretinograms captured with a spatio-temporal optical coherence-tomography (STOC-T) system," *Biomedical Optics Express*, vol. 13, 4 2022, ISSN: 2156-7085. DOI: 10.1364/boe.444567.

[118] E. Auksorius, D. Borycki, P. Wegrzyn, B. L. Sikorski, K. Lizewski, I. Zickiene, M. Rapolu, K. Adomavicius, S. Tomczewski, and M. Wojtkowski, "Spatio-temporal optical coherence tomography provides full thickness imaging of the chorioretinal complex," *iScience*, vol. 25, 12 2022, ISSN: 25890042. DOI: 10.1016/j.isci.2022.105513.

[119] E. Auksorius, D. Borycki, and M. Wojtkowski, "Multimode fiber enables control of spatial coherence in fourier-domain full-field optical coherence tomography for in vivo corneal imaging," *Optics Letters*, vol. 46, 6 2021, ISSN: 0146-9592. DOI: 10.1364/ol.417178.

[120] D. J. Fechtig, B. Grajciar, T. Schmoll, C. Blatter, R. M. Werkmeister, W. Drexler, and R. A. Leitgeb, "Line-field parallel swept source MHz oct for structural and functional retinal imaging," *Biomedical Optics Express*, vol. 6, p. 716, 3 Mar. 2015, ISSN: 2156-7085. DOI: 10.1364/boe.6.000716.

[121] R. Huber, M. Wojtkowski, K. Taira, J. G. Fujimoto, and K. Hsu, "Amplified, frequency swept lasers for frequency domain reflectometry and OCT imaging: Design and scaling principles," *Opt. Express*, vol. 13, pp. 3513–3528, 9 Apr. 2005. DOI: 10.1364/OPEX.13.003513.

[122] T. Pfeiffer, M. Petermann, W. Draxinger, C. Jirauschek, and R. Huber, "Ultra low noise fourier domain mode locked laser for high quality megahertz optical coherence tomography," *Biomedical Optics Express*, vol. 9, p. 4130, 9 Sep. 2018, ISSN: 2156-7085. DOI: 10.1364/boe.9.004130.

[123] C. Grill, T. Blömker, M. Schmidt, D. Kastner, T. Pfeiffer, J. P. Kolb, W. Draxinger, S. Karpf, C. Jirauschek, and R. Huber, "Towards phase-stabilized fourier domain mode-locked frequency combs," *Communications Physics*, vol. 5, no. 1, p. 212, 2022.

[124] S. Slepneva, B. O'Shaughnessy, B. Kelleher, S. P. Hegarty, A. G. Vladimirov, and G. Huyet, "Dynamics of fourier domain mode locked lasers," vol. 2017-January, Institute of Electrical and Electronics Engineers Inc., Oct. 2017, pp. 1–2, ISBN: 9781943580279. DOI: 10.1364/OE.21.019240.

[125] S. Todor, B. Biedermann, R. Huber, and C. Jirauschek, "Balance of physical effects causing stationary operation of Fourier domain mode-locked lasers," *Journal of the Optical Society of America B*, vol. 29, 4 2012, ISSN: 0740-3224. DOI: 10.1364/josab.29.000656.

[126] B. R. Biedermann, W. Wieser, C. M. Eigenwillig, T. Klein, and R. Huber, "Dispersion, coherence and noise of Fourier domain mode locked (FDML) lasers," 2009. DOI: 10.1364/oe.17.009947.

[127] W. Wieser, B. R. Biedermann, T. Klein, C. M. Eigenwillig, and R. Huber, "Ultra-rapid dispersion measurement in optical fibers," *Optics Express*, vol. 17, 25 2009, ISSN: 1094-4087. DOI: 10.1364/oe.17.022871.

[128] R. Huber, D. C. Adler, and J. G. Fujimoto, "Buffered fourier domain mode locking: Unidirectional swept laser sources for optical coherence tomography imaging at 370,000 lines/s," *Optics Letters*, vol. 31, 20 2006, ISSN: 0146-9592. DOI: 10.1364/ol.31.002975.

[129] S. Lotz, M. Gob, W. Draxinger, A. Dick, and R. Huber, "13.4 MHz FDML laser for intra-surgical optical coherence tomography," in *Conference on Lasers and Electro-Optics/Europe (CLEO/Europe 2023) and European Quantum Electronics Conference (EQEC 2023)*, IEEE, 2023, ISBN: 9798350345995. DOI: 10.1109/CLEO/Europe-EQEC57999.2023.10231419.

[130] S. Burhan, N. Detrez, K. Rewerts, M. Göb, S. Buschschlüter, C. Hagel, M. M. Bonsanto, D. Theisen-Kunde, R. A. Huber, and R. Brinkmann, "Phase analysis strategies for Mhz OCE in the large displacement regime," in *Optical Coherence Tomography and Coherence Domain Optical Methods in Biomedicine XXVII*, J. A. Izatt and J. G. Fujimoto, Eds., SPIE, Mar. 2023, p. 66, ISBN: 9781510658394. DOI: 10.1117/12.2652847.

[131] W. Draxinger, D. Theisen-Kunde, L. Schützeck, N. Detrez, P. Strenge, V. Danicke, J. Kren, P. Kuppler, S. Spahr-Hess, M. M. Bonsanto, R. Brinkmann, and R. Huber, "High speed 4d in-vivo oct imaging of the human brain: Creating high density datasets for machine learning toward identification of malign tissue in real time," SPIE-Intl Soc Optical Eng, Mar. 2023, p. 41, ISBN: 9781510658851. DOI: 10.1117/12.2648505.

[132] J. P. Kolb, W. Draxinger, J. Klee, T. Pfeiffer, M. Eibl, T. Klein, W. Wieser, and R. Huber, "Live video rate volumetric OCT imaging of the retina with multi-MHz A-scan rates," *PLoS ONE*, vol. 14, 3 2019, ISSN: 19326203. DOI: 10.1371/journal.pone.0213144.

[133] W. Wieser, W. Draxinger, T. Klein, S. Karpf, T. Pfeiffer, and R. Huber, "High definition live 3d-OCT in vivo: Design and evaluation of a 4d OCT engine with 1 GVoxel/s," *Biomedical Optics Express*, vol. 5, 9 2014, ISSN: 2156-7085. DOI: 10.1364/boe.5.002963.

[134] C. Pfäffle, H. Spahr, K. Gercke, L. Puyo, S. Höhl, D. Melenberg, Y. Miura, G. Hüttmann, and D. Hillmann, "Phase-sensitive measurements of depth-dependent signal transduction in the inner plexiform layer," *Frontiers in Medicine*, vol. 9, 2022, ISSN: 2296858X. DOI: 10.3389/fmed.2022.885187.

[135] L. Puyo, H. Spahr, C. Pfäffle, G. Hüttmann, and D. Hillmann, "Retinal blood flow imaging with combined full-field swept-source optical coherence tomography and laser doppler holography," *Optics Letters*, vol. 47, 5 2022, ISSN: 0146-9592. DOI: 10.1364/ol.449739.

[136] W.-M. Zhang, G. Meng, and D. Chen, "Stability, nonlinearity and reliability of electrostatically actuated mems devices," *Sensors*, pp. 760–796, 2007, ISSN: 1424-8220. DOI: 10.3390/s7050760.

[137] B. Kögel, H. Halbritter, M. Maute, G. Böhm, M. C. Amann, and P. Meissner, "Singlemode and polarization stable MEMS-VCSEL with broadband tuning characteristics around 1.55m," 2006, ISBN: 9782912328397. DOI: 10.1109/ECOC.2006.4801075.

[138] P. Qiao, K. T. Cook, K. Li, and C. J. Chang-Hasnain, "Wavelength-swept VCSELs," *IEEE Journal of Selected Topics in Quantum Electronics*, vol. 23, 6 Nov. 2017, ISSN: 21910359. DOI: 10.1109/JSTQE.2017.2707181.

[139] S. D. Senturia, *Microsystem Design*. Springer, 2001. DOI: 10.1007/b117574.

[140] A. Simonsen, G. C. Park, T. E. Ansbæk, O. Hansen, and K. Yvind, "Design of a robust photonic crystal mirror for mems vcsels," *Optics Express*, vol. 31, 11 2023, ISSN: 10944087. DOI: 10.1364/oe.491411.

[141] H. K. Sahoo, T. Ansbak, L. Ottaviano, E. Semenova, F. Zubov, O. Hansen, and K. Yvind, "Tunable MEMS VCSEL on silicon substrate," *IEEE Journal of Selected Topics in Quantum Electronics*, vol. 25, 6 2019, ISSN: 21910359. DOI: 10.1109/JSTQE.2019.2927575.

[142] Z. Wang, B. Potsaid, L. Chen, C. Doerr, H.-C. Lee, T. Nielson, V. Jayaraman, A. E. Cable, E. Swanson, and J. G. Fujimoto, "Cubic meter volume optical coherence tomography," *Optica*, vol. 3, no. 12, pp. 1496–1503, Dec. 2016. DOI: 10.1364/OPTICA.3.001496. [Online]. Available: https://opg.optica.org/optica/abstract.cfm?URI=optica-3-12-1496.

[143] S. H. Yun, C. Boudoux, G. J. Tearney, and B. E. Bouma, "High-speed wavelength-swept semiconductor laser with a polygon-scanner-based wavelength filter," *Optics Letters*, vol. 28, 20 2003. DOI: 10.1364/OL.28.001981.

[144] W. Y. Oh, S. H. Yun, G. J. Tearney, and B. E. Bouma, "115 kHz tuning repetition rate ultrahigh-speed wavelength-swept semiconductor laser," *Opt Lett*, vol. 30, pp. 3159–3161, 23 2005. DOI: 10.1364/OL.30.003159.

[145] V.-F. Duma, K.-S. Lee, P. Meemon, and J. P. Rolland, "Experimental investigations of the scanning functions of galvanometer-based scanners with applications in oct," *Applied Optics*, vol. 50, pp. 5735–5750, 29 2011. DOI: 0003-6935/11/295735-15.

[146] A. Chong, W. H. Renninger, and F. W. Wise, "Properties of normal-dispersion femtosecond fiber lasers," *Journal of the Optical Society of America B*, vol. 25, 2 2008. DOI: 10.1364/JOSAB.25.000140.

[147] S. Yagi, K. Naganuma, T. Imai, Y. Shibata, S. Ishibashi, Y. Sasaki, M. Sasaura, K. Fujiura, and K. Kato, "A mechanical-free 150-kHz repetition swept light source incorporated a ktn electro-optic deflector," vol. 7889, SPIE, Feb. 2011, 78891J, ISBN: 9780819484260. DOI: 10.1117/12.876024.

[148] Y. Okabe, Y. Sasaki, M. Ueno, T. Sakamoto, S. Toyoda, S. Yagi, K. Naganuma, K. Fujiura, Y. Sakai, J. Kobayashi, K. Omiya, M. Ohmi, and M. Haruna, "200 kHz swept light source equipped with KTN deflector for optical coherence tomography," *Electronics Letters*, vol. 48, 4 2012, ISSN: 00135194. DOI: 10.1049/el.2011.4057.

[149] S. H. Yun, C. Boudoux, M. C. Pierce, J. F. D. Boer, G. J. Tearney, and B. E. Bouma, "Extended-cavity semiconductor wavelength-swept laser for biomedical imaging," *IEEE Photonics Technology Letters*, vol. 16, pp. 293–295, 1 Jan. 2004, ISSN: 10411135. DOI: 10.1109/LPT.2003.820096.

[150] T. Huo, J. Zhang, J.-g. Zheng, T. Chen, C. Wang, N. Zhang, W. Liao, X. Zhang, and P. Xue, "Linear-in-wavenumber swept laser with an acousto-optic deflector for optical coherence tomography," *Optics Letters*, vol. 39, p. 247, 2 Jan. 2014, ISSN: 0146-9592. DOI: 10.1364/ol.39.000247.

[151] M. Everson, G. Dobre, and V. F. Duma, "Aspects of vignetting in a polygon mirror-based spectral filter for swept source optical coherence tomography (SS-OCT)," in *Seventh International Conference on Lasers in Medicine*, C. Todea, A. Podoleanu, and V.-F. Duma, Eds., SPIE, Aug. 2018, p. 17, ISBN: 9781510622876. DOI: 10.1117/12.2282284.

[152] G. Wang, Y. Zhou, R. Min, E. Du, and C. Wang, "Principle and recent development in photonic time-stretch imaging," *Photonics*, vol. 10, 7 Jul. 2023, ISSN: 23046732. DOI: 10.3390/photonics10070817.

[153] H. Asghari, "Visible wavelength time-stretch optical coherence tomography," *Optics Express*, Jul. 2023, ISSN: 10944087. DOI: 10.1364/oe.492753.

[154] S. Tan, X. Wei, L. Yang, C. Li, N. Chen, K. K. Tsia, and K. K. Y. Wong, "Optical wavelength-swept source at 2.0 μm and its application for ultrafast microscopy," in *OSA Technical Digest (online) (Optica Publishing Group, 2017)*, 2017. DOI: 10.1364/CLEO_AT.2017.JW2A.65.

[155] Y. Qiu, J. Xu, K. K. Y. Wong, and K. K. Tsia, "Exploiting few mode-fibers for optical time-stretch confocal microscopy in the short near-infrared window," *Optics Express*, vol. 20, pp. 24 115–24 123, 22 2012. DOI: 10.1364/OE.20.024115.

[156] J. L. Wu, Y. Q. Xu, J. J. Xu, X. M. Wei, A. C. Chan, A. H. Tang, A. K. Lau, B. M. Chung, H. C. Shum, E. Y. Lam, K. K. Wong, and K. K. Tsia, "Ultrafast laser-scanning time-stretch imaging at visible wavelengths," *Light: Science and Applications*, vol. 6, 1 2017, ISSN: 20477538. DOI: 10.1038/lsa.2016.196.

[157] S. Moon and D. Y. Kim, "Ultra-high-speed optical coherence tomography with a stretched pulse supercontinuum source," *Optics Express*, vol. 14, pp. 11 575–11 585, 24 2006. DOI: 10.1364/OE.14.011575.

[158] S. Caujolle, R. Cernat, G. Silvestri, M. J. Marques, A. Bradu, T. Feuchter, G. Robinson, D. K. Griffin, and A. Podoleanu, "Speckle variance OCT for depth resolved assessment of the viability of bovine embryos," *Biomedical Optics Express*, vol. 8, p. 5139, 11 Nov. 2017, ISSN: 2156-7085. DOI: 10.1364/boe.8.005139.

[159] M. Bondu, M. J. Marques, P. M. Moselund, G. Lall, A. Bradu, and A. Podoleanu, "Multispectral photoacoustic microscopy and optical coherence tomography using a single supercontinuum source," *Photoacoustics*, vol. 9, pp. 21–30, Mar. 2018, ISSN: 22135979. DOI: 10.1016/j.pacs.2017.11.002.

[160] S. Chen, X. Shu, J. Yi, A. Fawzi, and H. F. Zhang, "Dual-band optical coherence tomography using a single supercontinuum laser source," *Journal of Biomedical Optics*, vol. 21, 6 2016. DOI: 10.1117/1.

[161] S. R. D. S, M. Jensen, L. Grüner-Nielsen, J. T. Olsen, P. Heiduschka, B. Kemper, J. Schnekenburger, M. Glud, M. Mogensen, N. M. Israelsen, and O. Bang, "Shot-noise limited, supercontinuum-based optical coherence tomography," *Light: Science and Applications*, vol. 10, 1 Dec. 2021, ISSN: 20477538. DOI: 10.1038/s41377-021-00574-x.

[162] U. Morgner, W. Drexler, X. D. Li, C. Pitris, E. P. Ippen, and J. G. Fujimoto, "Spectroscopic optical coherence tomography," *Optics Letters*, vol. 25, 2 2000. DOI: 10.1364/OL.25.000111.

[163] R. Eilkaer, "Mid-infrared supercontinuum based spectroscopic oct," Ph.D. dissertation, Technical University of Denmark, Feb. 2023.

[164] E. Alarousu, L. Krehut, T. Prykäri, and R. Myllylä, "Study on the use of optical coherence tomography in measurements of paper properties," *Measurement Science and Technology*, vol. 16, 5 2005, ISSN: 09570233. DOI: 10.1088/0957-0233/16/5/012.

[165] J. Wu, Y. Xu, J. Xu, X. Wei, A. C. S. Chan, A. H. L. Tang, A. K. S. Lau, B. M. F. Chung, H. C. Shum, E. Y. Lam, K. K. Y. Wong, and K. K. Tsia, "Ultrafast laser-scanning time-stretch imaging at visible wavelengths email addresses," *Light Science and Applications*, 2017, ISSN: 2857-8486. DOI: 10.1038/lsa.2016.196.

[166] K. Goda, D. R. Solli, K. K. Tsia, and B. Jalali, "Theory of amplified dispersive fourier transformation," *Physical Review A - Atomic, Molecular, and Optical Physics*, vol. 80, 4 2009, ISSN: 10502947. DOI: 10.1103/PhysRevA.80.043821.

[167] C. Zhang, Y. Qiu, R. Zhu, K. K. Y. Wong, and K. K. Tsia, "Serial time-encoded amplified microscopy (STEAM) based on a stabilized picosecond supercontinuum source," *Optics Express*, vol. 19, 17 2011, ISSN: 10944087. DOI: 10.1364/oe.19.015810.

[168] K. K. Tsia, K. Goda, D. Capewel, and B. Jalali, "Performance of serial time-encoded amplified microscopy," 2010. DOI: 10.1364/oe.18.010016.

[169] C. Lei, B. Guo, Z. Cheng, and K. Goda, *Optical time-stretch imaging: Principles and applications*, Mar. 2016. DOI: 10.1063/1.4941050.

[170] S. Tan, X. Wei, B. Li, Q. T. K. Lai, K. K. Tsia, and K. K. Y. Wong, "Ultrafast optical imaging at 2.0 um through second-harmonic-generation-based time-stretch at 1.0 um," *Optics Letters*, vol. 43, 16 2018, ISSN: 0146-9592. DOI: 10.1364/ol.43.003822.

[171] T. T. W. Wong, A. K. S. Lau, K. K. Y. Wong, and K. K. Tsia, "Optical time-stretch confocal microscopy at 1 m," *Optics Letters*, vol. 37, 16 2012, ISSN: 0146-9592. DOI: 10.1364/ol.37.003330.

[172] D. Huang, F. Li, C. Shang, Z. Cheng, and P. K. A. Wai, "Reconfigurable time-stretched swept laser source with up to 100 MHz sweep rate, 100 nm bandwidth, and 100 mm oct imaging range," *Photonics Research*, vol. 8, p. 1360, 8 Aug. 2020, ISSN: 2327-9125. DOI: 10.1364/prj.390076.

[173] J. Xu, X. Wei, L. Yu, C. Zhang, J. Xu, K. K. Y. Wong, and K. K. Tsia, "Performance of megahertz amplified optical time-stretch optical coherence tomography (aot-oct)," *Optics Express*, vol. 22, p. 22 498, 19 Sep. 2014, ISSN: 1094-4087. DOI: 10.1364/oe.22.022498.

[174] T. Huo, C. Wang, X. Zhang, T. Chen, W. Liao, W. Zhang, S. Ai, J.-C. Hsieh, and P. Xue, "Ultrahigh-speed optical coherence tomography utilizing all-optical 40MHz swept-source," *Journal of Biomedical Optics*, vol. 20, p. 030 503, 3 Mar. 2015, ISSN: 1083-3668. DOI: 10.1117/1.jbo.20.3.030503.

[175] H. Chen, Y. Li, D. Huang, F. Li, C. Lu, and P. K. A. Wai, "114 nm broadband all-fiber nonlinear polarization rotation mode locked-laser and time-stretch optical coherence tomography," *Optics Express*, vol. 29, p. 33 322, 21 Oct. 2021, ISSN: 10944087. DOI: 10.1364/oe.438609.

[176] E. Genier, S. Grelet, R. D. Engelsholm, P. Bowen, P. M. Moselund, O. Bang, J. M. Dudley, and T. Sylvestre, "Ultra-flat, low-noise, and linearly polarized fiber supercontinuum source covering 670–1390 nm," *Optics Letters*, vol. 46, p. 1820, 8 Apr. 2021, ISSN: 0146-9592. DOI: 10.1364/ol.420676.

[177] Y. Nakazaki and S. Yamashita, "Fast and wide tuning range wavelength-swept fiber laser based on dispersion tuning and its application to dynamic fbg sensing," *Optics Express*, vol. 17, 10 2009, ISSN: 1094-4087. DOI: 10.1364/oe.17.008310.

[178] S. Yamashita and Y. Takubo, "Wide and fast wavelength-swept fiber lasers based on dispersion tuning and their application to optical coherence tomography," *Photonic Sensors*, vol. 3, 4 2013, ISSN: 16749251. DOI: 10.1007/s13320-013-0129-0.

[179] S. J. Park, G. H. Kim, H. D. Lee, C. S. Kim, and M. Jo, "Narrowing linewidth of wavelength-swept active mode locking laser based on cross gain modulation," *Applied Sciences (Switzerland)*, vol. 9, 19 2019, ISSN: 20763417. DOI: 10.3390/app9194029.

[180] C. Zhang, P. Liao, B. Burgoyne, Y. Kim, F. Trépanier, A. Villeneuve, and O. Liboiron-Ladouceur, "Low-cost dispersion-tuned active harmonic mode-locked laser with a 3-cm coherence length," *IEEE Journal on Selected Topics in Quantum Electronics*, vol. 20, 5 2014, ISSN: 1077260X. DOI: 10.1109/JSTQE.2014.2304540.

[181] H. D. Lee, G. H. Kim, J. G. Shin, B. Lee, C. S. Kim, and T. J. Eom, "Akinetic swept-source optical coherence tomography based on a pulse-modulated active mode locking fiber laser for human retinal imaging," *Scientific Reports*, vol. 8, 1 2018, ISSN: 20452322. DOI: 10.1038/s41598-018-36252-z.

[182] H. Nagai and S. Yamashita, "Coherence improvement in dispersion-tuned swept laser by pulse modulation," *Electronics Letters*, vol. 50, 23 2014, ISSN: 00135194. DOI: 10.1049/el.2014.2849.

[183] R. Riha, A. Bradu, and A. Podoleanu, "Dual resonance akinetic dispersive cavity swept source at 900 kHz using a cFBG and an intensity modulator," *Optics Letters*, vol. 47, 16 2022, ISSN: 0146-9592. DOI: 10.1364/ol.463675.

[184] S. Tozburun, M. Siddiqui, and B. J. Vakoc, "A rapid, dispersion-based wavelength-stepped and wavelength-swept laser for optical coherence tomography," *Optics Express*, vol. 22, p. 3414, 3 Feb. 2014, ISSN: 1094-4087. DOI: 10.1364/oe.22.003414.

[185] M. Siddiqui, A. S. Nam, S. Tozburun, N. Lippok, C. Blatter, and B. J. Vakoc, "High-speed optical coherence tomography by circular interferometric ranging," *Nature Photonics*, vol. 12, 2 2018, ISSN: 17494893. DOI: 10.1038/s41566-017-0088-x.

[186] G. H. Kim, S. J. Bak, T. J. Eom, and C.-S. Kim, "1.0-um broadband dispersion-compensated stretched-pulse mode locking wavelength-swept source for in-vivo retinal oct imaging," J. A. Izatt and J. G. Fujimoto, Eds., SPIE, Mar. 2023, p. 7, ISBN: 9781510663725. DOI: 10.1117/12.2650923.

[187] R. Khazaeinezhad, M. Siddiqui, and B. J. Vakoc, "16mhz wavelength-swept and wavelength-stepped laser architectures based on stretched-pulse active mode locking with a single continuously chirped fiber bragg grating," *Optics Letters*, vol. 42, p. 2046, 10 May 2017, ISSN: 0146-9592. DOI: 10.1364/OL.42.002046. [Online]. Available: https://opg.optica.org/abstract.cfm?URI=ol-42-10-2046.

[188] J. Joo, T. S. Kim, B. J. Vakoc, and W.-Y. Oh, "Robust and easy-to-operate stretched-pulse mode-locked wavelength-swept laser with an all-polarization-maintaining fiber cavity for 10 Mhz A-line rate optical coherence tomography," *Optics Letters*, vol. 46, 16 2021, ISSN: 0146-9592. DOI: 10.1364/ol.424835.

[189] P. G. Bowen, "Environmentally stable mode-locked fibre lasers in the near-infrared," Ph.D. dissertation, University of Auckland, 2017.

[190] P. Bowen, H. Singh, A. Runge, R. Provo, and N. G. Broderick, "Mode-locked femtosecond all-normal all-PM Yb-doped fiber laser at 1060 nm," *Optics Communications*, vol. 364, 2016, ISSN: 00304018. DOI: 10.1016/j.optcom.2015.11.043.

[191] P. Bowen, M. Erkintalo, and N. G. Broderick, "Large net-normal dispersion Er-doped fibre laser mode-locked with a nonlinear amplifying loop mirror," *Optics Communications*, vol. 410, 2018, ISSN: 00304018. DOI: 10.1016/j.optcom.2017.10.053.

[192] J. Y. Joo, B. J. Vakoc, and W.-Y. Oh, "Stretched-pulse mode-locked wavelength-swept laser with intra- and extra-cavity stretching for ultrahigh-speed optical coherence tomography," J. A. Izatt and J. G. Fujimoto, Eds., SPIE, Mar. 2022, p. 26, ISBN: 9781510647671. DOI: 10.1117/12.2610542.

[193] D. C. Adler, W. Wieser, F. Trepanier, J. M. Schmitt, and R. A. Huber, "Extended coherence length fourier domain mode locked lasers at 1310 nm," *Optics Express*, vol. 19, 21 2011, ISSN: 10944087. DOI: 10.1364/oe.19.020930.

[194] C. Grill, T. Blömker, M. Schmidt, D. Kastner, T. Pfeiffer, J. P. Kolb, W. Draxinger, S. Karpf, C. Jirauschek, and R. Huber, "Towards phase-stabilized Fourier domain mode-locked frequency combs," *Communications Physics*, vol. 5, 1 2022, ISSN: 23993650. DOI: 10.1038/s42005-022-00960-w.

[195] D. D. John, C. B. Burgner, B. Potsaid, M. E. Robertson, B. K. Lee, W. J. Choi, A. E. Cable, J. G. Fujimoto, and V. Jayaraman, "Wideband electrically pumped 1050-nm MEMS-tunable VCSEL for ophthalmic imaging," *Journal of Lightwave Technology*, vol. 33, pp. 3461–3468, 16 Aug. 2015, ISSN: 07338724. DOI: 10.1109/JLT.2015.2397860.

[196] I. R. Lamoso, A. M. Jiménez, J. Cesar, S. Preu, and A. G. H. Podoleanu, "Characterization of SiN/SiO2 based mems-vcsel at 1550 nm for optical coherence tomography," J. A. Izatt and J. G. Fujimoto, Eds., SPIE, Mar. 2023, p. 106, ISBN: 9781510658394. DOI: 10.1117/12.2652961.

[197] J. Zhang, "Mems-vcsel swept-source optical coherence tomography for multi-mhz endoscopic structural and angiographic imaging," 2021.

[198] S. Gloor, A. H. Bachmann, M. Epitaux, T. von Niederhäusern, P. Vorreau, N. Matuschek, K. Hsu, M. Duelk, and C. Vélez, "High-speed miniaturized swept sources based on resonant mems mirrors and diffraction gratings," vol. 8571, SPIE, Mar. 2013, p. 85712X, ISBN: 9780819493408. DOI: 10.1117/12.2007106.

[199] S. Paul, M. T. Haidar, J. Cesar, M. Malekizandi, B. Kögel, C. Neumeyr, M. Ortsiefer, and F. Küppers, "Far-field, linewidth and thermal characteristics of a high-speed 1550-nm MEMS tunable VCSEL," *Optics Express*, vol. 24, p. 13 142, 12 Jun. 2016, ISSN: 10944087. DOI: 10.1364/oe.24.013142.

[200] V. Jayaraman, C. Burgner, J. Carter, I. Borova, N. Bramham, C. Lindblad, and A. Cazabat, "Widely tunable electrically pumped 1050nm mems-vcsels for optical coherence tomography," C. Lei and L. A. Graham, Eds., SPIE, Feb. 2020, p. 27, ISBN: 9781510633636. DOI: 10.1117/12.2543819.

[201] M. E. Fermann and I. Hartl, "Ultrafast fibre lasers," *Nature Photonics*, vol. 7, pp. 868–874, 11 Nov. 2013, ISSN: 1749-4885. DOI: 10.1038/nphoton.2013.280.

[202] L. G. Cohen, "Comparison of single-mode fiber dispersion measurement techniques," *Journal of Lightwave Technology*, vol. 3, pp. 958–966, 5 1985, ISSN: 15582213. DOI: 10.1109/JLT.1985.1074327.

[203] B. Costa, D. Mazzoni, M. Puleo, and E. Vezzoni, "Phase shift technique for the measurement of chromatic dispersion in optical fibers using led's," *IEEE Transactions on Microwave Theory and Techniques*, vol. 30, pp. 1497–1503, 10 1982, ISSN: 15579670. DOI: 10.1109/TMTT.1982.1131283.

[204] J. Y. Lee and D. Y. Kim, *Versatile chromatic dispersion measurement of a single mode fiber using spectral white light interferometry*, 2006.

[205] M. Klufts, S. Lotz, M. Bashir, S. Karpf, and R. Huber, "Ultra-high-accuracy chromatic dispersion measurement in optical fibers," in *Optical Components and Materials XIX*, S. Jiang and M. J. F. Digonnet, Eds., International Society for Optics and Photonics, vol. 11997, SPIE, 2022, p. 119970L. DOI: 10.1117/12.2608773. [Online]. Available: https://doi.org/10.1117/12.2608773.

[206] S. Rivet, M. Maria, A. Bradu, T. Feuchter, L. Leick, and A. Podoleanu, "Complex master slave interferometry," *Optics Express*, vol. 24, p. 2885, 3 Feb. 2016, ISSN: 1094-4087. DOI: 10.1364/oe.24.002885.

[207] M. Maria, I. B. Gonzalo, M. Bondu, R. D. Engelsholm, T. Feuchter, P. M. Moselund, L. Leick, O. Bang, and A. Podoleanu, "A comparative study of noise in supercontinuum light sources for ultra-high resolution optical coherence tomography," in *Design and Quality for Biomedical Technologies X*, R. Raghavachari and R. Liang, Eds., International Society for Optics and Photonics, vol. 10056, SPIE, 2017, 100560O. DOI: 10.1117/12.2251500. [Online]. Available: https://doi.org/10.1117/12.2251500.

[208] E. Genier, P. Bowen, T. Sylvestre, J. M. Dudley, P. Moselund, and O. Bang, "Amplitude noise and coherence degradation of femtosecond supercontinuum generation in all-normal-dispersion fibers," *J. Opt. Soc. Am. B*, vol. 36, no. 2, A161–A167, Feb. 2019. DOI: 10.1364/JOSAB.36.00A161. [Online]. Available: https://opg.optica.org/josab/abstract.cfm?URI=josab-36-2-A161.

[209] ——, "Amplitude noise and coherence degradation of femtosecond supercontinuum generation in all-normal-dispersion fibers," *Journal of the Optical Society of America B*, vol. 36, 2 2019, ISSN: 0740-3224. DOI: 10.1364/josab.36.00a161.

[210] I. B. Gonzalo, R. D. Engelsholm, M. P. Sørensen, and O. Bang, "Polarization noise places severe constraints on coherence of all-normal dispersion femtosecond supercontinuum generation," *Scientific Reports*, vol. 8, 1 2018, ISSN: 20452322. DOI: 10.1038/s41598-018-24691-7.

[211] S. Rivet, A. Bradu, M. Maria, T. Feuchter, L. Leick, and A. Podoleanu, "From master slave interferometry to complex master slave interferometry: Theoretical work," in *2nd Canterbury Conference on OCT with Emphasis on Broadband Optical Sources*, O. Bang and A. Podoleanu, Eds., SPIE, Mar. 2018, p. 49, ISBN: 9781510616745. DOI: 10.1117/12.2303761.

[212] M. Jensen, I. B. Gonzalo, R. D. Engelsholm, M. Maria, N. M. Israelsen, A. Podoleanu, and O. Bang, "Noise of supercontinuum sources in spectral domain optical coherence tomography," *Journal of the Optical Society of America B*, vol. 36, 2 2019, ISSN: 0740-3224. DOI: 10.1364/josab.36.00a154.

[213] C. C. Rosa and A. G. Podoleanu, "Limitation of the achievable signal-to-noise ratio in optical coherence tomography due to mismatch of the balanced receiver," *Applied Optics*, vol. 43, 25 2004, ISSN: 15394522. DOI: 10.1364/AO.43.004802.

[214] A. F. J. Runge, C. Aguergaray, N. G. R. Broderick, and M. Erkintalo, "Coherence and shot-to-shot spectral fluctuations in noise-like ultrafast fiber lasers," *Optics Letters*, vol. 38, 21 2013, ISSN: 0146-9592. DOI: 10.1364/ol.38.004327.

[215] T. Imai, M. Ueno, Y. Sasaki, and T. Sakamoto, "Analyses of optical rays in KTN optical beam deflectors for device design," *Applied Optics*, vol. 56, p. 7277, 25 Sep. 2017, ISSN: 1559-128X. DOI: 10.1364/ao.56.007277.

[216] T. Imai, J. Miyazu, and J. Kobayashi, "Charge distributions in KTa1-xNbxO3 optical beam deflectors formed by voltage application," *Optics Express*, vol. 22, p. 14 114, 12 Jun. 2014, ISSN: 1094-4087. DOI: 10.1364/oe.22.014114.

[217] Y. Ling, X. Yao, and C. P. Hendon, "Highly phase-stable 200 kHz swept-source optical coherence tomography based on KTN electro-optic deflector," *Biomedical Optics Express*, vol. 8, 8 2017, ISSN: 2156-7085. DOI: 10.1364/boe.8.003687.

[218] Y. Sasaki, M. Fujimoto, S. Yagi, S. Yamagishi, S. Toyoda, and J. Kobayashi, "Ultrahigh-phase-stable swept source based on KTN electro-optic deflector towards doppler OCT and polarization-sensitive OCT," vol. 8934, SPIE, Mar. 2014, 89342Y, ISBN: 9780819498472. DOI: 10.1117/12.2036078.

[219] M. Fujimoto, M. Yamada, K. Yamamoto, Y. Sasaki, S. Toyoda, T. Sakamoto, J. Yamaguchi, T. Sakamoto, M. Ueno, T. Imai, E. Sugai, and S. Yagi, "Stable wavelength-swept light source designed for industrial applications using KTN beam-scanning technology," *Photonic Instrumentation Engineering IV*, vol. 10110, 2017, ISSN: 1996756X. DOI: 10.1117/12.2250229.

[220] M. Ohmi, A. Fukuda, J. Miyazu, M. Ueno, S. Toyoda, and J. Kobayashi, "Development of novel high-speed en face optical coherence tomography system using KTN optical beam deflector," *Applied Physics Express*, vol. 8, p. 027 001, 2 Feb. 2015, ISSN: 18820786. DOI: 10.7567/APEX.8.027001.

[221] M. Ohmi, Y. Shinya, J. Miyazu, S. Toyoda, and T. Sakamoto, "High-speed time-domain en face optical coherence tomography system using KTN optical beam deflector," *Optics and Photonics Journal*, vol. 09, pp. 53–59, 05 2019, ISSN: 2160-8881. DOI: 10.4236/opj.2019.95006.

[222] V. Damodaran, N. J. Vasa, and R. Sarathi, "KTN-based high-speed axial and lateral scanning technique for an optical coherence tomography system and application to dental imaging," *Applied Optics*, vol. 57, 11 2018, ISSN: 1559-128X. DOI: 10.1364/ao.57.002915.

[223] G. R. Römer and P. Bechtold, "Electro-optic and acousto-optic laser beam scanners," *Physics Procedia*, vol. 56, C 2014, ISSN: 18753892. DOI: 10.1016/j.phpro.2014.08.092.

[224] Y. Ling and C. P. Hendon, "Ultrahigh phase-stable swept-source optical coherence tomography as a cardiac imaging platform (conference presentation)," 2016. DOI: 10.1117/12.2216438.

[225] H. Sunaga, K. Endo, T. Ogawa, M. Shinagawa, S. Toyoda, M. Ueno, Y. Sasaki, M. Chen, and T. Sakamoto, "Voltage noise and jitter analysis for swept source optical coherence tomography using kta1xnbxo3 deflector," *Measurement: Journal of the International Measurement Confederation*, vol. 135, pp. 753–761, Mar. 2019, ISSN: 02632241. DOI: 10.1016/j.measurement.2018.11.091.

[226] K. Nakamura, J. Miyazu, M. Sasaura, and K. Fujiura, "Wide-angle, low-voltage electro-optic beam deflection based on space-charge-controlled mode of electrical conduction in KTa 1-xNbxO3," *Applied Physics Letters*, vol. 89, 13 2006, ISSN: 00036951. DOI: 10.1063/1.2357335.

[227] J. P. Kolb, T. Klein, W. Wieser, W. Draxinger, and R. Huber, "High definition in vivo retinal volumetric video rate OCT at 0.6 giga-voxels per second," OSA - The Optical Society, Jul. 2014, ISBN: 9781628417012. DOI: 10.1117/12.2183768.

[228] S. Hariri, A. A. Moayed, A. Dracopoulos, C. Hyun, S. Boyd, and K. Bizheva, "Limiting factors to the OCT axial resolution for in-vivo imaging of human and rodent retina in the 1060nm wavelength range," *Optics Express*, vol. 17, 26 2009, ISSN: 10944087. DOI: 10.1364/oe.17.024304.

[229] M. Klufts, S. Lotz, M. A. Bashir, T. Pfeiffer, A. Mlynek, W. Wieser, A. Chamorovskiy, V. Shidlovski, and R. Huber, "850 nm FDML: performance and challenges," in *Optical Coherence Tomography and Coherence Domain Optical Methods in Biomedicine XXVII*, J. A. Izatt and J. G. Fujimoto, Eds., International Society for Optics and Photonics, vol. 12367, SPIE, 2023, p. 1 236 705. DOI: 10.1117/12.2649646. [Online]. Available: https://doi.org/10.1117/12.2649646.

[230] I. Standard, "Safety of laser products - part 1: Equipment classification and requirements," *Iec 60825-1:2014*, May 2014.

[231] L. von der Emde, M. Saßmannshausen, O. Morelle, G. Rennen, F. G. Holz, M. W. Wintergerst, and T. Ach, "Reliability of retinal layer annotation with a novel, high-resolution optical coherence tomography device: A comparative study," *Bioengineering*, vol. 10, 4 2023, ISSN: 23065354. DOI: 10.3390/bioengineering10040438.

[232] K. S. Park, E. Park, H. Lee, H. J. Lee, S. W. Lee, and T. J. Eom, "Phase stable swept-source optical coherence tomography with active mode-locking laser for contrast enhancements of retinal angiography," *Scientific Reports*, vol. 11, 1 Dec. 2021, ISSN: 20452322. DOI: 10.1038/s41598-021-95982-9.

[233] N. Huang, T. Hormel, G. LIANG, X. Wei, Y. Guo, S. Chen, and Y. Jia, "Optimizing numerical k-sampling for swept-source optical coherence tomography angiography," *Optics Letters*, Feb. 2024, ISSN: 0146-9592. DOI: 10.1364/ol.518720.

[234] A. Podoleanu, R. Cernat, and A. Bradu, "Down-conversion en-face optical coherence tomography," *Biomedical Optics Express*, vol. 10, p. 772, 2 Feb. 2019, ISSN: 2156-7085. DOI: 10.1364/boe.10.000772.

[235] T. Ansbaek, I. S. Chung, E. S. Semenova, O. Hansen, and K. Yvind, "Resonant MEMS tunable VCSEL," *IEEE Journal on Selected Topics in Quantum Electronics*, vol. 19, 4 2013, ISSN: 1077260X. DOI: 10.1109/JSTQE.2013.2257164.

[236] T. Ansbaek, I. S. Chung, E. S. Semenova, and K. Yvind, "1060-nm tunable monolithic high index contrast subwavelength grating VCSEL," *IEEE Photonics Technology Letters*, vol. 25, pp. 365–367, 4 2013, ISSN: 10411135. DOI: 10.1109/LPT.2012.2236087.

[237] A. G. Podoleanu, G. M. Dobre, D. J. Webb, and D. A. Jackson, *Coherence imaging by use of a newton rings sampling function*, 1996.

[238] A. M. Jimenez, S. Grelet, V. Tsatourian, P. B. Montague, A. Bradu, and A. Podoleanu, "400 Hz volume rate swept-source optical coherence tomography at 1060 nm using a KTN deflector," *IEEE Photonics Technology Letters*, vol. 34, pp. 1277–1280, 23 Dec. 2022, ISSN: 1041-1135. DOI: 10.1109/LPT.2022.3212015.

[239] Y. Shi, J. Liu, Z. Gong, C. Burger, V. Jayaraman, and R. K. Wang, "Multichannel delay sampling to extend imaging depth in high-speed swept-source OCT systems," *Optics Letters*, vol. 49, p. 2217, 9 May 2024, ISSN: 0146-9592. DOI: 10.1364/ol.517493.

[240] M. Siddiqui and B. J. Vakoc, "Optical-domain subsampling for data efficient depth ranging in Fourier-domain optical coherence tomography," *Optics Express*, vol. 20, p. 17 938, 16 Jul. 2012, ISSN: 1094-4087. DOI: 10.1364/OE.20.017938.

[241] M. J. Marques, R. Cernat, J. Ensher, A. Bradu, and A. Podoleanu, "Akinetic swept-source master–slave-enhanced optical coherence tomography," *Photonics*, vol. 8, no. 5, 2021, ISSN: 2304-6732. DOI: 10.3390/photonics8050141.

[242] H. Kikuta, K. Iwata, and R. Nagata, "Distance measurement by the wavelength shift of laser diode light," *Applied optics*, vol. 25, no. 17, pp. 2976–2980, 1986.

[243] H. Kikuta, K. Iwata, and R. Nagata, "Absolute distance measurement by wavelength shift interferometry with a laser diode: Some systematic error sources," *Applied optics*, vol. 26, no. 9, pp. 1654–1660, 1987.

[244] J. A. Stone, A. Stejskal, and L. Howard, "Absolute interferometry with a 670-nm external cavity diode laser," *Applied optics*, vol. 38, no. 28, pp. 5981–5994, 1999.

[245] X. Wei, A. K. S. Lau, Y. Xu, K. K. Tsia, and K. K. Y. Wong, "28 MHz swept source at 10 um for ultrafast quantitative phase imaging," *Biomedical Optics Express*, vol. 6, p. 3855, 10 Oct. 2015, ISSN: 2156-7085. DOI: 10.1364/boe.6.003855.

[246] T. Klein and R. Huber, "High-speed oct light sources and systems [invited]," *Biomedical Optics Express*, vol. 8, p. 828, 2 Feb. 2017, ISSN: 2156-7085. DOI: 10.1364/boe.8.000828.

[247] B. Schulte, M. Göb, A. P. Singh, S. Lotz, W. Draxinger, M. Heimke, M. Pieper, T. Heinze, T. Wedel, M. Rahlves, *et al.*, "High-resolution rectoscopy using MHz optical coherence tomography: A step towards real time 3D endoscopy," *Scientific Reports*, vol. 14, no. 1, p. 4672, 2024. DOI: 10.1038/s41598-024-55338-5.

[248] M. J. Marques, R. Green, R. King, S. Clement, P. Hallett, and A. Podoleanu, "Sub-surface characterisation of latest-generation identification documents using optical coherence tomography," *Science Justice*, vol. 61, no. 2, pp. 119–129, 2021, ISSN: 1355-0306. DOI: https://doi.org/10.1016/j.scijus.2020.12.001. [Online]. Available: https://www.sciencedirect.com/science/article/pii/S1355030620303336.

[249] R. Cernat, A. M. Jimenez, and A. Podoleanu, "Downconversion master slave optical coherence tomography for simultaneous en-face imaging at two depths," *Opt. Express*, vol. 32, no. 17, pp. 30 756–30 774, Aug. 2024. DOI: 10.1364/OE.530325. [Online]. Available: https://opg.optica.org/oe/abstract.cfm?URI=oe-32-17-30756.

[250] A. Martınez Jiménez, R. Cernat, A. Bradu, R. Riha, E. A. Proano Grijalva, B. Meyer, T. Ansbaek, K. Yvind, and A. Podoleanu, "Downconversion master slave oct with a bidirectional sweeping laser," *Journal of Biophotonics*, e202400201, 2024.